UNIVERSITY OF CALIFORNIA SAN DIEGO

Alternative Weld Details and Design for Continuity Plates and Doubler Plates for Applications in Special Moment Frames

A dissertation submitted in partial satisfaction of the requirements for the degree

Doctor of Philosophy

in

Structural Engineering

by

Mathew Reynolds

Committee in charge:

Professor Chia-Ming Uang, Chair
Professor Joel Conte
Professor Veronica Eliasson
Professor Pui-Shum Shing
Professor Kenneth Vecchio

2020

The Dissertation of Mathew Reynolds is approved, and it is acceptable in quality and form for publication on microfilm and electronically:

_____

_____

_____

_____

_____

Chair

University of California San Diego

2020

EPIGRAPH

When you're thinking about something you don't understand, you have a terrible, uncomfortable feeling called confusion, it's a very difficult and unhappy business, and so most of the time you're rather unhappy actually… Now the confusion is because we're all some kind of ape, that are kind of stupid, working to try to put the two sticks together to reach the banana and we can't quite make it…. I get that feeling all the time, that I'm an ape trying to put two sticks together, so I always feel quite stupid. Once in a while, though, the sticks go together on me and I reach the banana.

R. Feynman

TABLE OF CONTENTS

LIST OF FIGURES

LIST OF TABLES

ACKNOWLEDGEMENTS

This project was sponsored by the American Institute of Steel Construction (AISC). The Herrick Corporation donated the fabrication of the specimens and the Smith & Emery Company donated inspection services. The author also would like to acknowledge the advice from the Advisory Committee composed of Tim Fraser, Tom Kuznik, Kim Roddis, Subhash Goel, and Brian Volpe with James Malley as the Chair. Dr. Devin Huber, Director of Research at AISC, served as the project manager. Tom Kuznik, Chief Engineer at the Herrick Corporation, was instrumental in the fabrication of the specimens to be tested.

Experimental testing was performed in the Charles Lee Powell Structural. The research is indebted to the commitment and hard work of the staff members: Dr. Christopher Latham, Darren McKay, Mike Sanders, Ander Sander, Abdullah Muhammad, and Noah Aldrich. Steve Porter is also thanked for this production of tension coupons for materials testing.

The author has been privileged to work with Professor Chia-Ming Uang for the supervision of this doctoral work. Special thanks are extended to Professor Francesco Lanza di Scalea for the loading of a high-speed air turbine kit to perform hole drilling for residual stress measurements and to Professor Kenneth Vecchio and Stephen Horvath for their help to use the facilities in the Nano Engineering-Materials Research Center. The author is indebted to Professor Machel Morrison for his thoughtful discussions.

Chapters 1 through 5 of this dissertation has been published as a Structural Systems Research Project (SSRP) Report: Reynolds, M., C-M., Uang, “Alternative Weld Details and Design for Continuity Plates and Doubler Plates for Applications in Special and Intermediate Moment Frames,” *Report No. SSRP-19/03,* and submitted to AISC as the final project deliverable.

Parts of Chapters 2 through 4 are being prepared for submission for publication and may appear in *AISC Engineering Journal*. The author of this dissertation is the primary author of this work; Prof. Chia-Ming Uang will coauthor this work.

VITA

2011 Bachelor of Science in Civil Engineering, University of Alberta, Edmonton.

2012 Master of Science in Engineering, University of Oxford, Oxford.

2012-2016 Bridge Engineer, Buckland and Taylor, Vancouver.

2020 Doctor of Philosophy, University of California San Diego

PUBLICATIONS

Refereed Journals

Reynolds, M., Redl, E., Uang, C-M., (2020), "Method of Instantaneous Centers for the Solution of Eccentric Bolted Connections," *ASCE Journal of Structural Engineering* (Pending).

Reynolds, M., Quang, H., Rafezy, B., Uang, C-M., (2020), "Strength of Partial-Joint-Penetration Groove Welds as Affected by Root Opening, Reinforcing, and Loading Direction," *ASCE Journal of Structural Engineering*, (Accepted).

Reynolds, M., Uang, C-M., (2019), "Updated Equivalent Axial Load Method for Design of Steel Beam-Columns," *AISC Engineering Journal*, Vol. 56, No. 3.

Conference Publications

Reynolds, M., Uang, C-M., (2020), "Alternative Weld Details and Design for Continuity Plates and Doubler Plates for Applications in Special and Intermediate Moment Frames," *Proceedings of 17th World Conference on Earthquake Engineering*, Sendai, Japan.

Saxey, B., Vadimar, Z., Li, C-H., Reynolds, M., Uang, C-M., (2020), "A Predictive Low-Cycle Fatigue Model for Buckling Restrained Braces," *Proceedings of 17th World Conference on Earthquake Engineering*, Sendai, Japan.

Saxey, B., Vadimar, Z., Li, C-H., Reynolds, M., Uang, C-M., (2019), "Predicting low-cycle fatigue life of buckling-restrained braces," *Proceedings of Pacific Conference on Earthquake Engineering*, Auckland, New Zealand.

Technical Reports

Reynolds, M., Uang, C-M., (2019), "Alternative Weld Details and Design for Continuity Plates and Doubler Plates for Applications in Special and Intermediate Moment Frames," *Report No. SSRP-19/03*, University of California San Diego.

Mansing, R., Reynolds, M., Uang, C-M., (2019), "Qualification Testing of CoreBrace Buckling-Restrained Braces for Metro Sports Facility (New Zealand)," *Report No. TR 19/04*, University of California San Diego.

Reynolds, M., Uang, C-M., (2019), "Cyclic Testing of DuraFuse (DF) Moment Frame Connections for SMF and IMF Applications: Series H," *Report No. TR 19/02*, University of California San Diego.

Reynolds, M., Uang, C-M., (2019), "Cyclic Testing of DuraFuse (DF) Moment Frame Connections for SMF and IMF Applications: Series E, F, and G Specimens," *Report No. TR 19/01*, University of California San Diego.

Li, C-H., Reynolds, M., Uang, C-M., (2018), "Fatigue Testing of CoreBrace Buckling-Restrained Braces," *Report No. TR 18/07*, University of California San Diego.

Reynolds, M., Uang, C-M., (2018), "Monotonic Testing of Bolted SidePlate Steel Moment Frame Connections: Transverse Beams of B Series Specimens," *Report No. TR 18/06*, University of California San Diego.

Reynolds, M., Uang, C-M., (2018), "Testing of a Trunnion for Roof Structure Erection of the Los Angeles Stadium at Hollywood Park (LASED)," *Report No. 18/05*, University of California San Diego.

Reynolds, M., Uang, C-M., (2018), "Cyclic Testing of Bolted SidePlate Steel Moment Frame Connections for Biaxial SMF Applications: B Series Specimens," *Report No. TR 18/02*, University of California San Diego.

Reynolds, M., Uang, C-M., (2018), "Cyclic Testing of CoreBrace Buckling-Restrained Braces for Vincent Thomas Bridge," *Report No. TR 18/01*, University of California San Diego.

Reynolds, M., Uang, C-M., (2017), "Effects of Reinforcing, Root Opening and Loading Direction on the Strength of Partial-Joint-Penetration Groove Welds," *Report No. TR 17/03*, University of California San Diego.

Reynolds, M., Uang, C-M., (2017), "Cyclic Testing of Bolted SidePlate Steel Moment Connections for SMF Applications: Specimens U4 and U5," *Report No. 17/02*, University of California San Diego.

ABSTRACT OF THE DISSERTATION

Alternative Weld Details and Design for Continuity Plates and Doubler Plates for Applications in Special Moment Frames

by

Mathew Reynolds

Doctor of Philosophy in Structural Engineering

University of California San Diego, 2020

Professor Chia-Ming Uang, Chair

Steel Special Moment Frames (SMF) are regularly used as seismic force-resisting systems due to their excellent ductility and wide accommodation of building floor plans and heights. The current AISC Seismic Provisions require the use of reinforcing continuity plates and dictate their size based on a set of rules conservatively inferred from experimental testing. These rules often result in the unnecessary reinforcement of columns and usually require costly complete-joint-penetration (CJP) groove welds to fasten the reinforcing plates. Full-scale testing of 10 moment frames was performed to investigate the design of these continuity plates and their weldments. Six of these frames were exterior connections utilizing the prequalified Reduced Beam Section (RBS) connection, while the remaining four were interior connections utilizing the prequalified Welded Unreinforced Flange-Welded Web (WUF-W) connection. While violating the current continuity

plate requirements, all 10 connections surpassed the 0.04 rad story drift requirement of SMF according to the prequalification criteria of the AISC Seismic Provisions. Experimental testing was also performed to measure, for the first time, the in situ residual stresses of a continuity plate.

Detailed parametric finite element modelling and modern fracture mechanics using the Cyclic Void Growth Model for ductile fracture prediction was used to develop an amended set of limit states of reinforced columns. These amended limit states, in conjunction with a newly proposed width-to-thickness requirement, permit the design of column reinforcement based on a rational plastic approach. A fillet weld design that capacity protects the weldments based on a von Mises yield surface is included in this new plastic design method. This new experimentally verified design basis for fillet weldments of continuity plates results in significant fabrication savings. It was also found that sizing the doubler plate weldments for the average developed shear flow according to the relative doubler plate stiffness was adequate to fasten the doubler plate. This results in significant savings over current requirements which currently require welds to develop the shear strength of the doubler plate.

1. INTRODUCTION

1.1. Introduction

Steel moment frames are a common Seismic Force-Resisting System (SFRS) because of the architectural freedom they offer. Moment frames permit open bays and eliminate the need for braced frames or shear walls. These systems develop plastic hinging through the plastification of the beams and the base of the first story-column. The use of relatively stocky width-to-thickness ratios prevents undesirable levels of strength degradation due to local buckling of the flange or web of the beam. Stable hysteretic behavior of the frames is encouraged by providing lateral bracing of the beams, which prevents lateral-torsional instability. These SFRS have excellent levels of ductility which allow designers significant reductions of the required elastic seismic design forces. However, after the 1994 Northridge Earthquake, significant damage to steel moment frames was observed at drift levels far below their assumed capacity. The observed damage instigated a significant research effort, which made significant changes to the detailing of steel moment frames.

The magnitude 6.7 Northridge Earthquake (1994) in the San Fernando Valley resulted in numerous fractures at the complete-joint-penetration (CJP) groove weld between the beam flanges and column flange of a steel moment frame connection. Similar fractures were also observed in steel moment frame buildings following the magnitude 6.9 Kobe Earthquake (1995) in Japan. An after-earthquake survey of the damage found nearly 1000 weld fractures. Following this, a consortium of associations and researchers known as the SAC Joint Venture initiated an 6-year research program to investigate the source of the fractures. They found that a combination of low fracture toughness weld metals, a lack of control of base metal properties, and connection geometries susceptible to high localized strain conditions were the main cause of the fractures.

After the findings of the SAC Joint Venture, strict control of the use of steel moment frames has been imposed through AISC 341, the Seismic Provisions for Structural Steel Buildings (AISC 2016b), AISC 358, the Prequalified Connections for Special and Intermediate Steel Moment Frames for Seismic Applications (AISC 2016c), and AWS D1.8 the Structural Welding Code-Seismic Supplement (AWS 2016).

These controls involve mandatory use of notch-tough weld electrodes for welds designated as Demand Critical (DC), modified access hole geometries, and weld root treatments to minimize sharp discontinuities. However, the most important provision requires that Special Moment Frames (SMF) and Intermediate Moment Frames (IMF) match the dimensions and detailing of previously qualified connections. For example, the Seismic Provisions stipulate that Special Moment Frames (designated as special due to their 'special' detailing requirements) must complete one cycle of 0.04 radian (rad) drift without significant strength degradation. The imposed drift follows a standard loading protocol, which gradually ramps up the imposed displacement. Due to their high ductility, SMF enjoys a high Response Modification Factor, R, and have no height limits for any Seismic Design Category tabulated in ASCE 7-16 (ASCE 2016).

The Prequalified Connections document (AISC 358) summarizes the geometry limitations and detailing requirements of prequalified connections since connection testing would be prohibitively expensive to perform on a project basis. A number of these connections are proprietary, wherein the intellectual property is licensed during the design phase. Two standard non-proprietary connections are the Reduced Beam Section (RBS) and the Welded Unreinforced Flange with Welded Web (WUF-W). When the prescriptive detailing requirements are adhered to, these two connections demonstrate the ability to satisfy the ductility requirements of SMF. Some of the prescriptive detailing requirements enacted after the Northridge Earthquake are recognized

to be conservative. Specifically, the welding requirements of continuity plates and doubler plates for SMF and IMF. These plates are installed between the column flanges to stiffen the connection and ensure the desired inelastic behavior of the frame. The stiffening elements accomplish this by preventing excessive column flange deformation which would otherwise lead to premature failure of the connection, and by reinforcing the high shear panel zone such that plastic hinging occurs in the beam.

The Seismic Provisions have two requirements dictating when a continuity plate shall be used in a connection. They are: (1) when the available strength of the column as computed for the Web Local Yielding (WLY) or the Flange Local Bending (FLB) limit states of Section J10 of the Specification for Structural Steel Buildings (AISC 2016) are insufficient to resist the flange force from the moment connection, and (2) when the column flange thickness is less than the beam flange width divided by 6. The latter requirement is referred to as the 'Lehigh' Criterion herein for the institution of the founding study. When either of these requirements dictates the use of a continuity plate, the plate thickness shall be 50% of the adjacent beam flange thickness for exterior (one-sided) connections or 75% of the thicker adjacent beam flange for interior (two-sided) connections. The current requirement of the weld between the continuity plate and the column flange is shall be a CJP groove weld; the use of a CJP weld rather than a fillet weld has significant economic implications. These welds require additional fabrication to bevel the edge of the plates and install a backing bar, additional weld volume, and more stringent inspection requirements. As per Section N of the AISC Specifications, CJP welds in Risk Category III or IV (as defined in ASCE 7-16) require 100% Ultrasonic Testing (UT). This inspection requirement for CJP welds significantly increases the cost of fabricating the continuity plates—an increase so significant that

some designers prefer to increase the size of the column to mitigate the need for additional stiffening elements (Carter 1999).

Adequately designing the fillet welds for continuity plates would require the reconciliation of the flow of forces through the joints. A CJP weld does not possess this requirement as the weld develops the strength of adjacent plates—implying that failure of the plate would occur before the weld. Intimately linked to the continuity plate is the doubler plate. When present, this plate acts to double up the web to resist the high shear forces that develop within the panel zone of the moment connection. The high shear force is a result of the concentrated flange forces which resolve the beam moment as a force-couple. These flange forces flow through the column flanges into the continuity plates before ultimately loading the panel zone in shear. According to the Seismic Provisions, vertical weldments of the doubler plates to the column flanges are required to develop the shear strength of the plate—irrespective of the demand that may exist for the plate.

A pilot study that used a flexibility design method (Tran et al. 2013) tested two exterior RBS connections with fillet welded continuity plates (Mashayekh and Uang 2018). The flexibility design methodology was developed under the assumption that the continuity plates remain elastic. However, intentional under sizing of a continuity plate demonstrated excellent performance when continuity plates are permitted to yield. The inception of this testing program occurred after the preliminary success of the pilot study.

1.2. Research Objective and Scope

The objective of the research project was to conduct full-scale testing and detailed finite element analysis to explore more efficient design methodologies for the welding of the column stiffening. The physical testing forms the phenomenological evidence to adopt a plastic methodology in the design of continuity plates, and the weldments of continuity and doubler plates. Included in this are vertical doubler plate welds that do not develop the strength of the plate and fillet welds for the continuity plate to column connection. Two types of prequalified connections tested in interior and exterior configurations are used to explore these two objectives. Phase 1 of the research includes RBS exterior connections (only one beam attached to the column) using both shallow and deep columns. Phase 2 of the research includes WUF-W interior connections (two beams attached to the column). For Phase 2, shallow columns were not considered as the AISC 341 requirement of Strong Column Weak Beam (SCWB) to prevent soft story mechanisms force thick flanges that do not require stiffening. The specimens with continuity plates were designed using a plastic methodology similar to that which exists in AISC 360-16 §J10. The ultimate continuity plate strength is verified by using a plastic interaction equation. These specimens used fillet welds to join the continuity plates to the column flanges using a simple fillet weld design rule.

The Phase 1 specimens are also designed to explore the current limit states of column stiffening (FLB and WLY) by omitting continuity plates in three specimens. The omission of the continuity plates in these specimens violates the Lehigh Criterion. This criterion is found to be the only code provision that requires the use of a continuity plate for these specimens (i.e., the strength limit state of FLB does not require a stiffening plate). For one of these specimens, the WLY limit state shows that the column web alone is insufficient for the concentrated flange force. A doubler

plate instead of the convention of using a continuity plate was used to reinforce the column web. A new procedure was used to design vertical welds that do not develop the shear strength of the doubler plate. The Phase 2 specimens endeavored to test fillet welded continuity plates in WUF-W connections. These connections typically see much higher flange forces than an RBS connection, thereby challenging the continuity plate welds. Table 2.1 shows the test matrix for both phases of the testing.

1.3. Literature Review

1.3.1. The Pre-Northridge Connection

Before exploring the changes that occurred after 1994, a brief history of steel moment frames is provided. The use of steel moment frames for lateral force-resisting systems has been in everyday use since the turn of the 20th century. Construction of the first moment frames used built-up 'H' shapes made from riveting four angles to a plate that formed the web. Connections were stiffened using gusset plates at the connection to provide a fully-restrained connection. Concrete encasement of the steel framing in these structures was standard for added fire protection of the steel skeleton. The 1906 San Francisco Earthquake and devastating fires demonstrated the excellent ductility of steel moment frames—some of the only surviving buildings in the downtown core were steel buildings. However, it is possible this was primarily due to the internal redundancy of these steel frames due to the riveted connections and built-up shapes, and the concrete encasement providing superior fire resistance (Hamburger et al. 2016).

After World War II, the predominant architectural style began to change with a transition to the use of glass curtain walls. This transition saw the robust gusseted connection replaced with smaller angles and 'T' sections to form the connection. In the 1960s, there was a preferential use of steel moment frames over other systems due to their previously demonstrated excellent

performance and lack of height of limits governing their use; nearly every tall building constructed in this era on the west coast of the United States employed steel moment frames. Innovative research at this time focusing on several different configurations of field welded moment connections demonstrated sufficient ductility (Popov and Pinkney 1969). In the 1970s, riveting fell out of everyday use, which led to using high-strength bolted shear tabs and CJP welds on each beam flange. Shielded Metal Arc Welded (SMAW) was the welding process of choice for field welding as tanks of inert gas were not required when performing the field welding.

During the 1980s, a sharp increase in the cost of labor resulted in engineers attempting to minimize the amount of welding. Concentrating the lateral force-resisting system into a limited number of bays was a common measure to decrease the cost of construction. Decreasing the number of moment frames in a building decreases the system-level redundancy. In 1988 the Uniform Building Code (UBC) codified the prequalified bolted web-welded flange moment connection, this connection has become known as the "pre-Northridge" moment connection (UBC 1988). Additionally, during this time, fabricators transitioned to using a self-shielded variety of Flux-Core Arc Welding (FCAW). This welding process has high deposition rates and does not require the welder to interrupt welding to reinsert a new stick electrode. Figure 1.1 shows a typical pre-Northridge Connection. Prior to events of 1994 there was little indication that the modern moment frame connection would develop less ductility than expected. The only known indication came in 1993 with a testing program which demonstrated significant variability in ductility capacity when using common FCAW welding electrodes and bolted shear tabs (Englehardt and Hussan 1993).

1.3.2. The Northridge Earthquake Damage

The 1994 magnitude 6.7 Northridge Earthquake saw many steel moment frame structures with brittle fractures in the connection region. Figure 1.2 shows an example of one of the fractures observed after the earthquake. Many of these fractures occurred after being subjected to rotations not more than 0.01 rad (Englehart and Sabol 1997). The damage due to the earthquake was immediately apparent as several of the buildings which experienced fractured connections were under construction, and as such, the steel frame was easily accessible. Similar fractures were observed in Japan after the 1995 magnitude 6.9 Kobe Earthquake.

The Northridge Earthquake caused an estimated 30 billion dollars of damage in Southern California (FEMA 2000e). Although damage to structures, especially older structures, was not peculiar, extensive damage to steel moment frames, once thought invulnerable, troubled the engineering community. Steel structures had performed well in previous earthquakes, which had precipitated significant changes in seismic detailing of other building materials. For example, the 1971 San Fernando Earthquake is seen as an incipient event for prescriptive ductile detailing of concrete in the United States (Hamburger 2006). These previous earthquakes did not demonstrate the steel fractures observed in 1994 since relatively few steel buildings were present in the areas affected by the most severe ground motions. After the Northridge earthquake, a significant inspection effort revealed fractures in moment frames in the San Francisco Bay area that were believed the result of the 1989 Loma Prieta Earthquake (FEMA 2000e). In response to the unanticipated damage, the Federal Emergency Management Agency (FEMA), with coordinated efforts from the National Science Foundation (NSF) and the National Institute of Standards and Technology (NIST), sponsored the SAC Joint Venture to investigate the fractures. The SAC Joint Venture consisted of the Structural Engineers Association of California (SEAOC), the Applied

Technology Council (ATC), and California Universities for Research in Earthquake Engineering (CUREe) made up of eight academic institutions in California at the time.

1.3.3. The Post-Northridge Connection

Over the 6 years following the Northridge Earthquake, the findings of the SAC Joint Venture were published in over 50 reports. The results from the SAC reports are distilled in a series of reports published by FEMA:

- FEMA 350–Recommended Seismic Design Criteria for New Steel Moment-Frame Buildings (FEMA 2000a).
- FEMA 351–Recommended Seismic Evaluation and Upgrade Criteria for Existing Welded Steel Moment Frame Buildings (FEMA 2000b).
- FEMA 352–Recommended Postearthquake Evaluation and Repair Criteria for Welded Steel Moment-Frame Buildings (FEMA 2000c).
- FEMA 353–Recommended Specifications and Quality Assurance for Steel Moment Frame Construction for Seismic Applications (FEMA 2000d).
- FEMA 354–A Policy Guide to Steel Moment Frame Construction (FEMA 2000e).

The first four reports are abridged recommendations, with the fifth report, FEMA 354, provided as a non-technical guide to explain the inherent risk and mitigation strategies. Detailed reports which show the basis of the first four reports are published as reports FEMA 355A through FEMA 355F (FEMA 2000f).

The organized research effort looked critically at the standard pre-Northridge connection fabricated during the 1970s and 1980s. It became apparent as the steel moment frames evolved with emerging technologies and were influenced by the higher cost of labor that their behavior

drifted from the earlier demonstrably ductile steel frames. Some of the fundamental underlying causes and resulting modifications which define a post-Northridge connection are as follows:

- The most common weld electrodes in the pre-Northridge era were either E70T-4 or E70T-7 using the self-shielded FCAW process (Engelhardt and Sabol 1997). Although these electrodes realize the minimum specified strength of 70 ksi, they typically have poor toughness, achieving a Charpy V-Notch (CVN) Toughness of 5 to 10 ft-lbs at room temperature. Experimental testing of SMF connections with weld electrodes that realize a higher notch toughness (E70TG-K2 or E70T-6) demonstrates significantly higher inelastic drift capabilities (Johnson et al. 2000). A Post-Northridge connection classifies the CJP welds adjoining the beam-to-column as Demand Critical (DC). AWS D1.8 stipulates that DC welds must achieve a CVN toughness of 20 ft-lbs at 0°F and 70 ft-lbs at 70°F (AWS 2016).
- The use of bolted shear tabs and welded beam flanges was found not to be conducive to the intended behavior transmitting the beam shear through the web. Experimental testing demonstrated that bolted shear tabs permit relative slip at the faying surface. This slip has two consequences: (1) flexural forces are carried almost entirely through the beam flanges, and (2) the web does not carry the shear of the section as assumed. Carrying the beam shear through the flanges results in high secondary bending stresses, which exacerbate the strain condition at the extreme fiber of the flange. Most post-Northridge connections use field welded beam webs to prevent slip. Field welding of the beam web is readily accomplished by using the shear tab with bolts to frame and plumb the structure as before but also act as a backing bar for a vertically orientated CJP weld to fasten the web of the beam to the column web. In some connection types, it is also required to supplement this weld with a

perimeter weld around the shear tab to stiffen the web of the section. The welding of the beam weld has not eliminated the issue of secondary stresses due to a complicated stress pattern in the beam adjacent to a moment connection. Goel et al. (1997) showed that classical beam theory fails to capture the behavior in this region and that a modest portion of shear transfers through the flanges regardless of the welded beam web.

- A survey of the damage following the Northridge Earthquake revealed that a significant portion of the damage originated at the bottom flange backing bar and propagated through the column flange or beam flange. The column fractures either propagated transversely through the column or by taking a divot out of the column face (Engelhardt and Sabol 1997). Backing bars are required in most CJP welds to catch the molten weld metal during the initial passes of the weld. These backing bars would commonly be left in place as their presence was not believed to greatly influence the performance of the connection. However, research has shown that the discontinuity between fused and unfused portions of metal at the weld root results in a notch-like condition, increasing the fracture potential (Chi et al. 1997). This imperfection is impossible to detect visually, and UT testing has a low sensitivity to flaw detection at the root (Paret 2000). This notch-like condition is the most critical at the beam bottom flange where it exists at the extreme fiber. A post-Northridge connection requires removal of the bottom flange backing bar after welding the CJP weld. A reinforcing fillet weld is added after the removal of the backing bar to reinforce the root of the CJP. A concession is made at the top flange, wherein the backing bar can remain, but a reinforcing fillet must be made to underside of the backing bar.

The most significant impact on the steel moment frame construction following the Northridge Earthquake is the requirement that connections intended for use in Special or

Intermediate Moment Frames must be shown to demonstrate an adequate level of ductility through full-scale testing. For SMF, the drift requirement is 0.04 rad, while for IMF, the drift requirement is 0.02 rad in AISC 341 (AISC 2016b). The Prequalified Connections for Special and Intermediate Steel Moment Frames for Seismic Applications (AISC 358) was released to assist engineers in selecting an appropriate connection (AISC 2016c). These connections adopt one of two strategies to improve the ductility of steel moment frames: they may reinforce the connection at the face of the column, or they may weaken the beam. In either strategy, the goal is to force the plastic hinge to occur away from the face of the column to limit the strain demand on the beam-to-column CJP welds. There are limitations to these connections based on the geometry of the connections that have successfully demonstrated adequate performance through testing. The prequalification requirement has spawned several proprietary connections that have been developed by private enterprises. All SMF and IMF connections are reviewed by a standards committee, the Connection Prequalification Review Panel (CPRP) of AISC. Figure 1.3 shows examples of prequalified RBS and WUF-W connections.

During the experimental testing of the SAC Joint Venture, most of the moment connections utilized continuity plates with CJP welds—a response to the surveyed damage of the Northridge Earthquake, revealing that more damage occurred in frames that did not have continuity plates (Tremblay et al. 1998). Since the initial development of the prequalified connections, several relaxations have been made to the provisions. These concessions are: (1) the CJP weld fastening the continuity plate to the column flange may have its backing bar in place, and (2) the weld fastening the continuity plate the column web (or doubler plate) may be any weld that develops the strength of the plate.

1.3.4. Development of Fracture Mechanics to Simulate Beam-to-Column Fracture

The beam-to-column moment connection is a highly restrained location subjected to large scale cyclic strains. Traditional fracture mechanics, either Linear Elastic Fracture Mechanics (LEFM) or Elastic-Plastic Fracture Mechanics (EPFM), are based on the nature of the stress field around a pre-existing flaw and are valid only in situations where the stress fields in the vicinity of the crack behave in a bijective manner. For example, the critical stress intensity, K_{IC}, or the critical value of the J-integral, J_{IC}, must resemble the singularity stress field derived using Elasticity in their respective regions (Kanvinde 2017). Generally, this is true under small-scale yielding, where the plastic region around a crack tip is small. When the stress fields lose their uniqueness in a significant region during large scale plastic flow, or when a pre-existing flaw is not present, these methods fail to provide a reliable fracture metric. In these situations, local fracture models can characterize the fracture potential. To build local fracture models, researchers have turned to work done by Rice and Tracy (1969), which solved for the rate of growth of a spherical microvoid in a stress field or the Gurson-Tvergaard-Needleman (GTN) metal plasticity model which models the metal as a softening porous medium (Anderson 2017). The drawback to these local models is that a high-fidelity finite element simulation with calibrated plasticity models must be used to track the related indices.

These ductile fracture models attempt to fracture as the nucleation, growth, and coalescence of microvoids. The nucleation of these microvoids is due to plastic flow around material inclusion or dislocation pileups at grain boundaries. The growth of microvoids occurs due to the localization of strain around the void. Ductile fracture propagates as the plastic strain localizes across a dominate plane of voids. Rice and Tracy derived the growth rate of a spherical void in the stress field as a function of the triaxiality of the stress state (see Eq. 1.1).

$$\frac{dR}{dR_0} = 0.283\, d\bar{\epsilon}^p e^{1.5T} \tag{1.1}$$

where R and R_0 are the current and original radius of a void and T is the triaxiality ratio, expressed as the ratio of hydrostatic stress, σ_H, to von Mises stress, σ_{vm}:

$$T = \frac{\sigma_H}{\sigma_{vm}} \tag{1.2}$$

The hydrostatic stress is related to the Cauchy stress tensor as $\sigma_H = \sigma_{\alpha\alpha}/3$, and the von Mises stress is given as $\sigma_{vm} = \sqrt{\frac{3}{2}\sigma'_{ij}\sigma'_{ij}}$ where σ'_{ij} are the deviatoric components of the Cauchy stress tensor. Finally, $d\bar{e}^p$ is an increment of effective plastic strain ($PEEQ$):

$$\bar{\epsilon}^p = \sqrt{\frac{2}{3}\epsilon'_{ij}\epsilon'_{ij}} \tag{1.3}$$

Hancock and Mackenzie (1976) postulated that the plastic strain at failure is inversely proportional to the rate of void growth:

$$\bar{\epsilon}^f = \alpha e^{-1.5T} \tag{1.4}$$

where α is a material property typically between 1 and 3 for plain steel. Hancock and Mackenzie demonstrated reasonable predictions of ductile fracture using this approach. They were also able to demonstrate a significantly lower failure strain of a hot-rolled material when loaded through-thickness rather than parallel to the direction of rolling. The interpretation of Rice and Tracey's work to generate a failure strain by Hancock and Mackenzie forms the foundation of the Stress Modified Critical Strain (SMCS) model to predict fracture. Using triaxiality ratio allows the characterization of the stress state into high ($T \geq 1.5$), moderate ($0.75 \leq T < 1.5$), and low ($T < 0.75$). The connection region of a SMF demonstrates high triaxiality—resulting in a low plastic strain at fracture.

Several researchers leveraged ductile fracture mechanics by using indices rooted from the work of Rice and Tracy. For Example, Ricles et al. (2003) used the $PEEQ$ Index (Eq. 1.5) and detailed finite element analysis to compare differences in the detailing of the weld access holes in WUF-W connections.

$$PEEQ_I = \frac{\bar{\epsilon}^p}{\epsilon_y} \tag{1.5}$$

El-Tawil et al. (2000) used the rupture index to investigate the required thickness of continuity plates and the size of weld access holes:

$$RI = \frac{\frac{\bar{\epsilon}^p}{\epsilon_y}}{e^{-1.5T}} \tag{1.6}$$

A key unknown in using these fracture metrics to determine the point of fracture is a characteristic length in which the metric has a positive indication (Hancock and Cowling 1980, and El-Tawil et al. 1999). The characteristic length is a well-known issue, as ductile fracture occurs only when an associated finite volume of material has reached a critical void growth rate (Kanvinde 2017). Using a representative characteristic length avoids erroneous conclusions that occur due to strain localizations that occur near strain risers in a finite element model. The suggested characteristic length is 2-10 times the material grain size; for mild steel, the characteristic length is suggested to be 0.005 in. The work done by Ricles and El-Tawil used either $PEEQ_I$ or RI as a relative metric to compare details without trying to predict the instance of fracture. Han et al. (2017) calibrated the RI from observed fractures of WUF-W specimens to determine a critical value of RI as 1,150 for the E71TG-1C notch-tough electrode. It was not cited what the characteristic length was used to determine this value.

Modern local fracture models that can capture the low-cycle fatigue condition at the beam-to-column interface are the Cyclic Void Growth Model (CVGM) discussed by Kanvinde and

Deierlein (2004), and more recently the Stress-Weighted Damage Model (SWDM) discussed by Smith et al. (2014). These two methods have shown viability in predicting ductile fracture in the high inelastic strain regions of SMF subjected to accidental defects (Abbas 2015). These modern methods integrate separately the plastic strain histories of tension and compression strain cycles. This separate is important as the assumed uniform expansion of a microvoid under tension is not simply equal and opposite when subjected to the reverse excursion. Instead compression strains compress the minor direction of the voids resulting in an oblate void perpendicular to the direction of loading. Locally increasing the curvature of the voids results in a stress riser which further localizes strains, or can lead to decohesion and cleavage (Kanvinde 2004).

1.3.5. Continuity Plate and Doubler Plate Research

Prior research related to the size and welding of continuity plates and doubler plates is summarized below.

- Popov et al. (1986) tested 8 half-scale, two-sided pre-Northridge connections. The tests compared the performance of the connection with and without continuity plates, with and without doubler plates, and with a fillet welded or CJP welded continuity plate. All of these specimens fractured near or at the beam flange CJP weld—most of them demonstrating little ductility. The authors observed that the presence of a continuity plate improved the performance. These continuity plates were designed based on the AISC Specifications at the time, using the nominal yielding flange force entering the column as a concentrated load. Two specimens used fillet-welded continuity plates with double-sided fillet welds of size 5/8 times the thickness of the continuity plate, t_{cp}. Of the two fillet welded specimens tested, one experienced a brittle fracture of the fillet welds. However, the same column experienced lamellar tearing when retested with a CJP welded continuity plate; poor

metallurgy is likely a culprit. Based on the results of this test, the authors recommended that CJP welds should be used for continuity plates. Additionally, the authors stipulate that designing a continuity plate based on the nominal yielding strength of the beam is unconservative based on the observed yielding and buckling of the continuity plates.

- Kaufman et al. (1996) tested several moment frame connections and determined that fillet-welded continuity plates were adequate when notch-tough electrodes were used for the beam flange CJP welds.
- In 1997 AISC released an advisory that welding of stiffeners and doubler plates must not be made within the k-area of the rolled column due to several observed fractures during fabrication (AISC 1997). Malley and Frank (2000) documented the fracture toughness of k-area of W-shaped sections of A992 steel. They determined that this area has 25% lower upper-shelf CVN toughness, which is postulated to be due to of the cold-working of the material during the straightening process. The authors determine that the lower toughness of the k-area material coupled with the high restraint of welding continuity plates and doubler plates leads to unanticipated fractures during fabrication. Tide (2000) corroborated this conclusion and reproduced the lower toughness material by straining a coupon of material to 15% and performing CVN testing after aging the material.

This research is the premise of AWS D1.8 §4.2, which dictates that continuity plate corner clips must extend at least 1.5 in. into the web from the tabulated *k* dimension. AISC 358 §3.6 repeats the corner clip criteria. Yee et al. (1998) further demonstrated by modeling the thermomechanical effects of welding that the high weld volumes associated with CJP-welded continuity plates develop higher residual stresses than a fillet-welded continuity plate. However, Deierlein and Chi (1999) found that the effect of welding residual stress

is most significant during the elastic behavior of the connection. This conclusion was corroborated by Matos and Dodds (2000), who found that the effects of residual stress have minimal effect on the connection after the beam has reached its plastic limit state.

- Engelhardt et al. (1998) tested five one-sided RBS connections using continuity plates matching the flange thickness of the adjacent beams and fastened to the column flanges using CJP welds. In an article summarizing testing of RBS connections during the SAC Joint Venture, Engelhardt et al. explains that no connections have been tested so far without continuity plates. As a cost-saving measure, it was mentioned that the removal of the steel backing of the continuity plate CJP weld is not required (Engelhardt 1999). More recent testing of exterior RBS connections using continuity plates of thickness equal to be the beam flange thickness was also only tested using CJP welds fastening the continuity plate to the column flange [Chi and Uang (2002) and Lee et al. (2005)]. Chi and Uang found that even continuity plates equal to the beam flange thickness may yield when using A36 steel plate. This research also found that RBS-type connections framing into deep columns are more susceptible to lateral-torsional buckling instability due to the lower warping stiffness of the column.
- Bjorhovde et al. (1999) tested nine different moment frame connections using fillet-welded continuity plates. All of the specimens utilized W14×176 columns and W21×122 beams with welded cover plates to reinforce the connection. Double-sided fillet welds of size $5/8t_{cp}$ were used to fasten continuity plates matching the thickness of the adjacent beam flange.
- El-Tawil et al. (1999) performed finite element analysis on a pre-Northridge connection tested during the SAC Joint Venture (Specimen PN3). This specimen was a W36×150

beam attached to a W14×257 column that only achieved 0.01 rad of inelastic drift before experiencing a brittle fracture (Popov et al. 1996). By comparing values of RI during a parametric finite element analysis, the authors concluded that a weak panel zone results in a higher fracture potential at the beam-to-column interface at high drift levels.

- El-Tawil et al. (2000) continued work on their finite element analysis of Specimen PN3. The authors concluded by comparing the RI at the beam flange-to-column interface that a continuity plate equal to 50% of the adjacent beam flange thickness was adequate in stiffening the joint. Continuity plates of thicknesses greater than this saw diminishing returns. Furthermore, the authors postulated that thicker continuity plates might result in a k-area fracture of the column due to the increased volume of welds required.
- Dexter et al. (2001) tested 47 pull plate specimens consisting of a monotonically loaded plate welded on each face of a column. The focus of the research was on the through-thickness strength of a heavy rolled section subjected to a tension force coming from a beam flange. In efforts to force a failure in the through-thickness direction, 100 ksi material was used for the pull plates. No instances of lamellar tearing were observed, which is postulated to be a consequence of modern material manufacturing processes. Only 1 of 12 specimens using a fillet-welded continuity plate demonstrated a fracture of the fillet welds. This specimen had inadequate corner clips of the continuity plate resulting in the continuity plate welds extending into the k-area of the column. The resulting fracture propagated through the fillet-welded continuity plate and the k-area of the column.
- Ricles et al. (2002) tested 6 one-sided (Specimens T1 to T6) and 5 two-sided (Specimens C1 to C6) moment frame connections. All of the specimens tested in this study utilized a W36×150 beam. These connections were the first WUF-W specimens tested with the

modified welded access hole developed by Mao et al. (2000). Several specimens did not use the modern shear tab connection detail with supplemental fillet welds—these specimens performed markedly worse than those with the modern shear tab connection. Additionally, one specimen fractured prematurely in the beam plastic hinge due to the presence of a welded shear stud. Four specimens (Specimens T5 and T6 with a W14×311 column, Specimen C1 with a W14×398 column and Specimen C3 with a W27×258 column) were tested without a continuity plate. All four of these specimens achieved at least 0.05 rad drift. Specimens C2 and C4 were nominally identical to Specimens C1 and C3, respectively, except that they used a continuity plate that matched the thickness of the adjacent beam flange. Both specimens achieved one cycle higher drift when tested with a pair of continuity plates. CJP welds were used to affix all of the continuity plates. In the case of Specimen C3 the beam flange width-to-column flange thickness ratio (b_{bf}/t_{cf}) was equal to 6.8—significantly over the suggested limit of 6.0 of the Lehigh Criterion.

- Ricles et al. (2003) provided a detailed finite element study of the previously tested 11 specimens. The study compared the $PEEQ$ demand at the root of the CJP weld across the testing cohort. Finite element results demonstrated that when the $b_{bf}/t_{cf} < 6.0$, the addition of a continuity plate only marginally influenced the $PEEQ$ across the width of the CJP weld; the only observed effect was that the $PEEQ$ demands became more uniform across the flange with the same resulting peak value. When the specimen with b_{bf}/t_{cf} of 6.8 was tested, the peak value of $PEEQ$ was observed to decrease when adding a continuity plate. However, whether a continuity plate was equal to one-half or the full thickness of the adjacent beam flange did not influence the results. Note that the clear beam span-to-depth ratio of Specimens C3 and C4 is equal to 9.1; this specimen is similar to Specimen

W1 tested and to be reported in Chapter 4. The study also corroborated an earlier conclusion from El-Tawil et al. (1999) that a weak panel zone with column kinking tends to exacerbate the fracture potential.

- Hajjar et al. (2003) tested a series of monotonic pull plate specimens to investigate the WLY and FLB limit states. Two of these specimens were fabricated with continuity plates half the thickness of the pull plate with fillet welds of size equal to (2/3)t_{cp}. The column size of these specimens was W14×132. It was observed that yielding occurred in the continuity plate and fracture of the fillet welds did not occur.
- Lee et al. (2005a) tested six two-sided WUF-W specimens. All of the specimens used a W24×94 beam, while the column size and column stiffening detail were varied. Three of these specimens (Specimens CR1, CR2, and CR5) did not use continuity plates, while Specimens CR2 and CR5 violated the FLB criterion by using the hardened beam flange force as a demand. All three of these specimens completed at least one cycle of 0.04 rad. Given this observation, the authors discuss that the FLB limit state contained in ASIC 360 §J10, developed for non-seismic applications, appears satisfactory for seismic demands when notch-tough electrodes are used. Specimen CR3 used a fillet-welded continuity plate with a thickness equal to 60% of the adjacent beam flange thickness. This thickness was chosen based on satisfying the width-to-thickness requirement of unstiffened plates subjected to axial compression:

$$\frac{b}{t} < 0.56\sqrt{\frac{E}{F_y}} \tag{1.7}$$

The fillet weld was sized to develop the strength of the continuity plate and resulted in a double-sided fillet weld of size $0.75t_{cp}$. This specimen completed 14 cycles of 0.04

rad drift before low-cycle fatigue occurred in the beam flange CJP weld. Strain gauging of the continuity plate revealed that the continuity plate did not yield across its breadth. Based on this observation, it was concluded that fillet welds might not need to develop the strength of the plate. The authors also observed ductile tearing at 0.03 rad of the beam flange CJP weld at the toe of the last weld pass, which creates a radius at the re-entrant corner of the CJP weld. One specimen of this study, Specimen CR4, experienced a brittle fracture at 0.02 rad drift. Material testing revealed that the CJP weld of this specimen had low toughness—despite being performed using an E70T-6 notch tough electrode.

Further investigation also revealed that Specimen CR1 failed to meet the notch toughness requirements of a post-Northridge connection. No conclusion was made regarding why these specimens had a lower notch toughness then expected despite using a qualified electrode. A companion paper published looked at the relative strength of the panel zones and concluded that weak panel zones could develop excellent inelastic performance (Lee et al. 2005b). These panel zones used doubler plates that utilized fillet welds sized to develop the shear strength of the doubler plate for the vertical weld attaching the doubler plate to the column. The doubler plates were beveled such that they cleared the radius of the column flange to column web junction.

- Shirsat and Englehardt (2012) investigated the attachment details for the doubler plate. This work was performed using finite element analysis and explored the effect of welding different edges of the doubler plate, extending the doubler plate beyond the connection region, and of using asymmetric doubler plates. This research effort demonstrated that welding the top horizontal edges of extended doubler plates provided minimal benefit beyond stabilizing doubler plates about to buckle. The authors also found that the demands

imposed on the vertical welds were between 0.5 and 1.3 times the expected shear yielding strength of the plate—an effect attributed to the strain hardening of the doubler plate. Gupta (2013) continues this research and further demonstrates that the loading condition at the flange level of a doubler plate is mostly in the transverse direction and well beyond the nominal yielding strength of the plate. The author observed that the welding of the continuity plate to the doubler plate does not result in overstressing the doubler plate. The final remark was that extending the doubler plates beyond the level of the beam flanges demonstrates better panel zone behavior.

- Han et al. (2014) tested four exterior WUF-W connections using beam depths of 27 in. and 35 in. The authors found that the deeper beam depths failed to satisfy the 0.04 rad drift requirement. They postulated that the root cause of this was due to two reasons: (1) the weld access hole, although still compliant to the AISC 358 (2016) detailing requirements, was quite steep relative to those shown to be satisfactory by Ricles et al. (2002); and (2) that the clear span-to-depth ratio was 6.8, slightly below the minimum value of 7.0 required by AISC 358 (2016). The continuity plates in these specimens matched the thickness of the beam flange and used CJP welds for the weldment to column flange. Han et al. later tested the same two specimens with shallower weld access holes and found satisfactory performance (Han et al. 2016). The authors then demonstrated using detailed finite element models and the Rupture Index, RI, that shallow welded access holes have less propensity to fracture (Han et al. 2017).
- Shim (2017) performed experimental testing on nine WUF-W connections and one Bolted Flange Plate (BFP) connection. The research explored the role of relative panel zone strength to the overall ductile performance of the moment frame and the role of axial

tension on the panel zone strength. The columns tested were either W33×263, W14×398, or W12×106. The only specimen which did not achieve at least 0.04 rad drift was Specimen UT05, which used a 1/16-in. tungsten electrode embedded into the doubler plate CJP weld as an intentional defect. It is unclear whether this intentional defect was the source of the fracture, as the fracture appeared to originate at the termination of the beam web to column flange CJP weld before propagating through the column flange. The author concluded that weak panel zones are a reliable and effective means of generating ductility capacity. Furthermore, the panels with weak panel zones demonstrated less beam buckling and required less lateral bracing. The study demonstrates that although the specimens with the weak panel zones generate higher fracture potential according to the Rupture Index, RI, experimental evidence does not support this conclusion.

1.4. Flexibility-Based Formulation

In response to uncertainty on how design fillet welds to fasten continuity plates to the column flanges of Special Moment Frames, Tran et al. (2013) developed a flexibility formulation. This method allows the designer to design the continuity plate and its weldments based on its relative stiffness dictating the proportion of hardened beam flange force, P_f, acting on the plate. The fundamental assumption in this theory is that the continuity plate remains elastic. The force entering a continuity plate is determined as:

$$P_{cp} = \left(\frac{P_f}{2}\right)\left(\frac{b_{bf} - t_{pz} - 2t_{cf}}{b_{bf}}\right)\left(\frac{B_{cf}}{B_{cf} + B_{cp}}\right) \tag{1.8}$$

where B_{cp} is the flexibility coefficient of the continuity plate and B_{cf} is the out-of-plane column flexibility coefficient. Given the short ‘span’ of the column flange and continuity plate, the flexibility coefficients include both a flexural and shear components. The second term of Eq. 1.8 refers to the amount of force that is assumed to transmit directly into the column web, assuming a

1:1 catchment through the column flange. The continuity plate was then designed based on satisfying an M-V-P interaction equation (Doswell 2015):

$$\frac{M_r}{M_c} + \left(\frac{P_r}{P_c}\right)^2 + \left(\frac{V_r}{V_c}\right)^4 < 1.0 \tag{1.9}$$

Axial force in the continuity plate is computed using Eq. 1.8. Shear in the continuity plate develops due to the moment equilibrium of the plate (see Figure 1.6); it was assumed that P_{cp} is centered about 0.6 the width of the continuity plate, b_n. The 0.6 was derived based on an assumed trapezoidal elastic stress distribution on the edge of the plate. Mashayekh (2017) identified an additional moment that is generated by the clipping of the continuity plate.

The strength of the weld connecting the continuity plate to column flange is designed to resist the resultant force:

$$R_{cp} = \sqrt{P_{cp}^2 + V_{cp}^2} \tag{1.10}$$

The strength of a fillet weld of size, w, and length, l_w, is then designed as per §J2.4 of AISC 360 (2016):

$$R_n = 2(0.6F_{EXX})wl_w\left(1 + \frac{1}{2}\sin(\theta)^{1.5}\right) \tag{1.11}$$

where F_{exx} is the weld electrode strength, and θ is the orientation of the fillet with respect to the orientation of the vector R_{cp}:

$$\theta = \tan^{-1}\left(\frac{P_{cp}}{V_{cp}}\right) \tag{1.12}$$

Mashayekh and Tran et al. both recommended designing for a maximum shear flow of the fillet weld:

$$q_{max} = \frac{1.6P_{cp}}{b} \tag{1.13}$$

which originates from the peak of the assumed trapezoidal force distribution on the edge of the continuity plate. The strength of the weld adjoining the continuity plate to the column web (or doubler plate) is designed for P_{cp} for an exterior connection or $\sum P_{cp}$ for an interior connection. The orientation of this weld suggests $\theta = 0°$ in Eq. 1.11.

Mashayekh and Uang (2018) validated the flexibility methodology with two exterior full-scale RBS connections. Specimen C1 was a W30×116 beam and a W24×176 column and Specimen C2 was a W36×150 beam and a W14×257 column. The thickness of the continuity plates tested were 1.8 and 1.3 times thicker than the recommended minimum thickness of 50% of the beam flange for an exterior connection. The large continuity plates are a consequence of the flexibility methodology whereby keeping the continuity plates elastic results in the attraction of significant load due to the relatively higher axial stiffness of the continuity plate versus the out-of-plane flexure of the column flange. Specimen C2 was designed such that the plastic interaction (Eq. 1.9) was violated, a conclusion which is corroborated by observed yielding of the continuity plates. The fillet weld sizes of Specimens C1 and C2 were $0.75t_{cp}$ and $0.8t_{cp}$, respectively. Both specimens performed well, achieving a maximum story drift of 0.05 rad and 0.07 rad, respectively.

Despite the success of the flexibility method, there are some critiques:

- The assumption that the continuity plate remains elastic is conservative, resulting in continuity plates thicker than those that have demonstrated adequate performance through prequalification. Several researchers during these tests have observed the yielding of the continuity plates.
- The flexibility formulation tends to be iterative, as the stiffness of the continuity plate is typically an order of magnitude larger than that of the column flange. This results in a runaway procedure as the continuity plate attracts more load as it's size is increased.

Testing of Specimens C1 and C2 in 2016 was a pilot project to verify the flexibility-based method of design (Mashayekh and Uang, 2018). Although the research objective of this study has pivoted, the performance of Specimens C1 and C2 are still presented herein as evidence of the efficacy of fillet-welded continuity plate.

1.5. Historical Review of AISC Requirements of Continuity Plate and Doubler Plate Design

A brief review of the requirement of continuity plates and weld attachments to the column in AISC 341 is summarized below.

- AISC 341 (1992) (pre-Northridge): continuity plate is sized such that $1.8F_{yb}b_f t_{bf} \leq 6.25\left(t_{cf}\right)^2 F_{yf}$ which relates an assumed beam flange force to the flange local bending limit state (§J10.1 of AISC 360). The attachment welds are not specified.
- AISC 341 (1997): continuity plates shall be provided to match the tested connection; almost all of the tested continuity plates which satisfy the drift requirement of SMF at this point equal in size to the beam flange thickness and use CJP welds to connect the plates to the beam flanges.
- AISC 341 (2005): the seismic specifications (AISC 341) refer to AISC 358 for the design of continuity plates in Special Moment Frames. The AISC 358 (2005) specification specifies that continuity plates are required unless both of the following are satisfied:

$$t_{cf} \geq 0.4\sqrt{1.8b_{bf}t_{bf}\frac{F_{yb}R_{yb}}{F_{yc}R_{yc}}} \tag{1.14}$$

$$t_{cf} \geq \frac{b_{bf}}{6} \tag{1.15}$$

The latter (Eq. 1.15) is referred to as the Lehigh Criterion herein. The required thickness of the continuity plates shall be one half of t_{bf} in an exterior connection, or equal to the larger t_{bf} in an interior connection. Additionally, the continuity plates were also required to conform to §J10 of AISC 360. The welds to the column flanges were required to be CJP welds.

- AISC 341 (2010): the continuity plate requirements are the same as listed in AISC 358 (2005).

According to the latest edition of AISC 341 (2016b), continuity plates are required if the predicted flange force exceeds the design strength at the column face as per §J10 AISC 360 (2016) or if the column flange thickness is less than one-sixth of the adjoining beam flange width [see Eq. (1.15)]. The strength requirement is equivalent to the previous proportion limit from AISC 341-05 (Eq. 1.14).

$$t_{cf} \geq \frac{b_{bf}}{6} \tag{1.16}$$

AISC 358 (2016c) generates the predicted flange force of a cyclically hardened beam undergoing large inelastic strains for the appropriate connection. For example, the flange force, P_f, for an RBS connection with a CJP-welded web connection is computed as:

$$P_f = \frac{0.85M_f}{d^*} = \frac{0.85}{d^*}\left(M_{pr} + V_{RBS}S_h\right) = \frac{0.85}{d - t_{bf}}\left(Z_{RBS}F_yR_yC_{pr} + V_{RBS}S_h\right) \tag{1.17}$$

The thickness of the continuity plates, according to §E3.6f.2(b) of AISC 341 (2016b), is determined as:

$$t_{cp} = \begin{cases} 0.5t_{bf} & \text{for exterior connections} \\ 0.75t_{bf} & \text{for interior connections} \end{cases} \tag{1.18}$$

§E3.6f.2(b) of AISC 341 (2016b) stipulates that the width of continuity plates shall at least extend to the edge of the beam flange.

As per the current specifications, the weld connecting the continuity plate to the column flange is required to be a CJP groove weld. However, the continuity plate to the column web can be either a groove weld or fillet weld. Currently, this weld must be sized to develop the lesser of the tension or shear strength of the continuity plate or the shear capacity of the doubler plate (if applicable) that it attaches to in the column panel zone.

The use of doubler plates are dictated when the panel zone shear, derived from the equilibrium between the flange force, P_f, and the column shear, exceeds the design strength as per §J10.6 of AISC 360 (2016):

$$R_n = 0.6F_y d_c t_{pz}\left(1 + \frac{3b_{cf}tcf^3}{d_b d_c t_p}\right) \tag{1.19}$$

Note that the resistance factor, ϕ, for panel zone shear has been equal to 1.0 since the 1997 Seismic Provisions (AISC 1997). When a doubler plate is required, the groove or fillet welds connecting the doubler plate to the column are required to develop the design shear yielding strength of the doubler plate thickness. This requirement has been the same since the first edition of the Seismic Provisions (AISC 1992). When fillet welds are used, the plate thickness must be maintained through the combined thickness of the weld throat and plate bevel at the inside radius of the column. To prevent premature instability of the doubler plate, AISC recommends the following stability limit:

$$t_{dp} \geq \frac{d_z + w_z}{90} \tag{1.20}$$

Up until the 2010 edition of AISC 341, horizontal welds at the top and bottom of the doubler plates were required regardless of the configuration. Modern requirements waive the requirements for

these welds unless the stability limit (Eq. 1.20) is violated when the doubler plate is extended at least 6 in. beyond the beam flange.

1.5.1. Lehigh Criterion

The Lehigh Criterion of §E3.6f.1(b) of AISC 341 stipulates that a continuity plate must be used when the column flange thickness is less than the beam flange width framing in divided by six (see Eq. 1.16). The source of this requirement is from Ricles et al. (2000), who explored the performance of WUF-W connections through finite element analysis and an experimental testing program of interior and exterior connections. This experimental testing program utilized the newly developed modified weld access hole by Mao et al. (2000). To develop the criterion, the authors leveraged ductile fracture mechanic indices.

Ricles et al. calibrated the material factor in Eq. 1.4 by testing A572 Gr. 50 material and two different weld metals, E70T-4 and E70TG-K2 (see Figure 1.4). The pre-Northridge electrode, E70T-4, demonstrates significantly less fracture strain for all triaxiality ratios. The research also demonstrates that the critical plastic strain is much lower for higher triaxiality, a condition which is typical for highly restrained regions. The authors selected a material constant of $\alpha = 2$, which is similar to the value of 2.6 selected by Chi et al. (2006). The authors developed a criterion for fracture based on the net section rupture of the material. A critical crack length is defined from Figure 1.5 as:

$$a_f = \left(1 - \frac{F_y}{F_u}\right) t \tag{1.21}$$

where t is the thickness of the material. To develop a model for cyclic loading, a fatigue law for constant strain range was assumed:

$$\ln(\Delta\epsilon^p) = \ln(\epsilon_f) - \frac{1}{k}\ln(n) \tag{1.22}$$

where $\Delta\epsilon^p$ is the strain range and ϵ_f is the engineering strain at failure. Converting the plastic strain at failure, $\bar{e}^f$, into engineering strain at failure allows the determination of k, a material parameter that now depends on triaxiality through the previously calibrated material parameter α. The authors found that for a triaxiality of 1.3, the value of k equals 2.26 for the A572 Gr. 50 steel and high-toughness weld electrode. Using a Paris fatigue law based on the effective plastic strain using two material parameters, C and B:

$$\frac{da}{dn} = Ca(\Delta\epsilon^{\mathrm{p}})^k \tag{1.23}$$

inverting this equation:

$$C = \frac{ln\ a|_{a_0}^{a_f}}{\epsilon_f^k} \tag{1.24}$$

Substituting the results from before and using an initial flaw size equal to 0.0012 in., an average flaw size observed at the root of the weld, allows for the determination of constant C. Eq. 1.18 to track the growth of a crack or the number of constant amplitude cycles to failure, N_f can be solved for as:

$$N_f = \left(\frac{\epsilon_f}{\Delta\epsilon^{\mathrm{p}}}\right)^k \tag{1.25}$$

Using the results of the low-cycle fatigue analysis, the authors correlated their findings to column flange flexural deformations. The authors found that at least 0.03rad of inelastic story drift ratio could be obtained if the column flange deflection at the edge of the beam flange, Δ_A, was limited to $l/520$, where l is the clear distance from the column web to the edge of the beam flange. Assuming that the moment of inertia of a cantilever section of the column flange has a width of $9t_{cf}$ and that the flange force is evenly distributed results in the criteria:

$$t_{cf} \geq 0.26\left[F_y t_{bf} l^3\right]^{\frac{1}{4}} \quad (1.26)$$

It was found that the beam size of W36×150, with a W14×311 column, satisfies Eq. 1.26 and achieved at least 0.03 rad of inelastic drift during their experimental testing. Therefore, to simplify the criterion, it was instead decided to set the b_{bf}/t_{cf} ratio of this specimen (equal to 5.2) to the limiting b_{bf}/t_{cf} ratio. This ratio was rounded up to 6.0 in FEMA 350 (2000).

This criterion was explicitly derived using WUF-W connections, which tend to have higher flange forces. Table 1.1 shows the results of a typical one-sided RBS connection using beams from the W36 shape family and columns from the W14 shape family. The figure demonstrates that the Lehigh Criterion is triggered for a significant number of combinations, while only a few violate the flange local bending limit state. Therefore, the Lehigh Criterion may be overly conservative for a significant number of potential RBS connections.

1.5.2. Development of Column Stiffening Limit States

The design of continuity plates uses either the minimum thickness as per Eq. 1.18 extending to at least the width of the beam flange or is designed as a typical stiffener using the concentrated force limit states of §J10 of AISC 360. Three limit states are applicable: Flange Local Bending (§J10.1), Web Local Yielding (§J10.2), and Web Local Crippling (§J10.3). The limit state of Web Local Crippling seldom governs and is not discussed in detail. A brief discussion of FLB and WLY follows.

1.5.2.1. Web Local Yielding (WLY)

The WLY yielding was first described in the AISC ASD Specifications in the 1937 Edition to prevent local yielding and crippling of the web of a wide flange shape subjected to a concentrated compressive load (Prochnow et al. 2000). At that time, the WLY limit state was

combined with the Web Local Crippling Limit State. The stress in the column web was to be limited to 24 ksi, and the assumed spread of the bearing force was assumed to be 1:1 through the column flange. Later, testing by Sherbourne and Jensen (1957) found that the 1:1 slope was conservative and recommended a 2:1 slope. In 1960 Graham et al. (1960) found that a 2.5:1 slope provided a better fit to the experimental data. To explain the 2.5:1 slope, the authors used an elastic stress distribution along the k-line of a rolled section. The incorporation of this slope did not occur until the 9th Edition of the AISC ASD Specifications in 1989 and the 1st Edition of the AISC LRFD Specifications in 1986. At this time, the Web Local Crippling limit state was separated from WLY. The WLY of AISC 360 (2016) for interior connections is:

$$R_n = (5k + N)F_y t_{cw} \tag{1.27}$$

where k is the dimension from the outside face of the column to the termination of the fillet, and N is the bearing width. Exterior connections have a similar expression except that the leading term takes on the value of $2.5k$. For moment frames it is a convention to take N as the thickness of the adjacent beam flange, t_{bf}. Figure 1.8 shows the WLY limit state of an interior connection.

1.5.2.2. Flange Local Bending (FLB)

The FLB is a tension limit state where insufficient stiffening of a column flange results in a concentration of the tension load at the center stiffer portion of the flange above the web of the column (Carter 1999). Figure 1.11 shows the FLB and the role of continuity plates in preventing it. The combined bending of the flanges with the concentration of the load leads to the rupture of the beam flange weld. Graham et al. (1960) developed the FLB limit state by using a yield line analysis to determine the strength of a column flange. The FLB as first specified in the 8th Edition of the AISC ASD Specification, which required stiffeners if:

$$t_{cf} < 0.4\sqrt{\frac{P_{bf}}{F_y}} \tag{1.28}$$

A set of lower bound values of key geometric variables from available section shapes were used to conservatively derive this equation. The yield line analysis is reposed to convert this expression for use in LRFD design (Prochnow et al. 2000):

$$R_n = 7t_{cf}^2 F_c + t_{bf} k F_y \tag{1.29}$$

where the first term describes the strength of the column flanges in bending, and the latter describes the capacity of the web directly below the adjacent beam flange. After taking a 20% reduction in capacity and imposing the experimental results of pull plate testing, the following equation for FLB in AISC 360 (2016) is realized:

$$R_n = 6.25t_{cf}^2 F_y \tag{1.30}$$

As an alternative derivation, Prochnow et al. (2000) developed a yield line analysis informed from the results of an experimental testing program of pull plates welded to W-shapes. Following their methodology, a yield line analysis was developed such that four hinges form on each side of the web to form a tent (see Figure 1.10). The clear span of the flange, q, is taken as:

$$q = \frac{b_{cf}}{2} - k_1 \tag{1.31}$$

The authors recommend the same value as Graham et al. used for the longitudinal length of the yield lines of:

$$p = 12t_{cf} \tag{1.32}$$

Defining the length of the inclined yield line as:

$$r = \sqrt{\left(\frac{p}{2}\right)^2 + q^2} \tag{1.33}$$

Solving for the internal energy of the yield lines results in:

$$W_I = M_p \Delta \left[\frac{p}{q} + \frac{8q}{p}\right] \tag{1.34}$$

Substituting with $M_p = \frac{1}{4} t_{cf}^2 F_y$ results in:

$$W_I = t_{cf}^2 \left[\frac{p}{4q} + \frac{2q}{p}\right] \Delta F_y \tag{1.35}$$

Solving for the external energy as:

$$W_E = \int_0^h w \left(\frac{\Delta}{q}\right) x \, dx = \frac{w\Delta}{2q} h^2 \tag{1.36}$$

where $h = \frac{b_{bf}}{2} - k_1$, and w is the assumed uniform load applied by the beam flange. Finally, equating the internal and external energy results in:

$$w = \frac{t_{cf}^2}{h^2} \left[\frac{p}{2} + \frac{4q^2}{p}\right] F_y \tag{1.37}$$

Solving for the maximum flange force then produces:

$$R_n = 2k_1 t_{bf} F_y + 2wh \tag{1.38}$$

Substituting in the result for w:

$$R_n = 2k_1 t_{bf} F_y + \frac{2}{h} \left[\frac{p}{2} + \frac{4q^2}{p}\right] t_{cf}^2 F_y \tag{1.39}$$

Prochnow et al. (2000) simplified Eq. 1.39 by taking the average minus one standard deviation of parameters for common column and girder combinations to find:

$$R_n = F_y\left(0.8 + 5.9 t_{cf}^2\right) \tag{1.40}$$

Graham et al. and Prochnow et al. both used the simplification that $p = 12 t_{cf}$; however, if the critical value of p is found by taking the derivative of 1.37 with respect to p:

$$\frac{dw}{dp} = \frac{t_{cf}^2}{h^2} F_y \left[\frac{1}{2} - \frac{4q^2}{p^2}\right] \tag{1.41}$$

Then solving for the minimum value by setting equal to zero:

$$p = 2\sqrt{2}q \tag{1.42}$$

This minimum value of p, as a function of q, results in a capacity for FLB of:

$$R_n = 2k_1 t_{bf} F_y + \frac{2}{h}\left[\sqrt{2}q + \frac{2q}{\sqrt{2}}\right] t_{cf}^2 F_y \tag{1.43}$$

Prochnow et al. found that Eq. 1.40 predicted the results of their pull plate specimens with greater accuracy. Figure 1.11 compares Eq. 1.30 and Eq. 1.40 to Eq. 1.43 for a W36×150 beam framing into either a W14 or W27 column. It is observed that the bounding performed by Prochnow et al. (2000) is very close to that performed by Graham et al. (1960). Both of these equations are conservative for the columns tested (W14×132 to W14×159) when compared with the unsimplified yield line equation (Eq. 1.43). Their experimental testing program corroborates this as none of the pull-plate specimens fractured (Hajjar et al. 2003). These specimens used E70T-6 weld electrodes for their CJP welds with a measured CVN toughness of 63.7 ft-lb at 70°F and 19.0 ft-lb at 0°F. It is noted that Eq. 1.40 and Eq. 1.30 both use a reduction factor of 0.8 which has not been incorporated into Eq. 1.43. This reduction factor was applied to original derivation in an attempt to make the upper bound strength estimate from the yield line method conservative.

The previous discussion indicates that the FLB is conservative when using notch-tough weld electrodes for monotonic pull-plate tests. The level of conservatism diminishes for heavier sections—sections that would be common in a modern moment frame subjected to a Strong Column Weak Beam (SCWB) philosophy. An additional concern when using an FLB derived based on a monotonic pull plate test is that the beam flange CJP rupture of a seismic moment frame is significantly different than from a pull-plate test. Firstly, the connection of a moment frame experiences large scale cyclic strains resulting in strain hardening and, secondly, significant secondary bending exists in the flanges of a moment frame connection.

1.6. Summary

The 1994 Northridge Earthquake was a pivotal event for the design of steel moment frames as an SFRS. Observation of brittle fractures in the connection region of the frames precipitated necessary changes in the detailing of these moment frames, including the use of notch-tough electrodes, careful treatment of backing bars, and welding of the beam web to the column to facilitate the shear transfer from the beam web. The most significant modification was the requirement that connections for SMF and IMF be prequalified to achieve a prescribed level of drift. Most of these early tests, which set the foundation for prequalified connections, utilized conservative column stiffening details, including the use of continuity plates as thick as the beam flange and the use of CJP groove welds for the continuity plate weldments.

Research in the 2000s attempted to set conservative bounds as to when a continuity plate was required and set minimum required thicknesses of the continuity plate. Several researchers have demonstrated the efficacy of using fillet welds for this joint in monotonic pull-plate specimens as well as full-scale cyclic moment frame tests. However, the use of a CJP groove for the weldment of the continuity plate to the column flange is still required. This weld tends to be costly due to the increased preparation to bevel the plate and install a backing bar, and the required UT testing of the joint after welding. In response to the steel industry's push to economize the connection, a new method was derived using the flexibility of the continuity plate and column. This new flexibility method was validated using the full-scale testing of two exterior RBS connections and relies on the assumption that continuity plates must remain elastic. This assumption results in relatively thick continuity plates, which are often thicker than plates that have already demonstrated adequate performance.

In response, this research program is designed to explore a plastic design methodology to design continuity plates and their welds. This program explored the currently defined limit states for stiffening columns as per the AISC Specifications and validates a simple design rule for designing fillet welds.

1.7. Thesis Organization

The organization of the remainder of the thesis is organized as follows:

- Chapter 2: describes the design methodology of the 10 full-scale moment connections that were tested. This includes the derivation of weld forces for the continuity plate and doubler plater weldments.
- Chapter 3: outlines the testing program by describing the methodology of testing and specimen construction. This chapter includes material properties of all steel elements as determined by uniaxial tension testing or Charpy V-Notch Impact testing.
- Chapter 4: details the testing of each of the ten specimens. The response of the specimens is broken up into observed and recorded responses. Observed responses document the chronological performance of each specimen during testing. Recorded responses are separated into global and local responses. Global responses are those derived from the global load-displacement response of the specimen while local responses include those obtained from the specimen strain gauges.
- Chapter 5: provides a detailed discussion and analysis of the testing. This chapter further elucidates the WLY and FLB limit states using the expected strengths of the columns while comparing the relative performance of each specimen.
- Chapter 6: is a stand-alone chapter that documents the procedure and results for in-situ measurement of welding residual stresses in continuity plates. The measurements were

performed with a high-speed air turbine to drill a hole in the center of a strain gauge rosette—the resulting relaxation strains are correlated to the in-situ stresses.

- Chapter 7: details the development and results of a parametric finite element study. The parametric finite element results augment to design methodology of Chapter 2 and supports the experimental testing results of Chapter 4.
- Chapter 8: details the development of ductile fracture mechanics and discusses the derivation of the Cyclic Void Growth Model (CVGM). CVGM is then used on several representative connections to show the influence of continuity plate thickness and of violating the Lehigh Criterion on ductile fracture.
- Chapter 9: is the summary and conclusions of the thesis. Recommendations for changes to AISC 341 and AISC 360 are made.

This chapter has been published as a Structural Systems Research Project (SSRP) Report: Reynolds, M., C-M., Uang, "Alternative Weld Details and Design for Continuity Plates and Doubler Plates for Applications in Special and Intermediate Moment Frames," *Report No. SSRP-19/03,* and submitted to AISC as the final project deliverable.

Table 1.1 Limit State Matrix (W14 Column and W36 Beam: One-Sided RBS Connection)

		Beam: W36×									
		302	282	262	247	231	194	182	170	160	150
Column: W14×	455										
	425										
	398										
	370										
	342										
	311										
	283										
	257										
	233							FLB	FLB		
	211									FLB	FLB
	193										FLB
	176										

	No CP Req'd	FLB	Governed by AISC 360 §J10.1
	Eq. (1.1) Triggered	WLY	Governed by AISC 360 §J10.2
	Violates SCWB		Phase 1 Testing

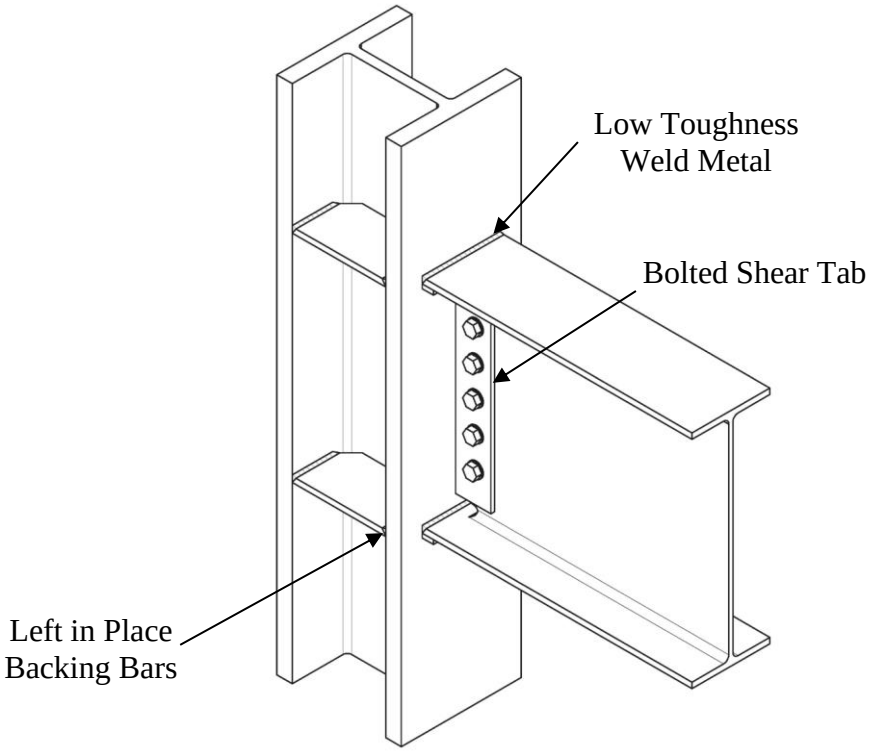

Figure 1.1 Pre-Northridge Connection (Hamburger et al. 2016)

Figure 1.2 Fracture at Beam Bottom Flange Steel Backing Bar (Hamburger et al. 2016)

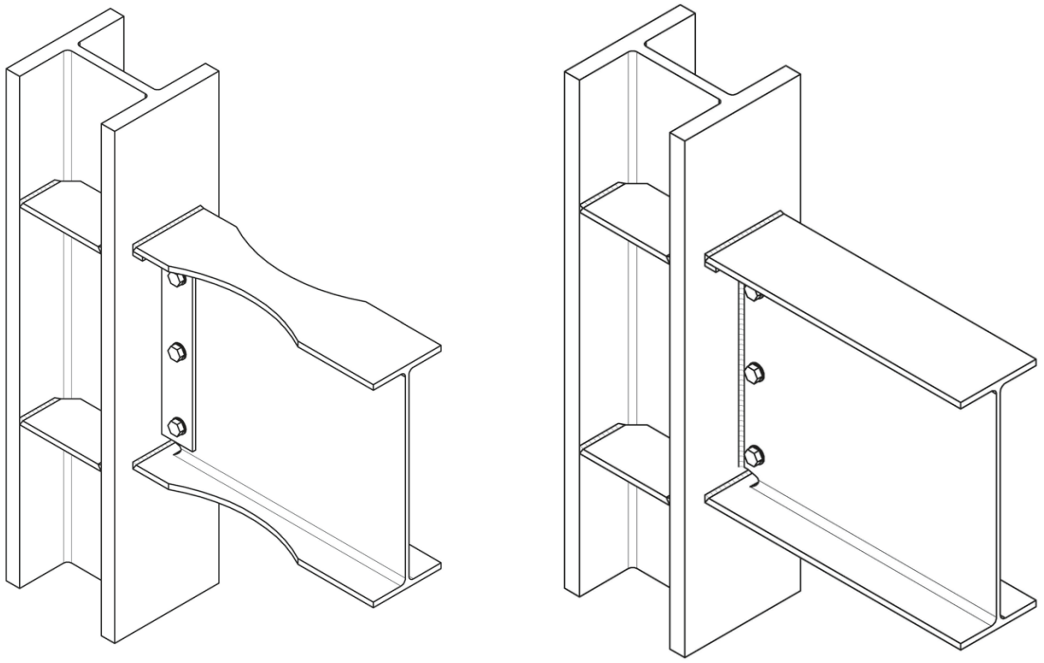

(a) RBS Connection (b) WUF-W Connection

Figure 1.3 Prequalified Moment Connections (Hamburger et al. 2016)

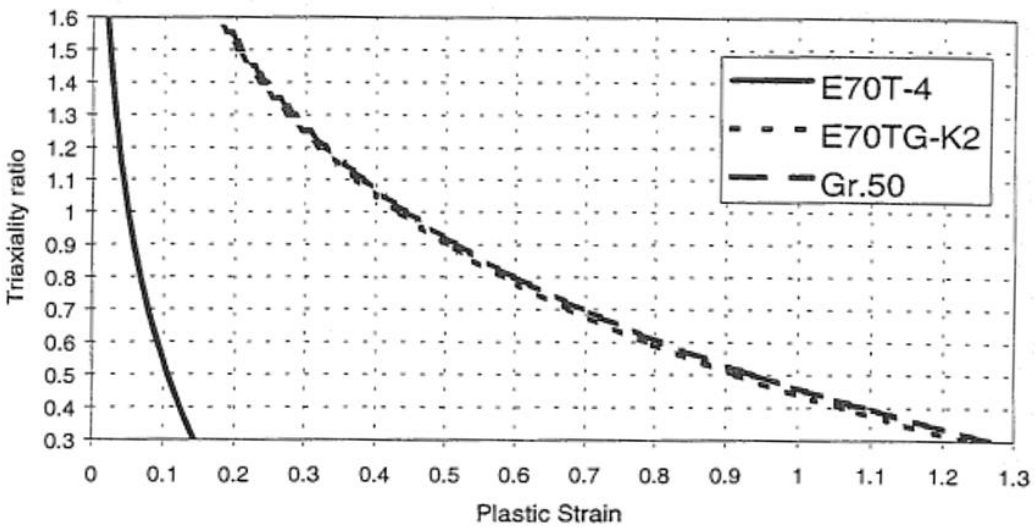

Figure 1.4 Plastic Strain versus Triaxiality Ratio (Ricles et al. 2000)

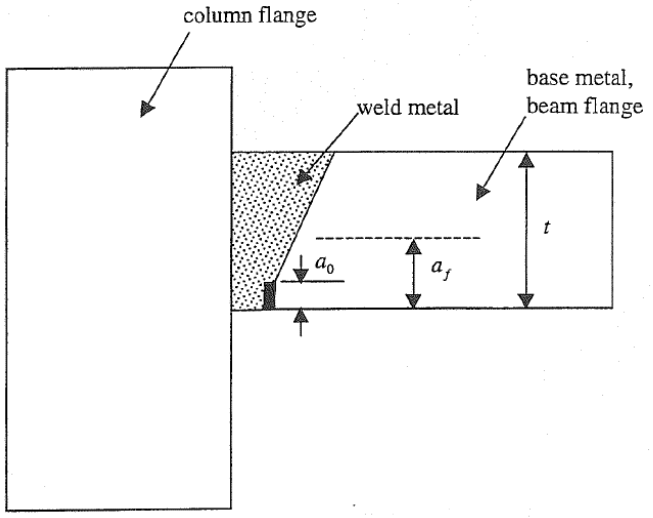

Figure 1.5 Net-Section Failure of Beam Flange (Ricles et al. 2000)

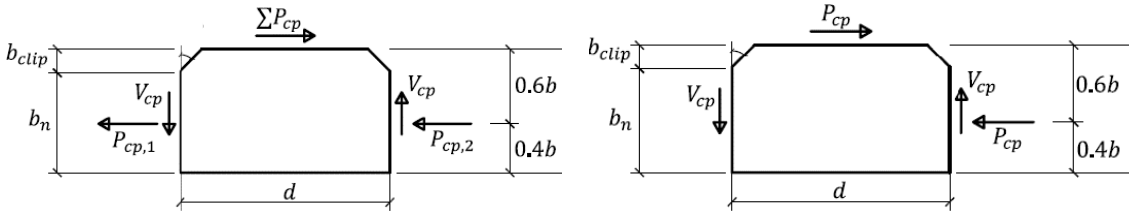

(a) Interior Connection (b) Exterior Connection

Figure 1.6 Continuity Plate Free Body Diagram (Mashayekh 2017)

(a) Specimen C1 (b) Specimen C2

Figure 1.7 Flexibility Method Verification (Mashayekh and Uang 2018)

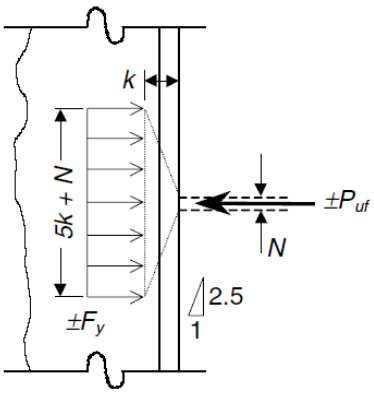

Figure 1.8 WLY Limit State (Carter 1999)

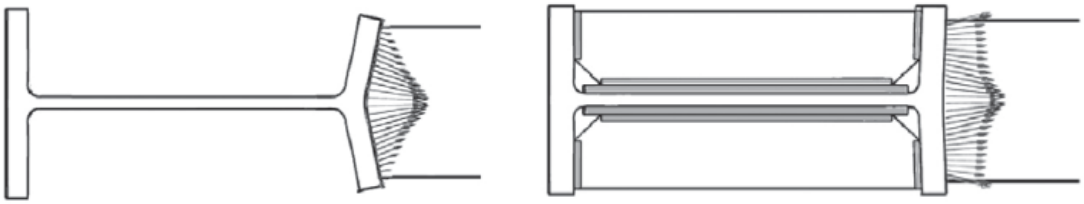

(a) Unstiffened Flange (b) Stiffened Flange

Figure 1.9 FLB Limit State (Tran et al. 2013)

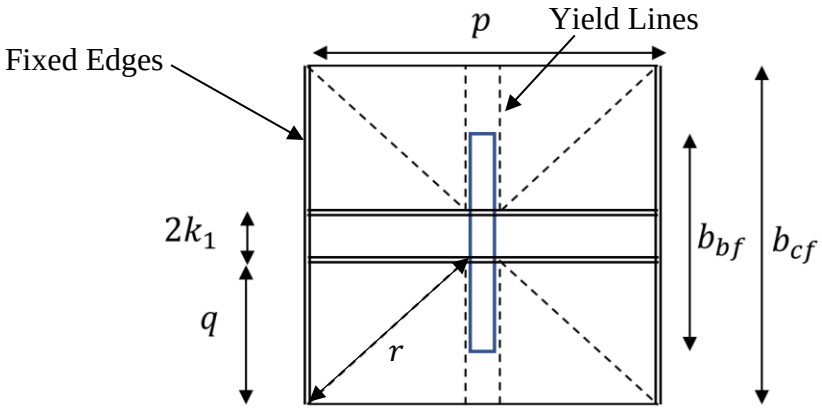

Figure 1.10 Yield Line Mechanism

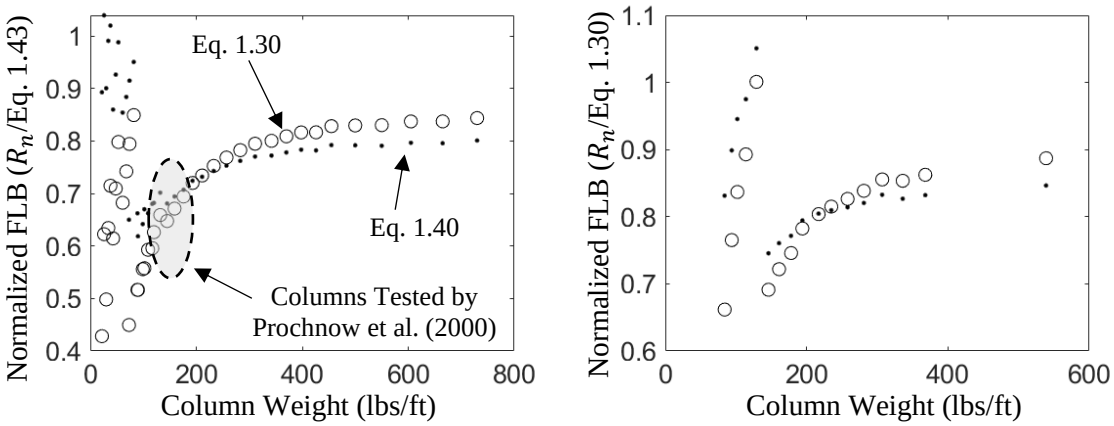

(a) W14 Column (b) W27 Column

Figure 1.11 Flange Local Bending Comparison

2. SPECIMEN DESIGN

2.1. General

This chapter discusses the design philosophy and research objective of Phase 1 (Specimens C3, C4, C5, C6, C6-G, and C7) and Phase 2 (Specimens W1, W2, W3, and W4). The Phase 1 specimens are one-sided specimens simulating an exterior moment frame RBS connection. These six specimens are engineered to characterize the limit states surrounding continuity plates. Specimens C1 and C2 were previously tested as part of the verification of the flexibility design method in 2016 (Mashayekh 2017). Although the research objective of this study has pivoted, the satisfactory performance of Specimens C1 and C2 are presented as evidence of the usability of fillet welds for the continuity plate-to-column flange weld. The Phase 2 specimens are two-sided WUF-W connections simulating an interior moment frame connection. These four specimens are engineered to challenge the continuity plate and its weldments with high flange forces.

The primary objective of this research is to economize the detailing of continuity plates. Improving the economy of continuity plates is accomplished in two ways: (1) by exploring the boundaries in which continuity plates are required, and (2) by providing a design methodology to use a fillet weld for the continuity plate-to-column flange weld. It is proposed that the continuity plate is designed for the plastic distribution of forces in accordance with the existing stiffener design procedure of §J10 in AISC 360 (2016) while using the strain hardened beam flange force for the applicable connection as per AISC 358 (2016c). This methodology differs from previous research (Tran et al. 2013, Mashayekh and Uang 2018), which used the elastic distribution of forces in the connection to size the continuity plates and their weldments. Subscription to this methodology requires a revaluation of the Lehigh Criterion (Eq. 1.16), which often necessitates continuity plates in connections with relatively low flange forces. These relatively low flange

forces result in connections where a strength limit state (either WLY or FLB) do not govern, This effect is demonstrated in Table 1.1, which illustrates the cohort of possible single-sided RBS connections between a W14 shape column and a W36 shape beam.

The second objective of the research program is to economize the detailing of doubler plates. Doubler plates are incorporated into this research because of their prevalence of use in conjunction with continuity plates. Doubler plate economy is improved by providing a design methodology to size the weld for the proportion of the panel zone shear in the doubler plate.

2.2. Design Philosophy

With the exception of the test parameters (see Table 2.1), the specimens are designed according to AISC 341 (2016b) and AISC 358 (2016c).

2.2.1. Continuity Plate Design

The continuity plate design uses the plastic design method, where the force demand, P_{cp}, imposed on the continuity plate is:

$$P_{cp} = (P_f - \min(FLB, WLY))/2 \quad (2.1)$$

where P_f is the hardened flange force as per AISC 358 (Eq. 1.17), and FLB and WLY are the column strengths associated with the limit states as per AISC 360 (Eqs. 1.27 and 1.30). The resistance factors are ϕ =0.9 and ϕ =1.0 for the FLB and WLY limit states, respectively. When the resultant plastic demand on the continuity plate is negative, which occurs when the column capacity according to FLB and WLY is greater than the flange force, a continuity plate is not required. The strength of the continuity plate is based on a plastic interaction equation (Eq. 2.2) between the shear and axial force in the continuity plate (Doswell 2015).

$$\left(\frac{P_{cp}}{P_c}\right)^2 + \left(\frac{V_{cp}}{V_c}\right)^4 \leq 1.0 \quad (2.2)$$

Shear forces in the continuity plate are found from the equilibrium of the continuity plate. The capacity of the continuity plate in axial compression, P_c, and shear, V_c, are evaluated as per the yielding limit states of AISC 360 §J4.1 and §J4.2 on the edge of the continuity plate in contact with the column flange. When the ratio of $V_{cp}/V_c \leq 0.4$ the shear contribution to the interaction is less than 2.5% and can be neglected for design purposes. Finite element analysis shows that the small amount of moment that exists at the edge of the continuity plate vanishes as the plate achieves its ultimate state.

2.2.2. Continuity Plate Weld Design

The high in-plane stiffness of the continuity plate relative to the out-of-plane stiffness of the column flange results in a significant portion of the beam flange force being transmitted to the plate. Extending the flexibility method (Section 1.4) for an elastic-plastically designed continuity plate allows for the prediction of the continuity plate force, P_{cp}. Figure 2.1 demonstrates this using Specimens C5 and C6 of this testing program. The figure shows that, for these two cases, the continuity plate is expected to yield until a thickness above the minimum specified in AISC 341 is reached (Eq. 1.18). Specimen C2 demonstrates this effect, where the plastic method does not require a continuity plate, but the flexibility method shows that a 5/8-in. thick continuity plate yields Yielding of this continuity plate was confirmed by the experimental testing of this specimen.

Additionally, the presence of high residual stresses due to the thermal stresses induced by welding promotes continuity plate yielding. Therefore, the continuity plate fillet welds fastening the continuity plate to the column flange are designed to develop the strength of the continuity plate. Traditionally a $(5/8)t$ rule, where t is the thickness of the plate in question, would be used to design a double-sided fillet weld that would develop the strength of a plate in tension. To verify

this rule, we equate the strength of a transversely orientated double-sided fillet weld of size, w, to the yield limit state of a plate:

$$\phi_w 0.6 F_{EXX} A_{we} (1.0 + 0.5 \sin^{1.5} \theta) = \phi_t F_y A_g \tag{2.3}$$

$$\phi_w 0.6 F_{EXX} 2 \frac{w}{\sqrt{2}} l_w (1.5) = \phi_t F_y t_{cp} l_w \tag{2.4}$$

$$w = 0.786 \frac{\phi_t F_y}{\phi_w F_{EXX}} t_{cp} \tag{2.5}$$

which for a Gr. 50 steel plate with a matched electrode ($F_{EXX} = 70$ ksi) results in:

$$w = \frac{5}{8} t_{cp} \tag{2.6}$$

However, to be consistent with a capacity design philosophy, the fillet weld of the specimen continuity plates is designed for the nominal yielding, not design, strength of the continuity plate such that:

$$\phi_w 0.6 F_{EXX} A_{we} (1.0 + 0.5 \sin^{1.5} \theta) = F_y A_g \tag{2.7}$$

$$w = 0.786 \frac{F_y}{\phi_w F_{EXX}} t_{cp} \tag{2.8}$$

which for a Gr. 50 steel plate with a matched electrode ($F_{EXX} = 70$ ksi) results in:

$$w = \frac{3}{4} t_{cp} \tag{2.9}$$

Since the column flange edges of the continuity plate experiences shear, V_{cp}, the assumption that the weld is only loaded in tension appears not be conservative. But including the shear in the analysis also modifies the design strength of the plate. Assuming that the continuity plate observes an elastic-plastic response (i.e., the plate will not be subjected to significant cyclic strains that would induce strain hardening) it will be shown below that the modified yield condition of the continuity plate offsets the decrease in the weld strength.

The direction-dependent term used for fillet welds, $(1.0 + 0.5\sin^{1.5}\theta)$, decays as additional shear modifies the direction of the resultant force vector, P_r, (see Eq. 2.10 and 2.11).

$$P_r = \sqrt{P_{cp}^2 + V_{cp}^2} \tag{2.10}$$

$$\theta = \tan^{-1}\left(\frac{P_{cp}}{V_{cp}}\right) \tag{2.11}$$

The shear at the forward edge of the plate is found as:

$$V_{cp} = \gamma P_{cp} \tag{2.12}$$

Assuming that P_{cp} acts at the center of the plate edge results in the following expressions for γ:

$$\gamma = \begin{cases} \dfrac{\left(b_{clip} + \dfrac{b_n}{2}\right)}{d} & \text{for exterior connections} \\ \dfrac{2\left(b_{clip} + \dfrac{b_n}{2}\right)}{d} & \text{for interior connections} \end{cases} \tag{2.13}$$

where b_{clip} is the distance clipped off the continuity plate to clear the radius of the column web-to-flange junction, and d is the depth of the continuity plate: $d = d_c - 2t_{bf}$ (see Figure 2.2). Assuming the continuity plate does not demonstrate significant strain hardening, the resultant force P_r must exist on the initial yield surface defined by the nominal yield strength of the material. For metal plasticity it is common to assume a von Mises yield surface:

$$\sigma_{vm}^2 = \frac{1}{2}\left[(\sigma_{11} - \sigma_{22})^2 + (\sigma_{22} - \sigma_{33})^2 + (\sigma_{33} - \sigma_{11})^2 + 6(\sigma_{23}^2 + \sigma_{31}^2 + \sigma_{12}^2)\right] \tag{2.14}$$

Assuming plane stress and conservatively setting $\sigma_{22} = 0$ results in:

$$F_y^2 = \sigma_{11}^2 + 3\sigma_{12}^2 \tag{2.15}$$

The average tension stress is $\sigma_{11} = P_{cp}/A_{cp}$ and the average shear stress is $\sigma_{12} = V_{cp}/A_{cp}$, where $A_{cp} = b_n t_{cp}$ is the area of the continuity plate in contact with the column flange. Substituting these expressions into Eq. 2.15 produces:

$$P_{cp} = \frac{P_y}{\sqrt{1 + 3\gamma^2}} \tag{2.16}$$

$$V_{cp} = \frac{\gamma P_y}{\sqrt{1 + 3\gamma^2}} \tag{2.17}$$

where $P_y = F_y A_{cp}$. Substituting these expressions into Eq. 2.10 results in:

$$\frac{P_r}{P_y} = \sqrt{\frac{1 + \gamma^2}{1 + 3\gamma^2}} \tag{2.18}$$

$$\theta = \tan^{-1}\left(\frac{1}{\gamma}\right) \tag{2.19}$$

The ratio of strengths of a transversely orientated ($\theta = 90°$) weld versus a resultant angle according to Eq. 2.19 is:

$$\frac{R_n(\theta = 90°)}{R_n(\theta)} = \frac{\frac{3}{2}}{1.0 + 0.5\sin^{1.5}\left(\tan^{-1}\left(\frac{1}{\gamma}\right)\right)} \tag{2.20}$$

The ratio of Eq. 2.18 to Eq. 2.20 represents the resulting demand-capacity ratio, *DCR* between a weld subjected to a vector resultant of axial and shear forces, limited by a von Mises yield criterion, to a weld design solely for tension:

$$DCR_{Weld} = \frac{3\sqrt{\frac{1 + \gamma^2}{1 + 3\gamma^2}}}{2\left[1.0 + 0.5\sin^{1.5}\left(\tan^{-1}\left(\frac{1}{\gamma}\right)\right)\right]} \tag{2.21}$$

Since $DCR_{Weld} \leq 1.0$ for all admissible values of γ, it is conservative to neglect the shear force acting on the weld (see Figure 2.3). Finite element analysis has also revealed that before the continuity plate yields, a small amount of moment is generated at the edge of the plate. This moment vanishes as the continuity plate yields due to the axial force. The weld fastening the continuity plate to the web of the continuity plate is designed to develop the strength of the axially

loaded portion of the continuity plate. For an exterior connection, this is equal to $A_{cp}F_y$, while for an interior connection, the force is doubled. Therefore, it is conservative to assume this weld is orientated longitudinally ($\theta = 0°$).

The continuity plate fillet welds in this research program were typical welds with no special requirements regarding the treatments at weld terminations. This use of typical detailing was intentional to represent a conservative fabrication case where the fillet weld may be fabricated with a start and stop of each weld pass contained within the breadth of the continuity plate.

2.2.3. Doubler Plate Vertical Weld Design

The vertical welds of a doubler plate are designed to resist the appropriate proportion of the panel zone shear based on the relative elastic shear stiffness of the doubler plate:

$$V_{dp} = \left(\frac{Gt_{dp}}{Gt_{dp} + Gt_{cw}}\right)V_{pz} = \left(\frac{t_{dp}}{t_{dp} + t_{cw}}\right)V_{pz} \quad (2.22)$$

where V_{dp} is the shear force in the doubler plate(s), and t_{dp} and t_{cw} are the thicknesses of the doubler plate and column web, respectively. The panel zone shear, V_{pz} is derived from the equilibrium between the flange force, P_f and the column shear, V_{col}. Assuming that the stress of the doubler plate is uniformly distributed across a shear area equal to $t_{dp}d_c$ results in shear flow of $q_{dp} = V_{dp}/d_c$. Moment equilibrium of the doubler plate itself results in (see Figure 2.4):

$$\frac{V_{dp}}{d_c}h_c d^* = V_{dp,v}h_c \quad (2.23)$$

$$V_{dp,v} = \frac{V_{dp}}{d_c}d^* \quad (2.24)$$

For design purposes, assume that the shear flow along the vertical edge is uniform:

$$q_{dp,v} = \frac{V_{dp,v}}{d^*} = q_{dp} \quad (2.25)$$

It is observed that the uniform shear flow along the vertical edge of the doubler plate is equal to the uniform shear flow along the horizontal edge. The above approach may result in a vertical shear force in excess of the shear yielding strength of the plate—a paradox that occurs because of the inelastic behavior assumed in the second term of Eq. 1.19. Therefore, the following requirement is necessary:

$$q_{dp,v} = \frac{V_{dp}}{d_c} \leq 0.6F_y t_{dp} \tag{2.26}$$

In practice, economic doubler plates designed solely for panel zone shear would not be designed differently than the current practice of sizing the weld to develop the shear strength of the doubler plate. However, there are two instances where the proposed approach realizes greater economy:

(1) When the strength design (Eq. 1.19) would suggest a doubler plate that would violate the stability limit (Eq. 1.20) and instead of using plug welds to stabilize the plate, a thicker doubler plate may be specified.

(2) When WLY governs the need for column stiffening, a doubler plate may be used in lieu of a continuity plate. Specimen C7 of this research project utilized this approach.

An additional complication to using fillet welds as the vertical weld to fasten the doubler plate to the column is maintaining the effective throat of the weld through the beveled portion of the doubler plate [see Figure 2.5(a)]. The commentary of §E3.6e.3 in AISC 341 (2016b) discusses the issue and recommends that the fillet weld size should be increased to accommodate any reductions in the effective throat due to the bevel of the doubler plate. For Specimen C7, a bevel angle of 45° was specified to circumvent this issue [see Figure 2.5(b)]. No fit-up issues of the 5/8-in. doubler plate on the W24×192 column was reported.

2.3. Specimen Design and Details

Table 2.1 summarizes the research objective of the specimens in both phases. The first two specimens of Phase 1 (Specimens C3 and C4) challenge the need for the Lehigh Criterion (Eq. 1.16) for a shallow and a deep column configuration. While Specimen C4 has a much higher SCWB ratio indicating a stiffer column, the deep column may be more susceptible to warping once a lateral-torsional instability is developed at the plastic hinge in the beam. Specimen C4 also possesses a markedly stronger panel zone than Specimen C3. Specimen C5 was designed with a continuity plate as per Eq. 2.2, resulting in a continuity plate that is 1/8 in. thinner than that required per Eq. 1.18. The resulting continuity plate has a high width-to-thickness ratio of 16.0; high width-to-thickness ratio plates are susceptible to local buckling. Specimen C5 also used a weak panel zone (DCR =1.18). The combination of column kinking and continuity plate buckling while the continuity plate is cycled plastically challenges the ductility capacity of the continuity plate fillet welds. The continuity plate-to-column flange fillet weld was the nearest standard weld size to satisfy $w = (3/4)t_{cp}$.

Specimen C6 was designed with a continuity plate as per Eq. 2.2, resulting in a continuity plate that is equal to that required per Eq. 1.18. The continuity plate fillet welds in this specimen were equal to t_{cp}. This was done to ensure that premature failure of the specimen did not occur such that Specimen C6-G, which was a duplicate specimen that was hot-dip galvanized, would have meaningful results when comparing the effects of galvanization. To maintain consistency for later comparison, Specimen C6-G is fabricated identically to Specimen C6—including maintaining metallurgical similarity by using rolled shapes from the same heat number. Specimen C7 aims to satisfy the governing column limit state, WLY, by the addition of a doubler plate in lieu of a continuity plate. The *DCR* for the FLB limit state is 0.92, which according to the plastic

design methodology does not require a continuity plate. The doubler plate fillet weld has been sized to resist the proportion of panel zone shear transmitted to the doubler plate based on its ratio of shear stiffness to the column web, according to Eq. 2.22 and Eq. 2.26. Table 2.2 shows the RBS dimensions of the Phase 1 specimens. Included in this table is the ratio of moment at the column face to the expected plastic moment, M_f/M_{pe}, which indicates the utilization of the RBS including hardening.

Specimen W1 used a 1/2-in. continuity plate as per Eq 2.2, which violates the current minimum thickness criterion for two-sided connections as per Eq. 1.18. This specimen used a pair of 5/8-in. extended doubler plates with a vertical PJP weld. Specimen W2 used a 3/4-in. continuity plate as per the minimum thickness of AISC 341 (Eq. 1.18). The plastic methodology predicts this plate as overloaded, with a *DCR* of 1.43. Overloading of the continuity plate was done intentionally to observe any negative consequences. This specimen used a pair of 3/4-in. extended doubler plates with a vertical PJP weld. Specimen W3 used a 1/2 -in. continuity plate as per Eq 2.2 which violates the current minimum thickness criterion for two-sided connections as per Eq. 1.18. This specimen used a pair of 1/2-in. extended doubler plates, which were insufficient based on the predicted panel zone shear (see Eq. 1.19) and violated the stability criteria (see Eq. 1.20). The weak and slender panel zone was designed intentionally to investigate any negative consequences. The slope of the weld access hole from the beam flange for WUF-W connections has been shown to be a critical parameter (Han et al. 2014). AWS D1.8 (2016) §6.11.1.2 is not explicit in specifying the slope of the weld access hole—only imposing a limit of 25° degrees. The design drawings for Phase 2 detailed the weld access as a standard weld access for WUF-W connections following the Alternate Geometry of AWS D1.8. As-built slopes of the access holes for the Phase 2 specimens were approximately 15°.

Specimen W4 used a 3/4-in. continuity plate as per Eq 2.2, which satisfied the current minimum thickness criterion for two-sided connections as per Eq. 1.18. This specimen used a doubler plate placed within the continuity plates. The vertical welds of the doubler plates were designed to develop the shear strength of the doubler plate. Only Specimen W4 used horizontal fillet welds to fasten the doubler plate to the continuity plate. This fillet weld was sized based on 75% of the available shear capacity of the doubler plate as per §E3.6e.3(b)(2) in AISC 341 (2016b).

Concrete slabs were not used in this testing as their presence significantly complicates the testing and impairs the visual assessment of the connection during testing. Experimental testing of SMFs using concrete slabs have demonstrated that their presence is generally beneficial by stabilizing the plastic hinge (Englehardt et al. 2000). In positive flexure the addition of a composite slab can increase the plastic strain demand at the beam bottom flange extreme fiber (Hajjar et al. 1998). However, a modern connection which prohibits the use of shear studs in the beam plastic hinge region lacks the shear transfer capability to develop significant composite behavior. Uang et al. (2000) found that the shift in the neutral axis for partially composite beams to be minor.

Table 2.3 shows the following specimen and continuity plate design metrics:

- The clear Span-to-Depth Ratio. AISC 358 (2016c) §5.3.j requires the ratio for SMF using RBS connections to be limited to 7 or greater. Similarly, AISC 358 (2016c) §8.3.j requires the ratio for SMF using WUF-W connections to be limited to 7 or greater.
- The Strong Column Weak Beam (SCWB) Moment Ratio. AISC 341 (2016b) §E3.4a requires that the ratio of the summation of projected column strengths to the summation of projected beam strengths shall be larger than one. The ratio listed in the table is:

$$SCWB = \frac{\sum M_{pc}^{*}}{\sum M_{pb}^{*}} \tag{2.27}$$

- The flange force, P_f as per Eq. 1.17 using the appropriate clause of AISC 358 (2016c) to compute the moment at the face of the column, M_f. Specifically, §5.8 in AISC 358 for RBS connections and §8.7 in AISC 358 for WUF-W connections.
- The resistance of the FLB, WLY column limit states computed as per §J10 in AISC 360 (2016) (Eq. 1.30 and Eq. 1.27) using the designed thickness of the panel zone (i.e., $t_{cw} + \sum t_{dp}$). The WLC limit state has been omitted since it does not govern.
- The resultant continuity plate force, P_{cp}, computed as per Eq. 2.1.
- The continuity plate DCR expressed as the resultant of the P-V interaction equation (Eq 2.2).
- The continuity plate width-to-thickness ratio (*b/t*).
- The fillet weld size, w, adjoining the continuity plate to the column flange.
- The ratio of fillet weld size to continuity plate thickness, w/t_{cp}.

Table 2.4 shows the following panel zone and doubler plate design metrics:

- The panel zone shear force, V_{pz} determined as the equilibrium between the flange force(s) and the column shear.
- The panel zone DCR expressed as the ratio of V_{pz} and R_n as per Eq. 1.19.
- The ratio of the combination of the panel zone width and depth to its thickness (see Eq. 1.20) computed for the column web and doubler plate.
- The vertical weld shear flow as computed per Eq. 2.26 and the upper bound of the shear flow defined as $0.6F_y t_{dp}$.

This chapter has been published as a Structural Systems Research Project (SSRP) Report: Reynolds, M., C-M., Uang, "Alternative Weld Details and Design for Continuity Plates and Doubler Plates for Applications in Special and Intermediate Moment Frames," *Report No. SSRP-*

19/03, and submitted to AISC as the final project deliverable. This chapter is also being prepared for submission for publication and may appear in *AISC Engineering Journal*. The author of this dissertation is the primary author of this work; Prof. Chia-Ming Uang will coauthor this work.

Table 2.1 Testing Objective Matrix

Spec. No.	Beam	Column	Connection Type	Research Objective
C1[a]	W30×116	W24×176	One-sided RBS	Continuity plate designed using the flexibility method (Section 1.4).
C2[a]	W36×150	W14×257	One-sided RBS	Continuity plate designed using the flexibility method (Section 1.4). Continuity plate expected to yield.
C3	W36×150	W14×257	One-sided RBS	Specimen violates Lehigh Criterion (Eq. 1.16). Strength Limit states predict plate not required (Eq. 2.1).
C4	W30×116	W27×235	One-sided RBS	Specimen violates Lehigh Criterion (Eq. 1.16). Strength Limit states predict plate not required (Eq. 2.1).
C5	W36×150	W14×211	One-sided RBS	Size of continuity plate designed as per Eq. 2.2. Column designed to have a weak panel zone to exacerbate column kinking. Beam designed to deliver a probable maximum beam flange force that results in a continuity plate thinner than Eq. 1.18. Continuity plate welds designed as the per the $w = (3/4)t_{cp}$ rule.
C6	W30×116	W24×176	One-sided RBS	Size of continuity plate designed per Eq. 2.2. The continuity plate also satisfied the minimum thickness as per Eq. 1.18. Welds conservatively designed ($w = t_{cp}$).
C6-G	W30×116	W24×176	One-sided RBS	Identical as Specimen C6 but, except all plates and the beam and column members were hot dip galvanized.
C7	W30×116	W24×192	One-sided RBS	Size of doubler plate to satisfy WLY limit state. FLB limit state satisfied without stiffening. Welds designed according to Eq. 2.22 and Eq. 2.26.
W1	W36×150	W27×258	Two-sided WUF-W	Size of continuity plate designed per Eq. 2.2. Extended doubler plate welded with PJP. Continuity plate welds designed as per the $w = (3/4)t_{cp}$ rule.
W2	W33×141	W27×217	Two-sided WUF-W	Size of continuity plate under-designed based per Eq. 2.2 (*DCR*=1.16). Continuity plate satisfied minimum thickness as per Eq. 1.18. Extended doubler plate welded with PJP. Continuity plate welds designed as per the $w = (3/4)t_{cp}$ rule.
W3	W30×116	W24×207	Two-sided WUF-W	Size of continuity plate designed per Eq 2.2. Weak panel zone (*DCR* of 1.07) per Eq. 1.19. Doubler plate stability criterion violated (Eq. 1.20). Extended doubler plate welded with vertical fillet welds to develop shear capacity. Continuity plate welds designed as per the $w = (3/4)t_{cp}$ rule.
W4	W24×94	W24×182	Two-sided WUF-W	Size of continuity plate designed per Eq. 2.2. Continuity plate satisfied minimum thickness as per Eq. 1.18. Doubler plate welds placed within continuity plates with vertical fillet welds to develop shear capacity. Continuity plate welds designed as per the $w = (3/4)t_{cp}$ rule.

a) Specimens tested and reported in Mashayekh and Uang (2018).

Table 2.2 Phase 1 Specimen RBS Dimensions

Spec. No.	a (in.)	b (in.)	c (in.)	R (in.)	$\frac{M_f}{M_{pe}}$
C1[a]	7.0	25.0	2.00	40.0	0.95
C2[a]	7.0	25.0	2.50	32.5	0.92
C3	6.0	24.0	2.50	30.0	0.91
C4	6.0	20.0	2.00	26.0	0.93
C5	6.0	24.0	2.00	37.0	0.88
C6	6.0	20.0	2.00	36.0	0.93
C6-G[b]	6.0	20.0	2.00	36.0	0.93
C7	6.0	20.0	2.25	23.3	0.89

a) Specimens tested and reported in Mashayekh and Uang (2018).

b) Specimen beam and column are galvanized.

Table 2.3 Continuity Plate Design Metric

Specimen No.	Span-to-Depth Ratio[a]	SCWB Ratio	t_{cp} (in.)	P_f (kips)	FLB (kips)	WLY (kips)	P_{cp} [b] (kips)	V_{cp} [b] (kips)	Cont. Plate *DCR*	b/t	w [c] (in.)	w/t_{cp}
C1	11.2	2.41	0.75	577	505	377	100	15.5	0.35	8.0	9/16	0.75
C2	9.6	1.58	0.63	719	1005	790	-36	-10.2	-	9.6	1/2	0.80
C3	9.9	1.60	-	709	1005	790	-41	-	-	-	-	-
C4	11.4	3.70	-	563	729	585	-11	-	-	-	-	-
C5	9.9	1.19	0.38	681	684	575	53	15.3	0.45	16.0	5/16	0.83
C6	11.6	2.48	0.50	563	505	377	93	14.5	0.68	12.0	1/2	1.00
C6-G	11.6	2.48	0.50	563	505	377	93	14.5	0.68	12.0	1/2	1.00
C7	11.6	2.84	-	538	600	764	-31	-	-	-	-	-
W1	6.8	1.05	0.50	1088	881	1532	104	28.4	0.86	12.0	3/8	0.75
W2	7.3	0.99	0.75	1040	633	1446	204	53.2	1.43	7.8	9/16	0.75
W3	8.2	1.11	0.50	849	693	1047	78	67.5	0.6	11.0	3/8	0.75
W4	10.1	1.22	0.75	710	419	926	146	41.9	0.95	7.3	9/16	0.75

a) Span-to-depth ratio for two-sided specimens listed for the shorter span.
b) Negative values result when continuity plates not required per §J10 in AISC 360 regarding the FLB and WLY limit states.
c) Weld size, w, tabulated for the continuity plate-to-column flange fillet weld.

Table 2.4 Doubler Plate Design Metric

Spec. No.	t_{dp} (in.)	V_{pz} (kips)	Panel Zone *DCR*	$\frac{d_z + w_z}{t_{cw}}$	$\frac{d_z + w_z}{t_{dp}}$	$q_{dp,v}$ (kips/in)	$0.6F_y t_{dp}$ (kips/in)	Doubler Plate Vertical Weld
C1	-	576	0.90	68	-	-	-	-
C2	-	692	0.96	40	-	-	-	-
C3	-	683	0.94	40	-	-	-	-
C4	-	562	0.63	59	-	-	-	-
C5	-	656	1.18	48	-	-	-	-
C6	-	562	0.88	68	-	-	-	-
C6-G	-	562	0.88	68	-	-	-	-
C7	0.63	537	0.43	63	81	9.2	18.8	7/16 in.
W1	0.63	2003	0.98	61	95	18.8	18.8	PJP
W2	0.75	1957	0.94	68	76	22.2	22.5	PJP
W3	0.50	1640	1.07	58	102	15.0	15.0	11/16 in.
W4	0.63	1431	0.93	64	72	18.3	18.3	7/8 in.

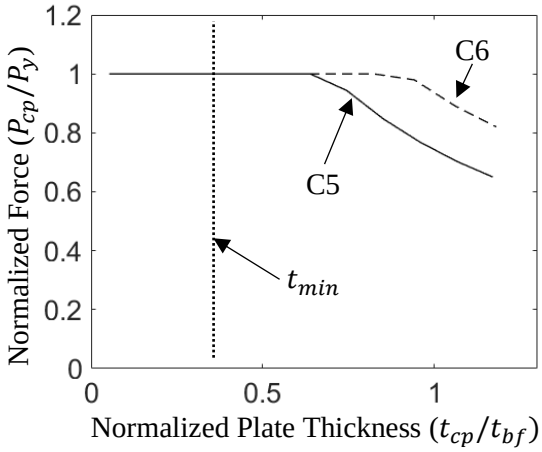

Figure 2.1 Continuity Plate Force Prediction

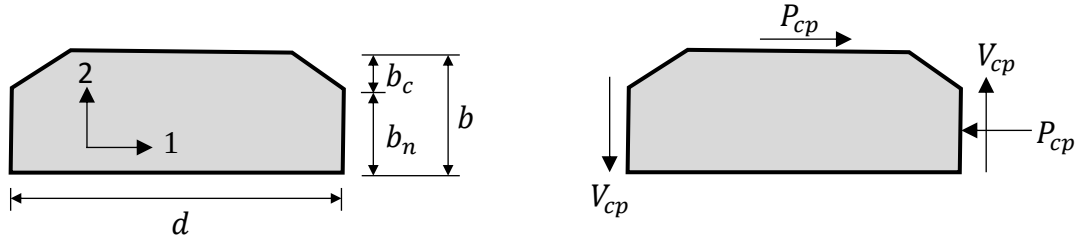

(a) Dimensions and Sign Convention (b) Free Body Diagram (Exterior)

Figure 2.2 Continuity Plate Diagrams

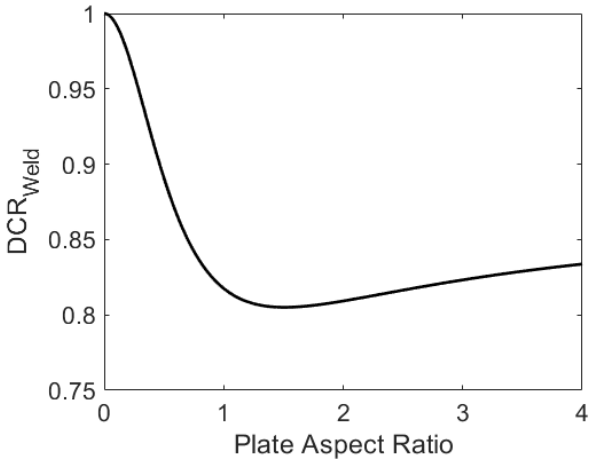

Figure 2.3 Continuity Plate Weld DCR Including Shear

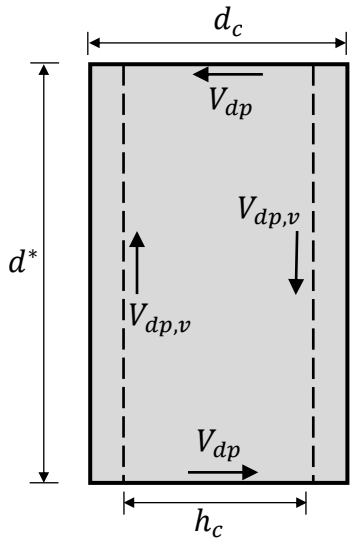

Figure 2.4 Doubler Plate Free Body Diagram

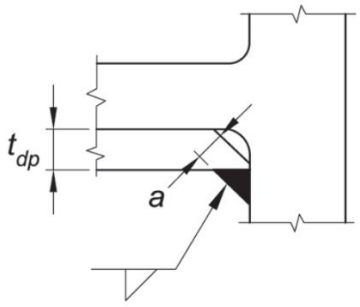

(a) Fig. C-E3.6.(b) AISC 341 (2016b)

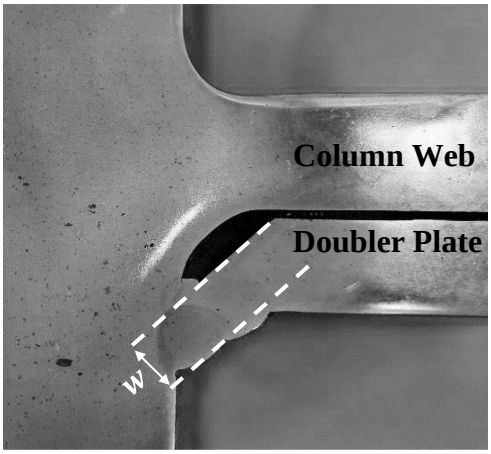

(b) Specimen C7

Figure 2.5 Doubler Plate Vertical Fillet Welds

3. EXPERIMENTAL PROGRAM

3.1. General

The testing was conducted in accordance with Section K2 of AISC 341 (2016b) at the Charles Lee Powell Structural Systems Laboratories of the University of California San Diego (UCSD). The full-scale testing program was divided into two phases. Phase 1 consisted of exterior (one-sided) beam-column subassemblies with Reduced Beam Section (RBS) moment connections. Table 3.1 shows the test matrix for the exterior RBS connections. The specimens used either a W36×150 beam or a W30×116 beam. Several shallow columns (W14×211 and W14×257) and several deeper column shapes (W24×176, W24×192, and W27×235) were tested. Three of the Phase 1 specimens (Specimens C5, C6, and C6-G) used a continuity plate that either met or was undersized according to §E3.6f.2(b) of AISC 341. The three specimens which did not use a continuity plate (Specimens C3, C4, and C7) violated the continuity plate requirement of §E3.6f.1(b) of AISC 341. Specimen C6-G was nominally identical to Specimen C6, except this specimen was hot-dip galvanized before simulated field welding. Specimen C7 was the only specimen of Phase 1 to use a doubler plate. Fillet welds were used for the vertical welds of this doubler plate.

Phase 2 consisted of four interior (two-sided) beam-column subassemblies with Welded Unreinforced Flange with a Welded Web (WUF-W) connections. Table 3.2 shows the beams and columns selected for the specimens. Specimen W1 used two W36×150 beams welded to a W27×258 column. Specimen W2 used two W33×141 beams welded to a W27×217 column. Specimen W3 used two W30×116 beams welded to a W24×207 column. Finally, Specimen W4 used two W24×94 beams welded to a W24×182 column. Specimens W2 and W4 used continuity plates which satisfied the minimum thickness as per AISC 341. The other two specimens used

continuity plates thinner than the minimum thickness requirement. All four specimens used doubler plates as symmetric plates placed on either side of the column. All of the doubler plates were extended 6 in. beyond the beam flange level, except for Specimen W4, which placed a doubler plate within the continuity plates. Specimens W1 and W2 used a PJP weld for the vertical welds, while Specimens W3 and W4 used fillet welds for the vertical welds.

All of the members satisfy the requirements of AISC 341 Section D1. Specifically, the members are proportioned to satisfy the requirements of a highly-ductile member. Except for Beam 1 of Specimen W1, all the specimens satisfy the clear span-to-depth ratio specified in either Chapter 5 or Chapter 8 of AISC 358-16. The remaining design details, including but not limited to Demand Critical (DC) welding of CJP beam-to-column welds, supplemental fillet welds, shear tab thickness, and continuity plate corner clips, satisfy the design requirements of AISC 341 or the connection-specific requirements of AISC 358.

3.2. Test Setups

The Phase 1 test setup is shown in Figure 3.1; each specimen was tested in the upright position. Frame inflection points are assumed to exist at the mid-height of each story, which are simulated by using three W14×257 hinge supports. The W14 shapes were mounted under the column and at the top and bottom as shown in Figure 3.2. The beam length represents half of the bay width, assuming an inflection point at the midspan of the beam. The loading end (south end of the specimen) is loaded through a 220-kip hydraulic actuator with an inline load cell. The load from the actuator is delivered to the free end of the beam through a loading corbel (see Figure 3.3). An intermediate top flange lateral restraint placed about 18 in. away from the RBS cut used for Specimens C3 and C5 is seen Figure 3.4. The top-flange lateral bracing outside of the RBS simulates the lateral restraint provided by a composite concrete slab in a real application. To

increase the stiffness of the intermediate lateral restraint, the two lateral columns were tied together. For the remainder of the specimens both the top and bottom flange of the beam was braced as the same location just beyond the reduced beam section (see Figure 3.5). A modular frame provides lateral bracing at the loading corbel at the end of the beam. All lateral restraints use a polished, greased sliding surface to minimize friction.

The Phase 2 test setup is shown in Figure 3.6; each specimen was tested in the horizontal position. As in Phase 1, frame inflection points are assumed to exist at the mid-height of each story. The lower end of the specimen is mounted in a clevis while the upper end uses a W14×311 hinge (see Figure 3.8). The clevis uses a 9-in. greased pin and a matching tang, which was designed to attach to the bottom of the specimens through a bolted base plate. The beam ends are loaded through loading corbels which slide on a greased plate elevated by a sliding block (see Figure 3.9). The load is delivered to the loading corbels through a 500-kip hydraulic actuator on each side of the specimen. Lateral restraint of the beam is achieved by sandwiching the beams between two HSS sections. These HSS sections are bolted to an HSS post which is post-tensioned to the laboratory strong floor.

3.3. Specimen Sizes and Test Order

Table 3.1 shows the member sizes and stiffening element details for the five specimens tested in Phase 1 as well as the two specimens previously tested by Mashayekh and Uang (2018). The Phase 2 specimens consisted of two identical beam shapes framing into a common column using the WUF-W connection. Table 3.2 summarizes the specimens of Phase 2. Table 3.3 shows the member cross-sectional dimensions for each test specimen. Detailed engineering drawings are included in the report by Reynolds and Uang (2019).

3.4. Specimen Construction and Inspection

The San Bernardino location (San Bernardino Steel) of The Herrick Corporation fabricated the test specimens. For reasons of economy, the field welding was simulated at Herrick's shop. The simulated field welding of Specimen C5 was observed on October 25 of 2018. Figure 3.10 to Figure 3.16 show the observed simulated field welding. At the time of welding, a visual inspection was performed by West Coast Inspection Services. After a 24-hour cool-down period, UT and magnetic particle testing were also performed by West Coast Inspection Services. Weld inspection of the Phase 2 specimens was completed by the Smith & Emery Company. See Reynolds and Uang (2019) for all Weld Inspection Reports. The inspections did not reveal any actionable flaws in the welding.

3.5. Material Properties

The W-shaped beams and columns were fabricated from ASTM A992 steel, while the continuity and doubler plates were fabricated from ASTM A572 Gr. 50 steel. Table 3.4 shows the mechanical properties of the base materials. Table 3.5 shows the chemical composition of the materials obtained from the Certified Mill Test Reports. Mill certificates and results of the tensile coupon testing is found in the report by Reynolds and Uang (2019).

The simulated field welding of the beam top and bottom flange CJP welds used an E70T-6 (Lincoln Electric NR-305) electrode in the flat position. The beam web CJP, beam top flange backing bar fillet, and beam bottom flange reinforcing fillet was welded with an E71T-8 (Lincoln Electric NR-232) electrode in the vertical and overhead positions. Continuity plate and doubler plate welds were shop-welded with an E70T-9C (Lincoln Electric OSXLH-70) electrode. These electrodes satisfy the requirements of AWS D1.8 (2016) for Demand Critical welds. Specifically, they satisfy the minimum Charpy V-Notch toughness requirements of 20 ft-lb at 0°F and 40 ft-lb

at 70°F. Table 3.6 shows the Charpy V-Notch toughness from the beam flange and beam web welds. Charpy samples were extracted in the transverse direction of a weld mockup fabricated on the same day as the Phase 2 specimens. Welding Procedure Specifications for shop and the simulated field welding are contained in the report by Reynolds and Uang (2019).

3.6. Instrumentation

A combination of displacement transducers, strain gauge rosettes, and uniaxial strain gauges were used to measure global and local responses. Figure 3.17 shows the location of the displacement transducers for the Phase 1 specimens. Displacement transducer L1 measured the displacement and controls the actuator for displacement-control testing. Transducer L2 was used to quantify slip, if any, between the loading corbel and beam tip. Panel zone deformations were measured from transducers L3 and L4. Column rotations were measured from transducers L5 and L6. Transducers L7 through L9 were used to monitor displacements at the supports, which were anticipated to be negligible.

Figure 3.18 shows the location of displacement transducers for the Phase 2 specimens. L1 and L2 measured the displacements and controlled the two actuators. Transducers L3 and L4 were used to quantify slip between the loading corbels and the beam ends. Column rotations were measured using transducers L5 and L6, while the panel zone deformation was measured by transducers L7 and L8. Transducers L12, L13, and L14 were used to monitor the out-of-plane displacement of the column. The remaining transducers were used to monitor the displacements at the supports, which were anticipated to be negligible.

Various rosettes and uniaxial strain gauges were used to measure the strains in the connection region (Reynolds and Uang 2019). It is typical practice to whitewash the specimens in the connection region prior to loading such that yielding can be photographed during testing. As

part of a pilot project to test the capabilities of Digital Imaging Correlation (DIC) software, the first two specimens tested (Specimens C3 and C5) were not whitewashed. Instead, a random speckle pattern was applied to key areas of the specimen. The remaining specimens were whitewashed to provide visual evidence of yielding.

3.7. Data Reduction

The Story Drift Angle (*SDA*) is the ratio between δ_{total} and L:

$$SDA = \delta_{total}/L \tag{3.1}$$

where δ_{total} is the total beam tip deflection measured by displacement transducer L1 (and L2 for Phase 2), and L is the length of the beam measured from the beam tip (i.e., loading point) to the centerline of the column.

The total plastic rotation (θ_p) of the specimen is calculated by dividing the plastic component (δ_p) of the beam tip displacement by L.

$$\Theta_p = \frac{\delta_p}{L} = \frac{1}{L}(\delta_{total} - \delta_e) = \frac{1}{L}\left(\delta_{total} - \frac{P}{K}\right) \tag{3.2}$$

where P is the applied load, δ_e is the elastic component of beam tip displacement, and K is the elastic stiffness determined from the initial low-amplitude response of P vs. δ_{total}.

The components of the beam tip displacement are separated into the displacements due to the flexure of the beam, the flexure of the column, and the shearing of the panel zone. Panel zone deformation, γ is computed using L3 and L4 in Phase 1 or L7 and L8 in Phase 2. Assigning the displacement recorded by L3 or L7 to δ_a and the displacement from L4 or L8 to δ_b, the average panel zone shear deformation is computed by:

$$\gamma = \frac{\sqrt{w_{pz}^2 + d_{pz}^2}}{2 w_{pz} d_{pz}}(\delta_b - \delta_a) \tag{3.3}$$

where w_{pz} and d_{pz} are the width and depth of the panel zone measure points. For specimens without a continuity plate, the transducers were placed within the panel zone to avoid spurious displacement caused by column out-of-plane flange flexure. Otherwise, the transducers were placed at the center of the cruciform formed by the beam flange, continuity plate, and column flange. A rigid-body correction is required when extrapolating the influence of the panel zone deformation on the beam tip deformation (Uang and Bondad 1996):

$$\delta_{pz} = \gamma L - \gamma d - \frac{d_b}{H}\left(L + \frac{d_c}{2}\right) \tag{3.4}$$

The contribution of the beam tip deformation due to the column flexure is found by transducers L5 and L6 in either phase. Assigning the displacement recorded by these transducers to δ_c and δ_d, respectively, results in:

$$\delta_{col} = \frac{\delta_d - \delta_c}{d_b} L - \gamma d_b \left(1 - \frac{d_b}{H}\right) \tag{3.5}$$

where the latter term is the correction to remove the panel zone deformation from the flexural deformations. Finally, the components of the beam tip deformation are as follows:

$$\delta_{total} = \delta_{beam} + \delta_{pz} + \delta_{col} \tag{3.6}$$

The contribution due to the beam can then be solved for as:

$$\delta_{beam} = \delta_{total} - \delta_{pz} - \delta_{col} \tag{3.7}$$

In the Phase 2 specimens an additional component of deformation exists due to the gap between the clevis and the pin, δ_{clevis}. The rigid-body motion of this is removed by incorporating the displacement recorded by transducer L15. Assigning δ_p to be the displacement recorded by transducer L15 results in:

$$\delta_{clevis} = \frac{2\delta_p}{H} L \tag{3.8}$$

Which gives the beam tip deformation for Phase 2 as:

$$\delta_{beam} = \delta_{total} - \delta_{pz} - \delta_{col} - \delta_{clevis} \tag{3.9}$$

The dissipated hysteretic energy is computed by integrating the load-displacement response such that:

$$E_{h,total} = E_{h,beam} + E_{h,pz} + E_{h,col} - E_{elastic} \tag{3.10}$$

where $E_{elastic}$ is the recoverable elastic energy. By convention, the integration of the dissipated energy includes only the drift cycles where the moment at the face of the column has not degraded beyond $0.8M_{pn}$, where M_{pn} equals the beam nominal plastic moment. This cutoff is imposed because strength degradation beyond this limit does not satisfy the SMF requirements of AISC 341. From the dissipated energy the cumulative plastic drift can be determined as:

$$\Sigma\theta_p = \frac{E_{h,total}}{M_p} \tag{3.11}$$

where M_p is the actual plastic moment of the section. The Reserved Energy Ratio. Ω_E, represents the amount of energy dissipated in excess of the first-cycle, 0.04 rad story drift angle requirement of SMF based on AISC 341. Setting the dissipated energy capacity, $E_{h,min}$, to be the dissipated energy after completing one cycle of 0.04 rad story drift results in:

$$\Omega_E = \frac{E_{h,total}}{E_{h,min}} \tag{3.12}$$

The peak connection strength factor, C_{pr}, accounting for strain hardening and local restraint, is used in predicting the seismic flange forces of the beams framing into the column (AISC 2016b). Specimen design has used the values provided in AISC 358-16 as 1.15 and 1.4 for the RBS and WUF-W connections, respectively. After testing of each specimen, C_{pr} is computed by normalizing the experimentally determined moment at the plastic hinge location by the expected moment, M_{pe}. For RBS connections, $M_{pe} = Z_{RBS}F_{ya}$, and for WUF-W connections, $M_{pe} = Z_xF_{ya}$, where F_{ya} is the measured yield strength of the material. Per AISC 358-16 The

plastic hinge location is assumed to take place at the center of the reduced section for RBS cuts and at the face of the column for WUF-W connections.

3.8. Loading Sequence

Testing is conducted in a displacement-control mode. The loading sequence used for all specimens was the standard AISC loading sequence specified in Section K2 of AISC 341 (2016). The AISC loading sequence specifies a series of load cycles at different *SDA*s. The loading history begins with six cycles each at 0.00375, 0.005, and 0.0075 rad drifts. These are followed by four cycles at 0.01 rad drifts, two cycles at 0.015 rad drifts, two cycles at 0.02, 0.03, 0.04 rad drifts, and etc., up until failure. Figure 3.19 shows the loading sequence.

3.9. Acceptance Criteria

According to Section E3.6b of the AISC Seismic Provisions for Structural Steel Buildings (AISC 2016b), beam-to-column connections used in special moment frames shall satisfy the following requirements:

(1) The connection shall be capable of accommodating a story drift angle of at least 0.04 rad.

(2) The measured flexural resistance of the connection, determined at the column face, shall equal at least $0.8M_{pn}$ of the connected beam at a story drift angle of 0.04 rad, where M_{pn} is the nominal plastic moment of the beam.

This chapter has been published as a Structural Systems Research Project (SSRP) Report: Reynolds, M., C-M., Uang, "Alternative Weld Details and Design for Continuity Plates and Doubler Plates for Applications in Special and Intermediate Moment Frames," *Report No. SSRP-19/03*, and submitted to AISC as the final project deliverable. This chapter is also being prepared for submission for publication and may appear in *AISC Engineering Journal*. The author of this dissertation is the primary author of this work; Prof. Chia-Ming Uang will coauthor this work.

Table 3.1 Phase One: Exterior RBS Connection Test Matrix

Spec. No.	Beam	Column	Continuity Plate (in.)	Continuity Plate Fillet Weld (in.)	Doubler Plate	Test Date
C1[a]	W30×116	W24×176	3/4	9/16	-	04/28/2016
C2[a]	W36×150	W14×257	5/8	1/2	-	04/04/2016
C3	W36×150	W14×257	-	-	-	11/02/2018
C4	W30×116	W27×235	-	-		1/29/2019
C5	W36×150	W14×211	3/8	5/16		11/14/2018
C6	W30×116	W24×176	1/2	1/2		2/08/2019
C6-G[b]	W30×116	W24×176	1/2	1/2		2/15/2019
C7	W30×116	W24×192	-	-	1 × 5/8”	2/04/2019

a) Specimens tested and reported in Mashayekh et al. (2017).

b) Specimen beam and column are galvanized.

Table 3.2 Phase Two: Interior WUF-W Connection Test Matrix

Spec. No.	Beam	Column	Continuity Plate (in.)	Continuity Plate Fillet Weld (in.)	Doubler Plate	Test Date
W1	W36×150	W27×258	1/2	3/8	2 × 5/8”	8/08/2019
W2	W33×141	W27×217	3/4	9/16	2 × 3/4”	7/31/2019
W3	W30×116	W24×207	1/2	3/8	2 × 1/2”	7/26/2019
W4	W24×94	W24×182	3/4	9/16	2 × 5/8”	7/22/2019

Table 3.3 Member Cross-Sectional Dimensions

Specimen No.	Member	d (in.)	t_w (in.)	b_f (in.)	t_f (in.)	Width-Thickness Ratio	
						Web	Flange
C1[a]	Beam (W30×116)	30.0	0.57	10.5	0.85	47.8	6.17
	Column (W24×176)	25.2	0.75	12.9	1.34	28.7	4.81
C2[a]	Beam (W36×150)	35.9	0.625	12.0	0.94	51.9	6.37
	Column (W14×257)	16.4	1.18	16.0	1.89	9.71	4.23
C3	Beam (W36×150)	35.9	0.625	12.0	0.94	51.9	6.37
	Column (W14×257)	16.4	1.18	16.0	1.89	9.71	4.23
C4	Beam (W30×116)	30.0	0.57	10.5	0.85	47.8	6.17
	Column (W27×235)	28.7	0.91	14.2	1.61	26.2	4.41
C5	Beam (W36×150)	35.9	0.625	12.0	0.94	51.9	6.37
	Column (W14×211)	15.7	0.98	15.8	1.56	11.6	5.06
C6, C6-G	Beam (W30×116)	30.0	0.57	10.5	0.85	47.8	6.17
	Column (W24×176)	25.2	0.75	12.9	1.34	28.7	4.81
C7	Beam (W30×116)	30.0	0.57	10.5	0.85	47.8	6.17
	Column (W24×192)	25.5	0.81	13.0	1.46	26.6	4.43

a) Specimens tested and reported in Mashayekh et al. (2017).

Table 3.3 Member Cross-Sectional Dimensions (continued)

Specimen No.	Member	d (in.)	t_w (in.)	b_f (in.)	t_f (in.)	Width-Thickness Ratio	
						Web	Flange
W1	Beam (W36×150)	35.9	0.625	12.0	0.94	51.9	6.37
	Column (W27×258)	29.0	0.980	14.3	1.77	24.4	4.03
W2	Beam (W33×141)	33.3	0.605	11.5	0.96	49.6	6.01
	Column (W27×217)	28.4	0.830	14.1	1.50	28.7	4.71
W3	Beam (W30×116)	30.0	0.565	10.5	0.85	47.8	6.17
	Column (W24×207)	25.7	0.870	13.0	1.57	24.8	4.14
W4	Beam (W24×94)	24.3	0.515	9.07	0.88	41.9	5.18
	Column (W24×182)	25.0	0.705	13.0	1.22	30.6	5.31

Table 3.4 Base Metal Mechanical Properties

Spec. No.	Component	Steel Type/ Heat No.	Yield Stress [a] (ksi)	Tensile Strength (ksi)	Elong.[b] (%)
C1	Beam Flange (W30×116)	A992 443484	56.9 (56.5)[b]	75.6 (72.0)[b]	34.5 (28.0)[b]
	Beam Web (W30×116)		58.5	73.2	39.5
	Column Flange (W24×176)	A992 442208	57.2 (57.5)[b]	70.6 (72.5)[b]	39.1 (27.0)[b]
	Column Web (W24×176)		58.5	72.2	37.3
	Continuity Plate (3/4 in.)	A572 Gr. 50 SB15106	68.1 (58.0)[b]	85.6 (81.0)[b]	36.9 (25.0)[b]
C2	Beam Flange (W36×150)	A992 60114091/04	53.5 (57.0)[b]	74.9 (75.1)[b]	38.3 (26.4)[b]
	Beam Web (W36×150)		57.9	74.7	38.1
	Column Flange (W14×257)	A992 317275	52.3 (57.0)[b]	74.3 (75.0)[b]	37.7 (26.0)[b]
	Column Web (W14×257)		54.8	74.8	38.6
	Continuity Plate (5/8 in.)	A572 Gr. 50 813K75180	54.1 (57.6)[b]	79.8 (82.6)[b]	35.1 (22.5)[b]
C3	Beam Flange (W36×150)	A992 421418	57.2 (57.0)[b]	72.4 (72.0)[b]	25.7 (26.0)[b]
	Beam Web (W36×150)		67.8	78.8	21.8
	Column Flange (W14×257)	A992 N039862	60.0 (59.0)[b]	80.4 (78.0)[b]	22.3 (28.0)[b]
	Column Web (W14×257)		52.6	75.5	29.6
C4	Beam Flange (W30×116)	A992 3G7361	59.7 (60.7)[b]	82.0 (82.8)[b]	22.7 (24.5)[b]
	Beam Web (W30×116)		65.7	85.4	-
	Column Flange (W27×235)	A992 488640	(53.0)[b]	(71.0)[b]	(27.0)[b]
	Column Web (W27×235)		60.0	75.0	24.8

Table 3.4 Base Metal Mechanical Properties (continued)

Spec. No.	Component	Steel Type/ Heat No.	Yield Stress [a] (ksi)	Tensile Strength (ksi)	Elong.[b] (%)
C5	Beam Flange (W36×150)	A992 440889	(55.0)[b]	(71.0)[b]	(28.0)[b]
	Beam Web (W36×150)		65.6	77.1	23.2
	Column Flange (W14×211)	A992 452443	54.3 (59.0)[b]	71.5 (75.0)[b]	24.2 (28.5)[b]
	Column Web (W14×211)		57.0	75.1	24.2
	Continuity Plate (3/8 in.)	A572 Gr. 50 N17266	59.9 (63.3)[b]	79.0 (82.0)[b]	20.5 (31.0)[b]
C6, C6-G	Beam Flange (W30×116)	A992 426935	56.9 (58.0)[b]	69.9 (72.0)[b]	24.3 (28.5)[b]
	Beam Web (W30×116)		62.8	76.4	22.2
	Column Flange (W24×176)	A992 463912	54.2 (57.0)[b]	73.0 (75.0)[b]	25.5 (26.5)[b]
	Column Web (W24×176)		61.0	74.3	23.6
	Continuity Plate (1/2 in.)	A572 Gr. 50 1202005567	(54.9)[b]	(75.2)[b]	(34.0)[b]
C7	Beam Flange (W30×116)	A992 A127163	57.1 (58.0)[b]	72.5 (72.0)[b]	24.3 (28.5)[b]
	Beam Web (W30×116)		61.7	74.2	23.7
	Column Flange (W24×192)	A992 H53207	57.6 (60.0)[b]	80.0 (80.0)[b]	22.8 (23.5)[b]
	Column Web (W24×192)		60.0	80.7	22.6
	Doubler Plate (5/8 in.)	A572 Gr. 50 N17707	51.2 (51.8)[b]	72.2 (70.8)[b]	23.9 (28.0)[b]

Table 3.4 Base Metal Mechanical Properties (continued)

Spec. No.	Component	Steel Type/ Heat No.	Yield Stress [a] (ksi)	Tensile Strength (ksi)	Elong.[b] (%)
W1	Beam Flange (W36×150)	A992 3110558	52.3 (57.0)[b]	78.8 (78.2)[b]	23.3 (26.1)[b]
	Beam Web (W36×150)		68.9	85.7	20.1
	Column Flange (W27×258)	A992 321553	52.6 (56.0)[b]	72.8 (74.0)[b]	25.3 (28.0)[b]
	Column Web (W24×258)		59.49	74.0	23.8
	Continuity Plate (1/2 in.)	A572 Gr. 50 N21707	(64.0)[b]	(80.2)[b]	(31.0)[b]
	Doubler Plate (2 × 5/8 in.)	A572 Gr. 50 N20741	(62.0)[b]	(80.5)[b]	(21.0)[b]
W2	Beam Flange (W33×141)	A992 506190	54.9 (53.0)[b]	70.4 (68.5)[b]	26.3 (29.5)[b]
	Beam Web (W33×141)		67.8	76.2	21.0
	Column Flange (W27×217)	A992 494737	59.7 (58.0)[b]	76.0 (75.0)[b]	24.2 (26.0)[b]
	Column Web (W27×217)		63.9	77.4	23.1
	Continuity Plate (3/4 in.)	A572 Gr. 50 S27292	(58.0)[b]	(81.0)[b]	(40.0)[b]
	Doubler Plate (2 × 3/4 in.)	A572 Gr. 50 S27292	(58.0)[b]	(81.0)[b]	(40.0)[b]
W3	Beam Flange (W30×116)	A992 504994	56.3 (53.5)[b]	71.3 (69.0)[b]	23.9 (27.5)[b]
	Beam Web (W30×116)		66.6	76.4	22.5
	Column Flange (W24×207)	A992 399018	58.3 (58.0)[b]	76.8 (76.5)[b]	22.9 (26.5)[b]
	Column Web (W24×207)		60.2	75.9	21.8
	Continuity Plate (1/2 in.)	A572 Gr. 50 N21707	(64.0)[b]	(80.2)[b]	(31.0)[b]
	Doubler Plate (2 × 1/2 in.)	A572 Gr. 50 N21707	(64.0)[b]	(80.2)[b]	(31.0)[b]

Table 3.4 Base Metal Mechanical Properties (continued)

Spec. No.	Component	Steel Type/ Heat No.	Yield Stress [a] (ksi)	Tensile Strength (ksi)	Elong.[b] (%)
W4	Beam Flange (W24×94)	A992 N 042176	53.5 (57.7)[b]	79.0 (76.6)[b]	21.6 (27.2)[b]
	Beam Web (W24×94)		60.5	81.3	23.6
	Column Flange (W24×182)	A992 H77491	57.4 (56.6)[b]	80.1 (76.9)[b]	22.3 (25.0)[b]
	Column Web (W24×182)		66.3	83.5	24.0
	Continuity Plate (3/4 in.)	A572 Gr. 50 S27292	(58.0)[b]	(81.0)[b]	(40.0)[b]
	Doubler Plate (2 × 5/8 in.)	A572 Gr. 50 N20741	(62.0)[b]	(80.5)[b]	(21.0)[b]

[a] Yield stress determined by 0.2% strain offset method

[b] Values in parentheses from Certified Mill Test Reports, others from testing at UCSD

Table 3.5 Chemical Compositions for Components from Mill Certificates

Spec. No.	Member	C	Mn	P	S	Si	Cu	Ni	Cr	Mo	V	CE (%)
C3	Beam (W36×150)	0.08	1.10	0.02	0.03	0.25	0.24	0.08	0.12	0.03	0.01	0.32
	Column (W14×257)	0.13	1.39	0.01	0.00	0.19	0.15	0.05	0.07	0.01	0.04	0.40
C4	Beam (W30×116)	0.17	1.03	0.02	0.01	0.13	0.23	0.10	0.15	0.02	0.03	0.40
	Column (W27×235)	0.08	1.31	0.01	0.02	0.20	0.27	0.13	0.19	0.05	0.04	0.38
C5	Beam (W36×150)	0.07	1.12	0.11	0.02	0.22	0.29	0.09	0.11	0.02	0.0	0.31
	Column (W14×211)	0.08	1.31	0.02	0.02	0.26	0.27	0.16	0.14	0.04	0.04	0.37
	Continuity Plate (3/8 in.)	0.14	1.08	0.01	0.00	0.22	0.01	0.05	0.02	0.00	0.02	0.33
C6, C6-G	Beam (W30×116)	0.08	1.10	0.01	0.02	0.25	0.23	0.09	0.12	0.04	0.0	0.32
	Column (W24×176)	0.08	1.36	0.02	0.02	0.21	0.25	0.12	0.14	0.05	0.05	0.37
	Continuity Plate (1/2 in.)	0.14	1.07	0.01	0.00	0.25	0.01	0.05	0.02	0.00	0.02	0.33
C7	Beam (W30×116)	0.07	1.23	0.01	0.03	0.23	0.30	0.10	0.10	0.031	0.04	0.33
	Column (W24×192)	0.26	1.03	0.01	0.01	0.22	0.20	0.09	0.09	0.017	0.03	0.40
	Doubler Plate (5/8 in.)	0.14	1.03	0.01	0.01	0.22	0.01	0.05	0.02	0.00	0.02	0.32

Table 3.5 Chemical Compositions for Components from Mill Certificates (continued)

Spec. No.	Member	C	Mn	P	S	Si	Cu	Ni	Cr	Mo	V	CE (%)
W1	Beam (W36×150)	0.17	1.02	0.07	0.01	0.14	0.24	0.08	0.13	0.02	0.03	0.39
	Column (W27×258)	0.07	1.38	0.02	0.02	0.24	0.30	0.09	0.11	0.03	0.05	0.37
	Continuity Plate (1/2 in.)	0.17	1.06	0.02	0.01	0.22	0.01	0.04	0.03	0.00	0.02	0.36
	Doubler Plate (2 × 5/8 in.)	0.14	1.10	0.02	0.01	0.23	0.01	0.05	0.02	0.00	0.05	0.38
W2	Beam (W33×141)	0.07	1.01	0.01	0.02	0.21	0.30	0.10	0.12	0.02	0.01	0.29
	Column (W27×217)	0.07	1.35	0.02	0.02	0.26	0.29	0.11	0.13	0.03	0.05	0.36
	Continuity Plate (3/4 in.)	0.14	1.34	0.01	0.00	0.31	0.01	0.01	0.02	0.00	0.07	0.39
	Doubler Plate (2 × 3/4 in.)	0.14	1.34	0.01	0.00	0.31	0.01	0.01	0.02	0.00	0.07	0.39
W3	Beam (W30×116)	0.08	1.00	0.01	0.02	0.20	0.32	0.13	0.10	0.04	0.01	0.31
	Column (W24×207)	0.07	1.35	0.01	0.03	0.29	0.25	0.11	0.15	0.04	0.05	0.37
	Continuity Plate (1/2 in.)	0.17	1.06	0.02	0.01	0.22	0.01	0.04	0.03	0.00	0.02	0.36
	Doubler Plate (2 × 1/2 in.)	0.17	1.06	0.02	0.01	0.22	0.01	0.04	0.03	0.00	0.02	0.36
W4	Beam (W24×94)	0.18	0.94	0.02	0.01	0.15	0.21	0.08	0.12	0.02	0.13	0.39
	Column (W24×182)	0.15	1.10	0.01	0.01	0.19	0.22	0.07	0.09	0.02	0.12	0.38
	Continuity Plate (3/4 in.)	0.14	1.34	0.01	0.00	0.31	0.01	0.01	0.02	0.00	0.07	0.39
	Doubler Plate (2 × 5/8 in.)	0.14	1.10	0.02	0.01	0.23	0.01	0.05	0.02	0.00	0.05	0.38

$$CE = C + \frac{Mn}{6} + \frac{Cr + Mo + V}{5} + \frac{Ni + Cu}{15}$$

Table 3.6 Weld Metal Charpy V-Notch Test Results

Weld Electrode	Energy (ft-lbs)							
	at 0°F				at 70°F			
E71T-8 (Lincoln Electric NR 232)	62	60	57		84	73	76	
	Average: 60				Average: 78			
E70T-6C (Lincoln Electric NR 305)	44	44	44	45	62	62	59	58
	Average: 44				Average: 60			

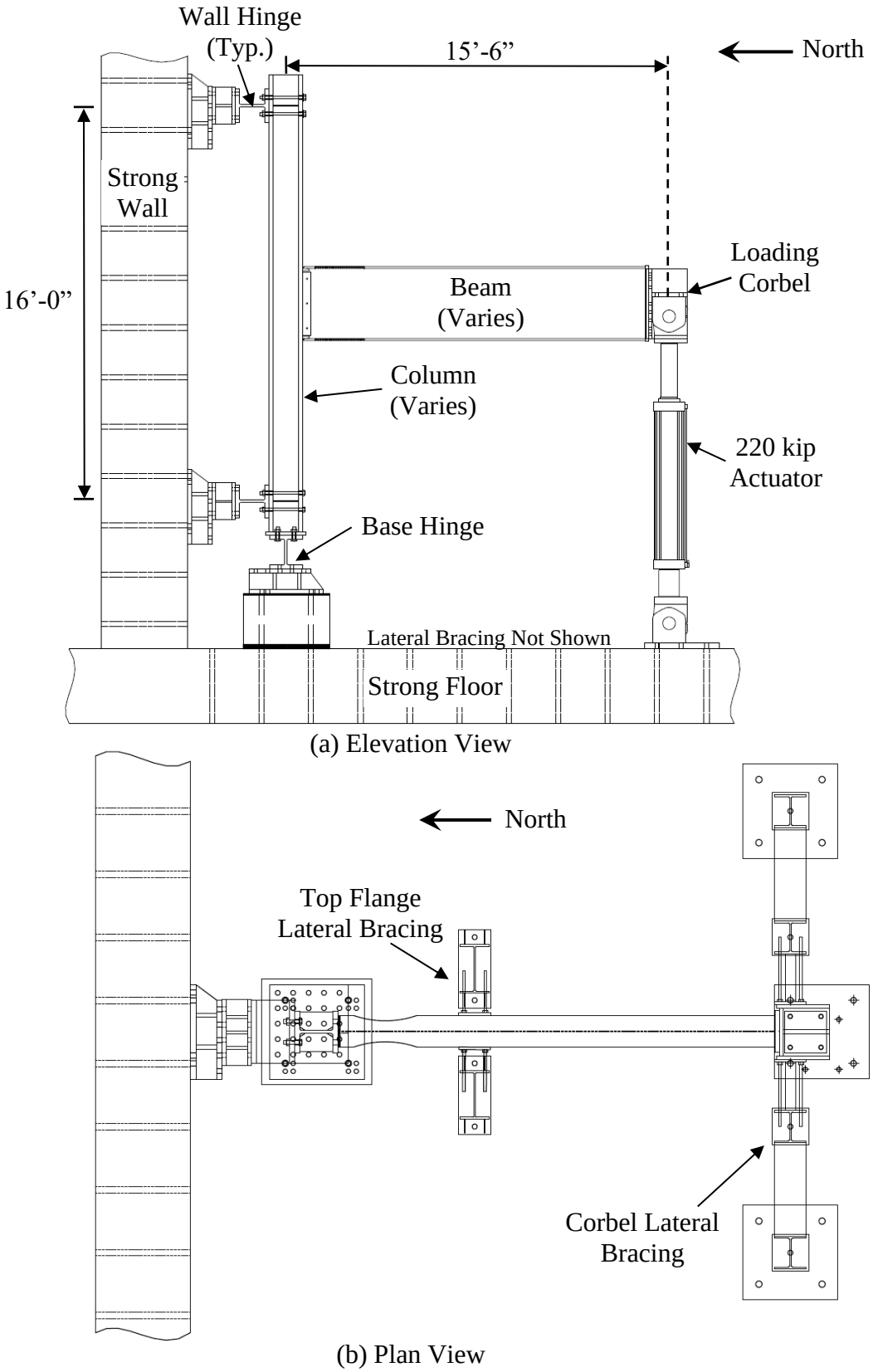

Figure 3.1 Exterior Moment Connection Test Setup (Phase 1)

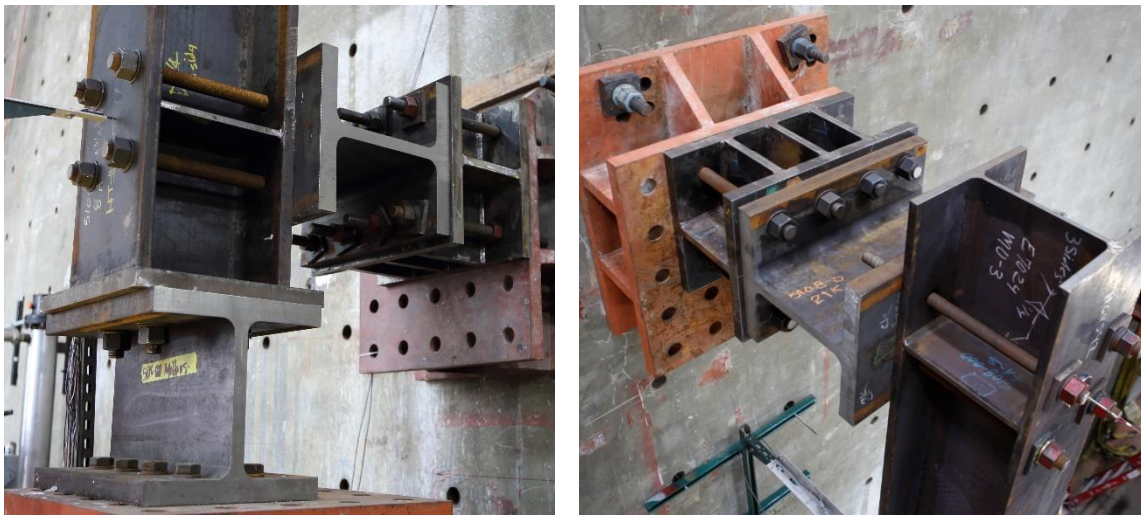

(a) Lower End (b) Upper End

Figure 3.2 Column Support (Phase 1)

Figure 3.3 Lateral Bracing at Loading End (Phase 1)

(a) Overview

(b) Detail

Figure 3.4 Top Flange Intermediate Lateral Restraint (Specimens C3 and C5)

Figure 3.5 Top Flange Intermediate Lateral Restraint (Specimens C4, C6, C6-G, and C7)

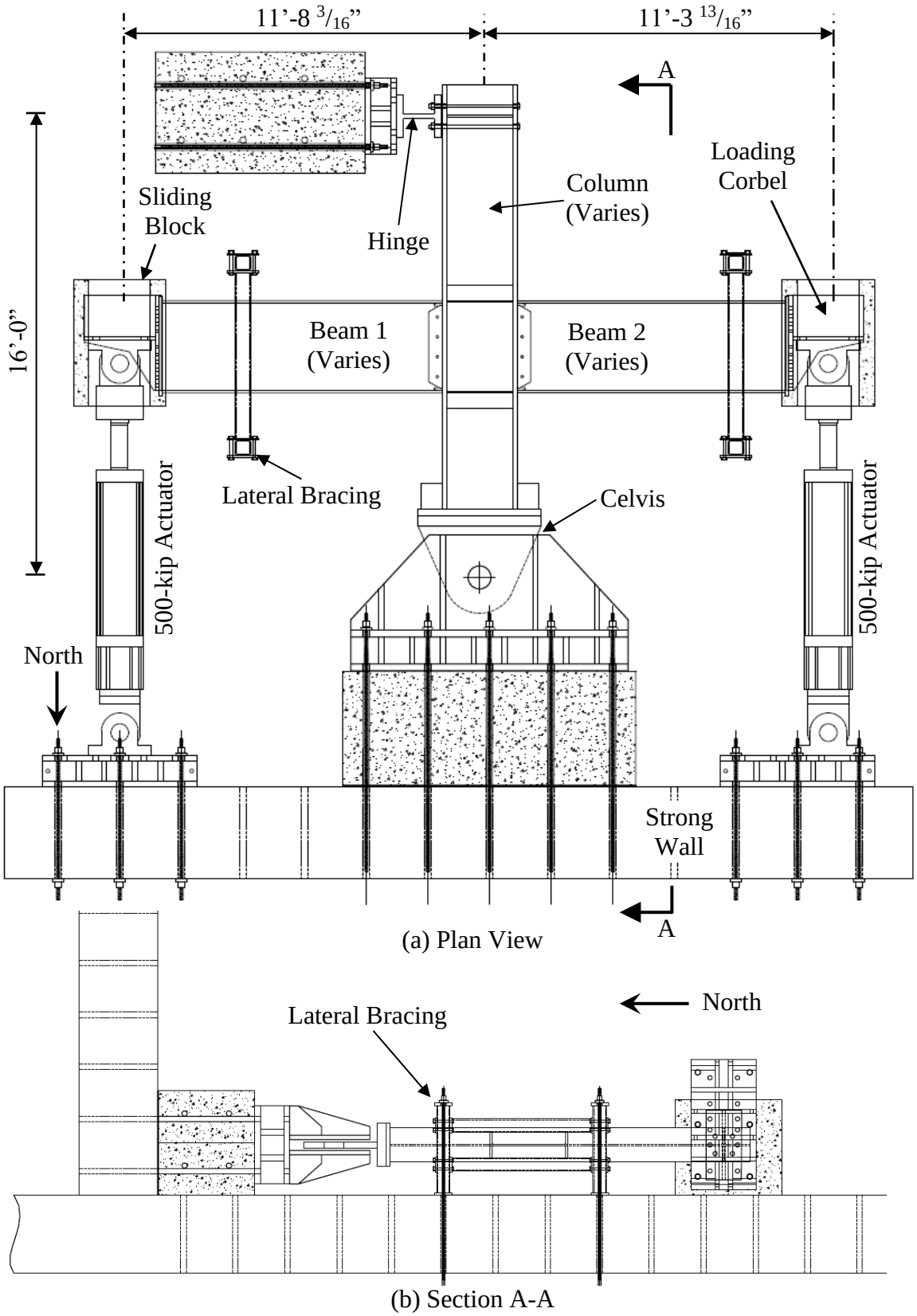

Figure 3.6 Interior Moment Connection Test Setup (Phase 2)

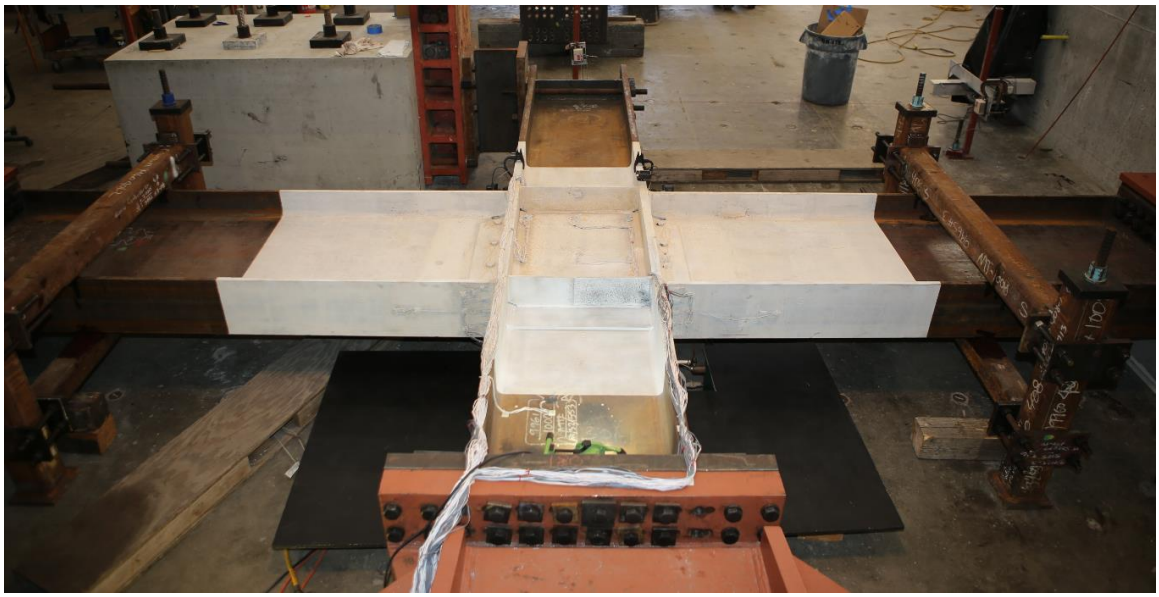

Figure 3.7 Test Setup (Phase 2)

(a) Column Base Support Clevis

(b) Top Column Support

Figure 3.8 Column Supports (Phase 2)

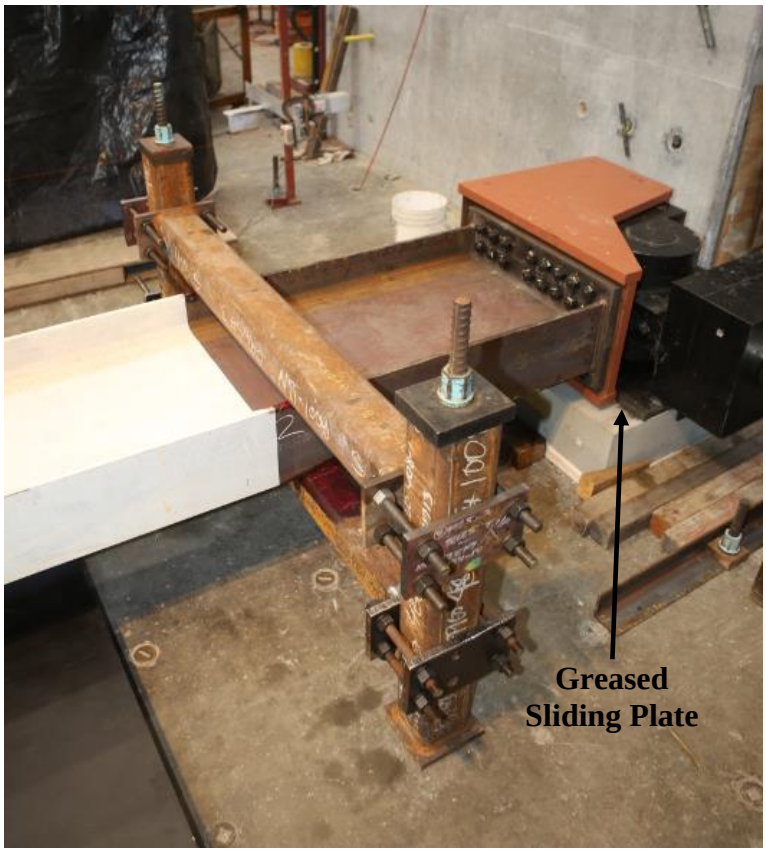

Figure 3.9 Beam Lateral Restraint and Loading End (Phase 2)

(a) Overview

(b) Weld Access Hole

(c) Run off Tab

Figure 3.10 Beam Bottom Flange and Web CJP Weld Preparation (Specimen C5)

(a) Backing Bar

(b) Groove

Figure 3.11 Beam Top Flange CJP Weld Preparation (Specimen C5)

(a) Beam Bottom Flange

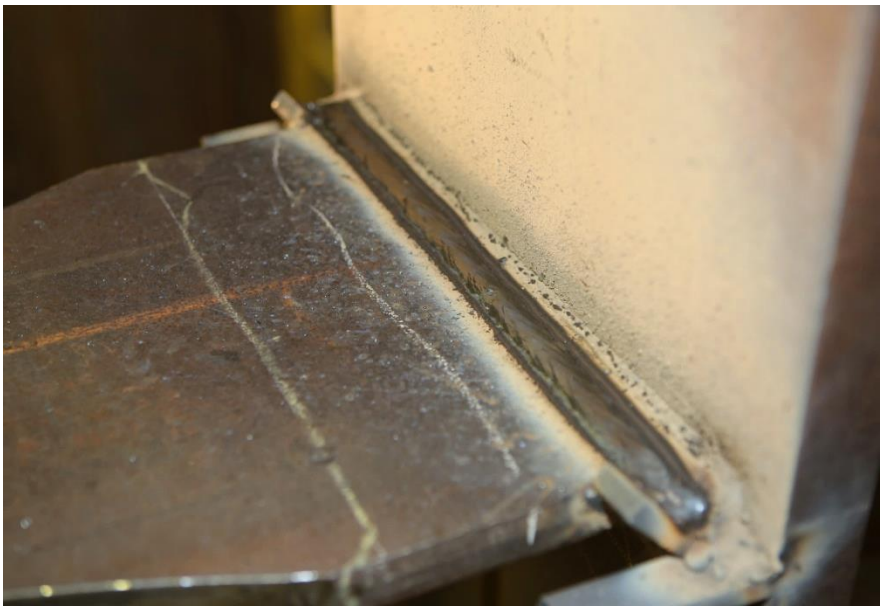

(b) Beam Top Flange

Figure 3.12 Beam Flange CJP Weld during Groove Welding (Specimen C5)

(a) Backgouging

(b) Reinforcing Fillet

Figure 3.13 Beam Bottom Flange Underside CJP Weld Treatment (Specimen C5)

(a) Reinforcing Fillet

(b) after Cleanup

Figure 3.14 Beam Top Flange Underside CJP Weld Treatment (Specimen C5)

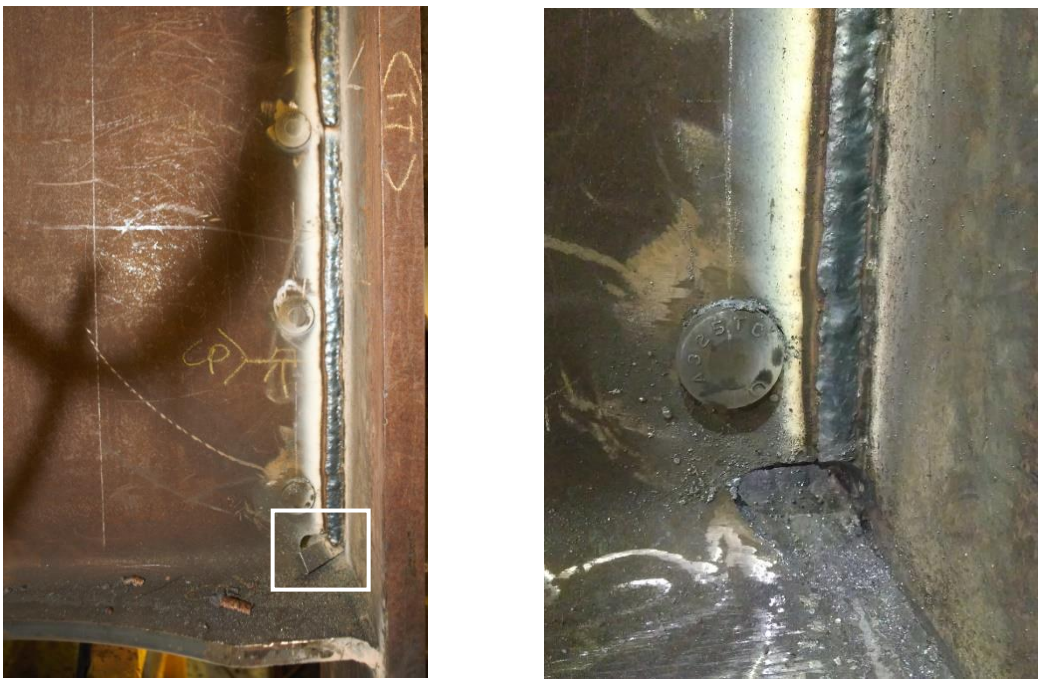

(a) Completed Weld (b) after Cleanup

Figure 3.15 Beam Web Weld (Specimen C5)

Figure 3.16 Continuity Plate Fillet Welds (Specimen C5)

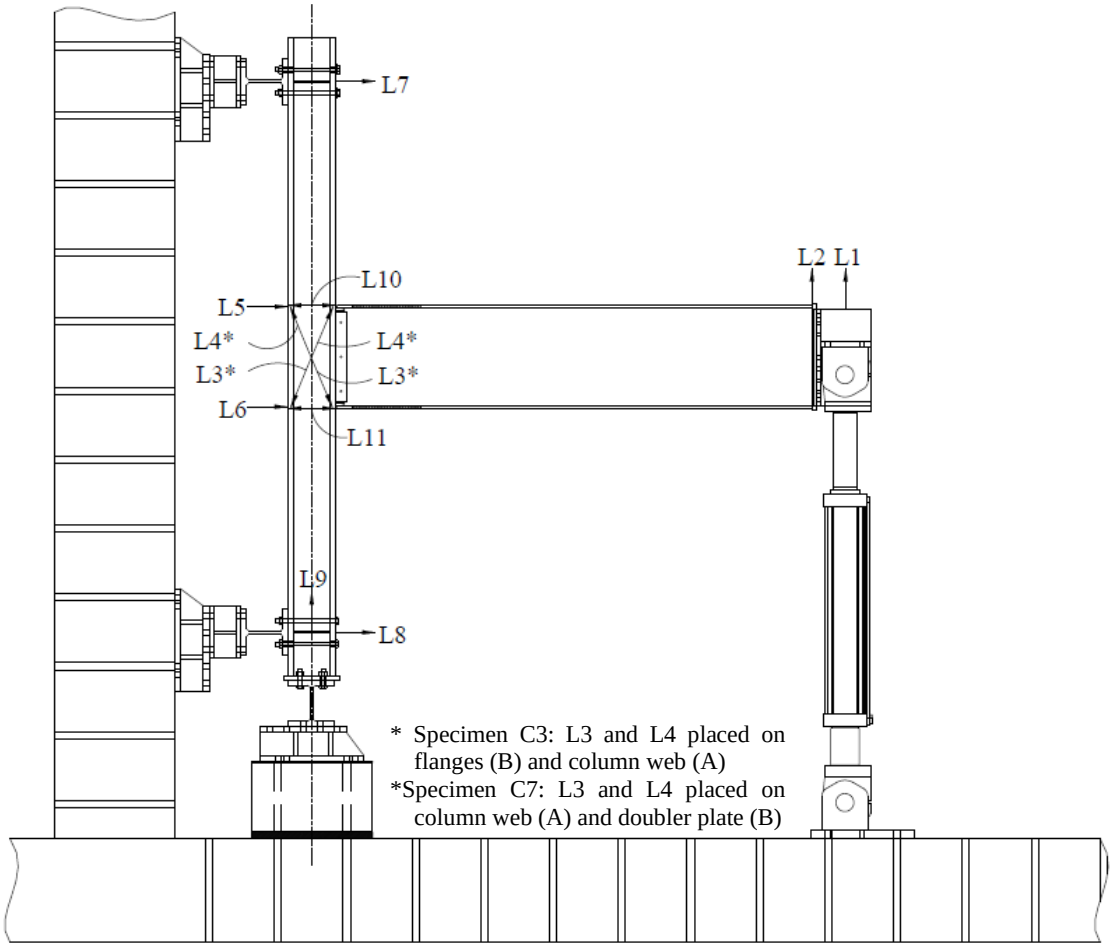

Figure 3.17 Exterior Moment Connection Transducer Layout (Specimens C3 to C7)

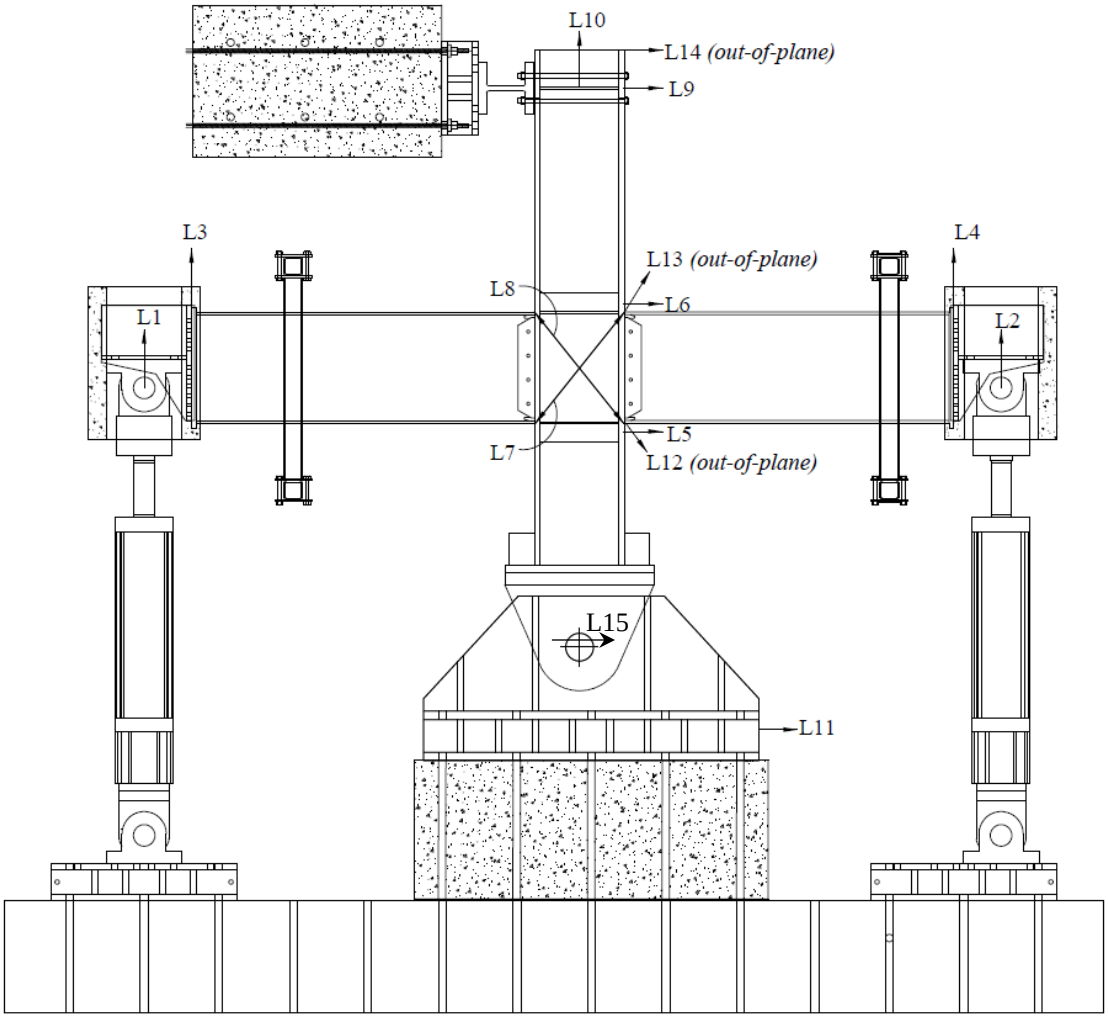

Figure 3.18 Interior Moment Connection Transducer Layout (Specimens W1 to W4)

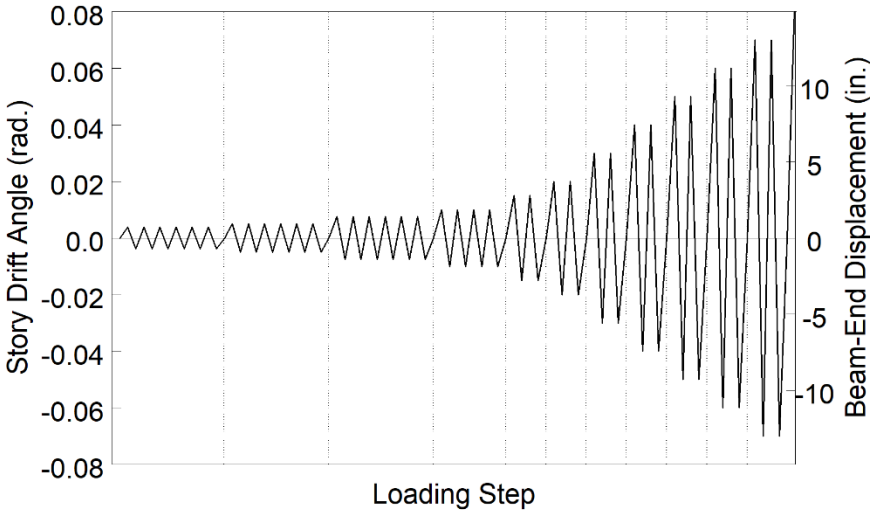

Figure 3.19 AISC Loading Protocol

4. TEST RESULTS

4.1. General

This section contains the observed and recorded response for the Phase 1 and 2 specimens. during the imposed AISC Loading protocol. The reported response is abbreviated here, a complete description is found in Reynolds and Uang (2019).

4.2. Specimen C3

4.2.1. General

Specimen C3 was designed to challenge the Lehigh Criterion. This was the only requirement of AISC 341 (2016) that would necessitate a continuity plate in this specimen; the flange force computed from AISC 358 (2016) for this connection does not exceed any column limit state of AISC 360 §J10 (2016). The specimen also closely matches Specimen C2 tested during the verification of the flexibility method, except that Specimen C2 used a 5/8-in. continuity plate. The panel zone of Specimen C3 has a high DCR of 0.94. Figure 4.1 shows the specimen before testing. The specimen failed by a complete fracture of the beam top flange CJP weld during the second cycle of 0.05 rad drift.

4.2.2. Observed Performance

The observed response for Specimen C3 is described below.

- Figure 4.2 shows the east side of the specimen at the peak excursions during the later cycles of the loading protocol. The specimen met the AISC acceptance criteria by completing one complete cycle at 0.04 rad drift while the flexural strength at the column face did not degrade below 80% of the beam nominal flexural strength. It was observed that beam web buckling initiated during the first cycle of 0.04 rad drift. Flange local bucking initiated at

the beam bottom flange within the RBS cut during the second cycle of 0.04 rad drift. By 0.05 rad drift flange local bucking was observed in both flanges.

- Figure 4.3 shows ductile tearing of the beam top flange CJP weld that was first observed during the 2nd negative excursion of 0.03 rad drift. Minor growth of this fracture occurred during the 0.04 rad cycles occurred during testing.
- Figure 4.4 shows the progression of web buckling. It was observed that the buckling orientation was mirrored in the web between positive and negative excursions.
- Figure 4.5(a) shows an incomplete beam top flange CJP weld fracture, that occurred during the first negative excursion to 0.05 rad extending from the west side of the flange to 2.5 in. beyond the center of the flange. Complete fracture of the CJP weld occurred at -0.013 rad drift of the second cycle of 0.05 rad drift. This shear type fracture originates at a toe of the prominent weld pass against the column and propagates through the flange at a 35-degree angle through the base metal. At the flange tips the fracture takes on a cup and cone with interlocking shear lips through the weld and base metal of the beam. The asymmetry in the fracture pattern was likely due to beam lateral-torsional buckling.
- Figure 4.6 shows the connection after testing. The top flange CJP weld fractured at -0.013 rad of the second cycle of 0.05 rad drift. Tearing of the web through the erection bolts occurred during continued negative excursion. Figure 4.7 shows the beam lateral-torsional buckling at the end of testing. The buckling was most pronounced in the unbraced bottom flange of the beam.
- Figure 4.8 shows the beam top flange CJP weld fracture after testing. The lateral-torsional buckling has produced a latent twist to the beam. A ductile shear fracture through the weld metal was observed at the center of the flange. A small fracture exists perpendicular to the

beam at the termination of this fracture at the center of the flange. The ends of the beam flange fractured as a typical tension fracture with interlocking shear lips.

4.2.3. Recorded Response

- Figure 4.9 shows the recorded displacement response of the beam tip measured with transducer L1. A hairline crack at the centerline of the beam top flange CJP weld was observed at the first negative excursion of 0.03 rad drift. The beam top flange CJP weld experienced an incomplete fracture at -0.029 rad of the first negative excursion of 0.05 rad drift. The beam top flange continued to tear in a ductile manner until the peak excursion was reached. At -0.015 rad drift during the second negative excursion of 0.05 rad drift the remaining portion of the beam top flange CJP weld fractured. Continued excursion saw tearing of the web which originated at the radius of the weld access hole and propagated through the first two bolt holes in the shear tab.
- Figure 4.10 shows the load-displacement response of the beam.
- Figure 4.11 shows the computed moment at the column face (M_f) versus the story drift angle. Two horizontal axes at 80% of the nominal plastic moment (M_{pn}) of the beam section are also added. In addition, two vertical axes at ±0.04 rad story drift show the drift required for SMF connections per AISC 341. It was observed that the beam developed its nominal plastic bending moment. If the moment is computed at the plastic hinge location and compared to the expected plastic moment, then the peak connection strength factor (C_{pr}) is 1.13.
- Figure 4.12 shows the plastic response of the specimen. The plastic response is computed using the procedure outlined in Section 3.7. The computed elastic stiffness of the specimen was determined to be 57.9 kips/in.

- Figure 4.13 shows the panel zone deformation determined from transducers L3 and L4. It was observed that modest panel zone yielding occurred.
- Figure 4.14 shows the dissipated energy of Specimen C3. The dissipated energy is obtained by integrating the load-displacement response of each constituent deformation. Dotted vertical lines on the graph demonstrate the completion of each group of cycles, and the dashed red vertical line shows the completion of the first cycle of 0.04 rad in the AISC loading. An additional vertical axis normalizes the hysteretic energy by the nominal plastic moment of the beam to determine the cumulative plastic rotation. It is observed that the completion of the first drift cycle of 0.04 rad (the requirement for SMF connections per AISC 341) occurs after 530 kip-ft of energy has been dissipated. The connection does not degrade below $0.8M_{pn}$ until 975 kip-ft of energy has been dissipated. Therefore, only 54% of the energy dissipation capacity was utilized after the completion of the 0.04 rad drift requirement. It is observed that most (71%) of the energy dissipation capacity occurred in the beam.

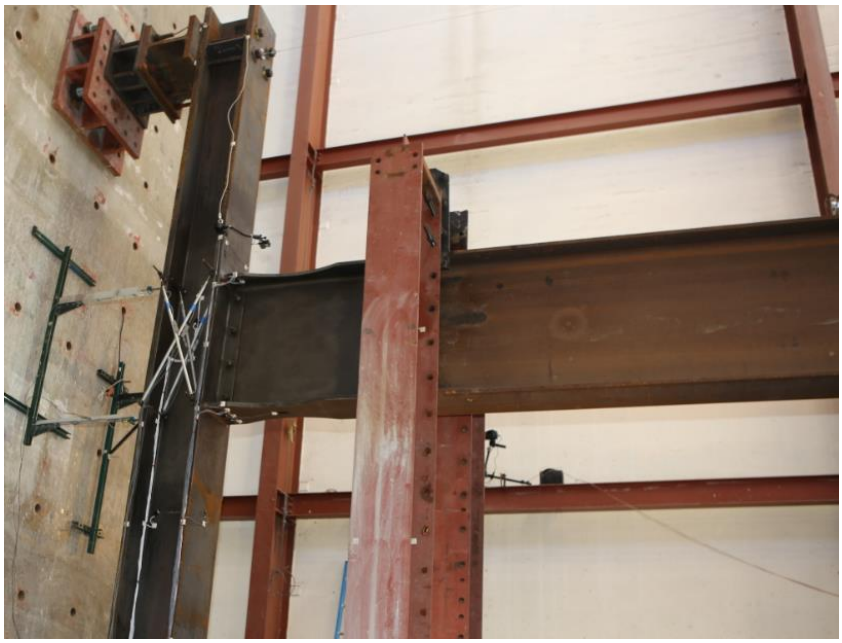

(a) West Side

(b) East Side

Figure 4.1 Specimen C3: Specimen before Testing

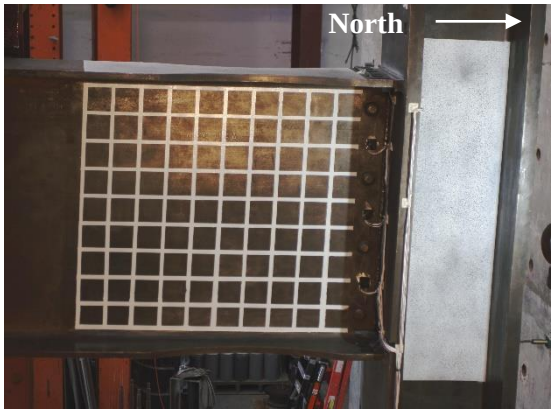

(a) +0.03 rad (2nd Cycle)

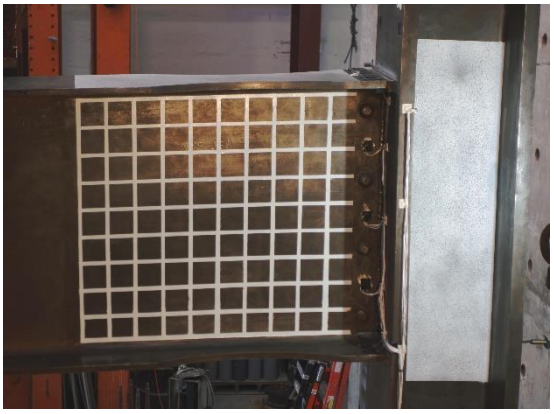

(b) -0.03 rad (2nd Cycle)

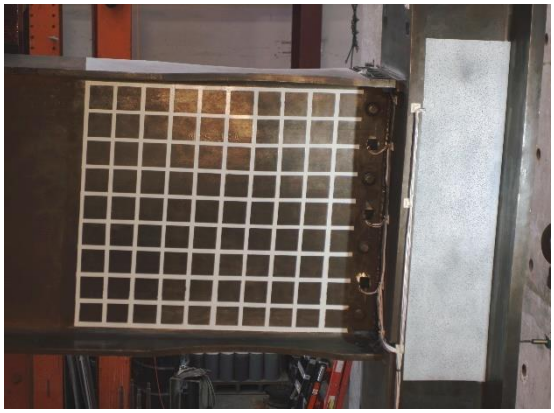

(c) +0.04 rad (2nd Cycle)

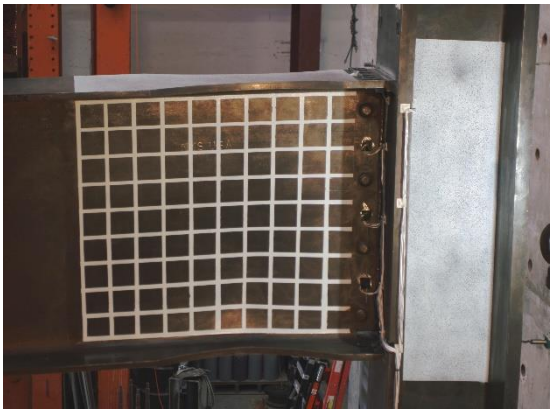

(d) -0.04 rad (2nd Cycle)

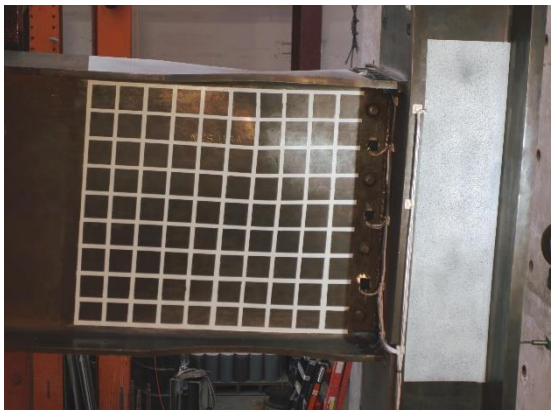

(e) +0.05 rad (1st Cycle)

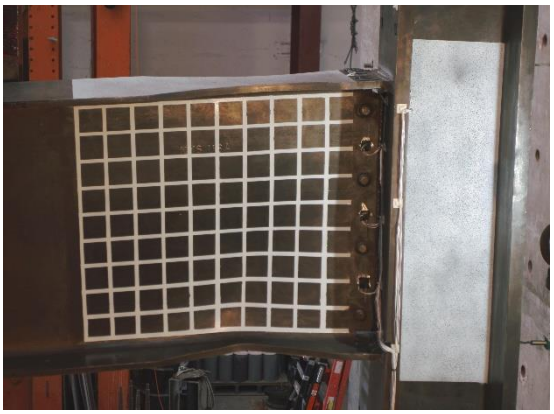

(f) -0.05 rad (1st Cycle)

Figure 4.2 Specimen C3: East Side of Connection

(a) Overview

(b) Tearing at -0.03 rad (2nd Cycle)

(c) -0.04 rad (1st Cycle)

(d) -0.04 rad (2nd Cycle)

Figure 4.3 Specimen C3: Beam Top Flange Weld Tearing

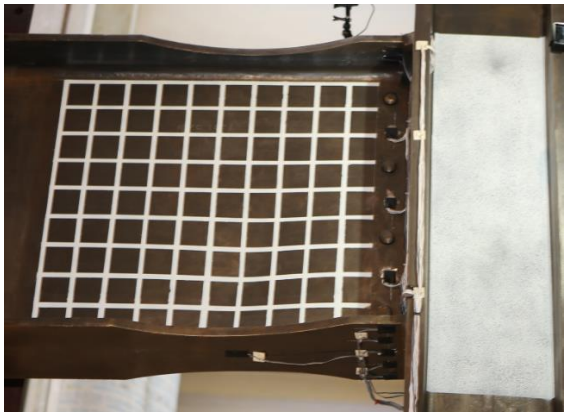

(a) -0.04 rad (1st Cycle)

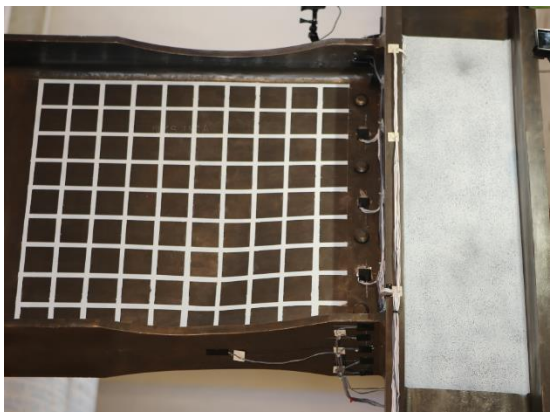

(b) -0.04 rad (2nd Cycle)

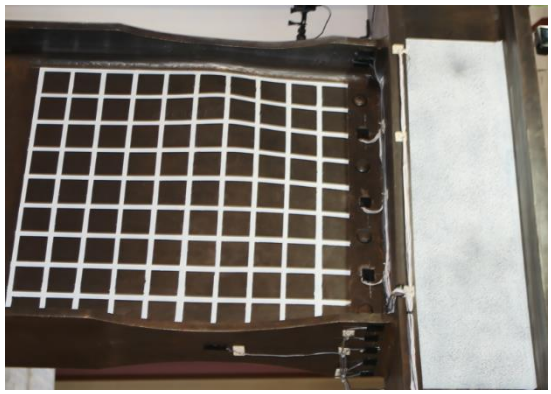

(c) +0.05 rad (1st Cycle)

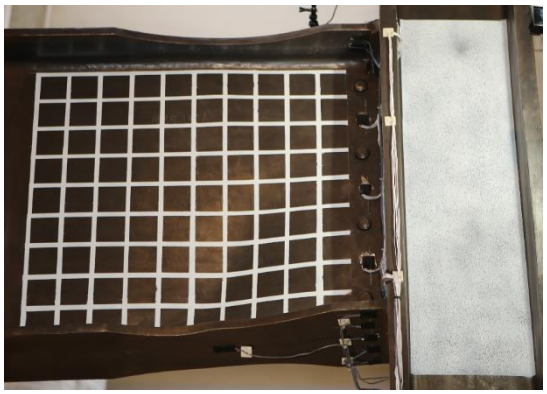

(d) -0.05 rad (1st Cycle)

Figure 4.4 Specimen C3: Beam Web Buckling

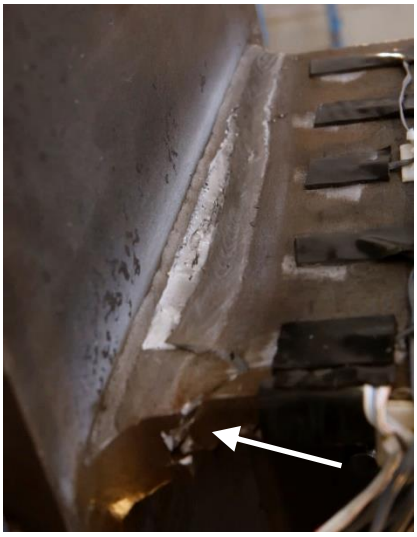

(a) -0.05 rad (1st Cycle)

(b) -0.013 rad (during 2nd Cycle at 0.05 rad Drift)

Figure 4.5 Specimen C3: Beam Top Flange Fracture

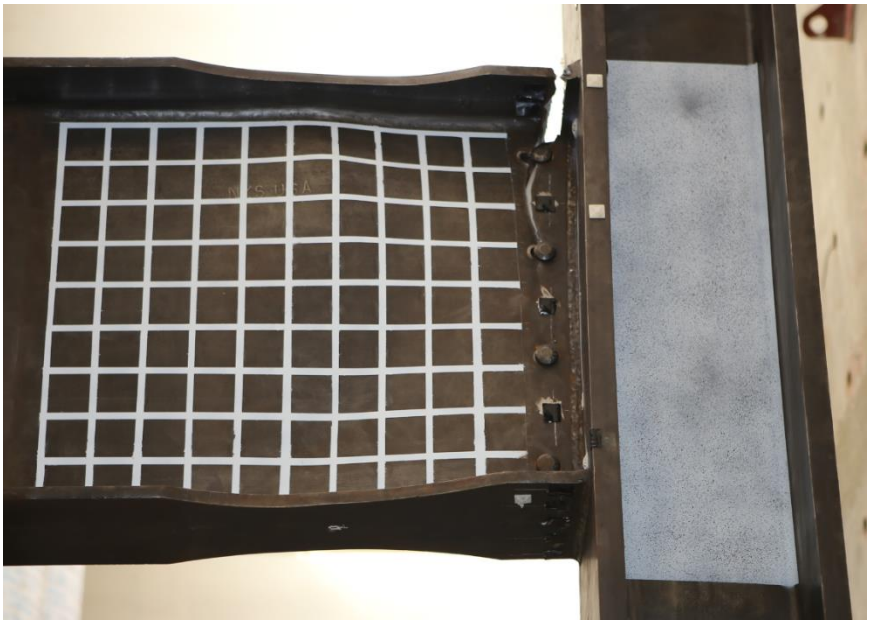

(a) East Side

(b) West Side

Figure 4.6 Specimen C3: Connection at End of Test

Figure 4.7 Specimen C3: Beam Lateral-Torsional Buckling (End of Test)

(a) Overview

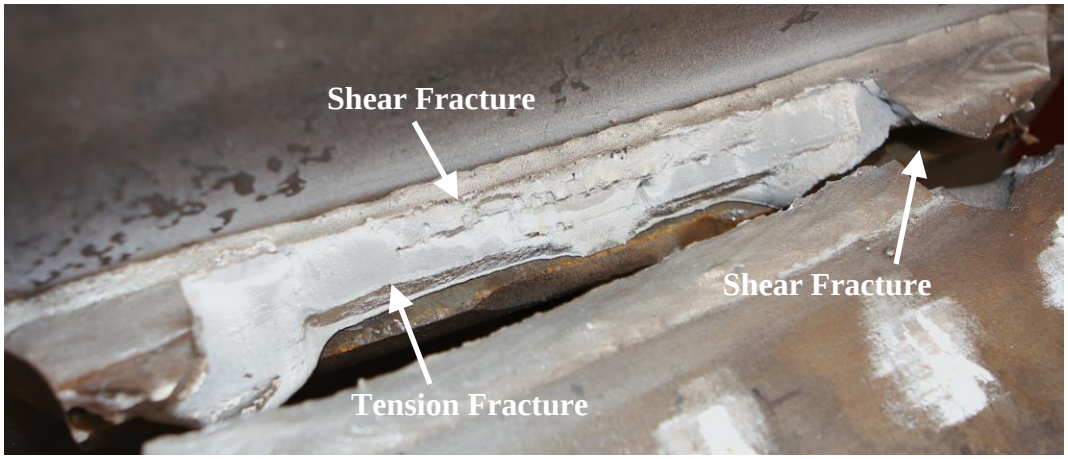

(b) Fracture Surface

Figure 4.8 Specimen C3: Beam Top Flange CJP Weld Fracture (End of Test)

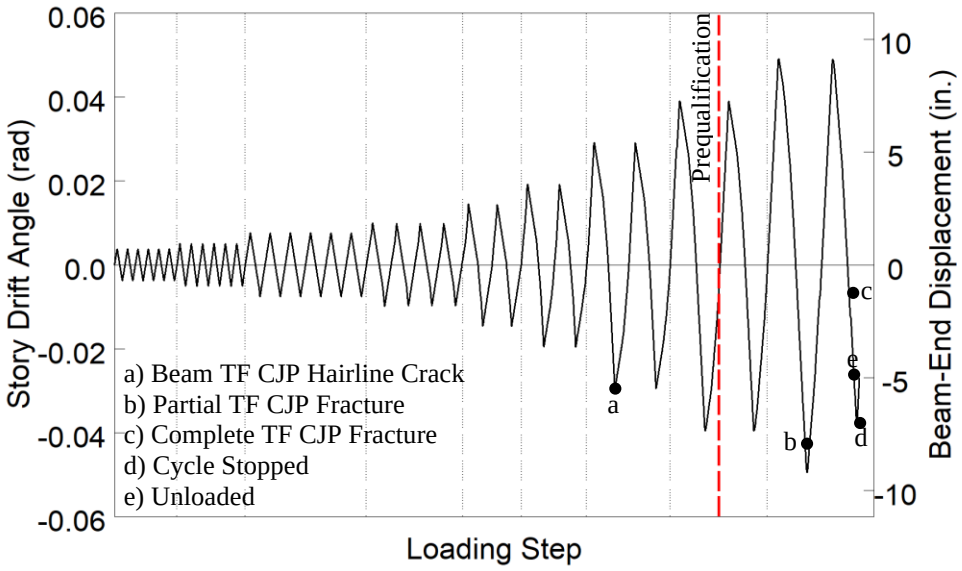

Figure 4.9 Specimen C3: Recorded Loading Sequence

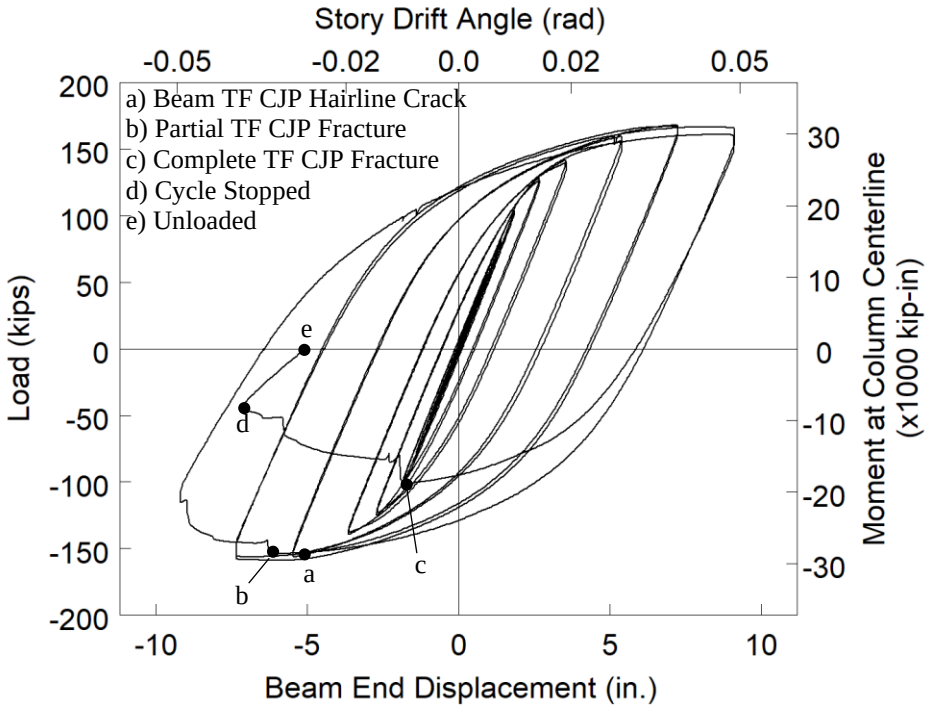

Figure 4.10 Specimen C3: Applied Load versus Beam End Displacement Response

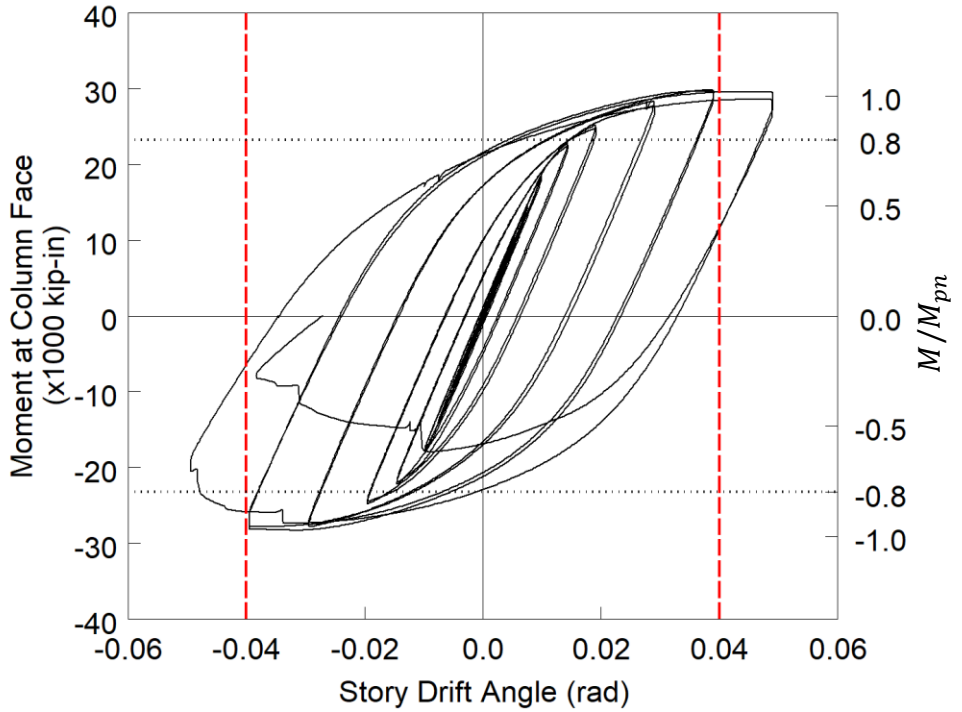

Figure 4.11 Specimen C3: Moment at Column Face versus Story Drift Response

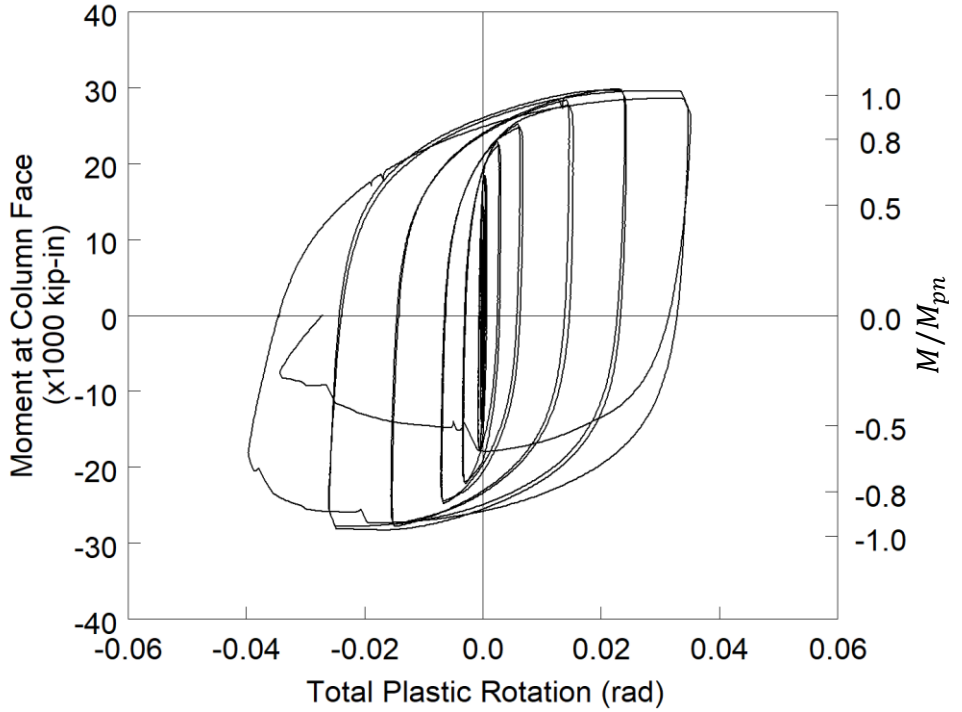

Figure 4.12 Specimen C3: Moment at Column Face versus Plastic Rotation Response

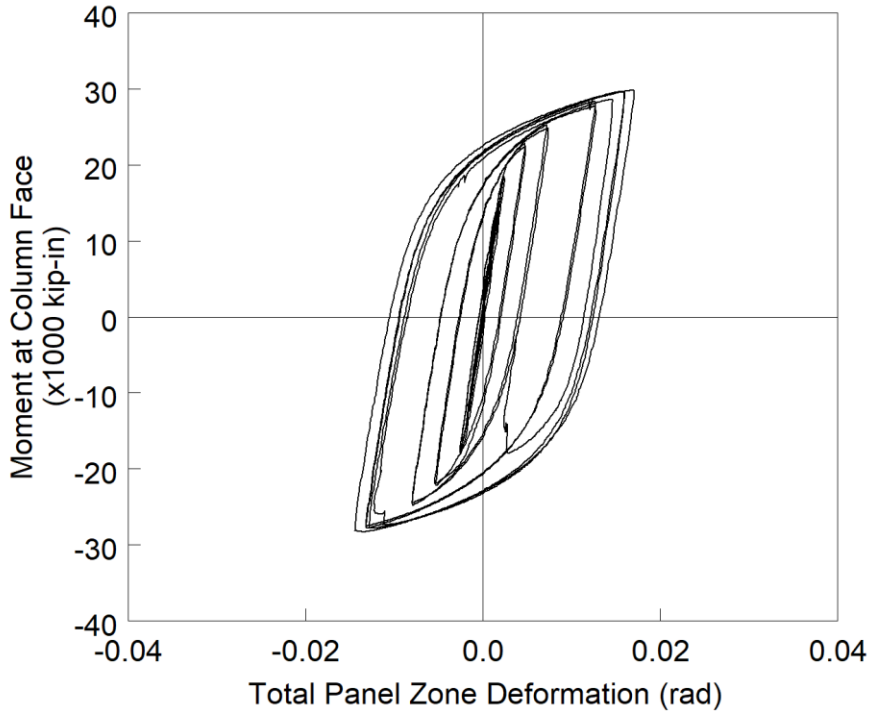

Figure 4.13 Specimen C3: Panel Zone Shear Deformation

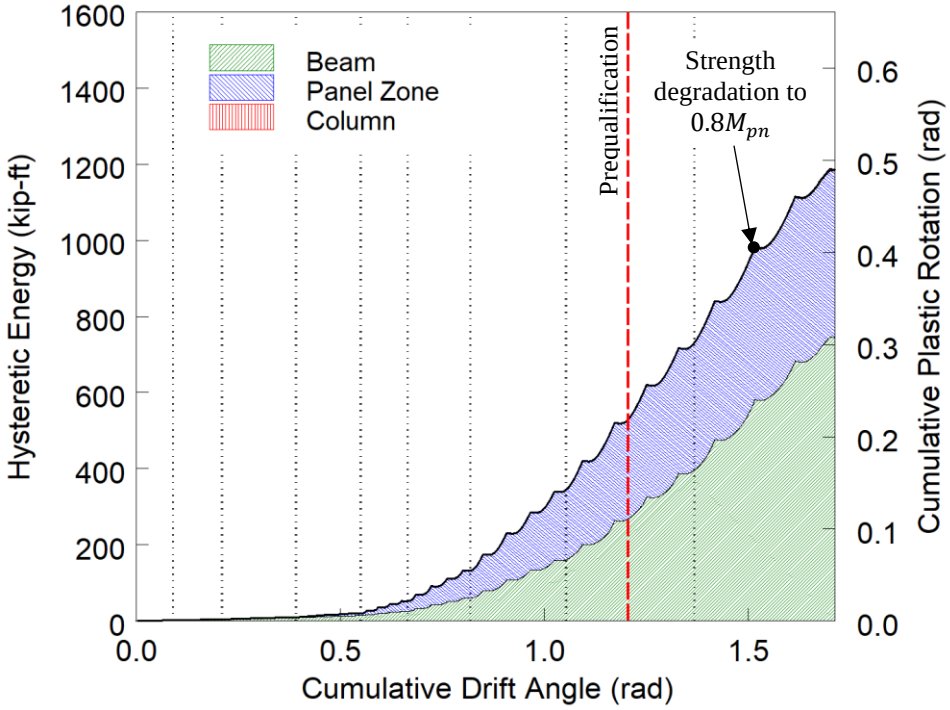

Figure 4.14 Specimen C3: Energy Dissipation

4.3. Specimen C4

4.3.1. General

Specimen C4 was similar to Specimen C3 as it was designed to challenge the Lehigh Criterion. This was the only requirement of AISC 341 (2016) that would necessitate a continuity plate in this specimen; the flange force computed from AISC 358 (2016) for this connection does not exceed any column limit state of AISC 360 §J10 (2016). In contrast to Specimen C3, Specimen C4 uses a deep column to reflect a modern practice in SMFs to control drift. Figure 4.15 shows the specimen before testing. The specimen ultimately failed by low-cycle fatigue of the beam bottom flange in the plastic hinge location during the second cycle of 0.06 rad drift.

4.3.2. Observed Performance

The observed response for Specimen C4 is described below.

- Figure 4.16 shows the east side of the specimen at the peak excursions during the later cycles of the loading protocol. The specimen met the AISC acceptance criteria by completing one complete cycle at 0.04 rad drift while the flexural strength at the column face did not degrade below 80% of the beam nominal flexural strength. Local buckling of the web and flange initiated during the second cycle of 0.03 rad drift. This progressed to result in modest flange local buckling during the 0.04 rad and 0.05 rad drift cycles.
- Beam bottom flange yielding started during the 0.01 rad cycles within the reduced beam section and near the column flange. Figure 4.17 shows the progression of the yielding which concentrates in the reduced beam section. Figure 4.17(c) shows lateral-torsional buckling initiating at the thinnest portion of the reduced beam section. This lateral-torsional buckling was first observed during the 2nd cycle of 0.03 rad drift. Lateral-torsional buckling

did not progress significantly beyond this level due to the top and bottom flange lateral restraint just beyond the reduced beam section.

- Beam web yielding was observed inboard of the k-area during the 0.02 rad drift cycles (see Figure 4.18). This was accompanied with observed yielding on the underside of the beam top flange.
- Significant beam top flange yielding was observed during the 0.04 rad drift cycles. Some minor distress was observed at the toe of an unintentional cover weld (see Figure 4.19). This distress did not progress further.
- During the first negative excursion of 0.04 rad drift significant beam flange local bucking was observed (see Figure 4.20). This was accompanied with modest web yielding propagating into the web from the k-area. This yielding occurred at the high double curvature portion of a uniform out-of-plane web buckling (see Figure 4.21).
- During the unloading portion at -0.047 rad after the 1st negative excursion to 0.06 rad the beam bottom flange partially fractured due to load cycle fatigue (see Figure 4.22). This fracture occurred at the apogee of the local buckling as the tension in the flange started to pull the curvature out. It is predicted that the fracture started at the underside of the flange at the most extreme curvature and propagated through. Upon resuming load, the remainder of the beam bottom flange immediately fractured (Figure 4.24). This fracture occurred near the smallest section of the reduced beam. Minor panel zone yielding was observed at the end of test [see Figure 4.24(a)].
- Figure 4.23 shows ductile tearing of the beam top flange similar to the condition of the beam bottom flange prior to fracture. It was observed that significant tearing occurs in the 'compression' side of the local buckling during load reversals.

- The complete bottom flange tear was accompanied with a 4-in. propagation into the web (see Figure 4.25). Most of the fracture surface consists of cleavage fracture with shear fracture surfaces at the peripheral edges of the flange.
- Column flange yielding behind the beam flanges, similar to a flange local bending phenomenon, was observed during the 0.05 rad cycles. Figure 4.26 shows the yielding of the column flanges at the end of the test.

4.3.3. Recorded Response

- Figure 4.27 shows the recorded displacement response of the beam tip measured with transducer L1. A partial beam bottom flange fracture occurred during the unloading portion of the first cycle of 0.06 rad drift. Immediately after resuming loading the remainder of the beam bottom flange fractured.
- Figure 4.28 shows the load-displacement response of the beam.
- Figure 4.29 shows the computed moment at the column face (M_f) versus the story drift angle. Two horizontal axes at 80% of the nominal plastic moment (M_{pn}) of the beam section are also added. In addition, two vertical axes at ±0.04 rad story drift show the drift required for SMF connections per AISC 341. It is observed that the beam developed 1.2 times its nominal plastic bending moment. If the moment is computed at the plastic hinge location and compared to the expected plastic moment, then the peak connection strength factor (C_{pr}) is 1.23.
- Figure 4.30 shows the plastic response of the specimen. The plastic response is computed using the procedure outlined in Section 3.7. The computed elastic stiffness of the specimen was determined to be 50.6 kips/in.

- Figure 4.31 shows the panel zone deformation determined from transducers L3 and L4. It is observed that negligible panel zone yielding occurred.
- Figure 4.32 shows the dissipated energy of Specimen C3. Dotted vertical lines on the graph demonstrate the completion of each group of cycles, and the dashed red vertical line shows the completion of the first cycle of 0.04 rad in the AISC loading. An additional vertical axis normalizes the hysteretic energy by the nominal plastic moment of the beam to determine the cumulative plastic rotation. It is observed that the completion of the first drift cycle of 0.04 rad (the requirement for SMF connections per AISC 341) occurs after 517 kip-ft of energy has been dissipated. The connection does not degrade below $0.8M_{pn}$ until after completing the first positive excursion to 0.06 rad drift dissipating 1,239 kip-ft of energy. Therefore, only 42% of the energy dissipation capacity was utilized after the completion of the 0.04 rad drift requirement. It is observed that all of the energy dissipation capacity occurred in the beam.

(a) West Side

(b) East Side

Figure 4.15 Specimen C4: Specimen before Testing

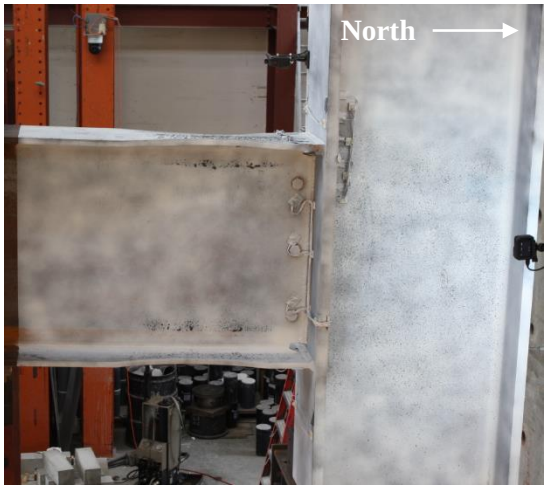

(a) +0.03 rad (2nd Cycle)

(b) -0.03 rad (2nd Cycle)

(c) +0.04 rad (2nd Cycle)

(d) -0.04 rad (2nd Cycle)

(e) +0.05 rad (1st Cycle)

(f) -0.05 rad (1st Cycle)

Figure 4.16 Specimen C4: East Side of Connection

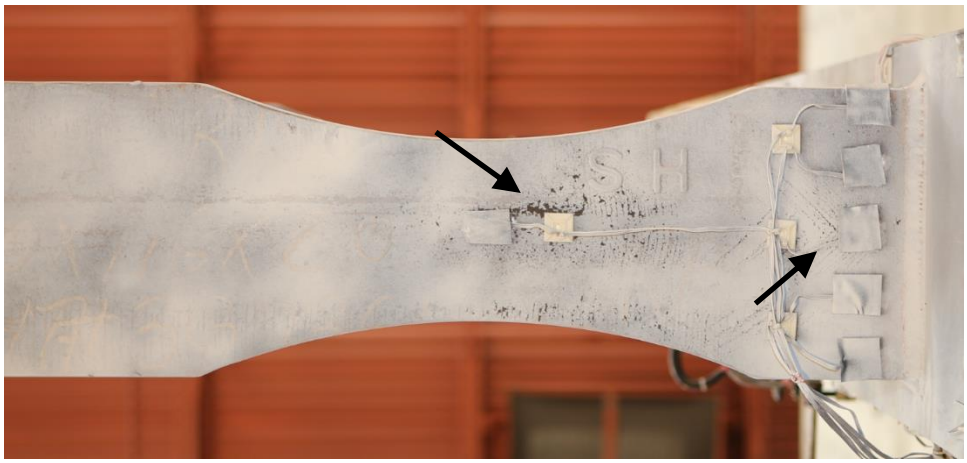

(a) -0.015 rad (2nd Cycle)

(b) -0.02 rad (2nd Cycle)

(c) -0.04 rad (2nd Cycle)

Figure 4.17 Specimen C4: Beam Bottom Flange Yielding and Buckling

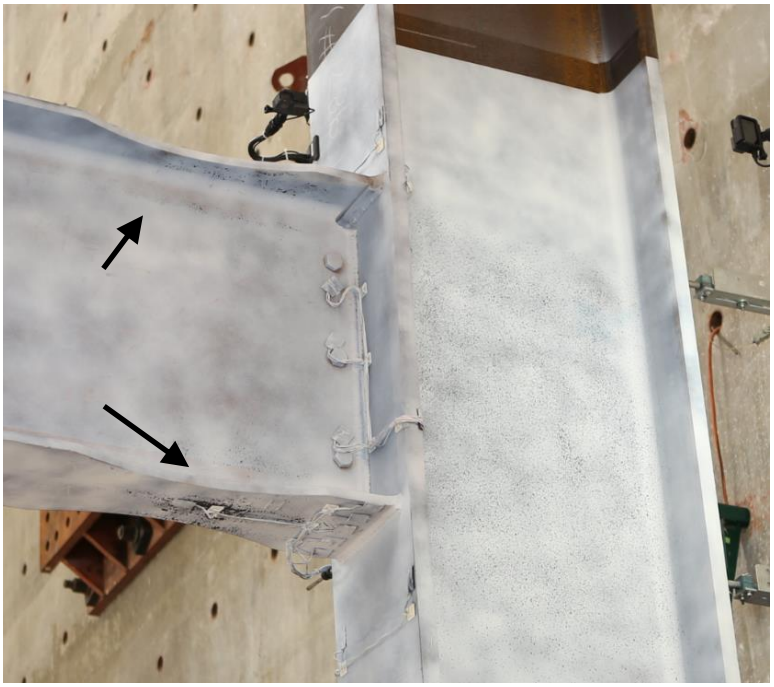

Figure 4.18 Specimen C4: Beam Web Yielding at +0.02 rad (2nd Cycle)

(a) Overview

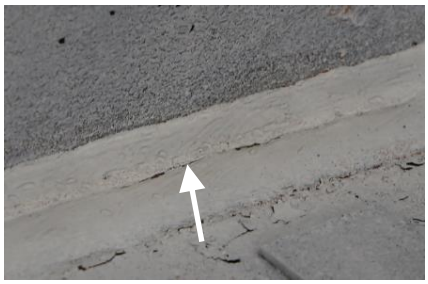

(b) CJP Weld

Figure 4.19 Specimen C4: Beam Top Flange at -0.04 rad (1st Cycle)

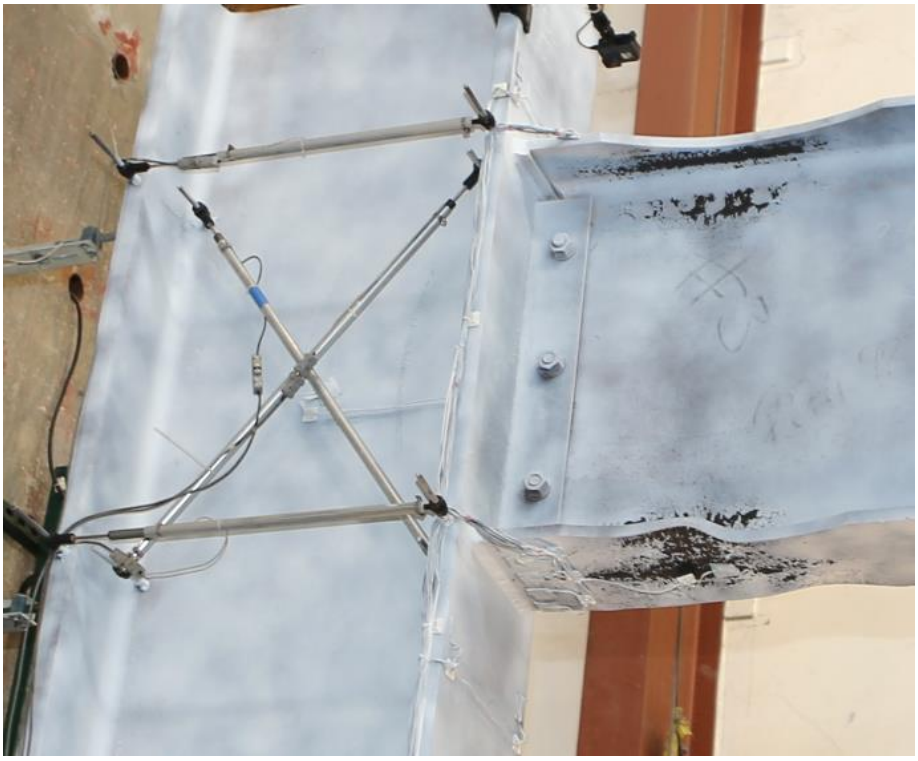

Figure 4.20 Specimen C4: Beam Flange and Web Yielding at -0.04 rad (1st Cycle)

Figure 4.21 Specimen C4: Beam Web Buckling at -0.04 rad (1st Cycle)

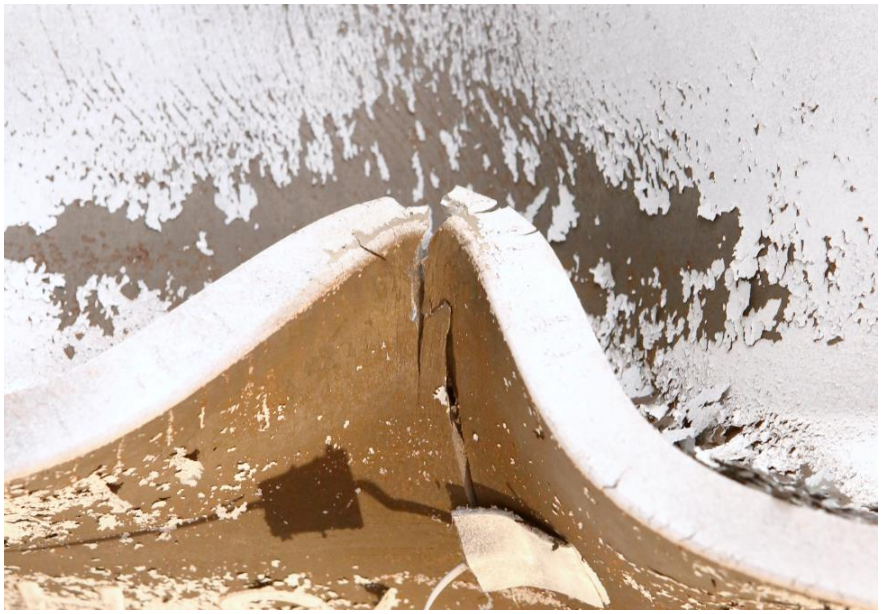

Figure 4.22 Specimen C4: Beam Bottom Flange Fracture after one cycle at 0.06 rad

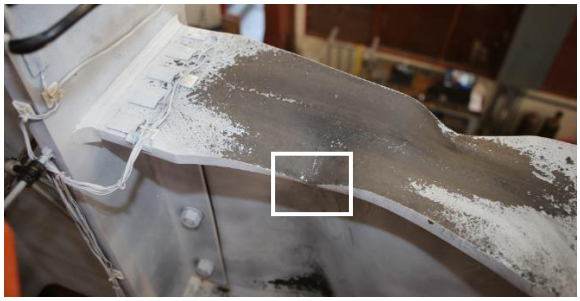

(a) Overview

(b) Ductile Tearing

Figure 4.23 Specimen C4: Beam Top Flange at -0.06 rad (2nd Cycle)

(a) West Side

(b) East Side

Figure 4.24 Specimen C4: Connection at End of Test

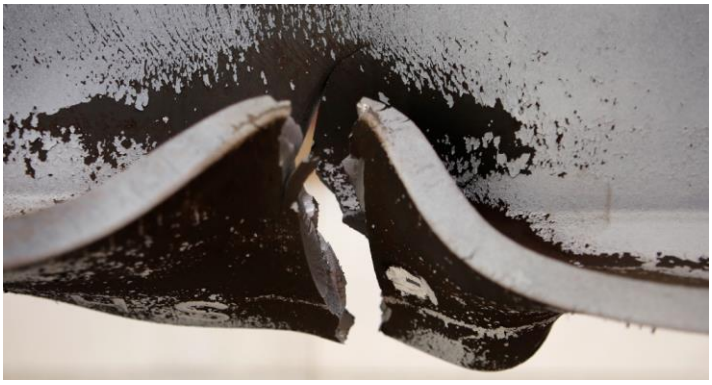

(a) Overview

(b) Fracture Surface

Figure 4.25 Specimen C4: Beam Bottom Flange Fracture (End of Test)

(a) Overview

(b) Flange Local Bending

Figure 4.26 Specimen C4: Column Flange (End of Test)

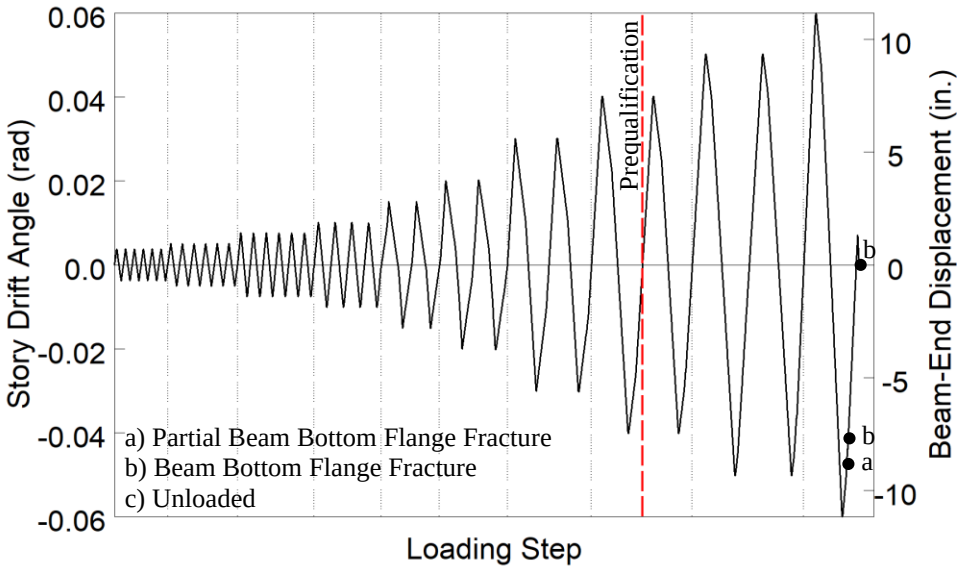

Figure 4.27 Specimen C4: Recorded Loading Sequence

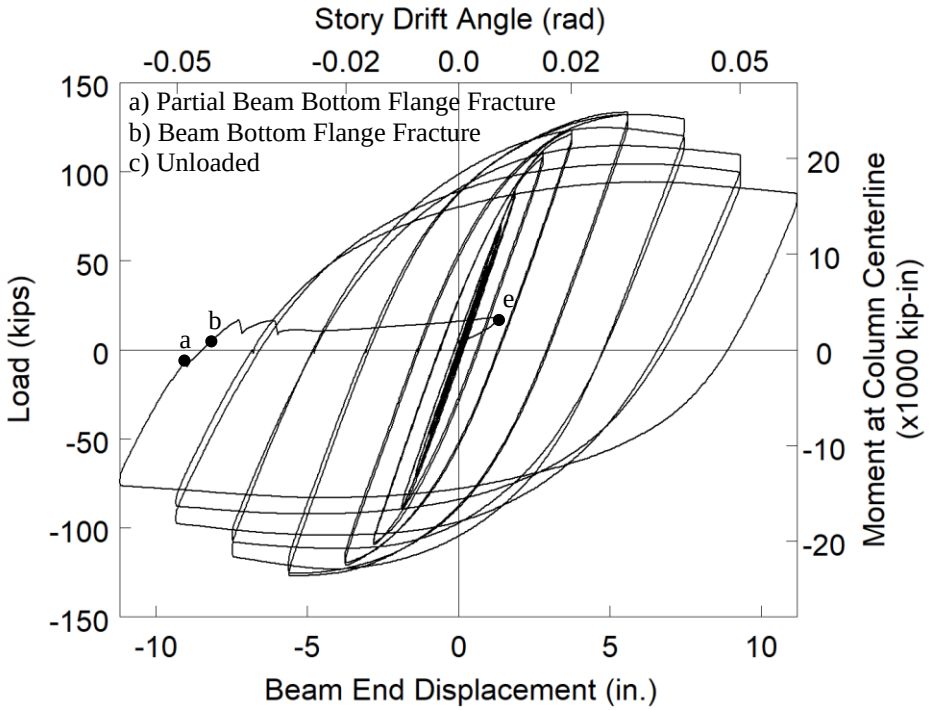

Figure 4.28 Specimen C4: Applied Load versus Beam End Displacement Response

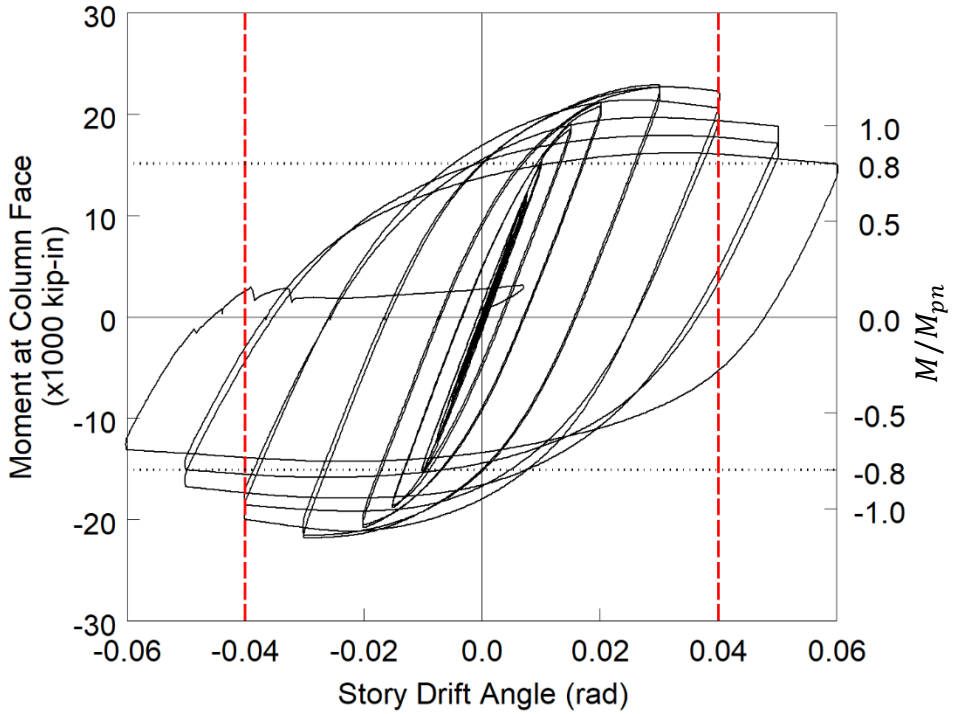

Figure 4.29 Specimen C4: Moment at Column Face versus Story Drift Response

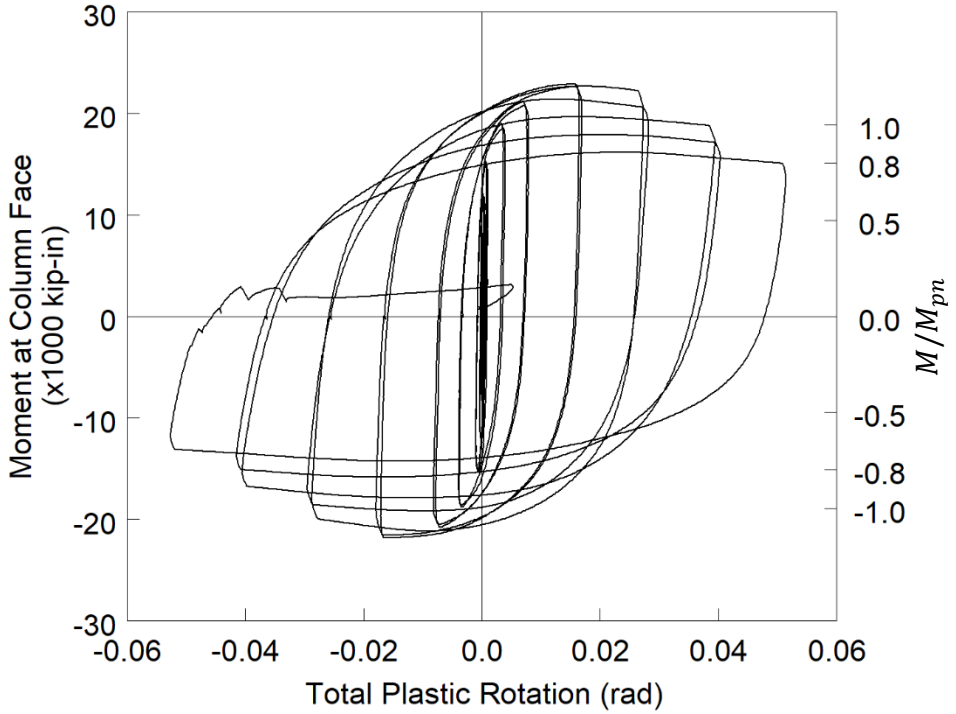

Figure 4.30 Specimen C4: Moment at Column Face versus Plastic Rotation Response

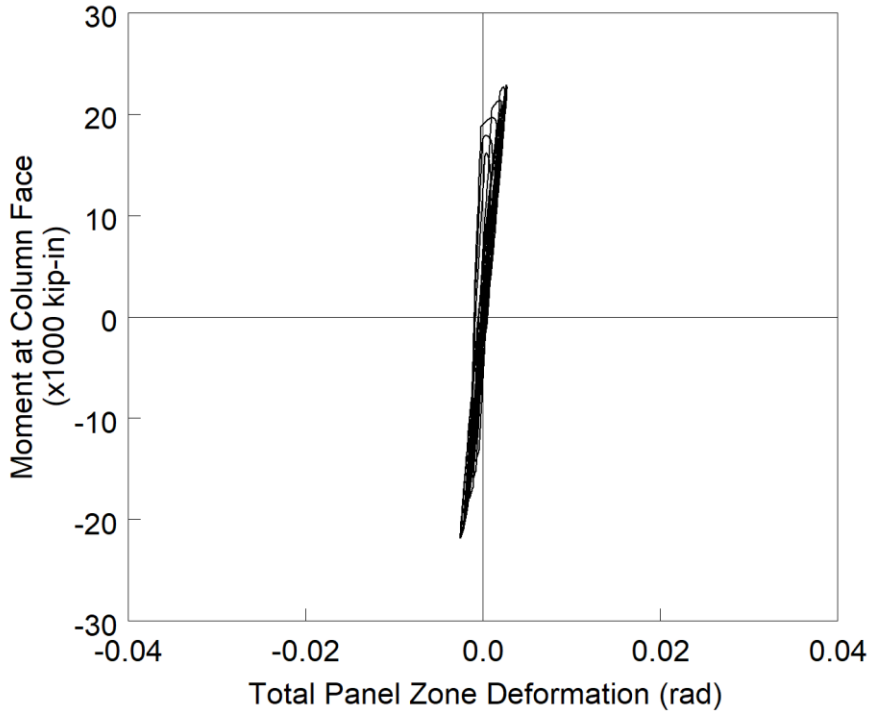

Figure 4.31 Specimen C4: Panel Zone Shear Deformation

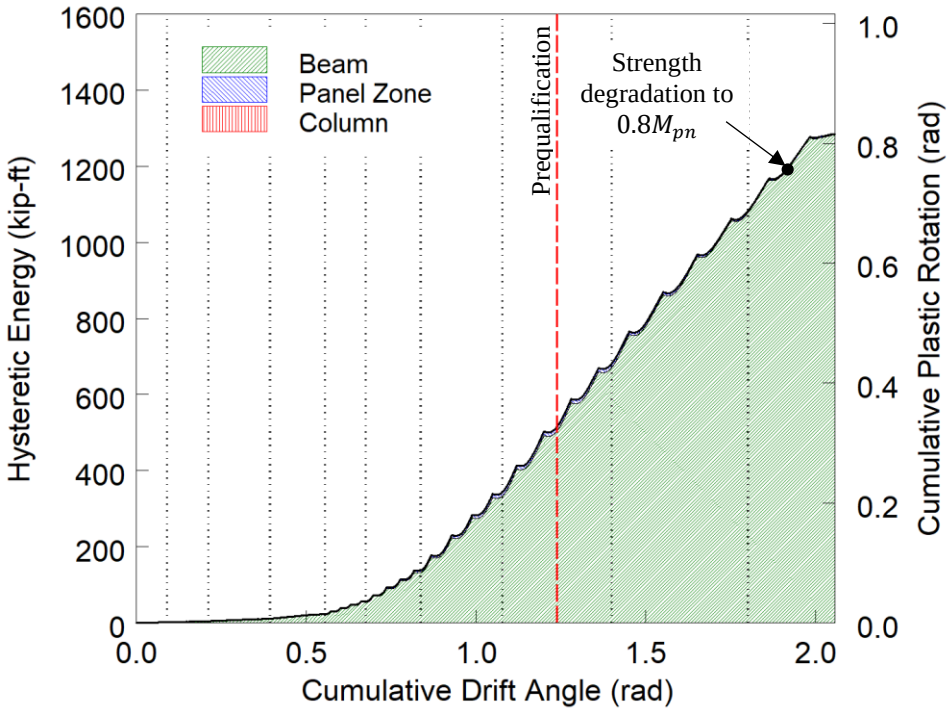

Figure 4.32 Specimen C4: Energy Dissipation

4.4. Specimen C5

4.4.1. General

Specimen C5 was designed to investigate the validity of using the plastic distribution to estimate the required strength of the continuity plate. The continuity plates were designed to satisfy the governing AISC 360 §J10 concentrated force column limit state; WLY, was the governing limit state exceed by the flange force. The panel zone strength of Specimen C5 was intentionally designed weak with a DCR of 1.18. The continuity plate was welded to the column flange and web using a fillet weld of size $w = 0.8t_{cp}$, which was the closest standard fillet weld size to $w = 0.75t_{cp}$. The specimen failed by fracture of the beam top flange CJP weld after completing two cycles of 0.05 rad drift. Figure 4.33 shows the connection before testing.

4.4.2. Observed Performance

The observed response for Specimen C5 is described below.

- Figure 4.34 shows the east side of the specimens at the peak excursions during the later cycles of the loading protocol. The specimen met the AISC acceptance criteria. It was observed that beam web buckling initiated during the first cycle of 0.04 rad drift. Flange local bucking initiated at the beam bottom flange within the RBS cut during the second cycle of 0.04 rad drift. By 0.05 rad drift flange local bucking was observed in both flanges.
- Figure 4.35 shows ductile tearing of the beam top flange CJP weld that was first observed during the 2nd negative excursion of 0.03 rad drift. Minor growth of this fracture occurred during the 0.04 rad cycles during testing.
- Figure 4.36 shows gradual progression of tearing of the beam top flange CJP weld. Figure 4.36(e) shows the complete beam top flange fracture. This shear type fracture originated at a toe of the prominent weld pass against the column and propagated through the flange at

a 35-degree angle through the base metal. At the flange tips the fracture took on a cup and cone with interlocking shear lips through the base metal of the beam.

- Significant column kinking was observed during the testing of the specimen (see Figure 4.37).
- Minor web buckling was evident at the end of testing [see Figure 4.38(a)]. Continued negative excursion after fracturing the beam top flange produced a fracture of the beam web [see Figure 4.38(b)]. This fracture originated in the weld access hole and propagated down though the erection bolt holes. Local necking was observed near this fracture.
- Figure 4.39 shows the slight beam lateral-torsional buckling at the end of testing.
- At the end of testing no damage was observed in any of the fillet welds fastening the continuity plates to the column. Figure 4.40 shows the continuity plates after testing. The east bottom flange and west top flange continuity plate experienced local plate buckling. The east bottom flange continuity plate started developed local buckling during the first negative excursion of 0.04 rad drift. At the time of failure, the specimen was experiencing a negative excursion which pulled the west top flange continuity plate straight with minor residual deformation. The east bottom flange shows the full extent of the buckling as this plate was in compression at the point of failure. Despite the significant plate buckling and column flange kinking, the continuity plate to column flange welds have remained intact [see Figure 4.40(b)].

4.4.3. Recorded Response

- Figure 4.41 shows the recorded displacement response of the beam tip measured with transducer L1. A hairline crack at the centerline of the beam top flange CJP weld was observed at the second negative excursion of 0.03 rad drift. A tear through the center of the

beam top flange CJP weld was observed at the peak excursion of 0.05 rad drift. At -0.035 rad drift during the second negative excursion of 0.05 rad drift, the remaining portion of the beam top flange CJP weld fractured. Continued excursion saw tearing of the web which originated at the radius of the weld access hole and propagated through the first bolt hole in the shear tab. Unanticipated bolt slip had occurred at the loading corbel during testing of the latter cycles. This slip resulted in a slight undershoot of the target displacements. For example, the computed drift during the targeted 0.04 rad story drift cycles was determined to be 0.0391 rad. It is not believed that this minor discrepancy affects the conclusions of this specimen.

- Figure 4.42 shows the load-displacement response of the beam.
- Figure 4.43 shows the computed moment at the column face (M_f) versus the story drift angle. Two horizontal axes at 80% of the nominal plastic moment (M_{pn}) of the beam section are also added. In addition, two vertical axes at ±0.04 rad story drift show the drift required for SMF connections per AISC 341. It is observed that the beam developed its nominal plastic bending moment. If the moment is computed at the plastic hinge location and compared to the expected plastic moment, then the peak connection strength factor (C_{pr}) is 1.16.
- Figure 4.44 shows the plastic response of the specimen. The plastic response is computed using the procedure outlined in Section 3.7. The computed elastic stiffness of the specimen was determined to be 56.3 kips/in.
- Figure 4.45 shows extensive inelastic behavior of the panel zone. It is possible that the deformation of the column flanges has erroneously influenced the computation of the panel zone shear given the significant deformation observed of the continuity plates.

- Figure 4.46 shows the dissipated energy of Specimen C5. Dotted vertical lines on the graph demonstrate the completion of each group of cycles, and the dashed red vertical line shows the completion of the first cycle of 0.04 rad in the AISC loading. It is observed that the completion of the first drift cycle of 0.04 rad (the requirement for SMF connections per AISC 341) occurs after 538 kip-ft of energy has been dissipated. The connection did not degrade below $0.8M_{pn}$ until 1,165 kip-ft of energy had been dissipated. Therefore only 46% of the energy dissipation capacity was utilized after the completion of SMF requirement. It is observed that most (65%) of the energy dissipation capacity occurred in the panel zone.

(a) West Side

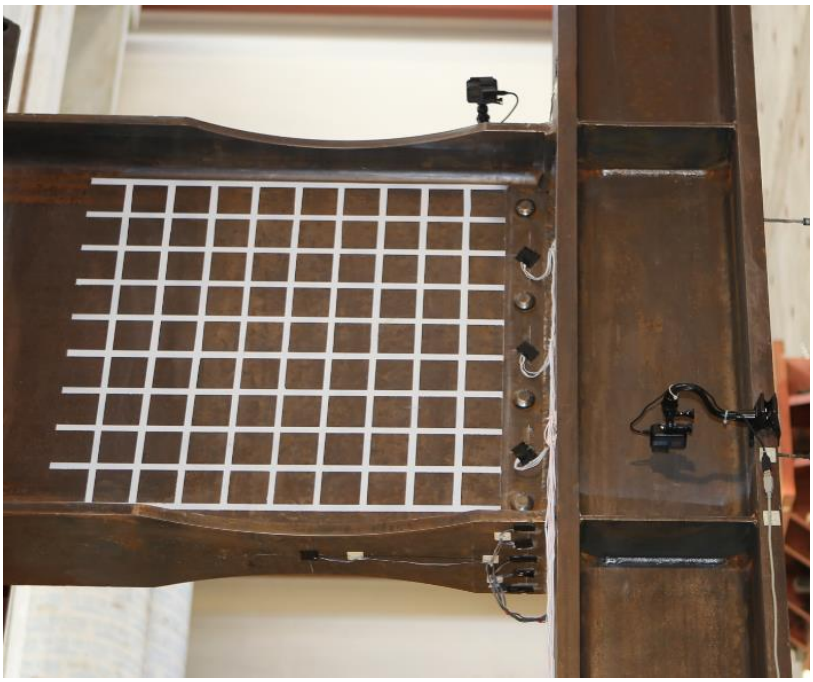

(b) East Side

Figure 4.33 Specimen C5: Specimen before Testing

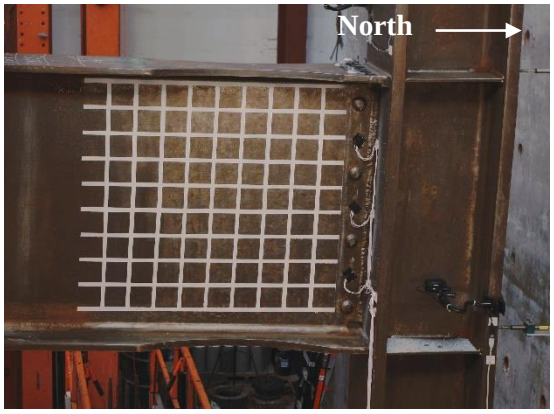

(a) +0.03 rad (2nd Cycle)

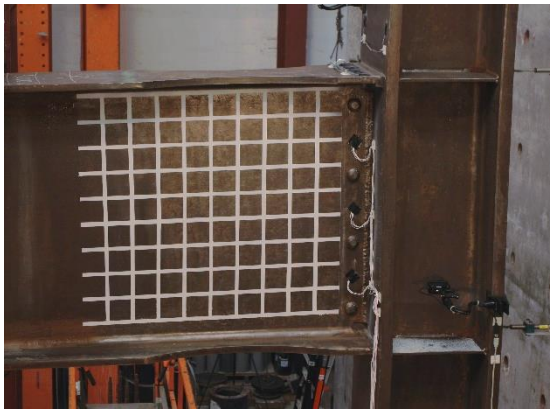

(b) -0.03 rad (2nd Cycle)

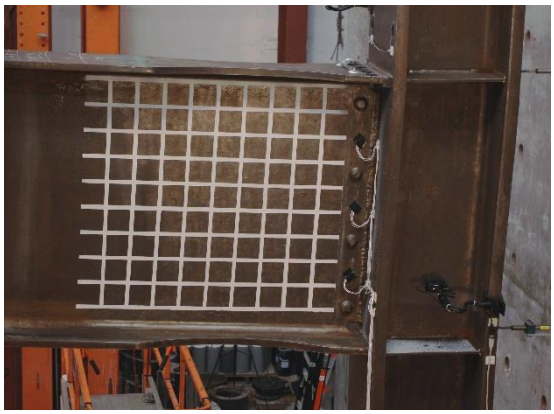

(c) +0.04 rad (2nd Cycle)

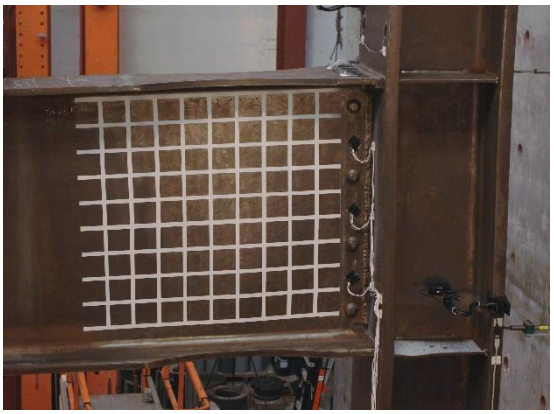

(d) -0.04 rad (2nd Cycle)

(e) +0.05 rad (1st Cycle)

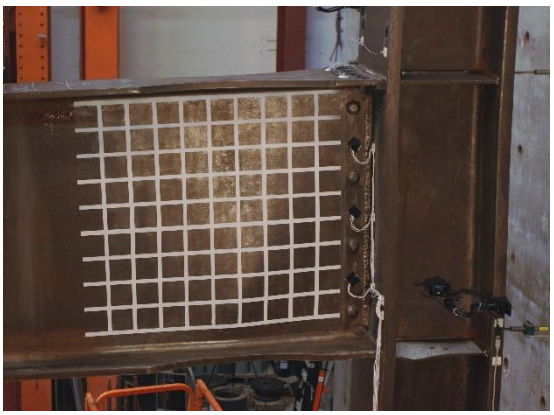

(f) -0.05 rad (1st Cycle)

Figure 4.34 Specimen C5: East Side of Connection

(a) -0.03 rad (1st Cycle)

(b) -0.03 rad (2nd Cycle)

(c) -0.04 rad (1st Cycle)

(d) -0.04 rad (2nd Cycle)

(e) -0.05 rad (1st Cycle)

(f) -0.05 rad (2nd Cycle)

Figure 4.35 Specimen C5: Beam Top Flange

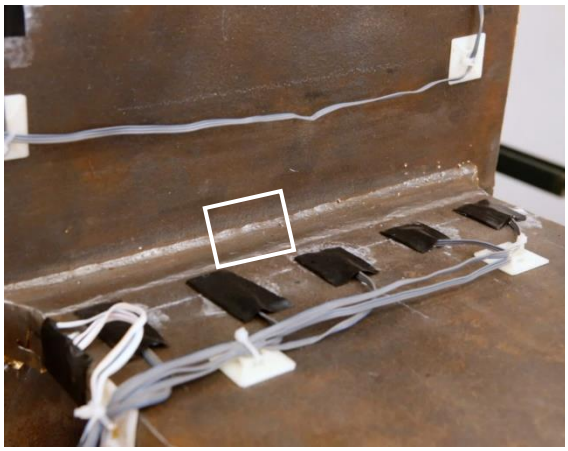

(a) Overview

(b) -0.03 rad (2nd Cycle)

(c) -0.04 rad (2nd Cycle)

(d) -0.05 rad (1st Cycle)

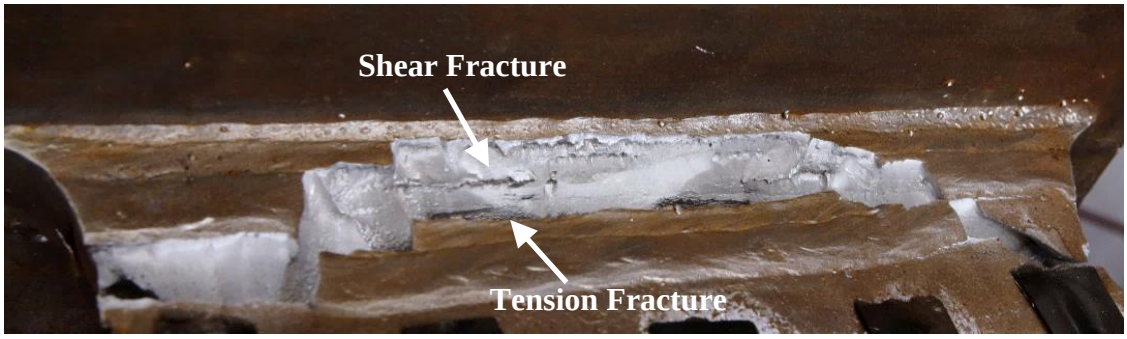

(e) Fracture (End of Test)

Figure 4.36 Specimen C5: Beam Top Flange CJP Weld Fracture Progression

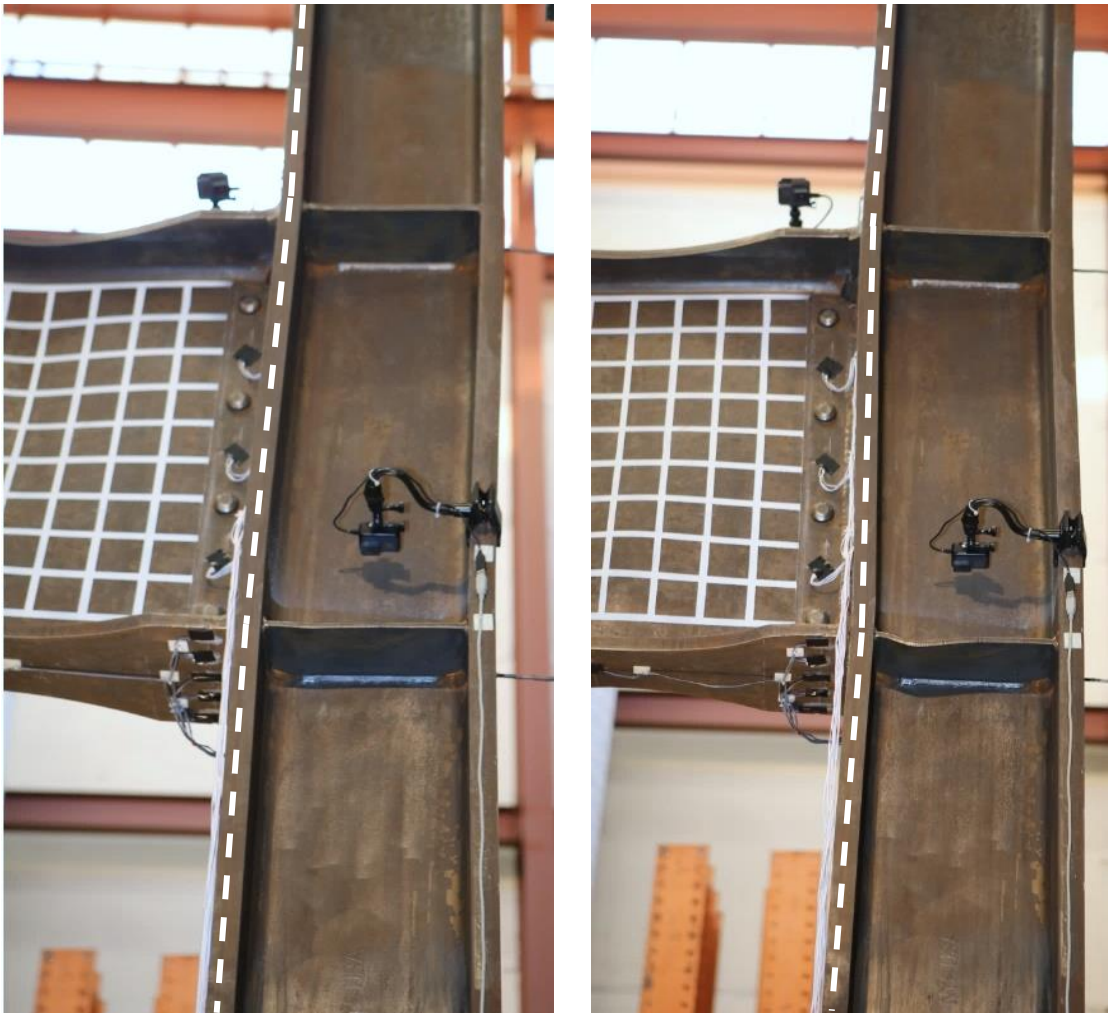

(a) +0.05 rad (2nd Cycle) (b) -0.05 rad (2nd Cycle)

Figure 4.37 Specimen C5: Column Kinking due to Panel Zone Deformation

(a) Beam Web Buckling

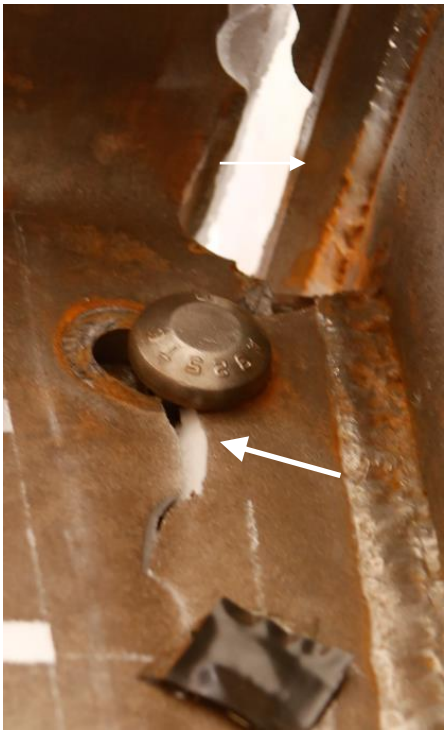

(b) Web Fracture

Figure 4.38 Specimen C5: Beam Web Buckling (End of Test)

Figure 4.39 Specimen C5: Beam Lateral-Torsional Buckling (End of Test)

(a) East Bottom Flange Continuity Plate

(b) Enlarged View of Weld

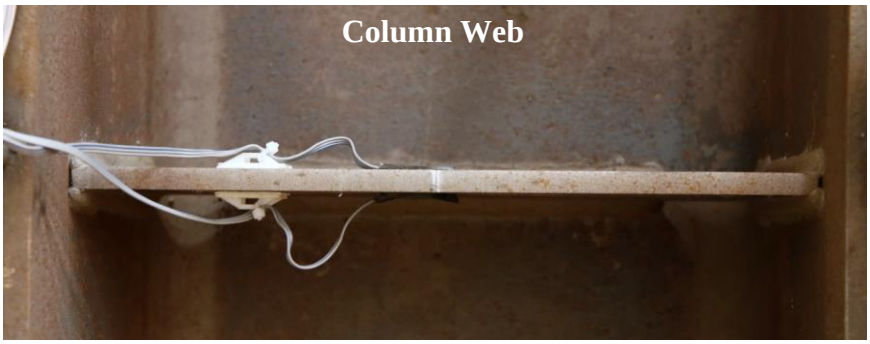

(c) West Bottom Flange Continuity Plate

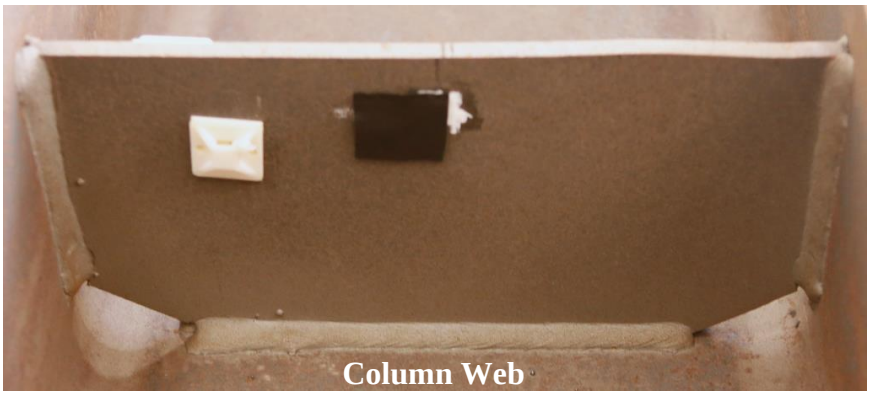

(d) West Top Flange Continuity Plate

Figure 4.40 Specimen C5: Continuity Plate (End of Test)

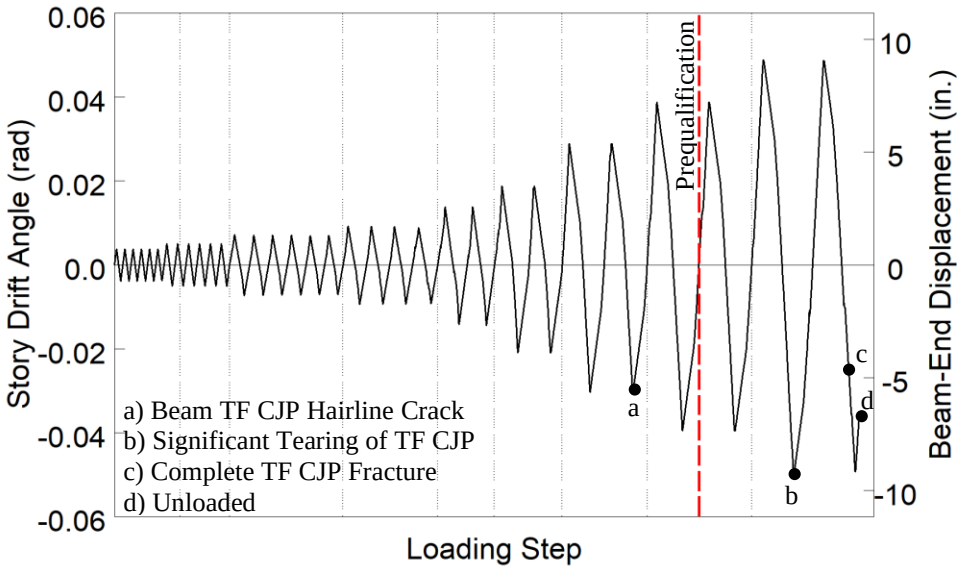

Figure 4.41 Specimen C5: Recorded Loading Sequence

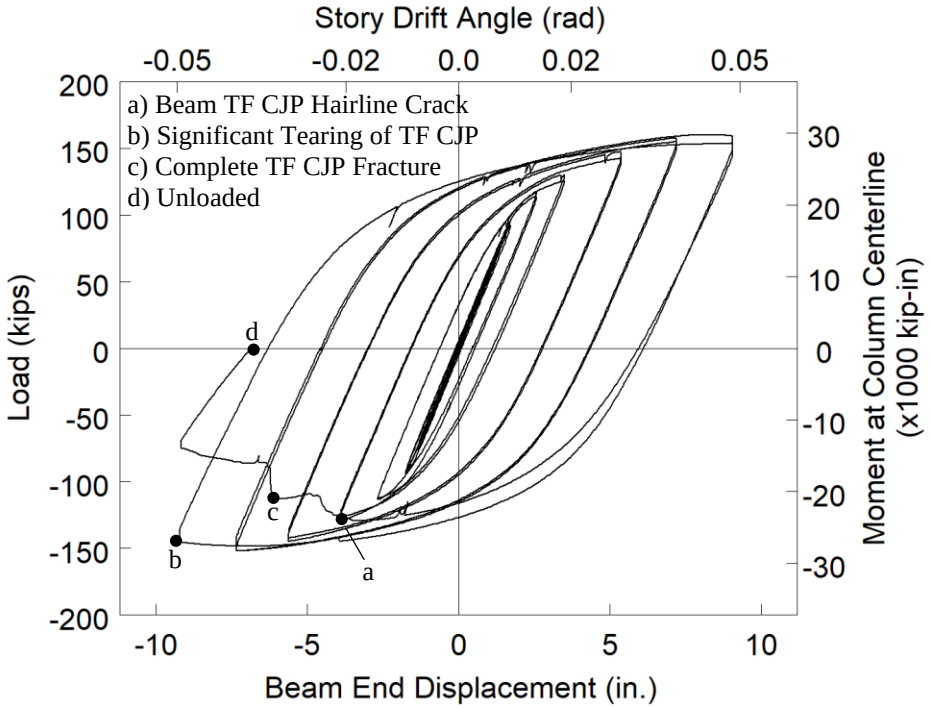

Figure 4.42 Specimen C5: Applied Load versus Beam End Displacement Response

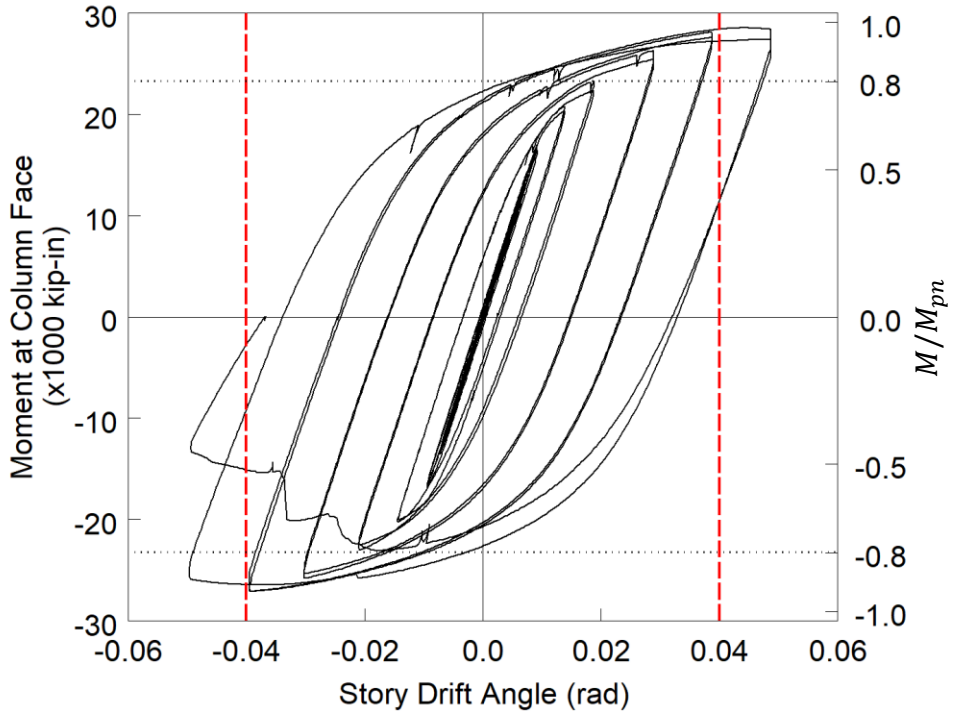

Figure 4.43 Specimen C5: Moment at Column Face versus Story Drift Response

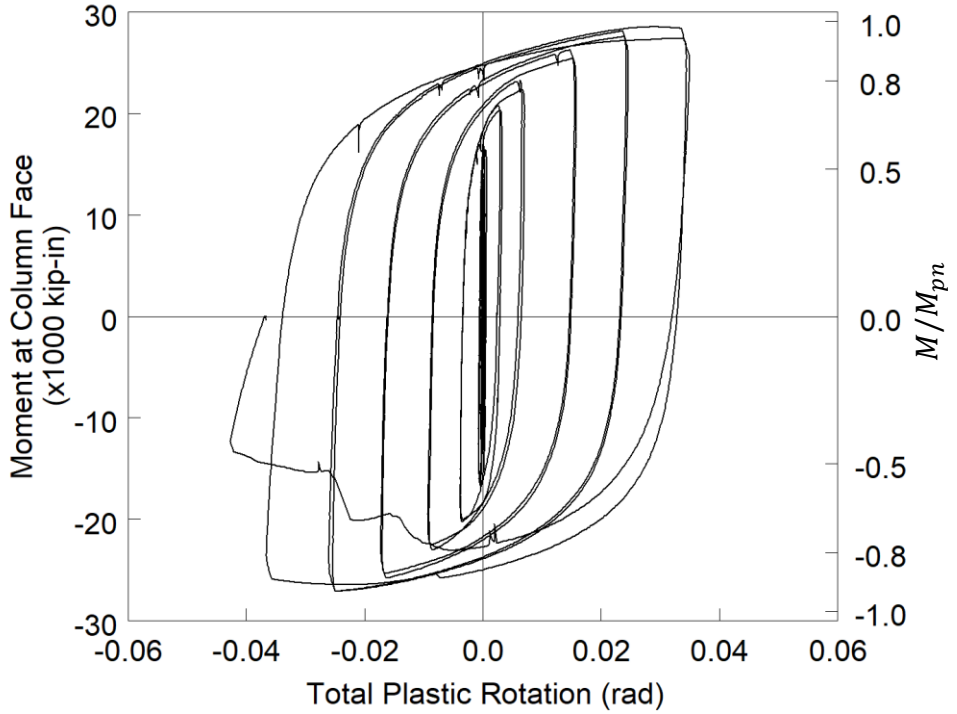

Figure 4.44 Specimen C5: Moment at Column Face versus Plastic Rotation Response

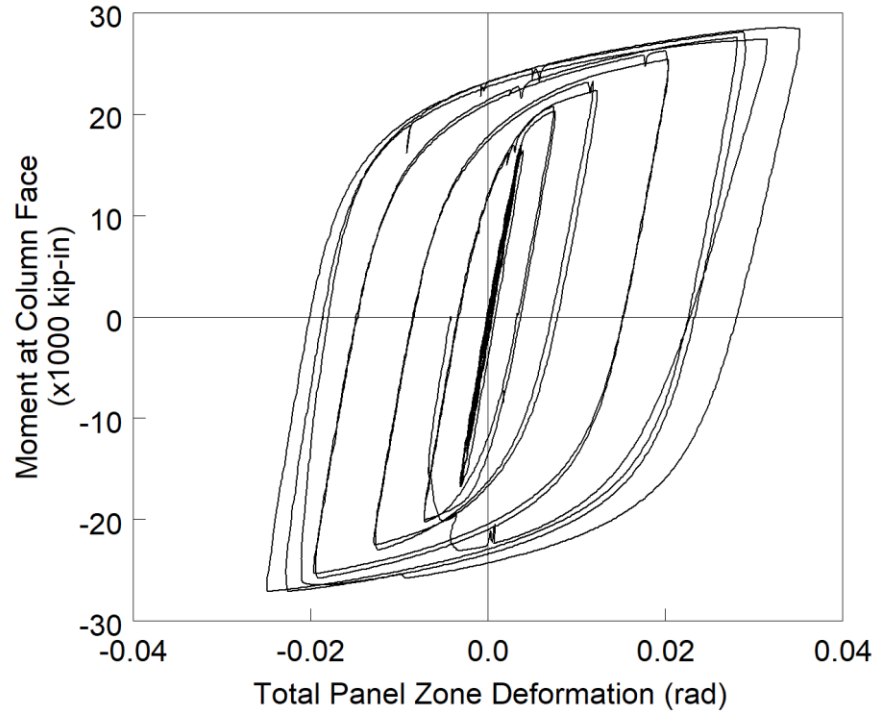

Figure 4.45 Specimen C5: Panel Zone Shear Deformation

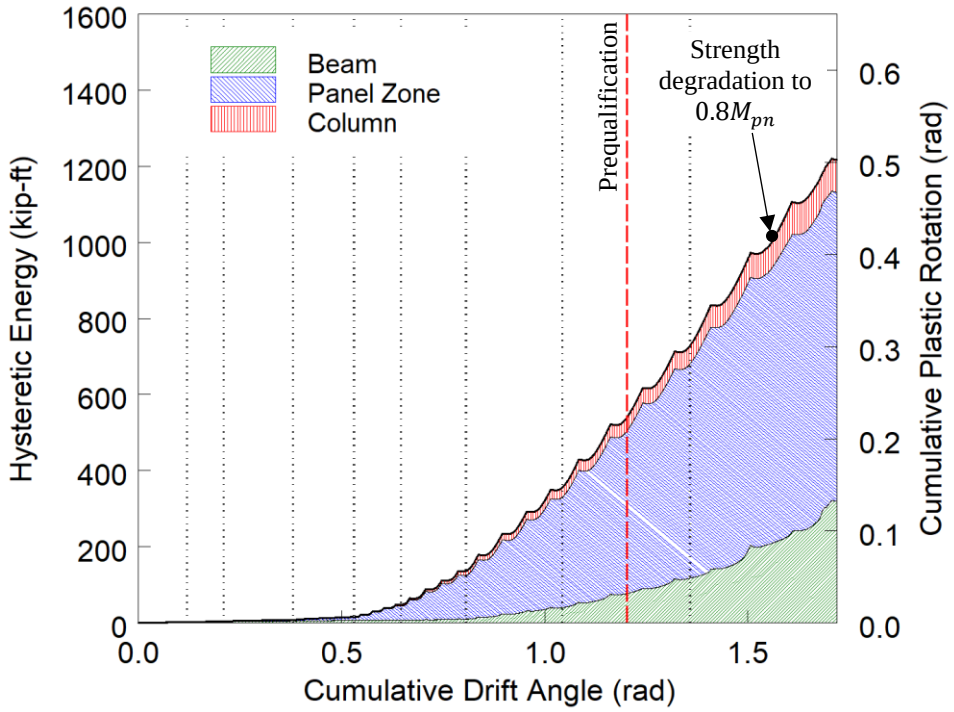

Figure 4.46 Specimen C5: Energy Dissipation

4.5. Specimen C6

4.5.1. General

Specimen C6 was designed to investigate the validity of using the plastic distribution to estimate the required strength of the continuity plate. The continuity plates were designed to satisfy the governing AISC 360 §J10 concentrated force column limit state; both the FLB and WLY limit dictate the need of a continuity plate in this specimen. The continuity plate was welded to the column flange and web using a fillet weld of size $w = 1.0t_{cp}$, which was oversized on purpose to ensure survivability of the fillet weld for this specimen and Specimen C6-G, which was essentially an identical twin of this specimen. The specimen eventually failed by fracture of the beam top flange CJP weld during the first negative excursion to 0.05 rad drift during the first excursion to 0.05 rad. Figure 4.47 shows the connection before testing.

4.5.2. Observed Performance

The observed response for Specimen C6 is described below.

- Figure 4.48 shows the east side of the specimen at the peak excursions during the later cycles of the loading protocol. The specimen met the AISC acceptance criteria. It was observed that beam web buckling and beam flange local buckling both initiated during the first cycle of 0.04 rad drift. Flange local bucking initiated at the beam bottom flange within the RBS cut during the second cycle of 0.04 rad drift. At 0.05 rad drift modest beam flange and beam web local buckling was observed.
- Figure 4.49 shows the progressive tearing of the beam top flange CJP weld. At the first negative excursion to 0.03 rad drift a minor crack was observed at the toe of prominent weld pass on the outward surface of the CJP weld. This crack progressed until -0.037 rad of the first negative excursion of 0.05 rad drift when a sudden fracture of the flange

propagated severing the east side of the beam flange connection. Continued excursion to -0.05 rad tore the remainder of the beam flange CJP weld.

- The gradual progression of the weld tearing is shown in Figure 4.50. The final fracture surface was observed to primarily be a shear fracture [see Figure 4.50(e)]. This picture also shows minor column flange yielding which only occurred at the center of the beam top flange location.
- Beam bottom flange yielding started during the 0.01 rad cycles within the reduced beam section and near the column flange (see Figure 4.51). This yielding progresses through testing. Minor lateral-torsional buckling was observed during testing.
- Figure 4.52 shows panel zone yielding on the west side of the specimen. This yielding commenced during the 0.015 rad drift cycles and progressed through testing. Figure 4.53 shows the beam flange and beam web local buckling.
- Figure 4.54 shows the connection after testing. Significant flange local buckling occurred during the first cycle of 0.05 rad drift.
- Figure 4.55 shows the continuity plates and their fillet welds after testing. No damage to the fillet welds was observed. Additionally, yielding of the continuity plates was not observed.

4.5.3. Recorded Response

- Figure 4.56 shows the recorded displacement response of the beam tip measured with transducer L1. A hairline crack at the centerline of the beam top flange CJP weld was observed at the first negative excursion of 0.03 rad drift. This gradually tore throughout testing until, during the first negative excursion of 0.05 rad drift, the beam top flange

partially ruptured at -0.037 rad drift. Continued excursion to -0.05 rad tore the remainder of the flange.

- Figure 4.57 shows the load-displacement response of the beam.
- Figure 4.58 shows the computed moment at the column face (M_f) versus the story drift angle. Two horizontal axes at 80% of the nominal plastic moment (M_{pn}) of the beam section are also added. In addition, two vertical axes at ±0.04 rad story drift show the drift required for SMF connections per AISC 341. It is observed that the beam developed 1.1 times its nominal plastic bending moment. If the moment is computed at the plastic hinge location and compared to the expected plastic moment, then the peak connection strength factor (C_{pr}) is 1.21.
- Figure 4.59 shows the plastic response of the specimen. The plastic response is computed using the procedure outlined in Section 3.7. The computed elastic stiffness of the specimen was determined to be 46.9 kips/in.
- Figure 4.60 shows modest inelastic behavior of the panel zone.
- Figure 4.61 shows the dissipated energy of Specimen C6. Dotted vertical lines on the graph demonstrate the completion of each group of cycles, and the dashed red vertical line shows the completion of the first cycle of 0.04 rad in the AISC loading. It is observed that the completion of the first drift cycle of 0.04 rad (the requirement for SMF connections per AISC 341) occurs after 489 kip-ft of energy has been dissipated. The connection did not degrade below $0.8M_{pn}$ until 834 kip-ft of energy had been dissipated. Therefore only 58% of the energy dissipation capacity was utilized after the completion of SMF requirement. It is observed that most (78%) of the energy dissipation capacity occurred in the beam.

(a) West Side

(b) East Side

Figure 4.47 Specimen C6: Specimen before Testing

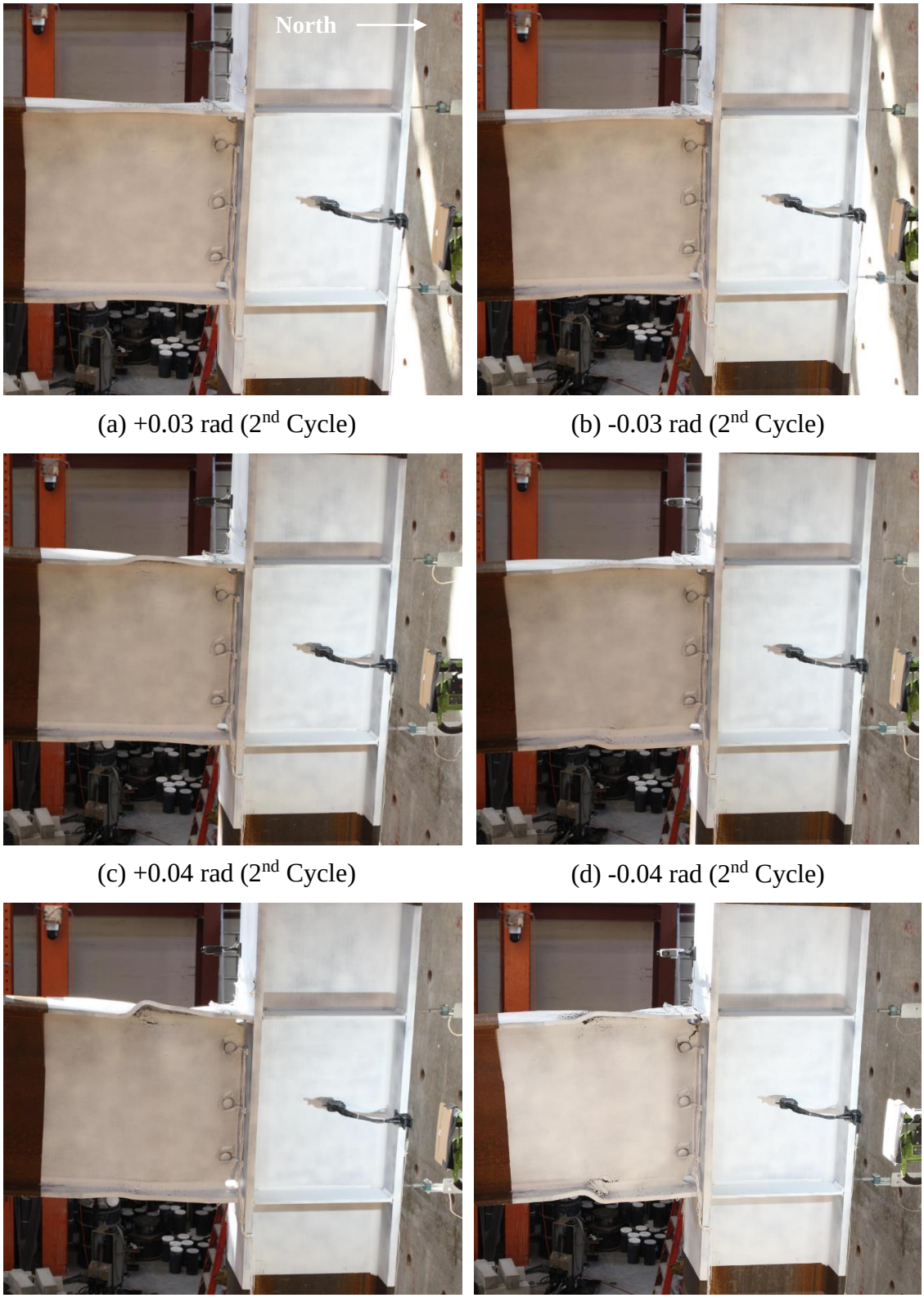

(a) +0.03 rad (2nd Cycle)

(b) -0.03 rad (2nd Cycle)

(c) +0.04 rad (2nd Cycle)

(d) -0.04 rad (2nd Cycle)

(e) +0.05 rad (1st Cycle)

(f) -0.05 rad (1st Cycle)

Figure 4.48 Specimen C6: East Side of Connection

(a) -0.03 rad (1st Cycle)

(b) -0.03 rad (2nd Cycle)

(c) -0.04 rad (1st Cycle)

(d) -0.04 rad (2nd Cycle)

(e) -0.037 rad (1st Cycle of 0.05 rad)

(f) -0.05 rad (1st Cycle)

Figure 4.49 Specimen C6: Beam Top Flange

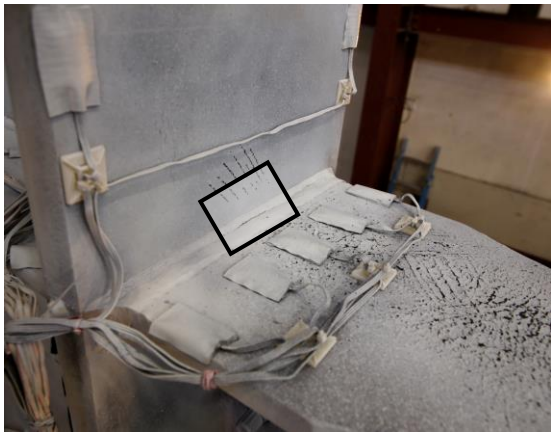

(a) Overview

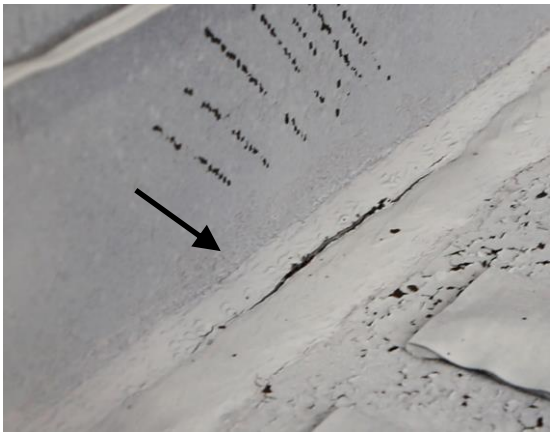

(b) -0.03 rad (2nd Cycle)

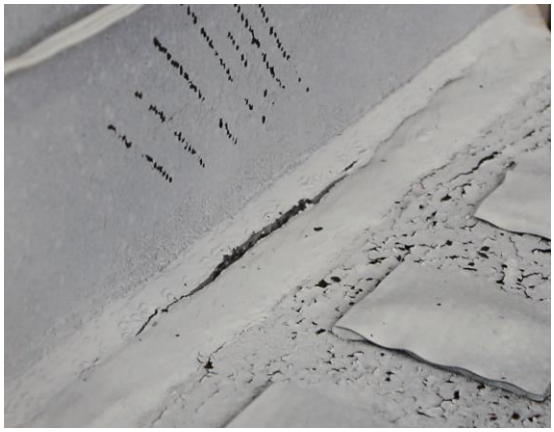

(c) -0.04 rad (1st Cycle)

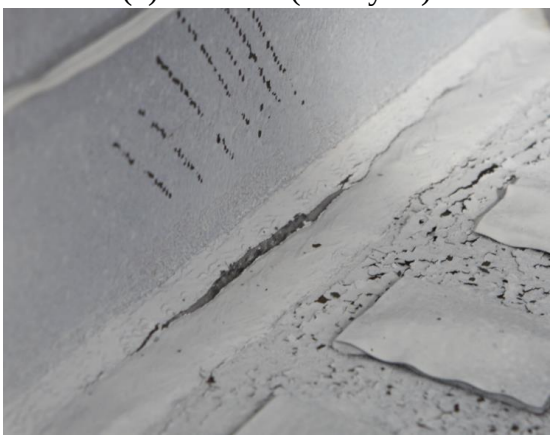

(d) -0.04 rad (2nd Cycle)

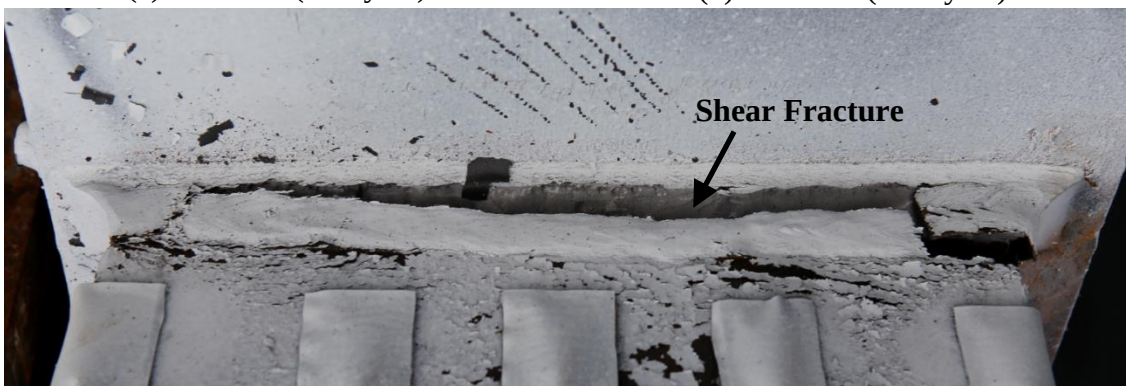

(e) Fracture (End of Test)

Figure 4.50 Specimen C6: Beam Top Flange CJP Weld Fracture Progression

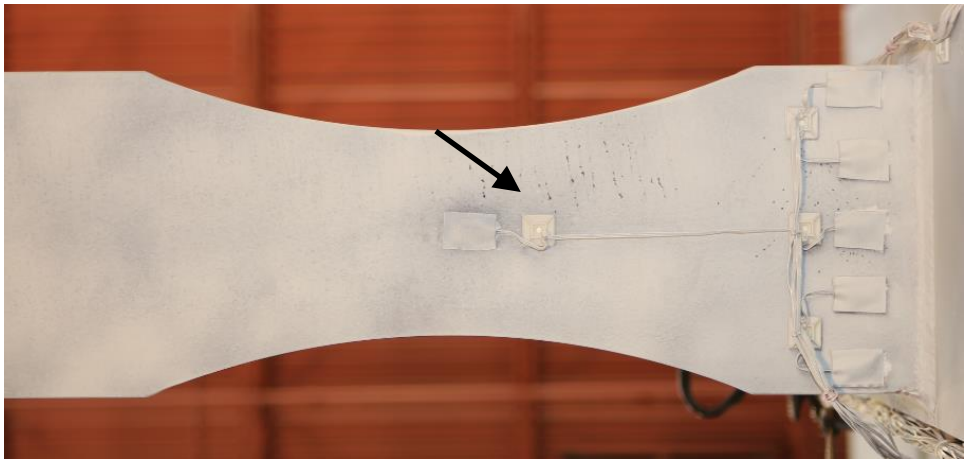

(a) -0.01 rad (4th Cycle)

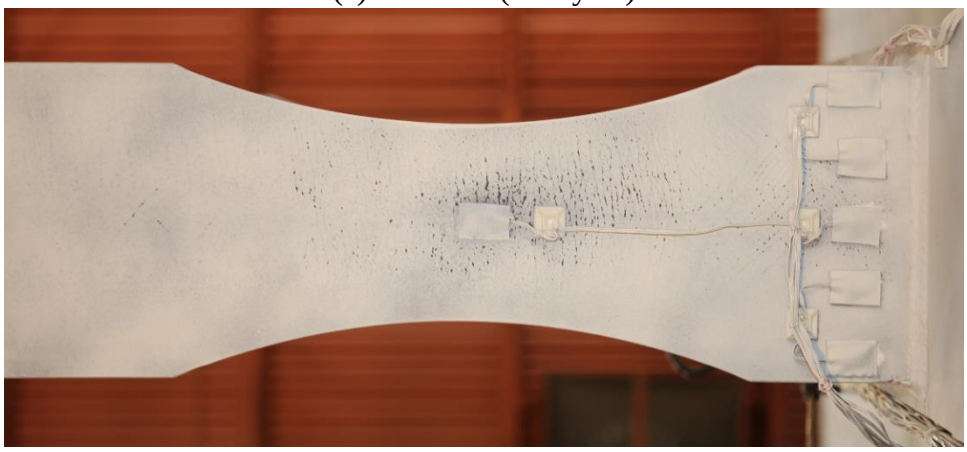

(b) -0.02 rad (2nd Cycle)

(c) +0.04 rad (2nd Cycle)

Figure 4.51 Specimen C6: Beam Bottom Flange Yielding

(a) +0.02 rad (2nd Cycle)

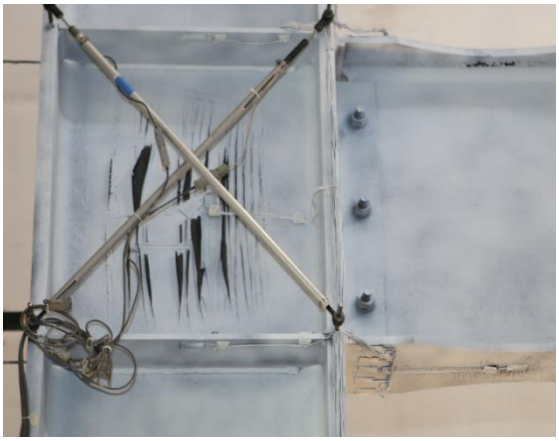

(a) +0.03 rad (2nd Cycle)

Figure 4.52 Specimen C6: Panel Zone Yielding

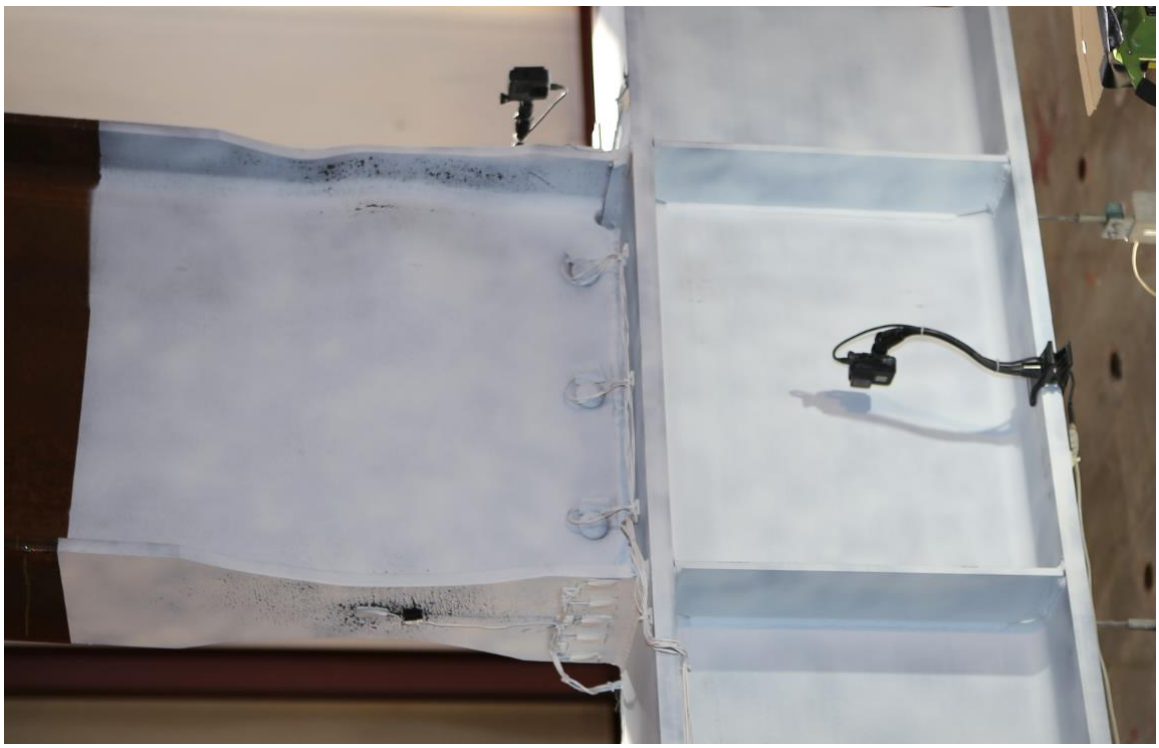

Figure 4.53 Specimen C6: Beam Web and Flange Local Buckling at +0.04 rad (2nd Cycle)

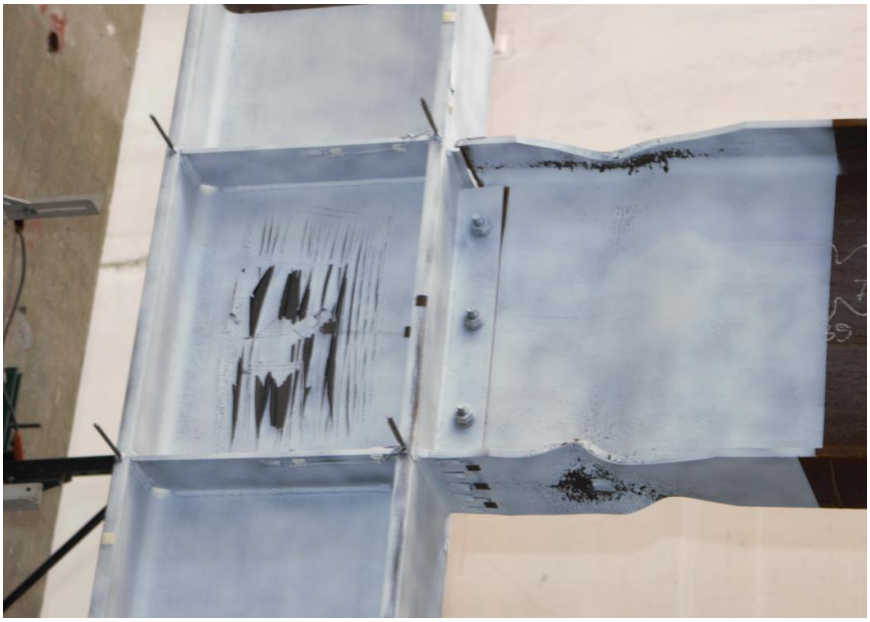

(a) West Side

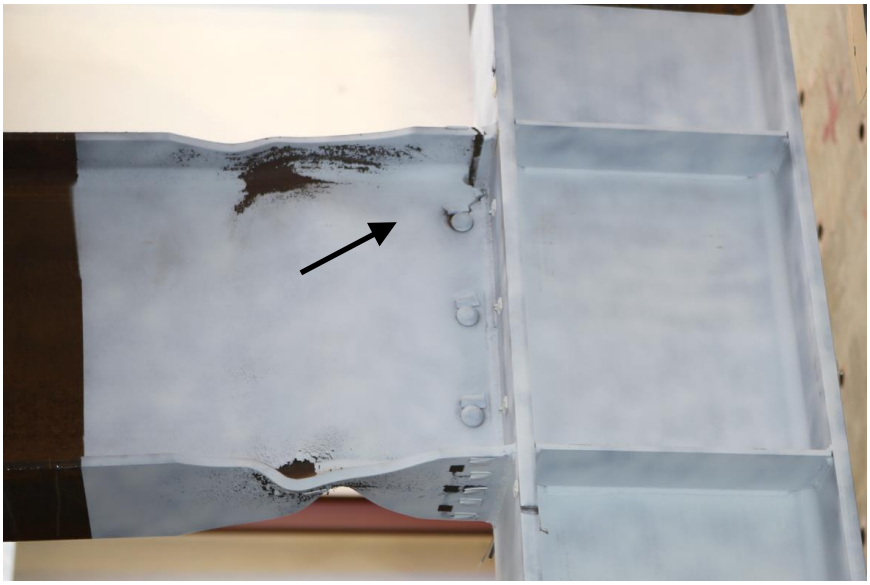

(b) East Side

Figure 4.54 Specimen C6: Connection at End of Test

(a) West Bottom Flange Continuity Plate

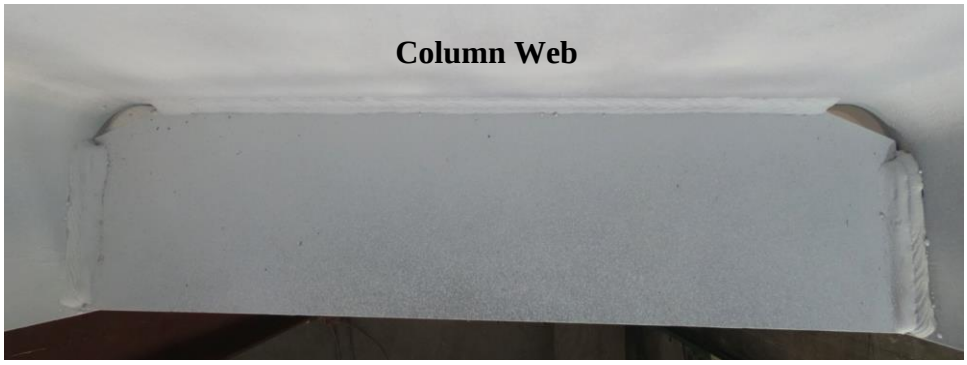

(b) East Top Flange Continuity Plate

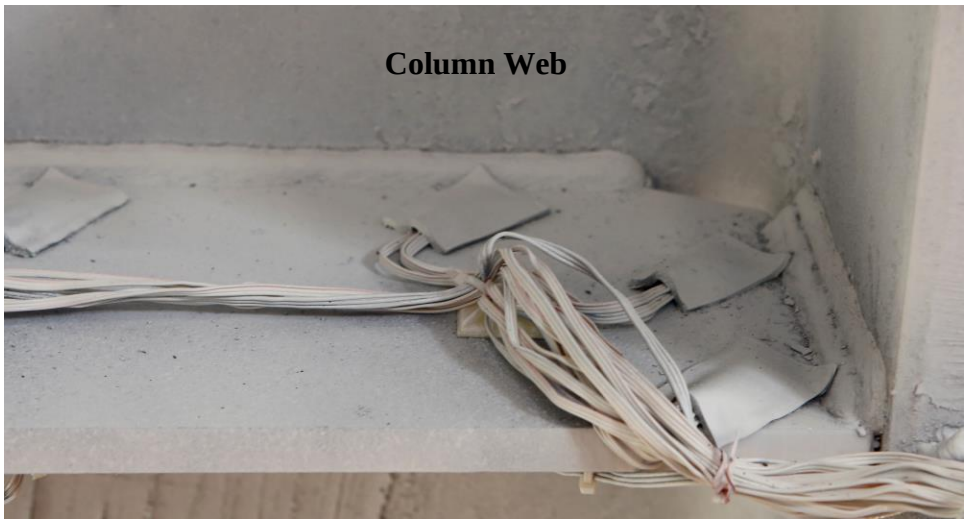

(c) West Top Flange Continuity Plate

Figure 4.55 Specimen C6: Continuity Plate (End of Test)

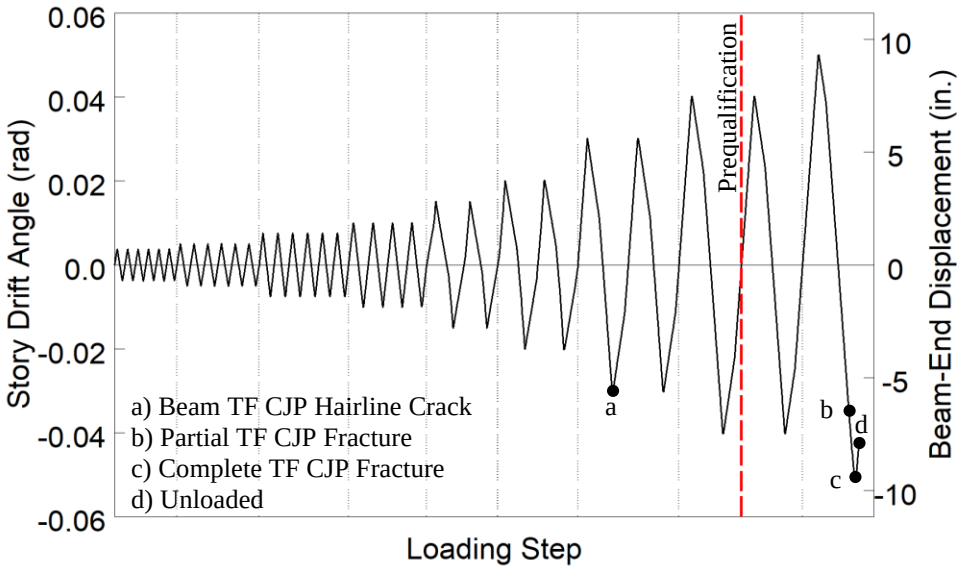

Figure 4.56 Specimen C6: Recorded Loading Sequence

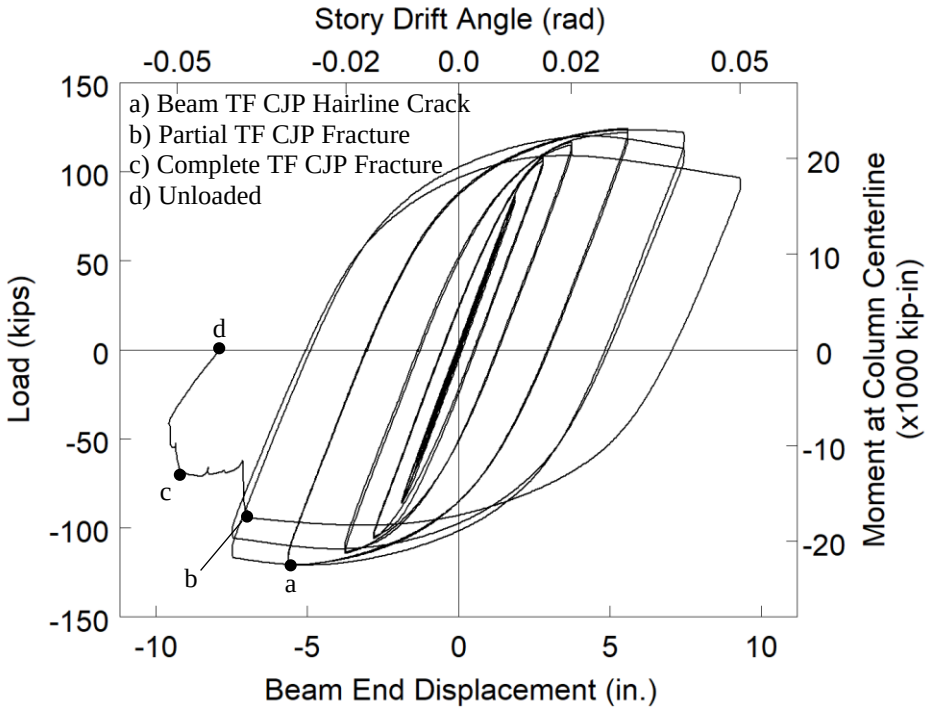

Figure 4.57 Specimen C6: Applied Load versus Beam End Displacement Response

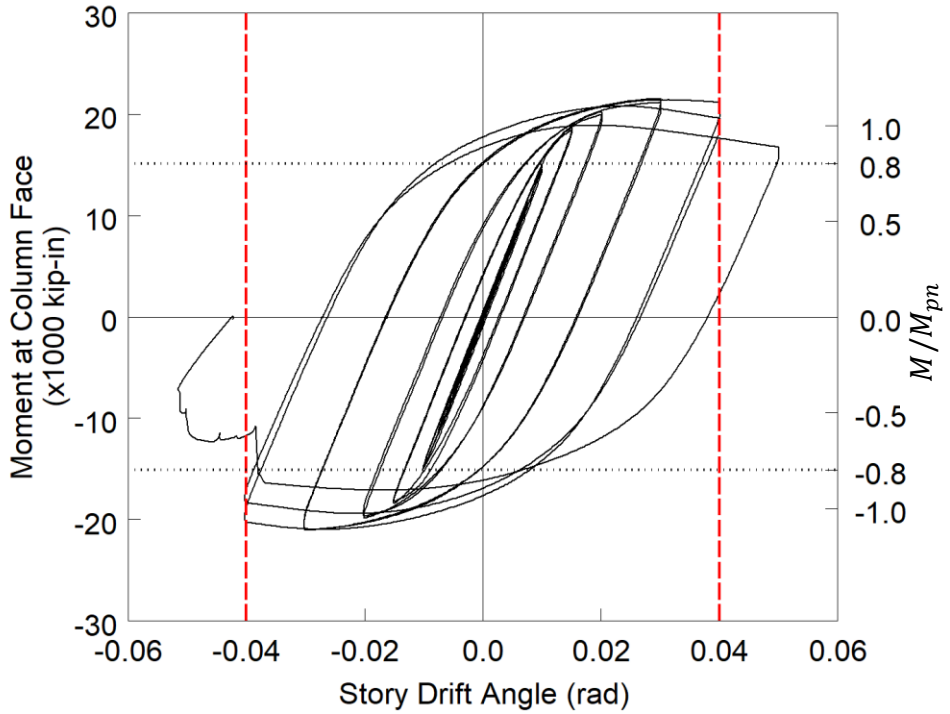

Figure 4.58 Specimen C6: Moment at Column Face versus Story Drift Response

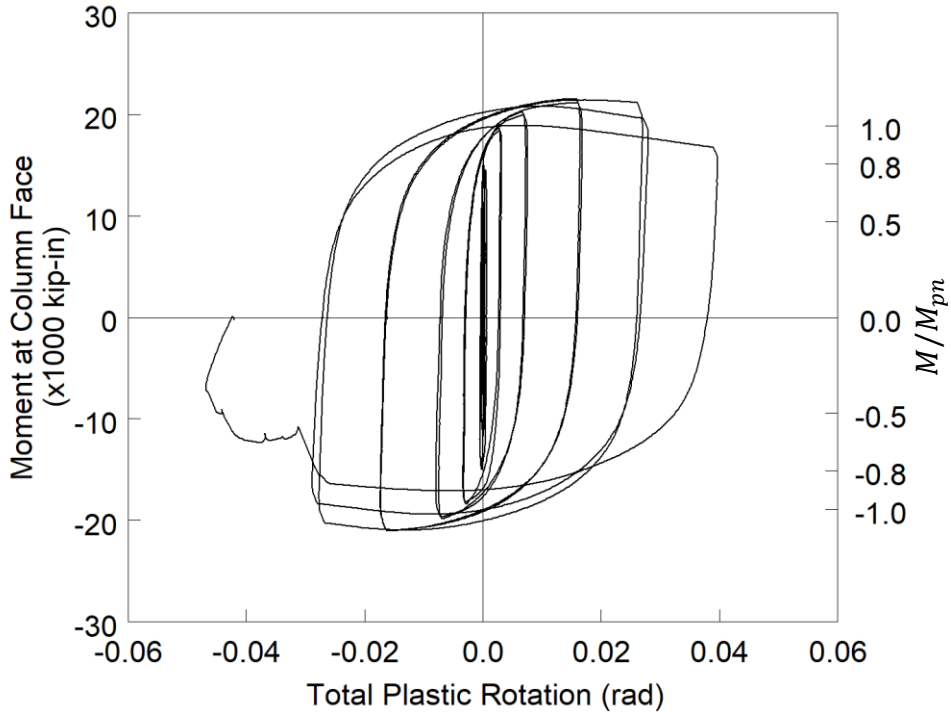

Figure 4.59 Specimen C6: Moment at Column Face versus Plastic Rotation Response

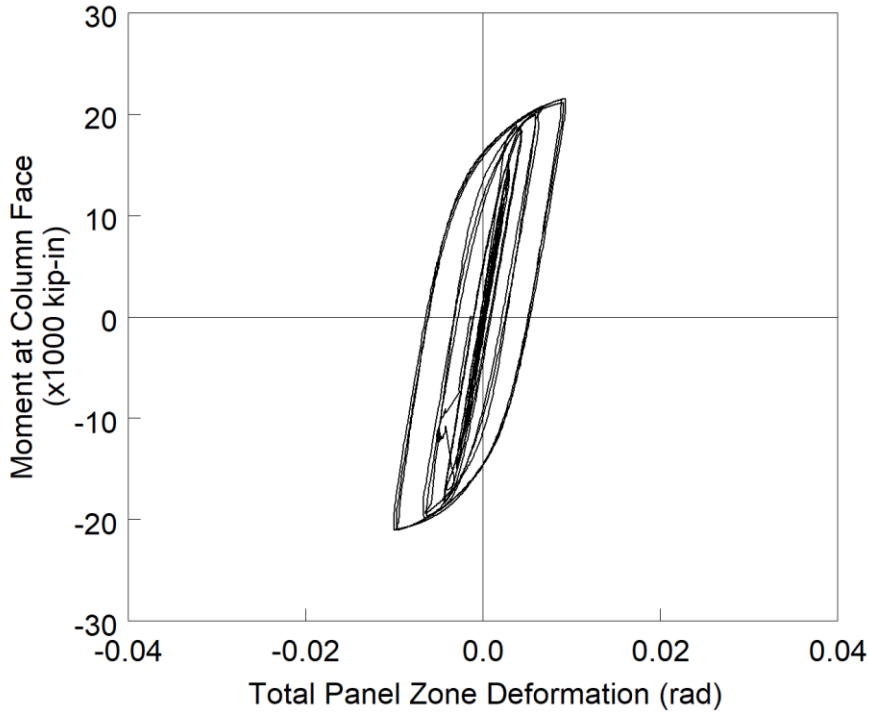

Figure 4.60 Specimen C6: Panel Zone Shear Deformation

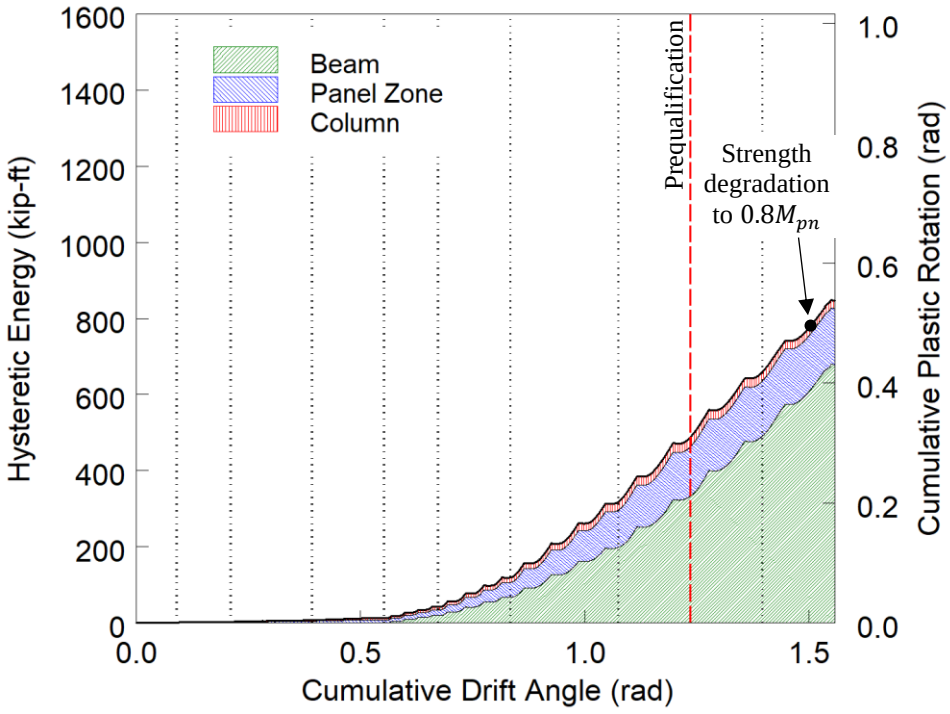

Figure 4.61 Specimen C6: Energy Dissipation

4.6. Specimen C6-G

4.6.1. General

Specimen C6-G was nominally identical to Specimen C6 except that the specimen was hot-dip galvanized prior to welding such that the effects of galvanization can be investigated. Figure 4.62 shows the specimen before testing. The specimen suffered a complete beam top flange fracture during the negative excursion of the first 0.05 rad drift.

4.6.2. Observed Performance

The observed response for Specimen C6-G is described below.

- Figure 4.63 shows the east side of the specimen at the peak excursions during the later cycles of the loading protocol. The specimen met the AISC acceptance criteria. It was observed that beam web buckling initiated during the first cycle of 0.04 rad drift. Flange local bucking initiated at the beam bottom flange within the RBS cut during the first cycle of 0.04 rad drift.
- Figure 4.64 shows cracking in the galvanization coating that first occurred at the RBS location during the second cycle of 0.02 rad drift. Once the cracked coating was brushed the bare pickled steel was left before the surface.
- A hairline crack was observed at the beam top flange CJP weld at the negative excursion of 0.03 rad drift (see Figure 4.65). This crack did not progress significantly during testing [see Figure 4.65(c)].
- Figure 4.66 shows the initiation of flange local buckling during the first negative excursion of 0.04 rad drift. Also demonstrated in this figure was flaking of the galvanization in the beam web in the regions of higher curvature due to beam web buckling. The shedding of the galvanization in sheets during yielding was observed in Figure 4.66(b).

- Beam web buckling was first observed during the 0.04 rad cycles. During the second cycle at -0.05 rad drift web buckling was pronounced and interacting with beam lateral-torsional buckling to create a step in the web (see Figure 4.67).
- During the first negative excursion of 0.06 rad drift the beam web k-area fractured in a region of high local curvature due to beam web buckling (see Figure 4.68). This fracture propagated to the top surface of the beam top flange [see Figure 4.68(c)]. The remainder of the top flange fractured once the negative excursion was resumed (see Figure 4.69). The surface of the fracture reveals that the partial fracture consisted of mainly cleavage fracture. Shear fracture dominated the secondary fracture which completed separation of the flange.
- Figure 4.70 shows the east side of the specimen at the end of testing. No damage was observed to the continuity plate fillet welds at the end of testing (see Figure 4.71).

4.6.3. Recorded Response

- Figure 4.72 shows the recorded displacement response of the beam tip measured with transducer L1. At 0.036 rad drift during the first negative excursion of 0.06 rad drift a partial fracture occurred in the k-area of the beam top flange. This fracture extended outward to the top surface of the beam top flange. Upon resuming negative excursion, the remainder of the top flange ruptured at 0.018 rad drift.
- Figure 4.73 shows the load-displacement response of the beam.
- Figure 4.74 shows the computed moment at the column face (M_f) versus the story drift angle. Two horizontal axes at 80% of the nominal plastic moment (M_{pn}) of the beam section are also added. In addition, two vertical axes at ±0.04 rad story drift show the drift required for SMF connections per AISC 341. It is observed that the beam developed 1.1 times its nominal plastic bending moment. If the moment is computed at the plastic hinge

location and compared to the expected plastic moment, then the peak connection strength factor (C_{pr}) is 1.18.

- Figure 4.75 shows the plastic response of the specimen. The plastic response is computed using the procedure outlined in Section 3.7. The computed elastic stiffness of the specimen was determined to be 46.9 kips/in.
- Figure 4.76 shows modest inelastic behavior of the panel zone.
- Figure 4.77 shows the dissipated energy of Specimen C6-G. Dotted vertical lines on the graph demonstrate the completion of each group of cycles, and the dashed red vertical line shows the completion of the first cycle of 0.04 rad in the AISC loading. It is observed that the completion of the first drift cycle of 0.04 rad (the requirement for SMF connections per AISC 341) occurs after 492 kip-ft of energy has been dissipated. The connection did not degrade below $0.8M_{pn}$ until 1,104 kip-ft of energy had been dissipated. Therefore only 44% of the energy dissipation capacity was utilized after the completion of SMF requirement. It is observed that most (90%) of the energy dissipation capacity occurred in the beam.

(a) West Side

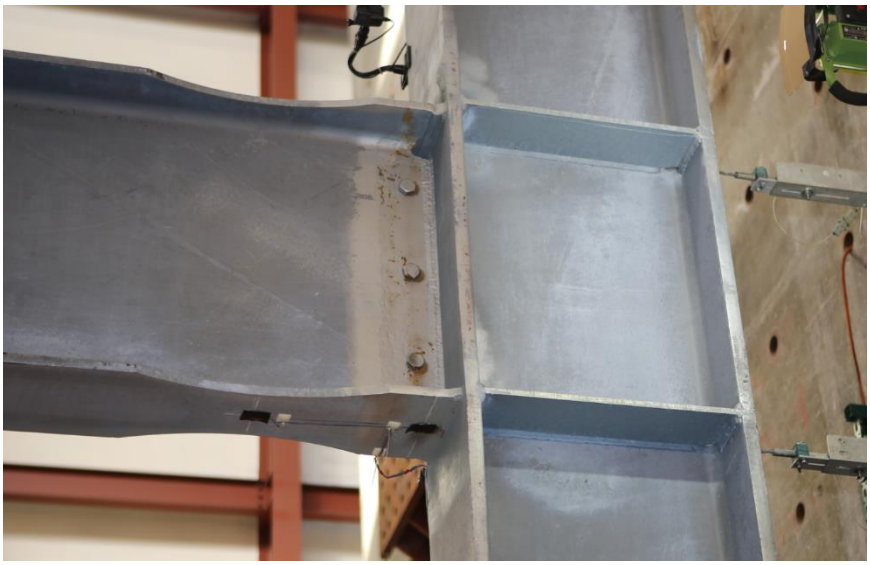

(b) East Side

Figure 4.62 Specimen C6-G: Specimen before Testing

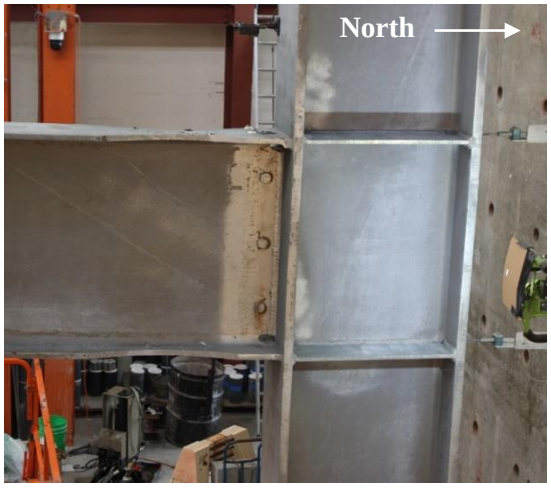

(a) +0.03 rad (2nd Cycle)

(b) -0.03 rad (2nd Cycle)

(c) +0.04 rad (2nd Cycle)

(d) -0.04 rad (2nd Cycle)

(e) +0.05 rad (1st Cycle)

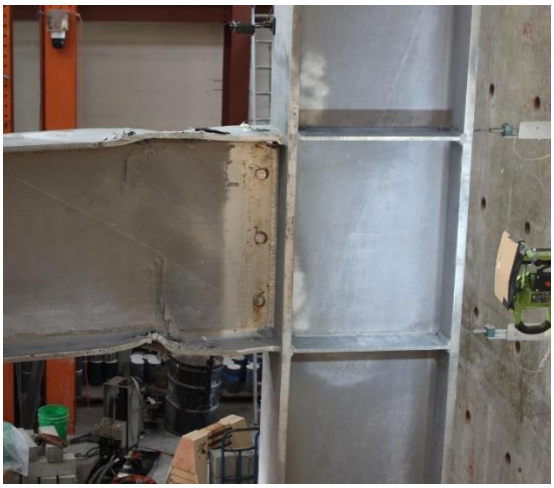

(f) -0.05 rad (1st Cycle)

Figure 4.63 Specimen C6-G: East Side of Connection

Figure 4.64 Specimen C6-G: Cracks in Galvanization Coating

(a) Overview

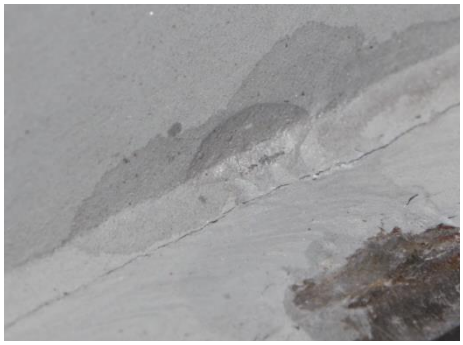

(b) -0.03 rad (1st Cycle)

(c) End of Test

Figure 4.65 Specimen C6-G: Hairline Crack at Beam Top Flange CJP Weld

(a) -0.04 rad (1st Cycle)

(b) -0.04 rad (2nd Cycle)

Figure 4.66 Specimen C6-G: Flange Local Buckling

Figure 4.67 Specimen C6-G: Web Local Buckling

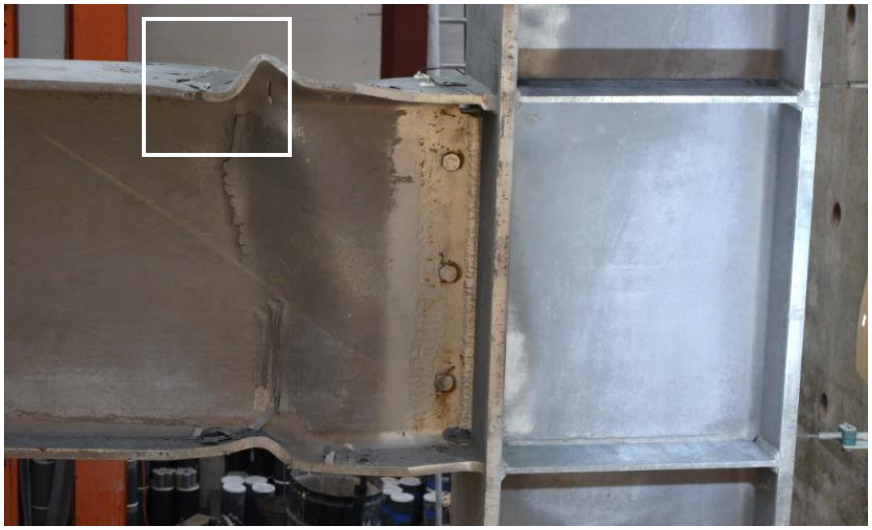

(a) Overview

(b) East Side

(c) Top Flange

Figure 4.68 Specimen C6-G: Beam Flange Partial Fracture at -0.06 rad (1st Cycle)

(a) West Side

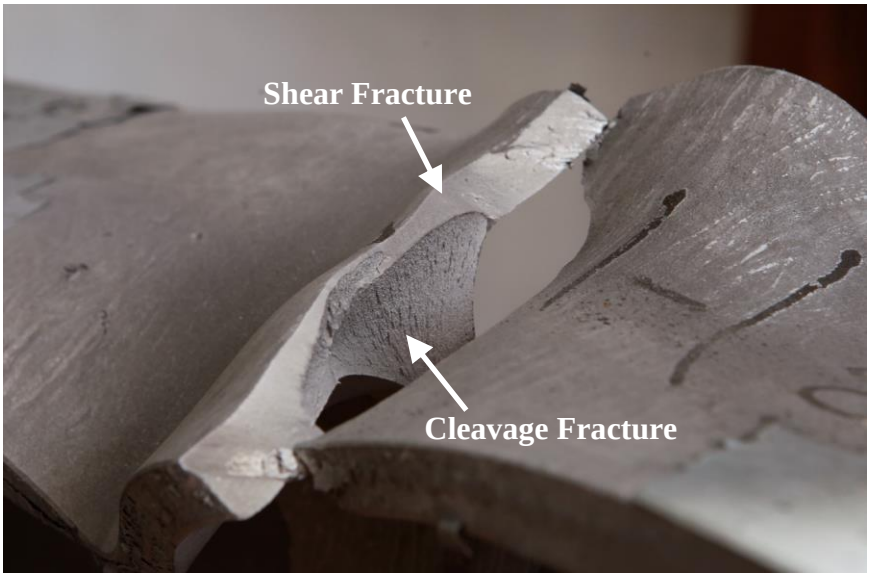

(b) Fracture Surface

Figure 4.69 Specimen C6-G: Complete Beam Fracture at -0.06 rad (1st Cycle)

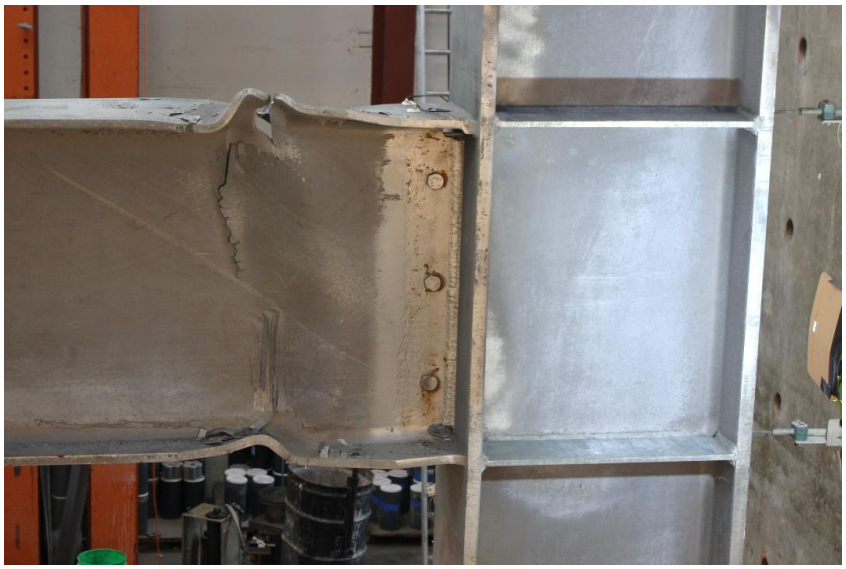

Figure 4.70 Specimen C6-G: East Side of Connection at End of Test

(a) West Top Flange

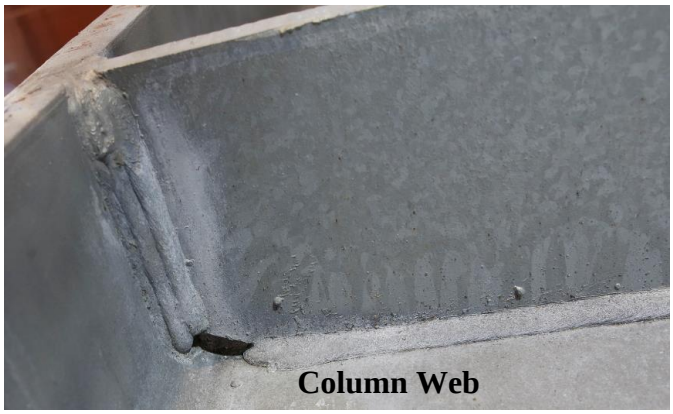

(b) East Top Flange

Figure 4.71 Specimen C6-G: Continuity Plate Welds at End of Test

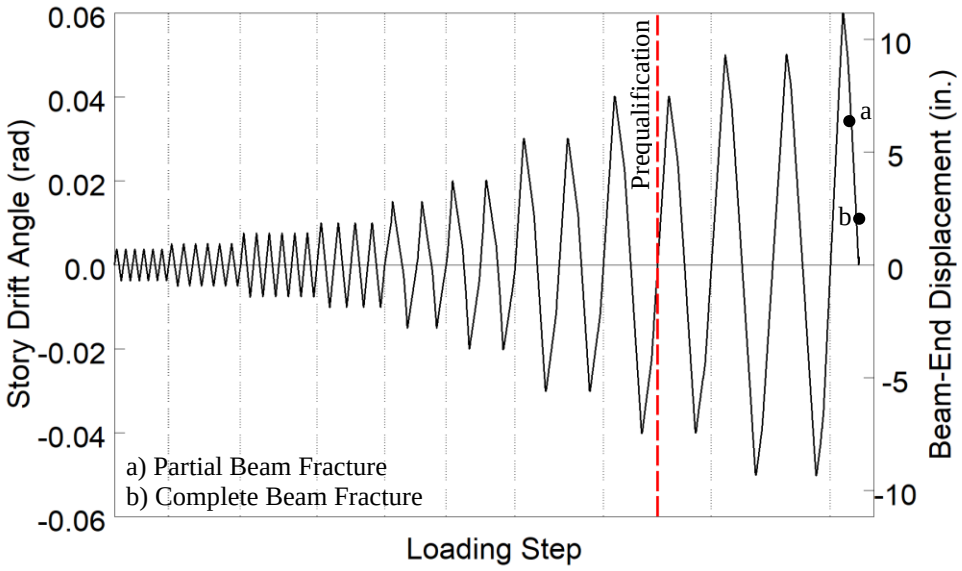

Figure 4.72 Specimen C6-G: Recorded Loading Sequence

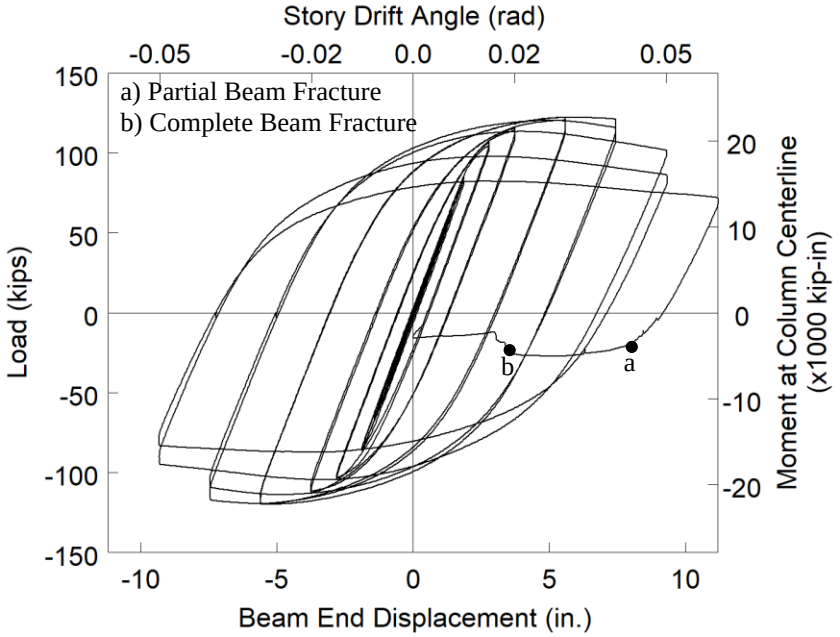

Figure 4.73 Specimen C6-G: Applied Load versus Beam End Displacement Response

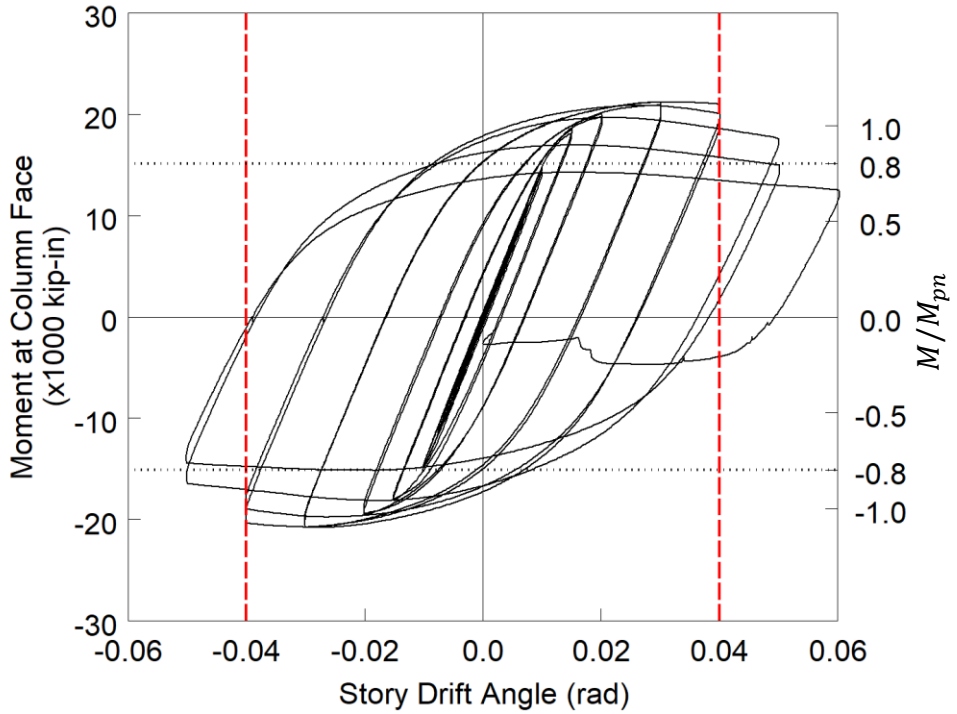

Figure 4.74 Specimen C6-G: Moment at Column Face versus Story Drift Response

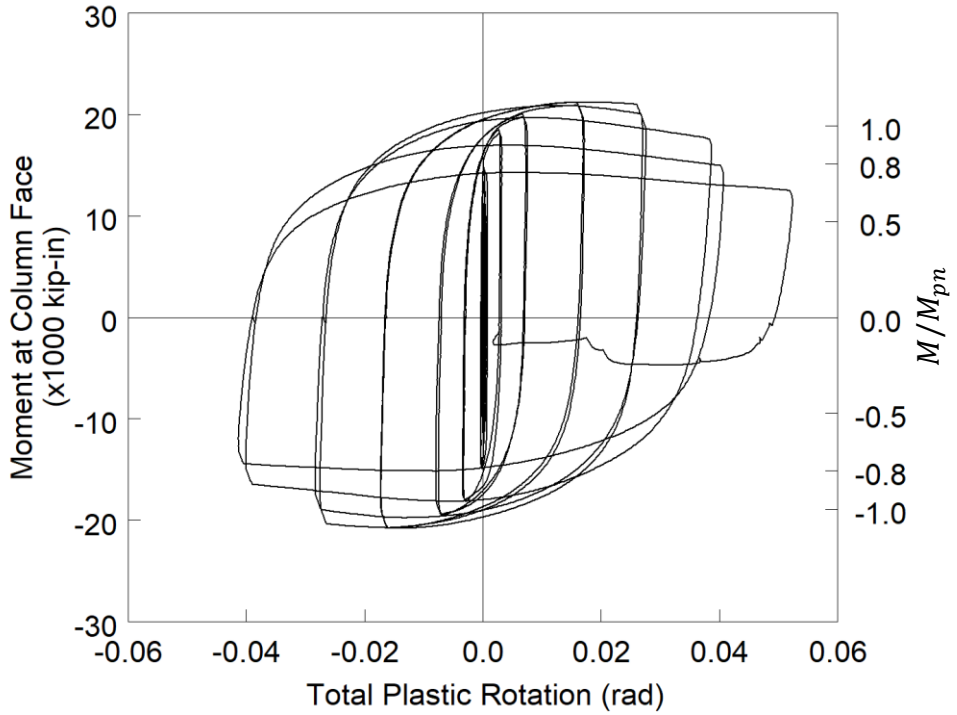

Figure 4.75 Specimen C6-G: Moment at Column Face versus Plastic Rotation Response

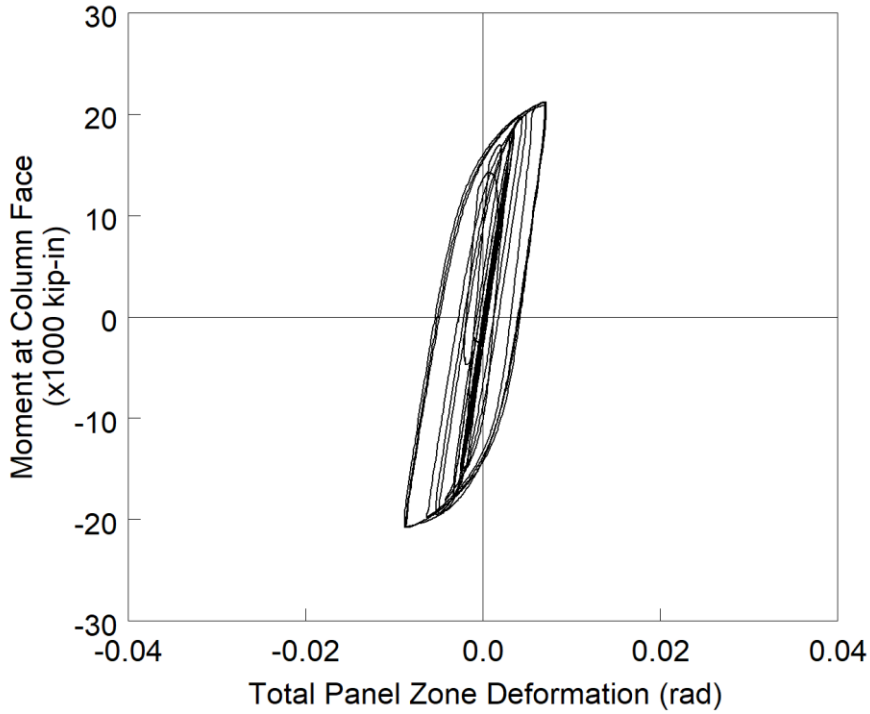

Figure 4.76 Specimen C6-G: Panel Zone Shear Deformation

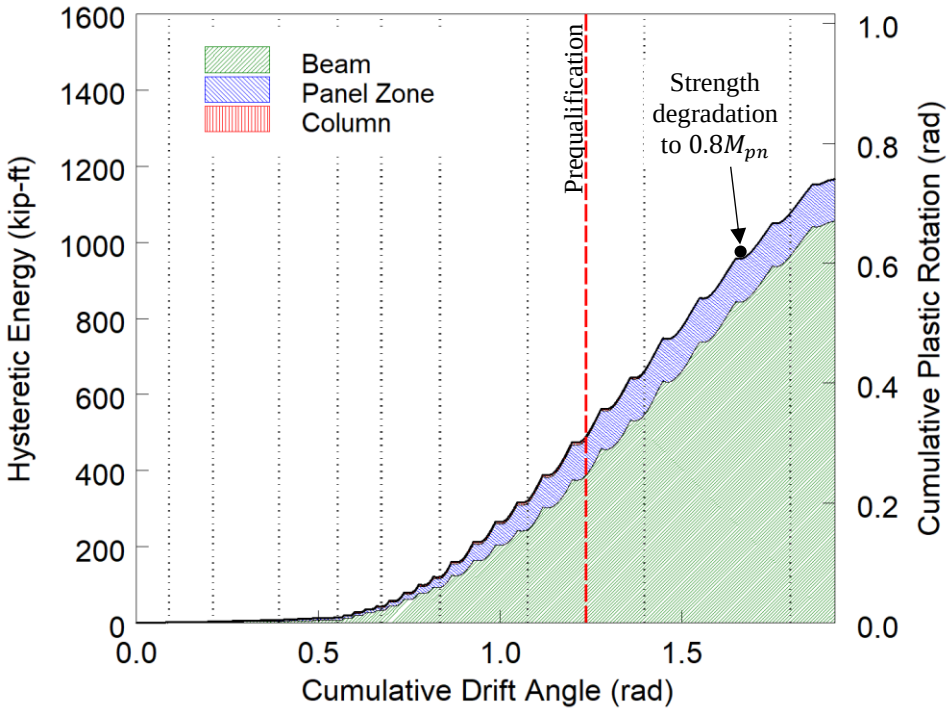

Figure 4.77 Specimen C6-G: Energy Dissipation

4.7. Specimen C7

4.7.1. General

Specimen C7 was designed to investigate the validity of using the plastic distribution to estimate the required strength of the continuity plate while violating the Lehigh Criterion. The continuity plates were designed to satisfy the governing AISC 360 §J10 concentrated force column limit state; WLY was the governing limit state that dictates the need of a continuity plate in this specimen. Instead of using a continuity plate to reinforce the column web, since it was found that the FLB limit state does not require reinforcement, a doubler plate was added to the east side of the specimen. The doubler plate was a minimum size such that the stability of the doubler plate was achieved without using plug welds within the doubler plate. The vertical welds fastening the doubler plate to the column were designed based on the distribution of shear force in the panel zone, which violates the current AISC 341 Provisions requiring vertical welds to develop the strength of the doubler plate. Horizontal welds were not used across the top and bottom edge of the extended doubler plate, which conforms to the current Provisions. Figure 4.78 shows the specimen before testing. The specimen developed a partial rupture of the beam bottom flange during the unloading portion of the second cycle of 0.05 rad drift; loading was not continued.

4.7.2. Observed Performance

The observed response for Specimen C7 is described below.

- Figure 4.79 shows the east side of the specimen at the peak excursions during the later cycles of the loading protocol. The specimen met the AISC acceptance criteria. It was observed that beam web buckling and beam flange local buckling both initiated during the first cycle of 0.04 rad drift. Flange local bucking initiated at the beam bottom flange within the RBS cut during the second cycle of 0.03 rad drift. Web local buckling started during

the 0.03 rad drift cycles. The beam bottom flange developed a partial rupture during the unloading portion of the second cycle of 0.05 rad drift.

- Beam bottom flange yielding initiated at 0.005 rad drift cycles two inches from the column flange [see Figure 4.80(a)]. At 0.01 rad drift this yielding had spread outward and into the reduced beam section [see Figure 4.80(b)]. Figure 4.80(c) shows that the yielding had distributed through most of the reduced beam section by 0.04 rad drift. Similar yielding observations occurred on the beam top flange (see Figure 4.81). By 0.02 rad drift the yielding had spread through the flange, showing yield lines on the underside of beam top flange (see Figure 4.82).
- Figure 4.83 shows web local yielding at the beam top flange location. The WLY was first observed at 0.02 rad drift and progressed slightly with each drift level. Figure 4.84 shows the WLY patterns at the end of testing. It was observed that the yielding was localized at the elevation just outside of the beam flange. Yielding was only observed on the side of the column which did not have a doubler plate.
- Web and flange local buckling started during the 0.03 rad drift cycles (see Figure 4.85). The flange local buckling continued to amplify during later cycles. A partial beam bottom flange occurred during the negative excursion of the second cycle of 0.05 rad.
- Figure 4.86 shows the condition of the connection at the end of testing.
- The partial beam flange tear was observed in Figure 4.87.
- The west side of the column demonstrated a yielding along a vertical line that runs the length of the beam web. This yield line was 2.5 in. from the beam web (see Figure 4.88).
- No damage was observed in the doubler plate fillet welds at the end of testing (see Figure 4.89).

4.7.3. Recorded Response

- Figure 4.90 shows the recorded displacement response of the beam tip measured with transducer L1. The beam bottom flange partially fractured during the unloading portion of the second 0.05 rad drift cycles; loading was not continued after developing the partial fracture.
- Figure 4.91 shows the load-displacement response of the beam.
- Figure 4.92 shows the computed moment at the column face (M_f) versus the story drift angle. Two horizontal axes at 80% of the nominal plastic moment (M_{pn}) of the beam section are also added. In addition, two vertical axes at ±0.04 rad story drift show the drift required for SMF connections per AISC 341. It is observed that the beam developed 1.1 times its nominal plastic bending moment. If the moment is computed at the plastic hinge location and compared to the expected plastic moment, then the peak connection strength factor (C_{pr}) is 1.20.
- Figure 4.93 shows the plastic response of the specimen. The plastic response is computed using the procedure outlined in Section 3.7. The computed elastic stiffness of the specimen was determined to be 49.0 kips/in.
- Figure 4.94 shows negligible inelastic behavior of the panel zone. The black and blue lines are the measured panel zone deformations from the transducers placed on the column web and doubler plate, respectively. Little difference is observed between these two sides of the specimen.
- Figure 4.95 shows the dissipated energy of Specimen C7. Dotted vertical lines on the graph demonstrate the completion of each group of cycles, and the dashed red vertical line shows the completion of the first cycle of 0.04 rad in the AISC loading. It is observed that the

completion of the first drift cycle of 0.04 rad (the requirement for SMF connections per AISC 341) occurs after 495 kip-ft of energy has been dissipated. The connection did not degrade below $0.8M_{pn}$ until 754 kip-ft of energy had been dissipated. Therefore only 65% of the energy dissipation capacity was utilized after the completion of SMF requirement. It is observed that most (93%) of the energy dissipation capacity occurred in the beam.

(a) West Side

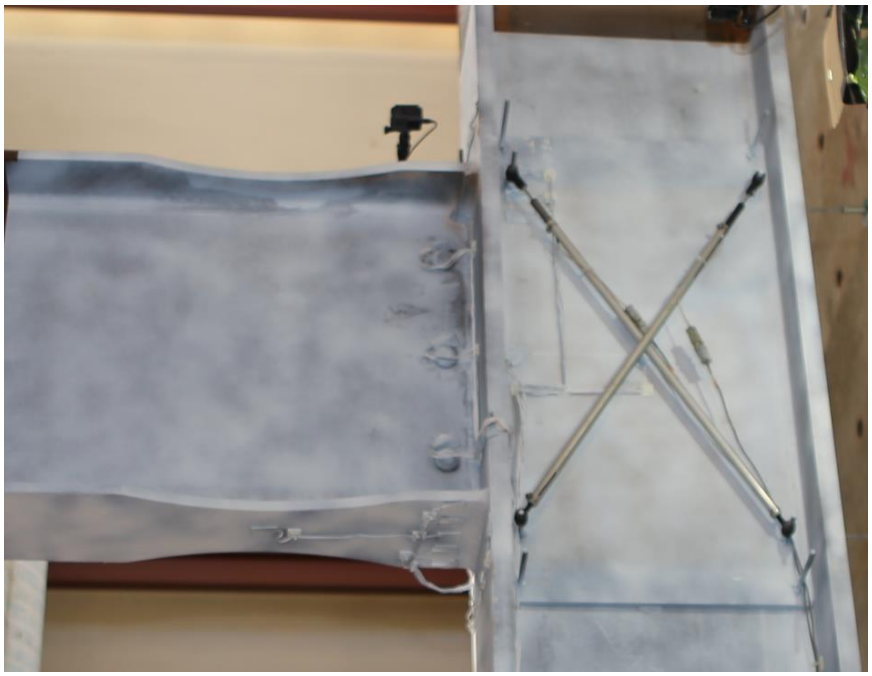

(b) East Side

Figure 4.78 Specimen C7: Specimen before Testing

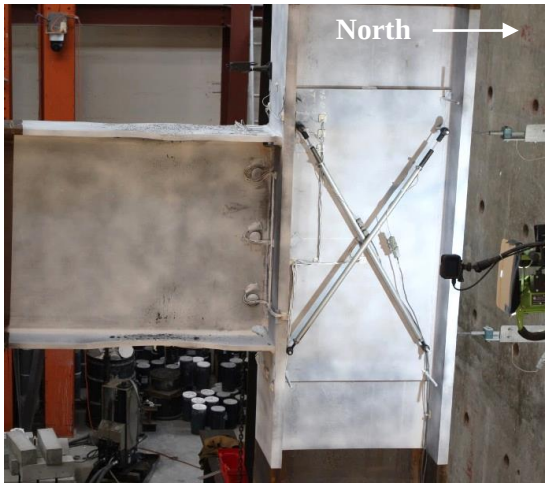

(a) +0.03 rad (2nd Cycle)

(b) -0.03 rad (2nd Cycle)

(c) +0.04 rad (2nd Cycle)

(d) -0.04 rad (2nd Cycle)

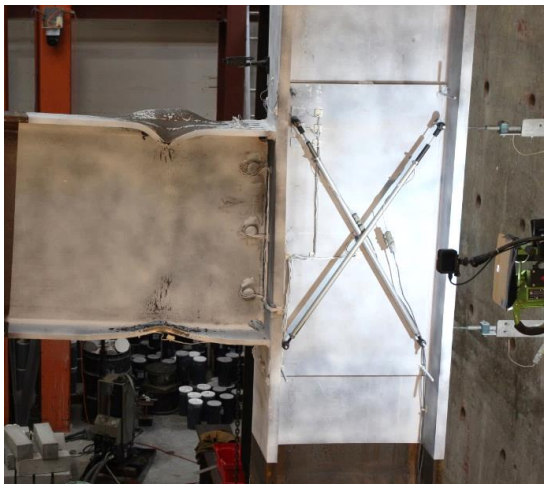

(e) +0.05 rad (1st Cycle)

(f) -0.05 rad (1st Cycle)

Figure 4.79 Specimen C7: East Side of Connection

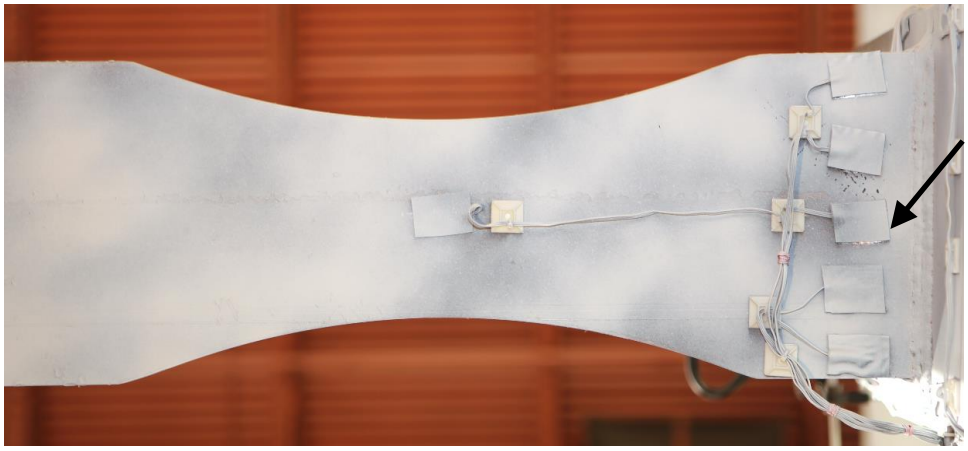

(a) -0.0005 rad (6th Cycle)

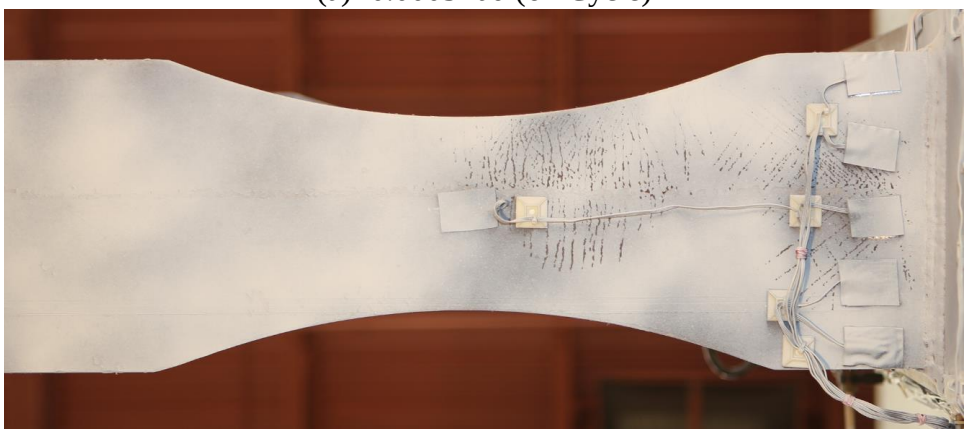

(b) -0.01 rad (2nd Cycle)

(c) +0.04 rad (1st Cycle)

Figure 4.80 Specimen C7: Beam Bottom Flange Yielding

Figure 4.81 Specimen C7: Beam Top Flange Yielding at -0.015 rad (2nd Cycle)

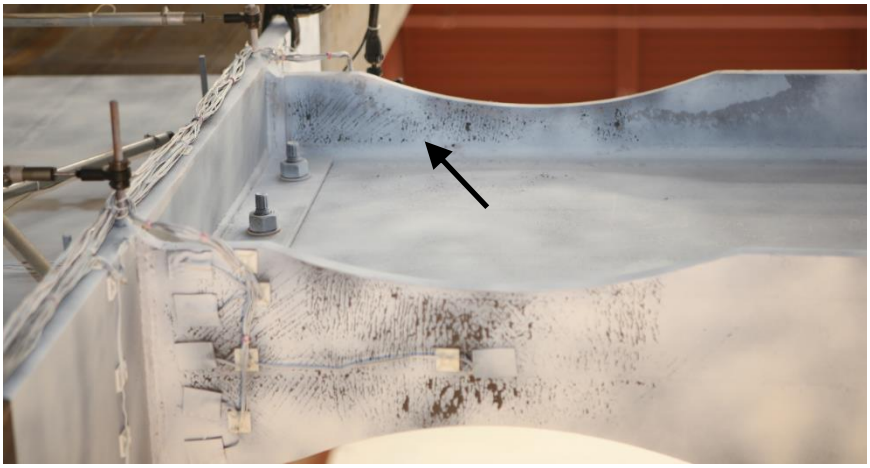

Figure 4.82 Specimen C7: Beam Top Flange Yielding at -0.02 rad (2nd Cycle)

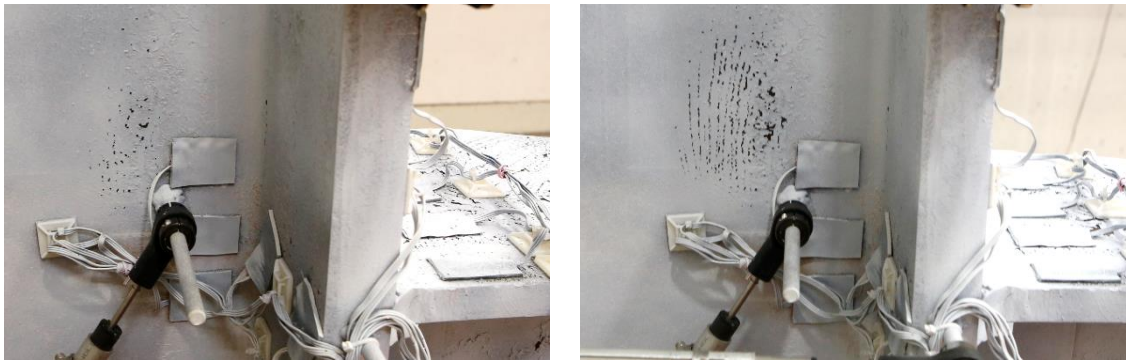

(a) -0.03 rad (2nd Cycle) (b) -0.04 rad (1st Cycle)

Figure 4.83 Specimen C7: Colum WLY at Beam Top Flange Level

(a) Beam Top Flange Level

(b) Beam Bottom Flange Level

Figure 4.84 Specimen C7: Colum WLY at End of Test

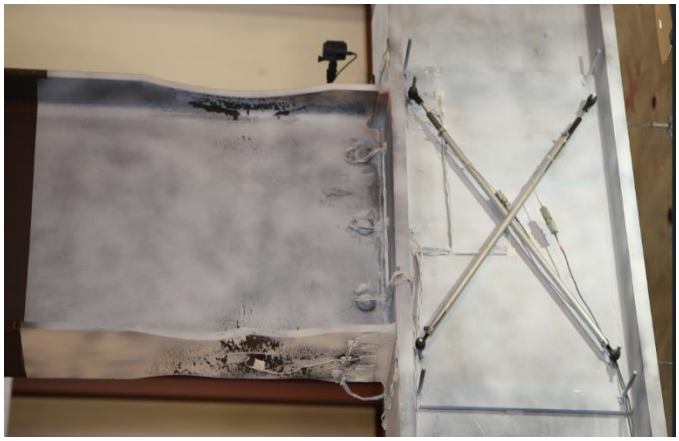

(a) -0.03 rad (1st Cycle)

(b) -0.04 rad (1st Cycle)

Figure 4.85 Specimen C7: Beam Flange Local Bucking

(a) West Side

(b) East Side

Figure 4.86 Specimen C7: Connection at End of Test

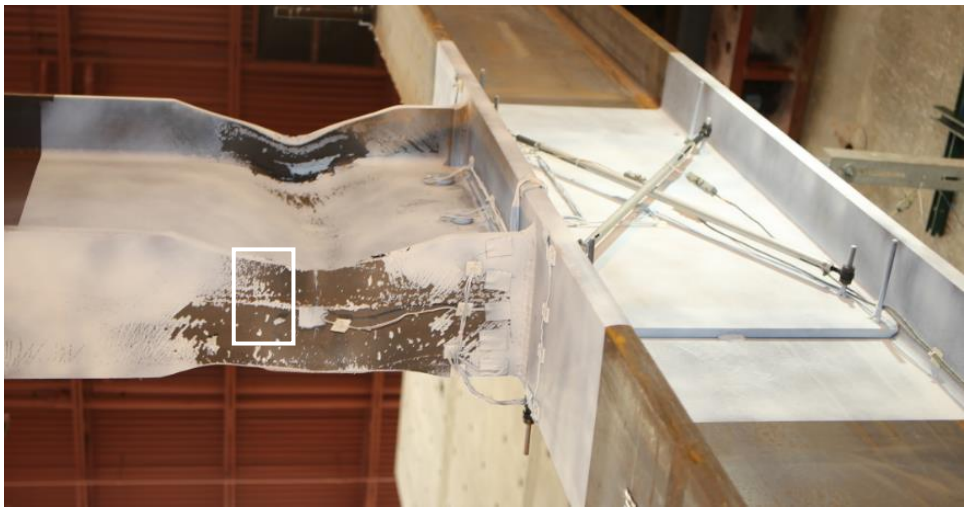

(a) Overview

(a) Fracture

Figure 4.87 Specimen C7: Beam Flange Partial Fracture

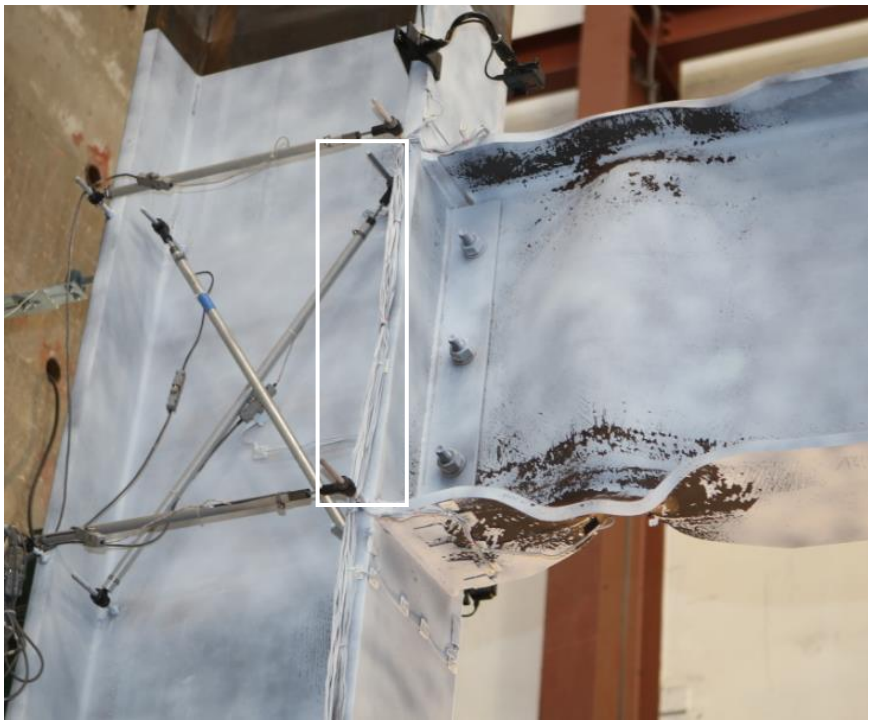

(a) Overview

(b) Column Yielding

Figure 4.88 Specimen C7: Column Yielding (End of Test)

Figure 4.89 Specimen C7: Doubler Plate at End of Test

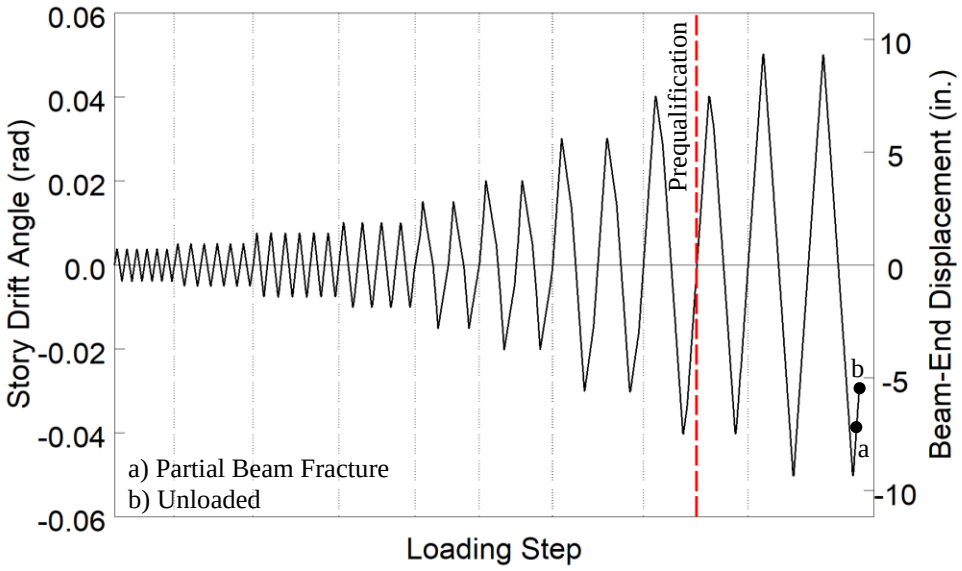

Figure 4.90 Specimen C7: Recorded Loading Sequence

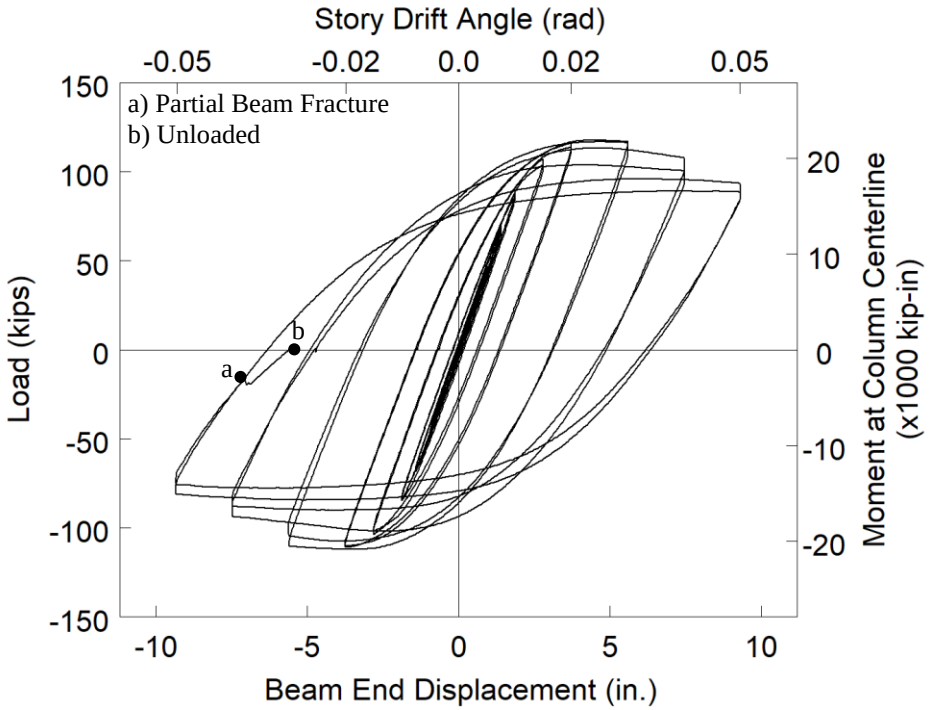

Figure 4.91 Specimen C7: Applied Load versus Beam End Displacement Response

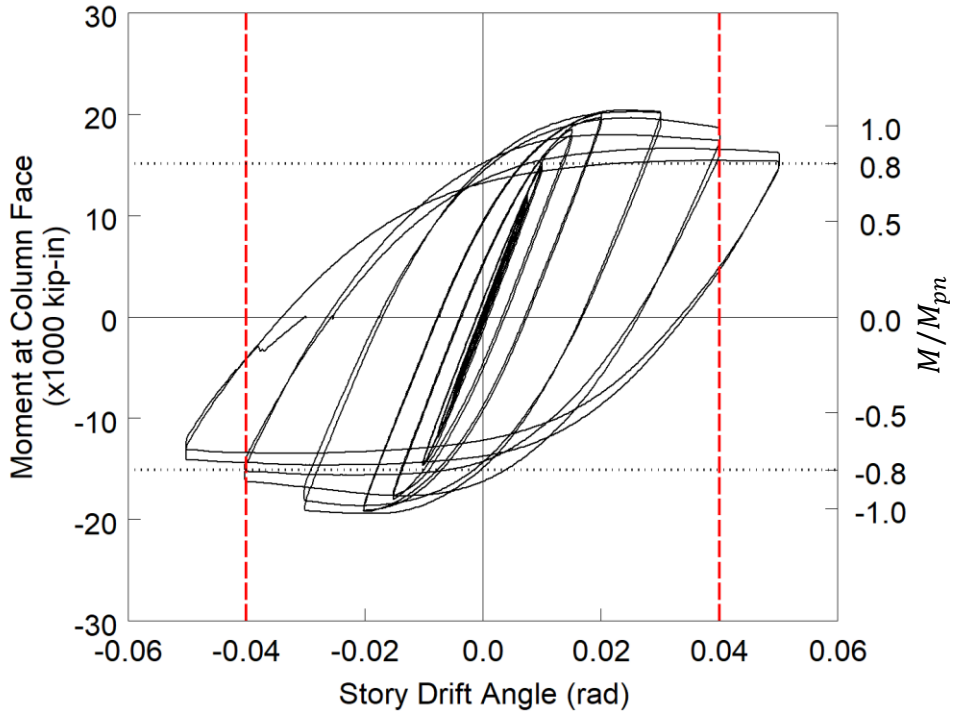

Figure 4.92 Specimen C7: Moment at Column Face versus Story Drift Response

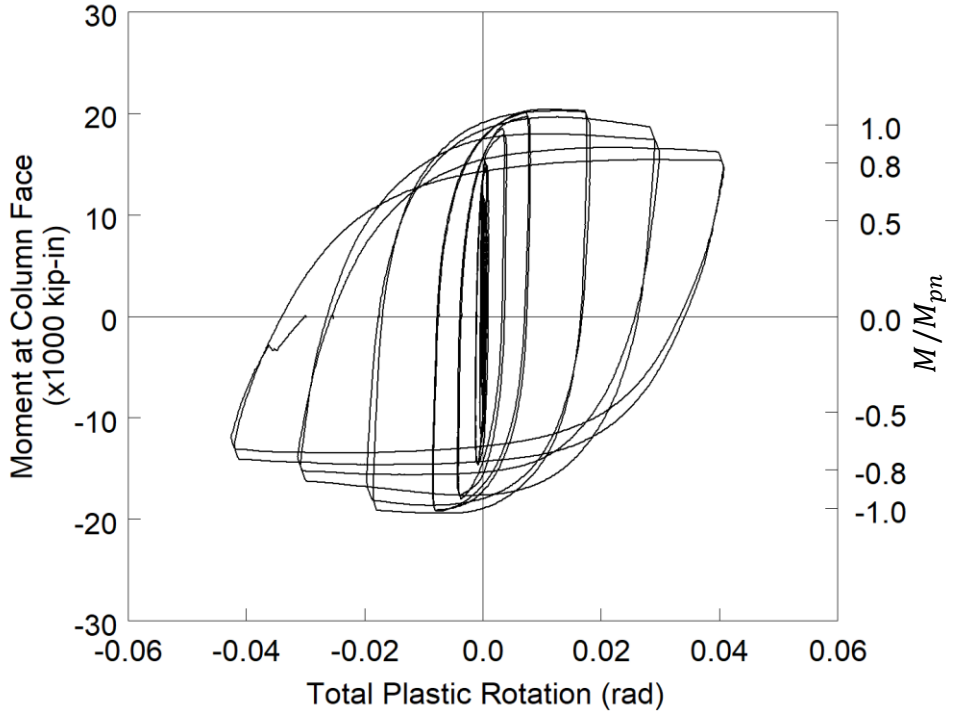

Figure 4.93 Specimen C7: Moment at Column Face versus Plastic Rotation Response

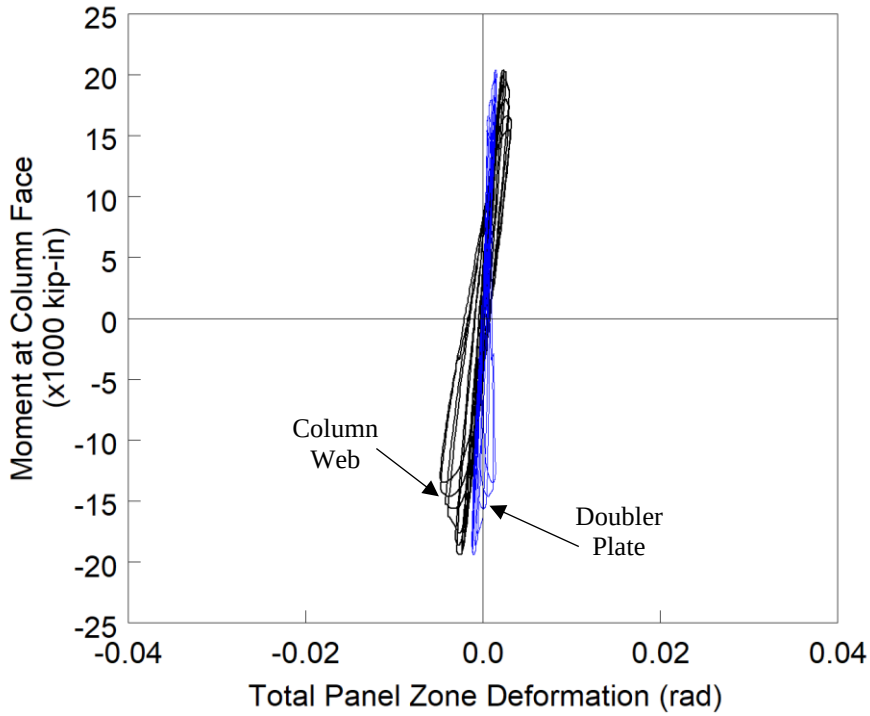

Figure 4.94 Specimen C7: Panel Zone Shear Deformation

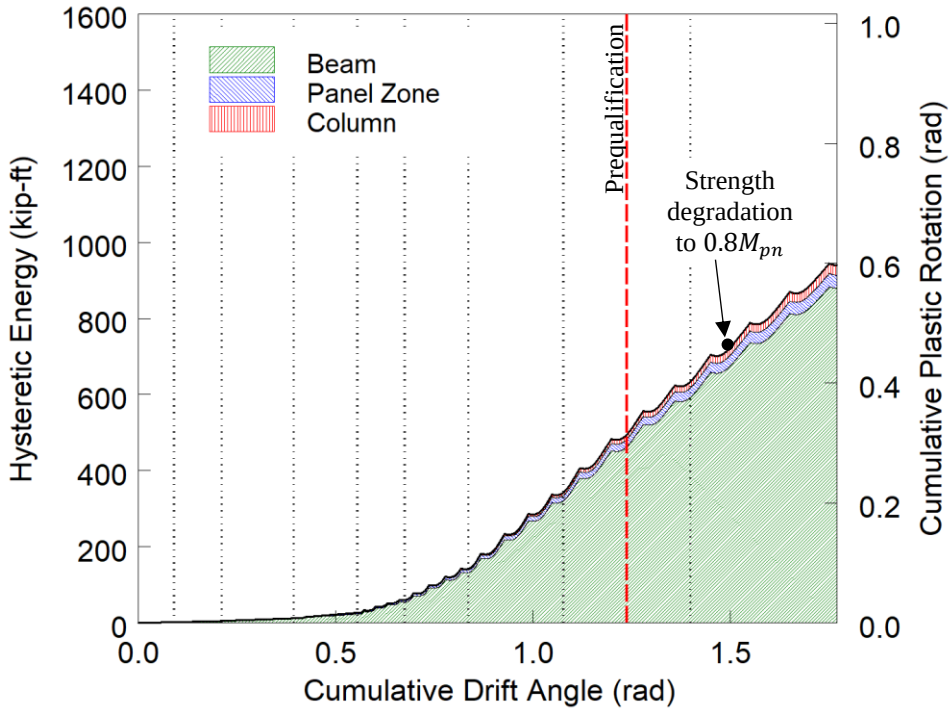

Figure 4.95 Specimen C7: Energy Dissipation

4.8. Specimen W1

4.8.1. General

Specimen W1 was designed to investigate use of the plastic methodology to design continuity plates. The resulting continuity plates were thinner than required by the current AISC 341 Provisions. Continuity plate double-sided fillet welds were sized such that $w = 0.75t_{cp}$. A pair of doubler plates stiffen the web of the column for panel zone yielding—these plates were extended 6 in. above and below the beam flange elevations. The doubler plate vertical welds use a PJP groove weld, and no horizontal welds were used in accordance with the current Provisions. Specimen W1 failed by a fracture of the east beam top flange CJP weld during the second cycle of 0.04 rad drift. Figure 4.96 shows the specimen before testing.

4.8.2. Observed Performance

The observed response for Specimen W1 is described below.

- Figure 4.97 shows the connection during testing. The loading protocol was applied symmetrically such that a clockwise rotation is a positive excursion on the east beam and a negative excursion on the west beam. The response is described such that a positive excursion refers to a clockwise rotation of the joint. The specimen met the AISC acceptance criteria by completing one complete cycle at 0.04 rad drift while the flexural strength at either column face did not degrade below 80% of the beam nominal flexural strength. Beam flange and web local buckling initiated at 0.03 rad drift and progressed throughout testing.
- Figure 4.98 and Figure 4.99 show the progressive beam yielding during testing. Yielding starts adjacent to the column flange and propagates outward, concentrating down the center of the beam.

- Figure 4.100 shows the progression of flange local bucking that developed in the east beam bottom flange. The local buckling develops in a opposite sense between the east and west beams depending on which flange of the beam was in compression.
- Figure 4.101 shows yielding in the panel zone observed at a at 0.03 rad drift. The yielding did not progress significantly further by the end of testing.
- Figure 4.102 shows the minor lateral-torsional buckling that developed in beam top flanges during the 0.04 rad drift cycles. The buckling was mirrored between positive and negative joint rotations, reflecting when the top flange experienced compression.
- Figure 4.103 shows the fractured east beam top flange CJP weld at -0.03 rad during the second negative excursion to 0.04 rad drift. The fracture started at the CJP Weld root on the underside of the specimen, on the tension side of the lateral-torsional buckling and propagated along the beam flange following the 30° bevel of the CJP weld. The progression of the fracture was observed in Figure 4.104. After initiating in the weld metal as a ductile tear the fracture transitioned to the bevel of the CJP weld after 0.75 in. The fracture continued its tearing in a ductile fashion until 50% of the flange was fractured when a secondary ductile fracture appeared in the reentrant corner in the center of the flange. The remainder of the fracture propagated due to cleavage through the flange (see Figure 4.105).
- Figure 4.106 shows the connection at the end of testing. Modest amounts of flange local bending and web local buckling were present. Additionally, modest levels of panel zone yielding were observed. Minor shear tab yielding was also observed.
- Continuity plates did not demonstrate yielding nor damage to any of the fillet welds during testing (see Figure 4.107 to Figure 4.109). A slight bow present in the continuity plates occurred before testing of the specimen and was not due to local buckling of the plate.

4.8.3. Recorded Response

- Figure 4.110 shows the recorded displacement response of the beam tip measured with transducer L1 for the east beam and L2 for the west beam. The response from the east and west beams are shown in black and blue, respectively. The east beam CJP weld fractured at -0.03 rad drift during the second negative excursion of 0.04 rad drift. Figure 4.111 shows the column shear versus the applied story drift response.
- Figure 4.112 shows the load-displacement response of the beams.
- Figure 4.113 shows the computed moment at the column face (M_f) versus the story drift angle. Two horizontal axes at 80% of the nominal plastic moment (M_{pn}) of the beam section are also added. In addition, two vertical axes at ±0.04 rad story drift show the drift required for SMF connections per AISC 341. It is observed that the beams developed about 1.5 times its nominal plastic bending moment. If the moment is computed at the plastic hinge location and compared to the expected plastic moment, then the peak connection strength factor (C_{pr}) is 1.40 and 1.41 for the east and west beams respectively.
- Figure 4.114 shows the plastic response of the specimen. The plastic response is computed using the procedure outlined in Section 3.7. The computed elastic stiffness of the specimen was determined to be 172.6 kips/in.
- Figure 4.115 shows modest hysteretic behavior in the panel zone.
- Figure 4.116 shows the dissipated energy of Specimen W1. Dotted vertical lines on the graph demonstrate the completion of each group of cycles, and the dashed red vertical line shows the completion of the first cycle of 0.04 rad in the AISC loading. It is observed that the completion of the first drift cycle of 0.04 rad (the requirement for SMF connections per AISC 341) occurs after 1,952 kip-ft of energy has been dissipated. The connection did not

degrade below $0.8M_{pn}$ until fracture of the east beam top flange occurred and 2,501 kip-ft of energy had been dissipated. Therefore 78% of the energy dissipation capacity was utilized after the completion of the SMF requirement. It is observed that most (82%) of the energy dissipation capacity occurred in the beam.

(a) Overview

(b) Connection Region

Figure 4.96 Specimen W1: Connection before Testing

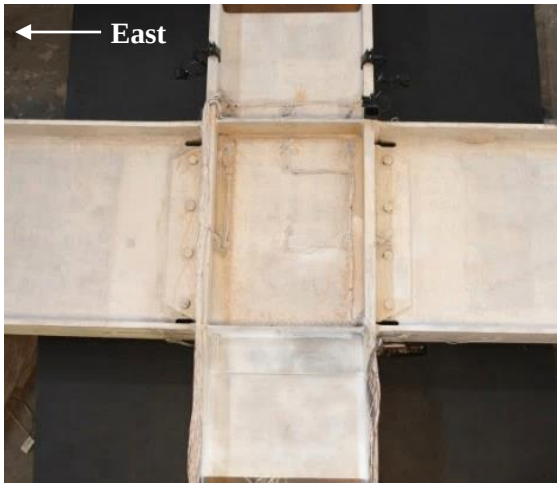

(a) +0.02 rad (2nd Cycle)

(b) -0.02 rad (2nd Cycle)

(c) +0.03 rad (2nd Cycle)

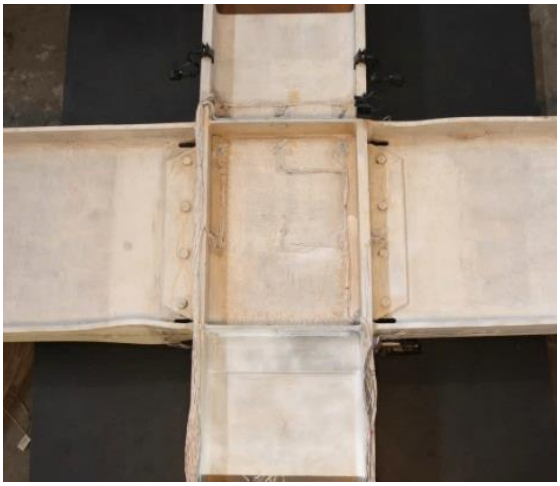

(d) -0.03 rad (2nd Cycle)

(e) +0.04 rad (2nd Cycle)

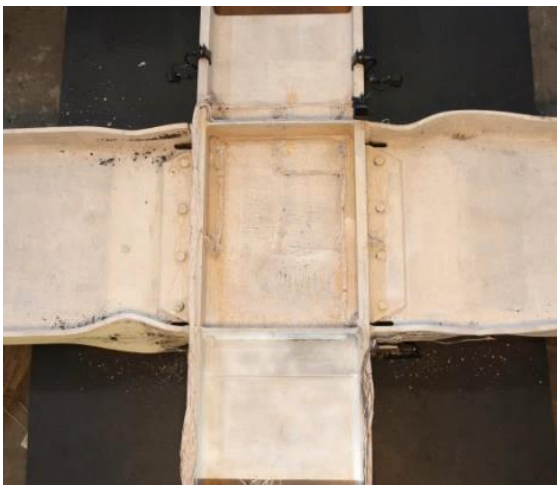

(f) -0.04 rad (2nd Cycle)

Figure 4.97 Specimen W1: Connection during Testing

(a) -0.015 rad (2nd Cycle)

(b) -0.02 rad (2nd Cycle)

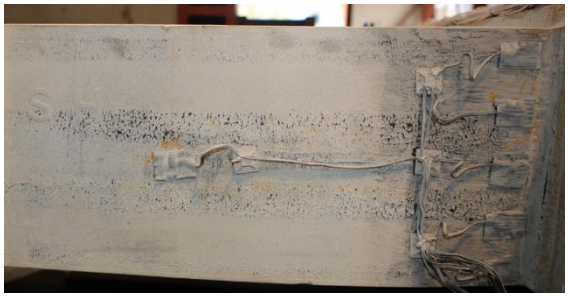

(c) -0.03 rad (2nd Cycle)

(d) -0.04 rad (1st Cycle)

Figure 4.98 Specimen W1: East Beam Bottom Flange Yielding

(a) -0.015 rad (2nd Cycle)

(b) -0.02 rad (2nd Cycle)

(c) -0.03 rad (2nd Cycle)

(d) -0.04 rad (1st Cycle)

Figure 4.99 Specimen W1: West Beam Bottom Flange Yielding

(a) -0.03 rad (2nd Cycle)

(b) -0.04 rad (1st Cycle)

Figure 4.100 Specimen W1: East Beam Bottom Flange Local Buckling

(a) Overview

(b) Yielding

Figure 4.101 Specimen W1: Panel Zone Yielding at +0.03 rad (2nd Cycle)

(a) West Beam Top Flange at +0.04 rad (1st Cycle)

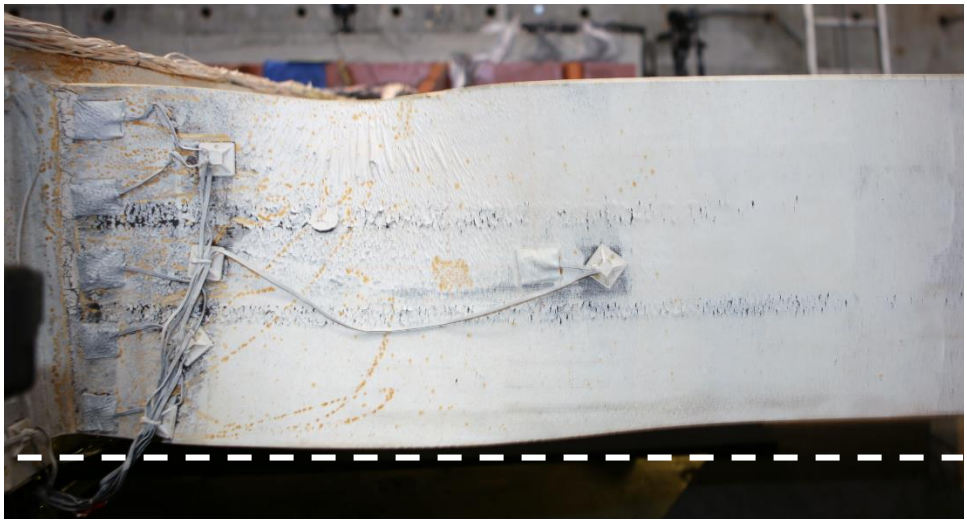

(a) East Beam Top Flange at +0.04 rad (2nd Cycle)

Figure 4.102 Specimen W1: Lateral-Torsional Buckling

(a) Overview

(b) Fracture

Figure 4.103 Specimen W1: East Beam Top Flange CJP Weld Fracture at -0.04 rad (2nd Cycle)

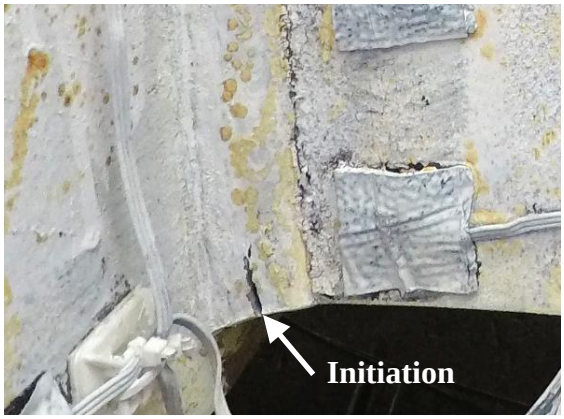

(a) Fracture Initiation

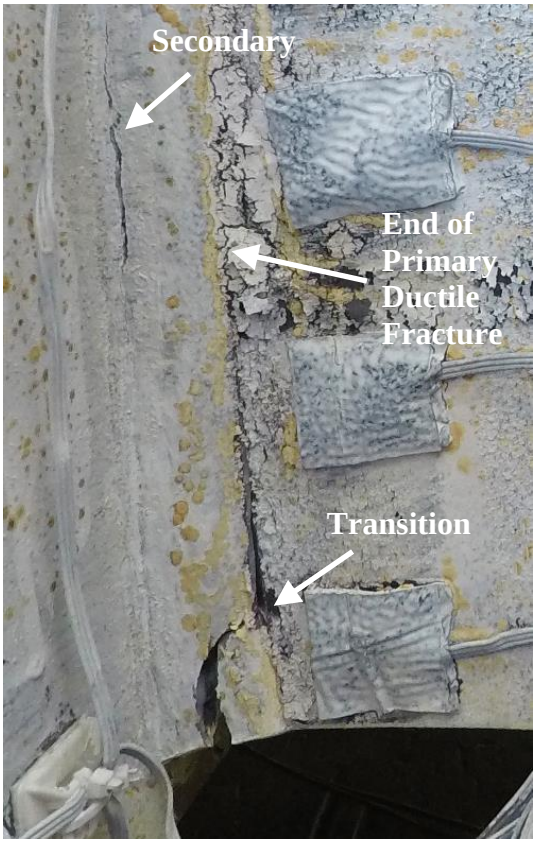

(b) during Propagation

(c) after Fracture

Figure 4.104 Specimen W1: East Beam Top Flange CJP Weld Fracture Progression

Figure 4.105 Specimen W1: East Beam Top Flange CJP Weld Fracture Surface

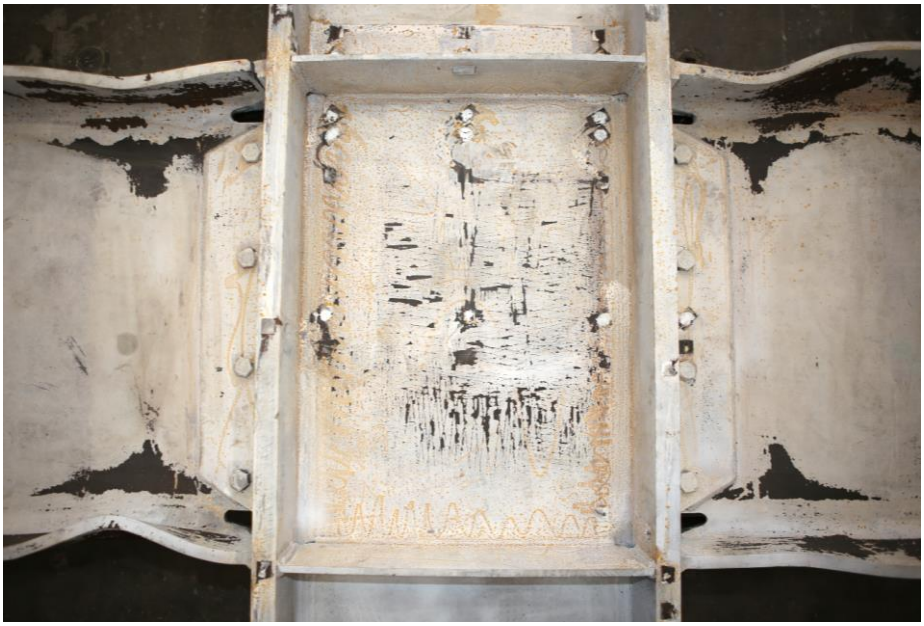

Figure 4.106 Specimen W1: Connection at End of Test

(a) Underside of Continuity Plate

(b) Edge of Continuity Plate

Figure 4.107 Specimen W1: Top Flange Continuity Plate (End of Test)

(a) Topside of Continuity Plate

(b) Underside of Continuity Plate

Figure 4.108 Specimen W1: Bottom Flange Continuity Plate (End of Test)

(a) Top Flange Continuity Plate

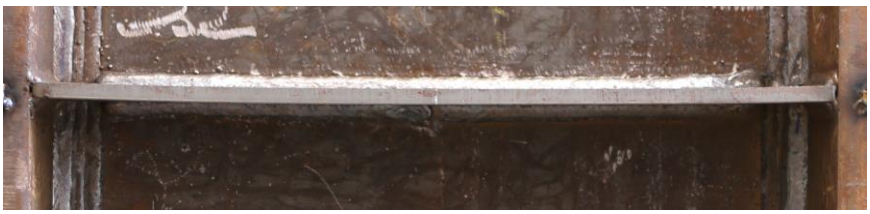

(b) Bottom Flange Continuity Plate

Figure 4.109 Specimen W1: Underside Continuity Plates (End of Test)

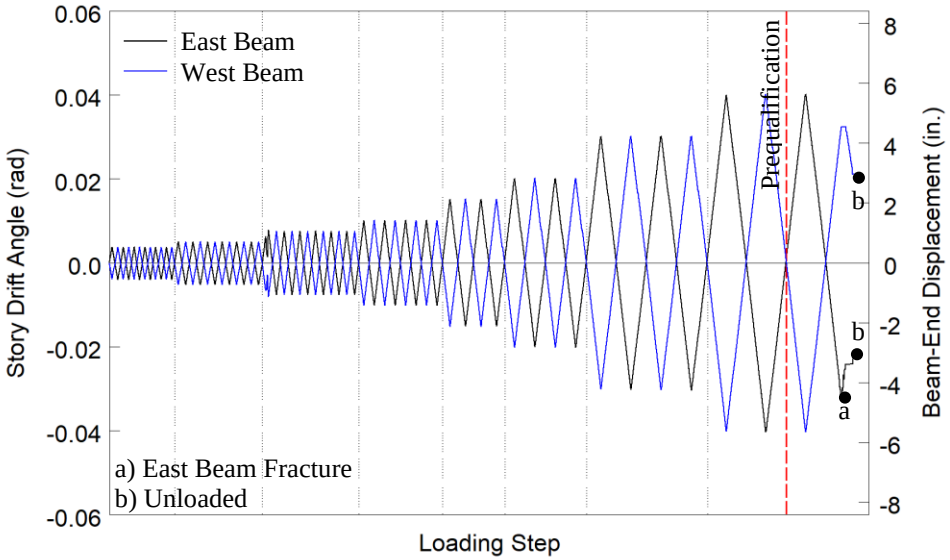

Figure 4.110 Specimen W1: Recorded Loading Sequence

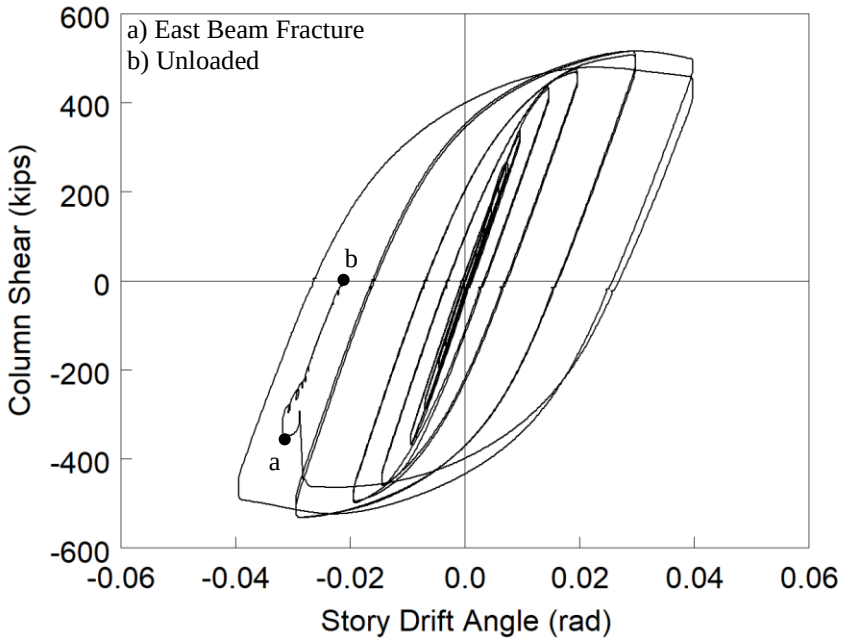

Figure 4.111 Specimen W1: Column Shear versus Story Drift Angle

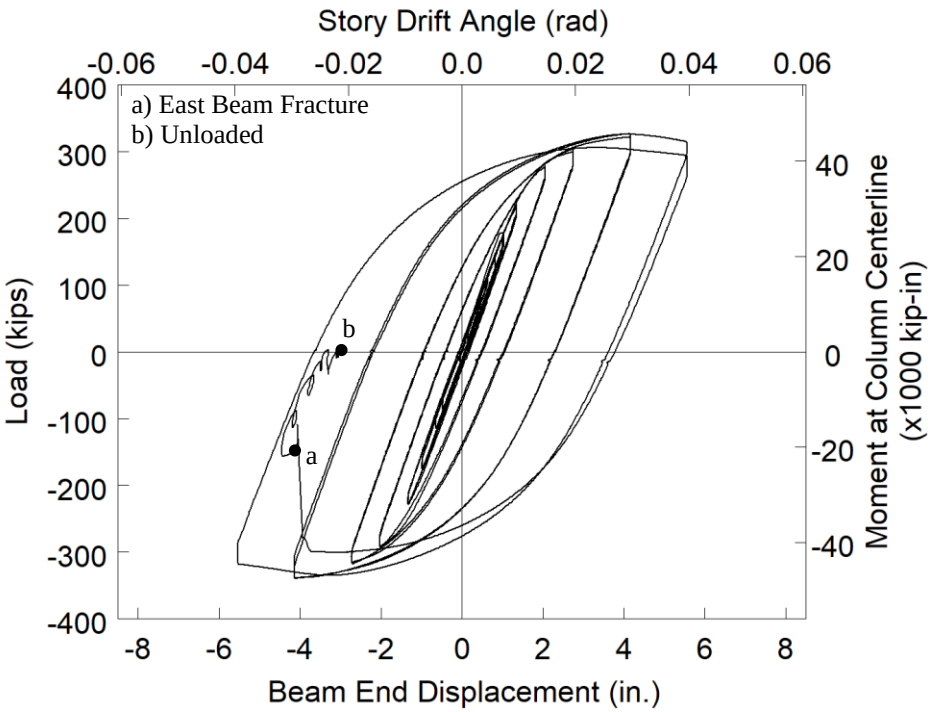

(a) East Beam

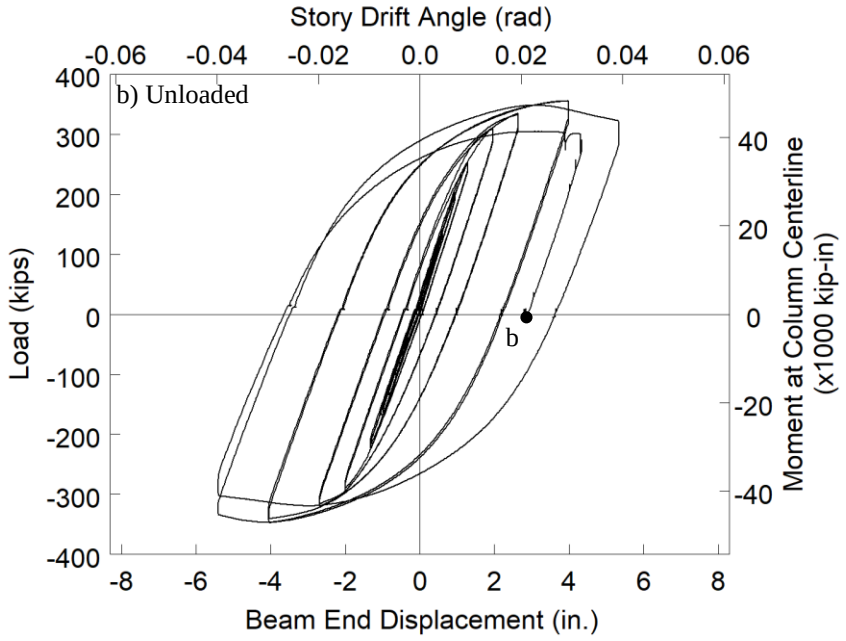

(b) West Beam

Figure 4.112 Specimen W1: Applied Load versus Beam End Displacement Response

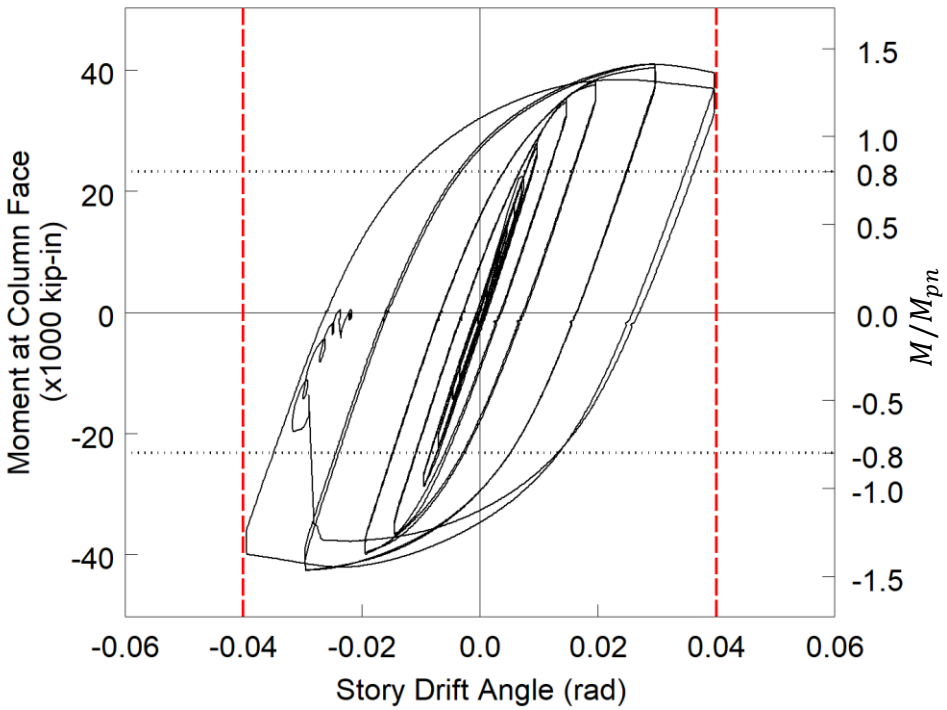

(a) East Beam

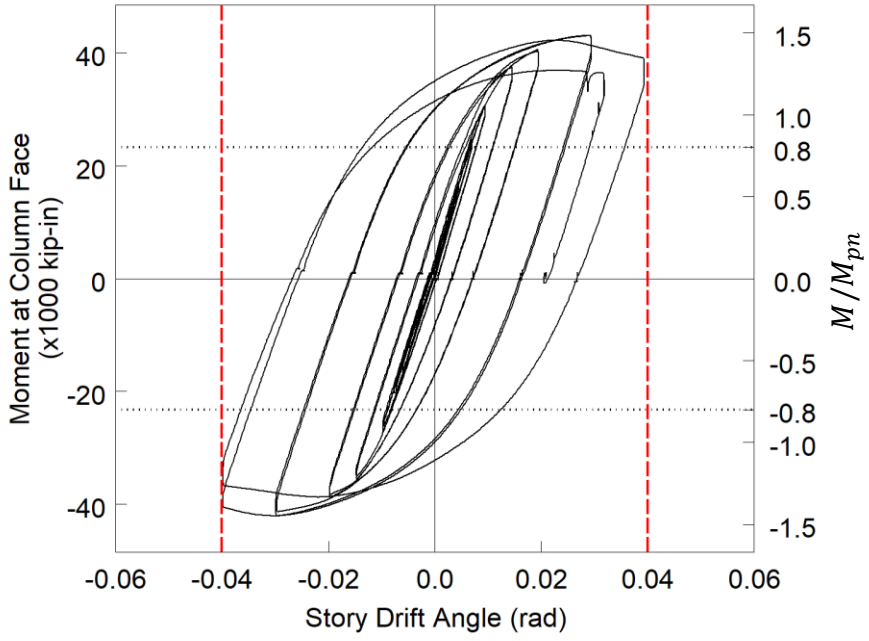

(b) West Beam

Figure 4.113 Specimen W1: Moment at Column Face versus Story Drift Response

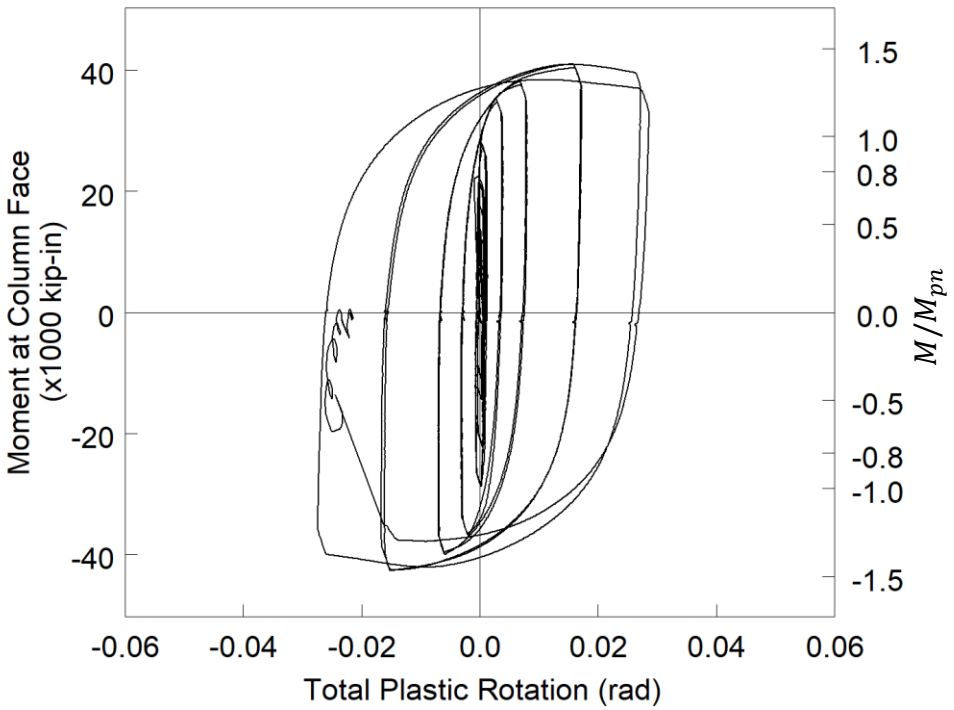

(a) East Beam

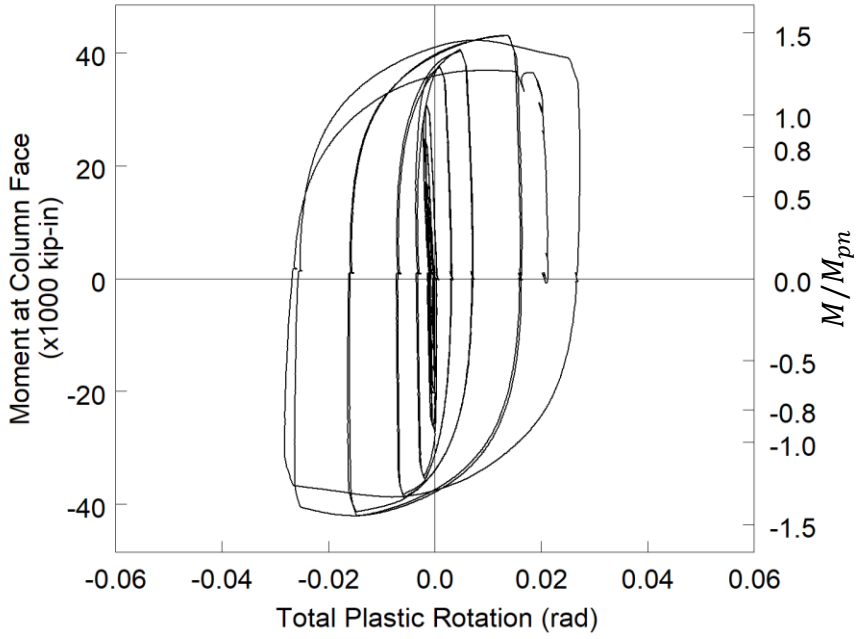

(b) West Beam

Figure 4.114 Specimen W1: Moment at Column Face versus Plastic Rotation Response

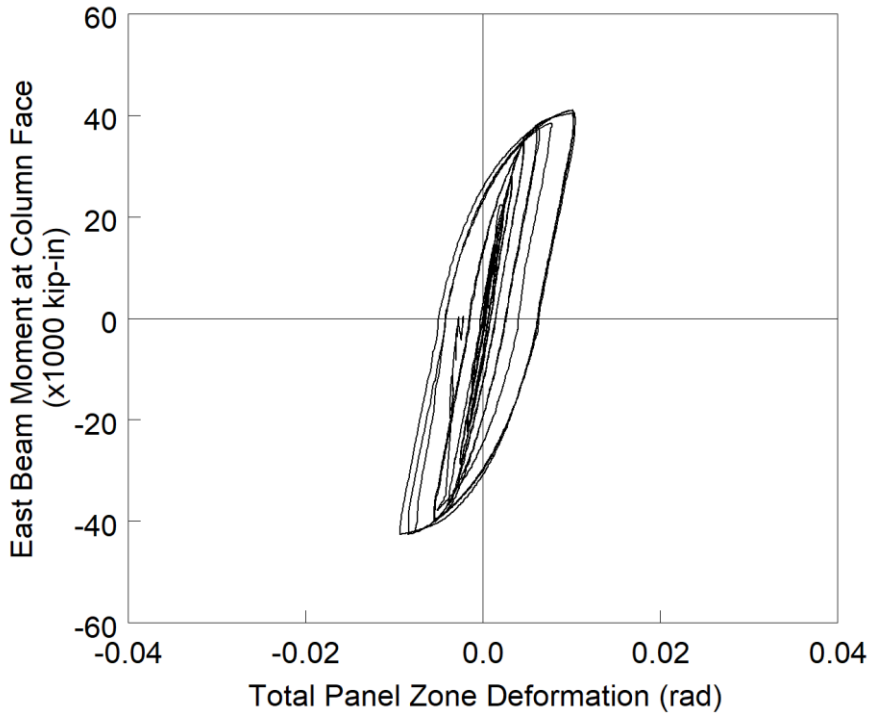

Figure 4.115 Specimen W1: Panel Zone Shear Deformation

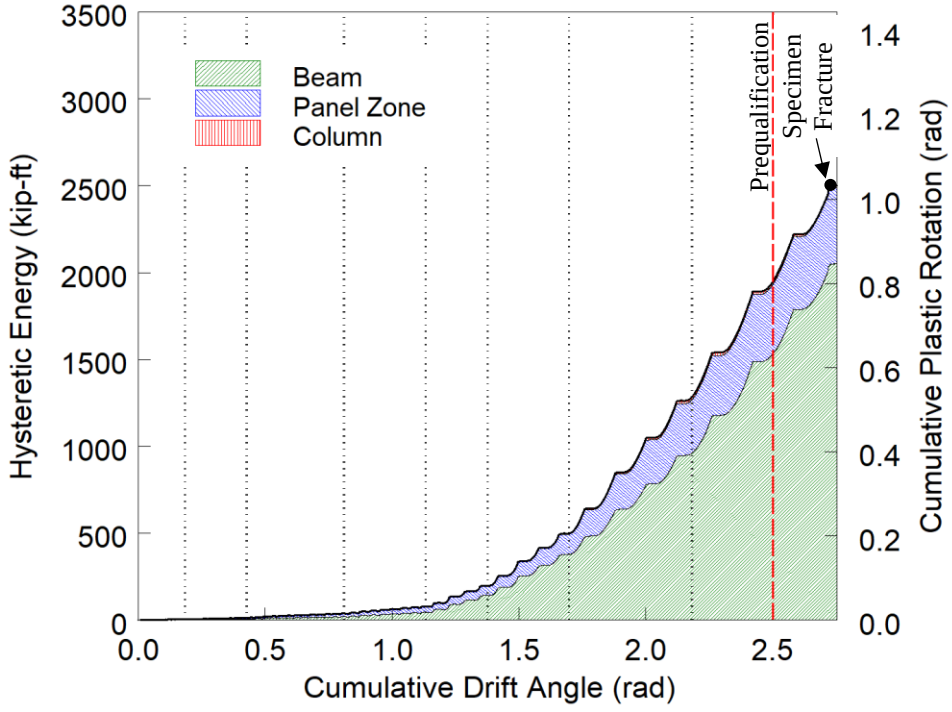

Figure 4.116 Specimen W1: Energy Dissipation

4.9. Specimen W2

4.9.1. General

Specimen W2 was designed to investigate use of the plastic methodology to design continuity plates. The continuity plate thickness was chosen to match the minimum thickness requirement of AISC 341, for which the plastic methodology results in an undersized continuity plate with a DCR of 1.43. Continuity plate double-sided fillet welds were sized such that $w = 0.75t_{cp}$. A pair of doubler plates stiffen the web of the column for panel zone yielding—these plates were extended 6 in. above and below the beam flange elevations. The doubler plate vertical welds use a PJP groove weld, and no horizontal welds were used in accordance with the current Provisions. Specimen W2 failed by a fracture of the east top and west bottom beam flange CJP weld during the second cycle of 0.06 rad drift. Figure 4.117 shows the specimen before testing.

4.9.2. Observed Performance

The observed response for Specimen W2 is described below.

- Figure 4.118 shows the connection during testing. The specimen met the AISC acceptance criteria by completing one complete cycle at 0.04 rad drift while the flexural strength at either column face did not degrade below 80% of the beam nominal flexural strength. Beam flange and web local bucking initiated at 0.03 rad drift and progressed throughout testing.
- Figure 4.119 and Figure 4.120 shows the bottom flange yielding and buckling of the east and west beams. The yielding of the flanges initiated during the 0.0075 rad drift cycles. It was observed that significant lateral-torsional buckling initiates at 0.04 rad drift and progresses in the later drift cycles.

- Figure 4.121 shows the progression of flange local bucking that developed in the east beam top flange. The local buckling develops in the flange of the beam in compression during that excursion and then is pulled relatively straight during the tension excursions.
- Figure 4.122 shows the initiation of a weld fracture during the second cycle of 0.03 rad drift. The fracture originates at the fusion face of the CJP weld and backing bar on the flange bevel side. Figure 4.123 shows the progression of this tear during the 0.04 rad and 0.05 rad drift cycles. At 0.05 rad drift cycles a weld tear on the top side of the west beam bottom flange CJP weld was observed (see Figure 4.124). A similar fracture was observed in the east beam bottom flange CJP weld at 0.06 rad drift (see Figure 4.125).
- Figure 4.126 shows the severe lateral-torsional buckling, flange local bucking, and web local buckling of the east beam during the 0.06 rad drift cycles. The west beam has a similar profile with flanges arching up. Significant lateral bracing forces restraining the beams result in localized yielding at the restraint points.
- At -0.018 rad during the negative excursion of the east beam to 0.06 rad drift (2^{nd} Cycle) the east beam top flange partially fractured (see Figure 4.127). This fracture extends from the top edge of the beam flange to about the centerline. The fracture initiated at the CJP weld root and deviated into the beam flange after traversing the CJP weld bevel for several inches. This weld fracture was accompanied by a tear at the far radius of the weld access hole (see Figure 4.128). Shortly after resuming load the west beam bottom flange experienced a similar fracture, propagating through 80% of the beam flange (see Figure 4.129).

- Figure 4.130 shows the connection after testing. Minor panel zone yielding was observed in the doubler plate after testing (see Figure 4.131). This picture also demonstrates that no continuity plate yielding was evident.
- No damage to the continuity plate fillet welds was observed during the testing or after test visual inspection (see Figure 4.132).

4.9.3. Recorded Response

- Figure 4.133 shows the recorded displacement response of the beam tip measured with transducer L1 for the east beam and L2 for the west beam. The response from the east and west beams are shown in black and blue, respectively. The east beam top flange partially fractured at 0.018 rad during the second negative excursion to 0.06 rad drift. The west beam bottom flange fractured slightly past neutral during the positive excursion to 0.06 rad drift. Figure 4.134 shows the column shear versus the applied story drift response.
- Figure 4.135 shows the load-displacement response of the beams.
- Figure 4.136 shows the computed moment at the column face (M_f) versus the story drift angle. Two horizontal axes at 80% of the nominal plastic moment (M_{pn}) of the beam section are also added. In addition, two vertical axes at ±0.04 rad story drift show the drift required for SMF connections per AISC 341. It is observed that the beams developed about 1.4 times its nominal plastic bending moment. If the moment is computed at the plastic hinge location and compared to the expected plastic moment, then the peak connection strength factor (C_{pr}) is 1.23 and 1.23 for the east and west beams respectively.
- Figure 4.137 shows the plastic response of the specimen. The plastic response is computed using the procedure outlined in Section 3.7. The computed elastic stiffness of the specimen was determined to be 144.8 kips/in.

- Figure 4.138 shows minor hysteretic behavior in the panel zone.
- Figure 4.139 shows the dissipated energy of Specimen W2. Dotted vertical lines on the graph demonstrate the completion of each group of cycles, and the dashed red vertical line shows the completion of the first cycle of 0.04 rad in the AISC loading. It is observed that the completion of the first drift cycle of 0.04 rad (the requirement for SMF connections per AISC 341) occurs after 1,755 kip-ft of energy has been dissipated. The connection did not degrade below $0.8M_{pn}$ until fracture of the east beam top flange occurred and 4,000 kip-ft of energy had been dissipated. Therefore only 44% of the energy dissipation capacity was utilized after the completion of the SMF requirement. It is observed that nearly all (96%) of the energy dissipation capacity occurred in the beam.

(a) Overview

(b) Connection Region

Figure 4.117 Specimen W2: Connection before Testing

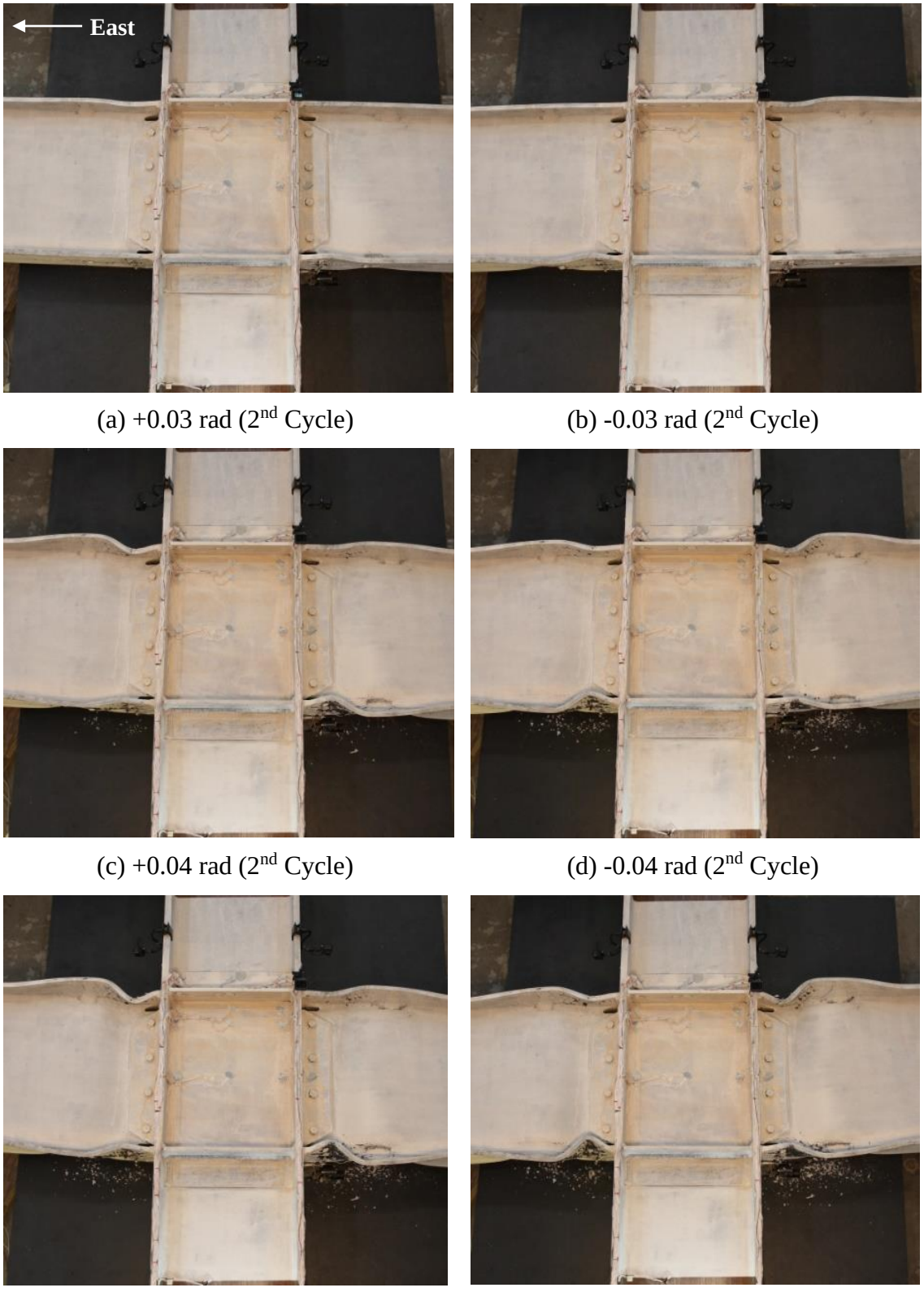

(a) +0.03 rad (2nd Cycle) (b) -0.03 rad (2nd Cycle)

(c) +0.04 rad (2nd Cycle) (d) -0.04 rad (2nd Cycle)

(e) +0.05 rad (1st Cycle) (f) -0.05 rad (1st Cycle)

Figure 4.118 Specimen W2: Connection during Testing

(a) -0.02 rad (2nd Cycle)

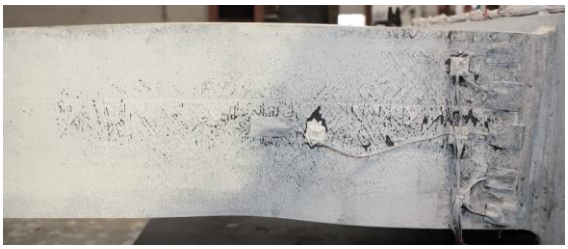

(b) -0.03 rad (2nd Cycle)

(c) +0.04 rad (2nd Cycle)

(d) -0.05 rad (2nd Cycle)

Figure 4.119 Specimen W2: East Beam Bottom Flange Yielding

(a) -0.02 rad (2nd Cycle)

(b) -0.03 rad (2nd Cycle)

(c) +0.04 rad (2nd Cycle)

(d) -0.05 rad (2nd Cycle)

Figure 4.120 Specimen W2: West Beam Bottom Flange Yielding

(a) +0.03 rad (2nd Cycle)

(b) +0.04 rad (2nd Cycle)

Figure 4.121 Specimen W2: East Beam Top Flange Local Buckling

(a) Overview

(b) Weld Fracture

Figure 4.122 Specimen W2: East Beam Top Flange CJP Weld Tear at -0.03 rad (2nd Cycle)

(a) -0.04 rad (2nd Cycle)

(b) -0.05 rad (2nd Cycle)

Figure 4.123 Specimen W2: East Beam Top Flange CJP Weld Tear Progression

(a) Overview

(b) Weld Fracture

Figure 4.124 Specimen W2: West Beam Bottom Flange CJP Weld Fracture at: -0.05 rad (2nd Cycle)

(a) Overview

(b) Weld Fracture

Figure 4.125 Specimen W2: East Beam Bottom Flange CJP Weld Fracture at: +0.06 rad (1st Cycle)

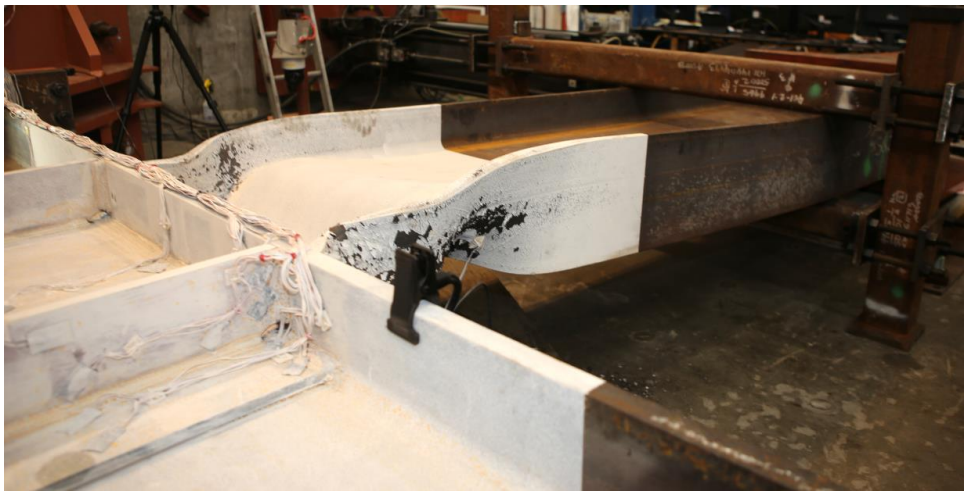

Figure 4.126 Specimen W2: East Beam Bottom Flange Lateral-Torsional Bucking at: -0.06 rad (1st Cycle)

Figure 4.127 Specimen W2: East Beam Top Flange Partial Fracture during Excursion to -0.06 rad (2nd Cycle)

(a) Overview (b) Weld Fracture

Figure 4.128 Specimen W2: East Beam Top Flange Weld Access Hole Tear at -0.06 rad

Figure 4.129 Specimen W2: West Beam Bottom Flange Fracture during Excursion to -0.06 rad (2nd Cycle)

Figure 4.130 Specimen W2: Connection at End of Test

Figure 4.131 Specimen W2: Panel Zone (End of Test)

(a) East Beam Top Flange

(b) West Beam Top Flange

(c) East Beam Bottom Flange

(d) West Beam Bottom Flange

Figure 4.132 Specimen W2: Continuity Plate Fillet Welds (End of Test)

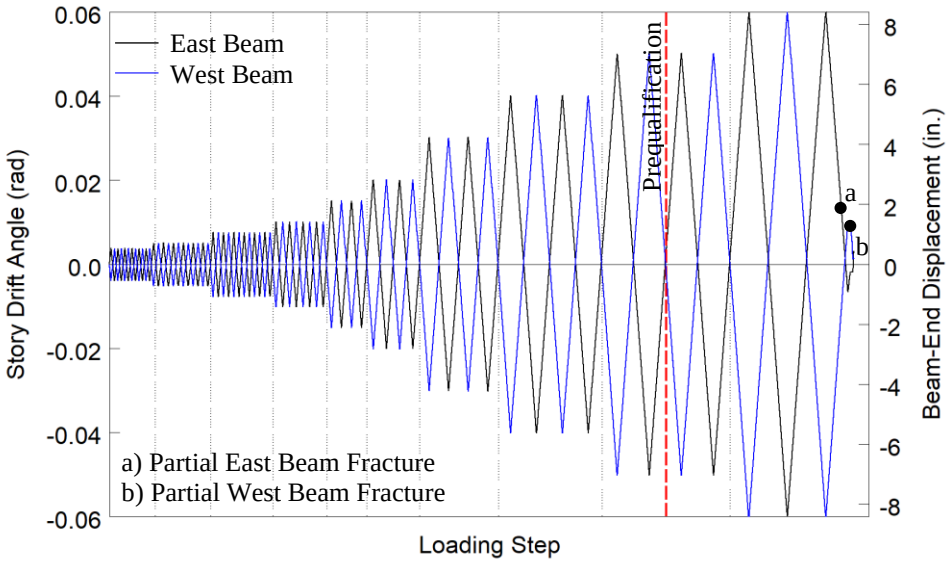

Figure 4.133 Specimen W2: Recorded Loading Sequence

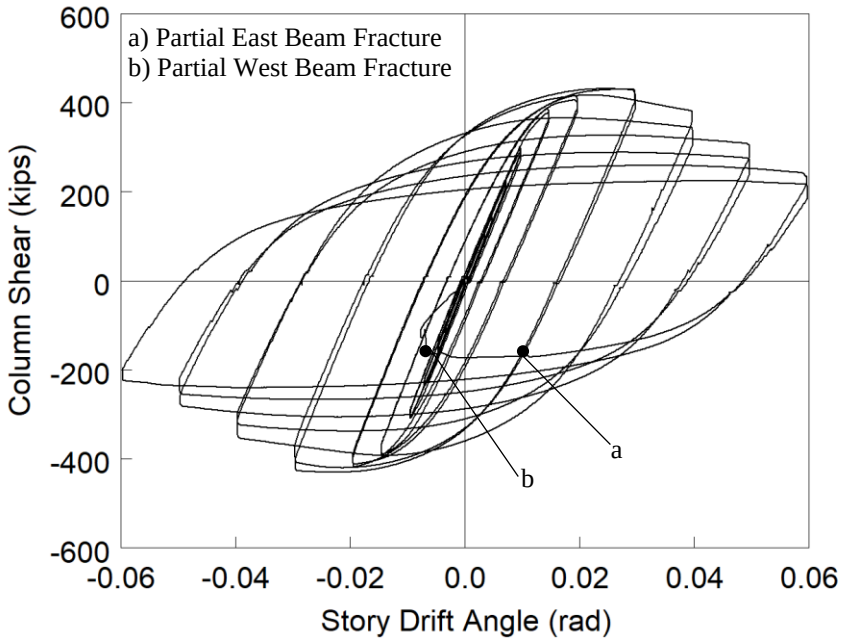

Figure 4.134 Specimen W2: Column Shear versus Story Drift Angle

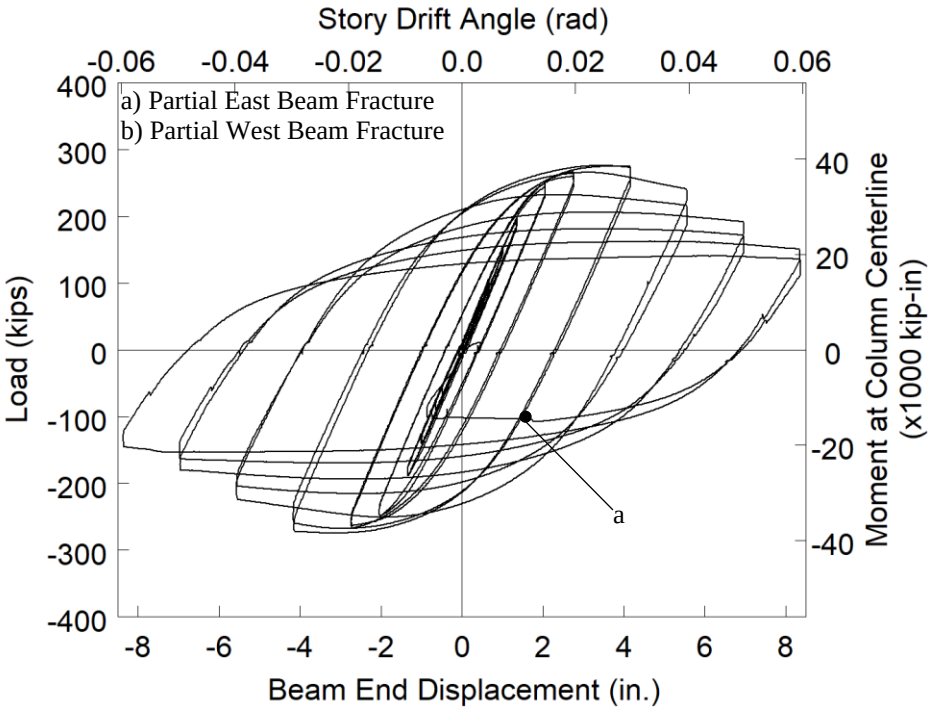

(a) East Beam

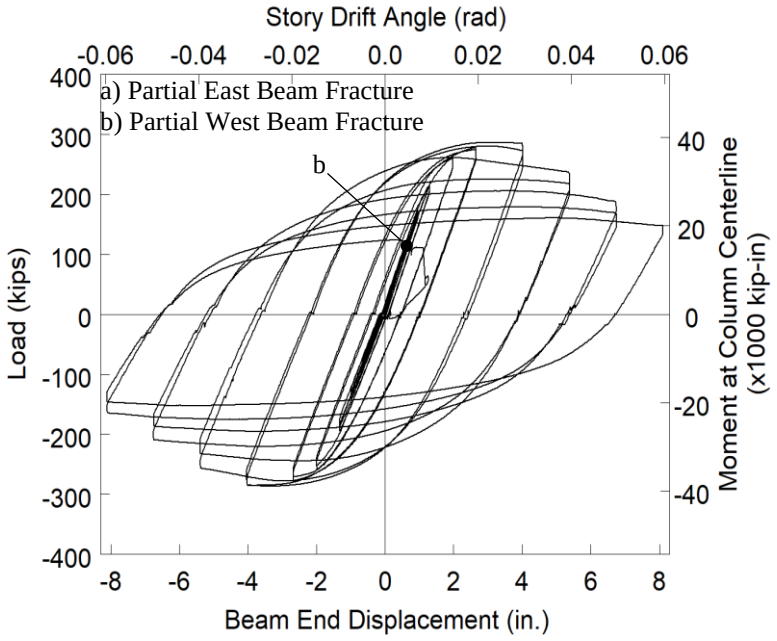

(b) West Beam

Figure 4.135 Specimen W2: Applied Load versus Beam End Displacement Response

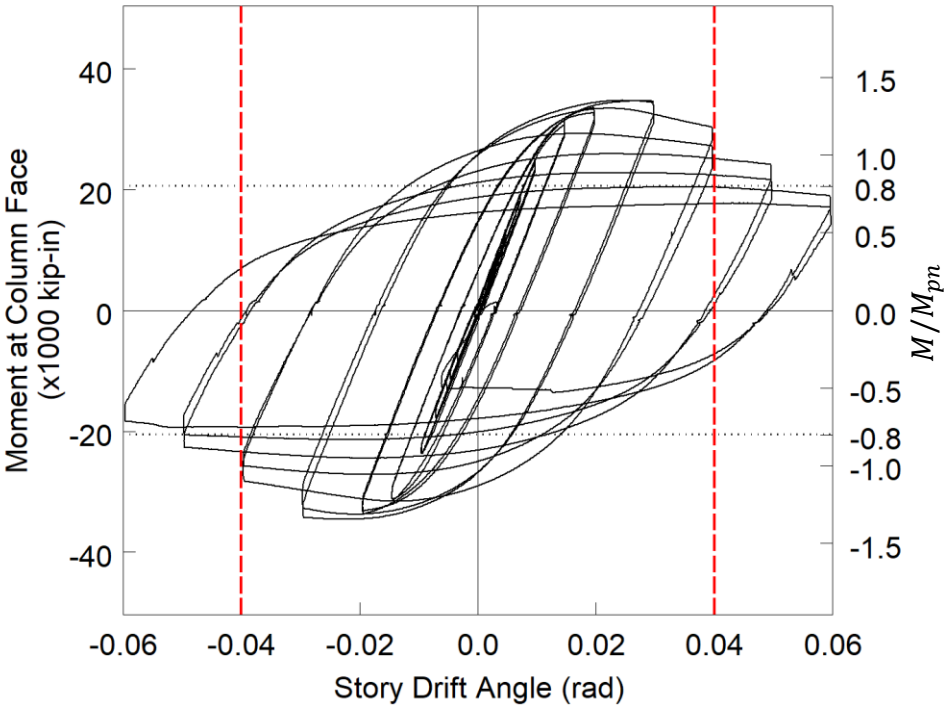

(a) East Beam

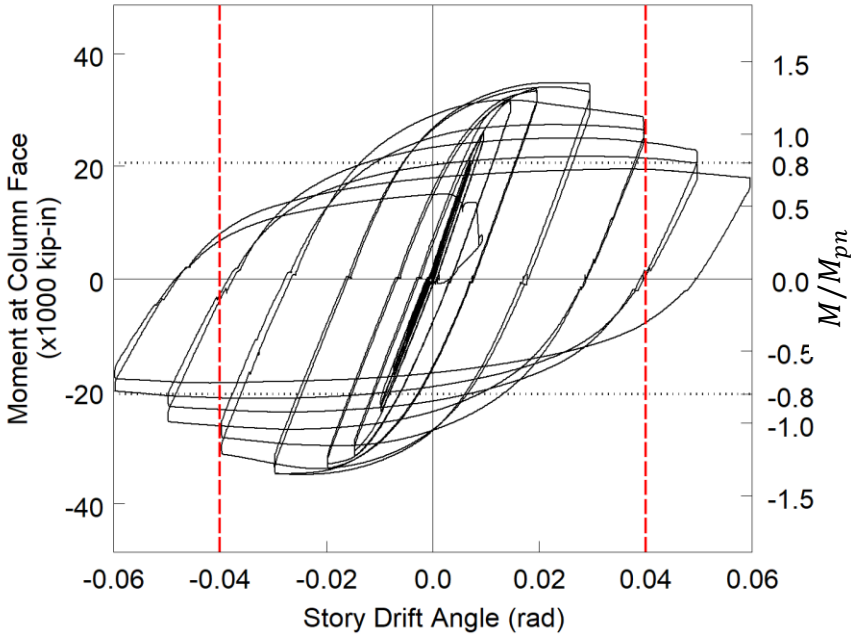

(b) West Beam

Figure 4.136 Specimen W2: Moment at Column Face versus Story Drift Response

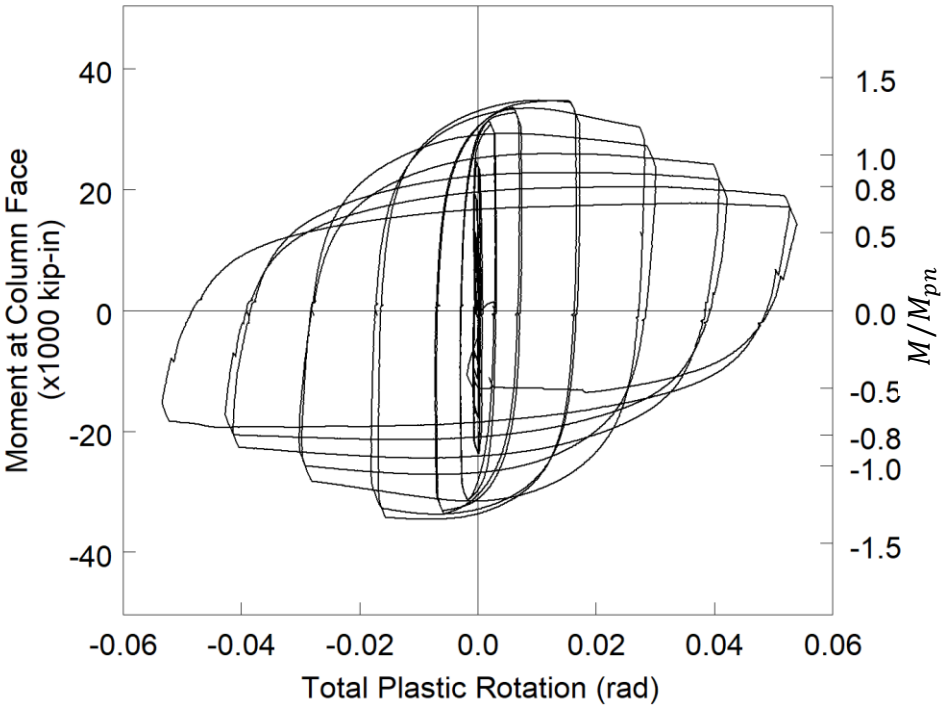

(a) East Beam

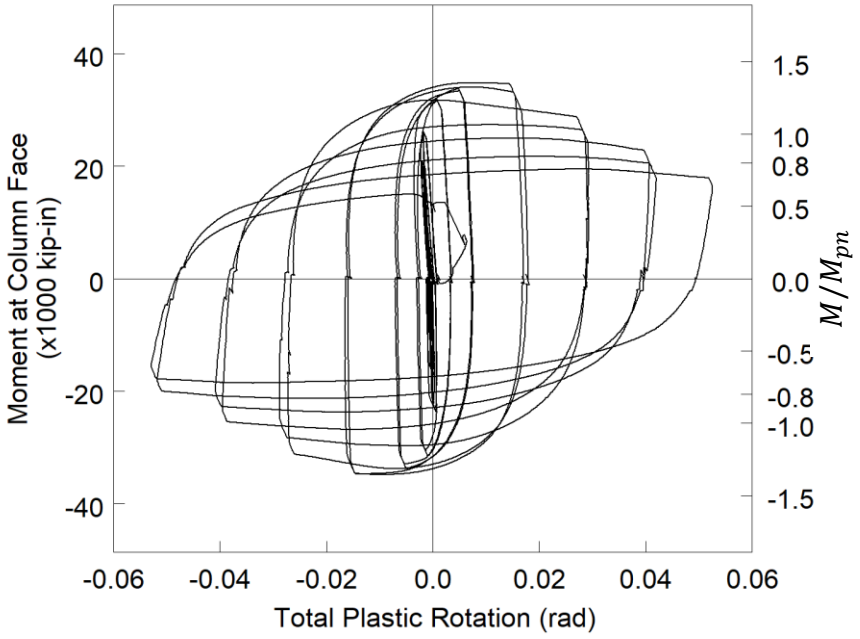

(b) West Beam

Figure 4.137 Specimen W2: Moment at Column Face versus Plastic Rotation Response

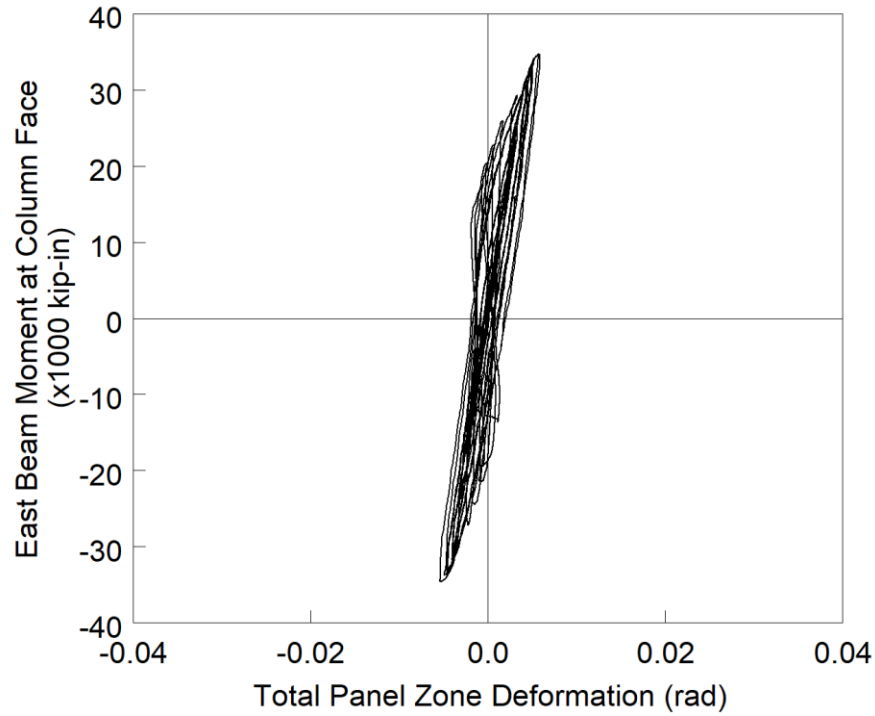

Figure 4.138 Specimen W2: Panel Zone Shear Deformation

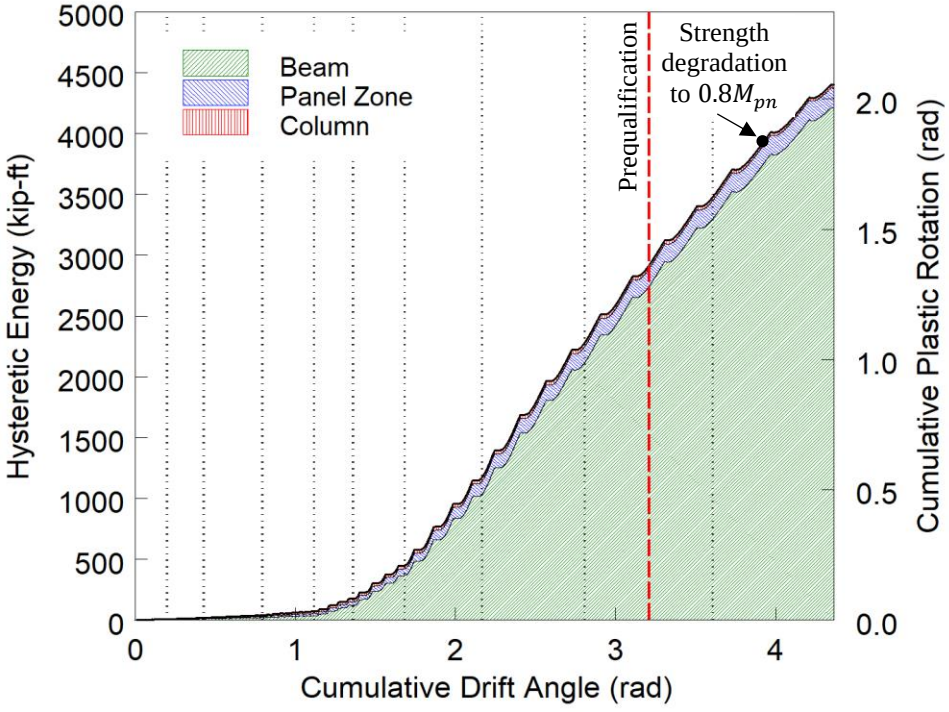

Figure 4.139 Specimen W2: Energy Dissipation

4.10. Specimen W3

4.10.1. General

Specimen W3 was designed to investigate use of the plastic methodology to design continuity plates. The resulting continuity plates were thinner than the current AISC 341 Provisions. Continuity plate double-sided fillet welds were sized such that $w = 0.75t_{cp}$. A pair of doubler plates stiffen the web of the column for panel zone yielding—these plates were extended 6 in. above and below the beam flange elevations. The doubler plates were designed to result in a weak panel zone, with a resulting DCR of 1.07; additionally, the stability criteria of the doubler plates were violated. The doubler plate vertical welds use a fillet weld sized to develop the shear strength of the plate, and no horizontal welds were used in accordance with the current Provisions. Specimen W3 failed by a fracture of the east beam top flange CJP weld during the second cycle of 0.06 rad drift. Figure 4.140 shows the specimen before testing.

4.10.2. Observed Performance

The observed response for Specimen W3 is described below.

- Figure 4.141 shows the connection during testing. The specimen met the AISC acceptance criteria by completing one complete cycle at 0.04 rad drift while the flexural strength at either column face did not degrade below 80% of the beam nominal flexural strength. Beam flange and web local buckling initiated at 0.03 rad drift and progressed throughout testing.
- Figure 4.142and Figure 4.143show the east beam bottom flange and west beam bottom flange during testing. The gradual progression of yielding, flange local buckling, and lateral-torsional buckling is observed. The progression of flange local buckling between the second cycle of 0.03 rad and the first cycle of 0.04 rad is shown in Figure 4.144.

- Figure 4.145 shows the initiation of tearing in the weld access holes. All four weld access holes show a similar behavior.
- Severe web buckling develops in both beams during the 0.05 rad drift cycles (see Figure 4.146). Figure 4.147 shows a similar severity of flange local buckling during the 0.05 rad drift cycles.
- Figure 4.148 shows the gradual progression of tearing in the east beam top flange CJP weld. The tear initiated at the CJP weld root during the second cycle of 0.04 rad drift. A similar tear was observed in the west beam top flange CJP weld (not pictured). During the first negative excursion to 0.06 rad drift the east beam top flange fractured through 60% of the width of the flange. The tear of the top flange was accompanied with a 5-in. tear of the beam web extending outward from the radius of the weld access hole (see Figure 4.149).
- Although the root of the CJP weld started to tear during earlier cycles the propagation of the tear to the top surface of the CJP weld occurred when the beam was under global compression during the first positive excursion of 0.06 rad drift (see Figure 4.150). This occurs due to the high local curvature of the flange local buckling. During the first negative excursion of 0.06 rad drift the fracture propagates to 60% of the beam flange width (see Figure 4.151). During the second negative excursion of 0.06 rad drift the east beam top flange fractures completely.
- Figure 4.152 shows the connection at the end of testing.
- Figure 4.153 shows a partial fracture of the west beam top flange at the end of testing. Also observed in this photo is minor column yielding above the beam flange.
- No yielding or damage to the continuity plate fillet welds was observed during testing (see Figure 4.154 and Figure 4.155). A detailed view of four of the continuity plate fillet welds

is shown in Figure 4.156. Similarly, no damage was observed to the doubler plate fillet weld.

4.10.3. Recorded Response

- Figure 4.157 shows the recorded displacement response of the beam tip measured with transducer L1 for the east beam and L2 for the west beam. The response from the east and west beams are shown in black and blue, respectively. The east beam top flange partially fractured at -0.038 rad during the first negative excursion to 0.06 rad drift. The remainder of the east beam top flange fractured during at 0.01 rad during the second negative excursion of 0.06 rad drift.
- Figure 4.159 shows the load-displacement response of the beams.
- Figure 4.160 shows the computed moment at the column face (M_f) versus the story drift angle. Two horizontal axes at 80% of the nominal plastic moment (M_{pn}) of the beam section are also added. In addition, two vertical axes at ±0.04 rad story drift show the drift required for SMF connections per AISC 341. It is observed that the beams developed about 1.4 times its nominal plastic bending moment. If the moment is computed at the plastic hinge location and compared to the expected plastic moment, then the peak connection strength factor (C_{pr}) is 1.18 and 1.20 for the east and west beams respectively.
- Figure 4.161 shows the plastic response of the specimen. The plastic response is computed using the procedure outlined in Section 3.7. The computed elastic stiffness of the specimen was determined to be 100.8 kips/in.
- Figure 4.162 shows minor hysteretic behavior in the panel zone.
- Figure 4.163 shows the dissipated energy of Specimen W3. Dotted vertical lines on the graph demonstrate the completion of each group of cycles, and the dashed red vertical line

shows the completion of the first cycle of 0.04 rad in the AISC loading. It is observed that the completion of the first drift cycle of 0.04 rad (the requirement for SMF connections per AISC 341) occurs after 1,255 kip-ft of energy has been dissipated. The connection did not degrade below $0.8M_{pn}$ until fracture of the east beam top flange occurred and 2,793 kip-ft of energy had been dissipated. Therefore only 45% of the energy dissipation capacity was utilized after the completion of the SMF requirement. It is observed that nearly all (94%) of the energy dissipation capacity occurred in the beam.

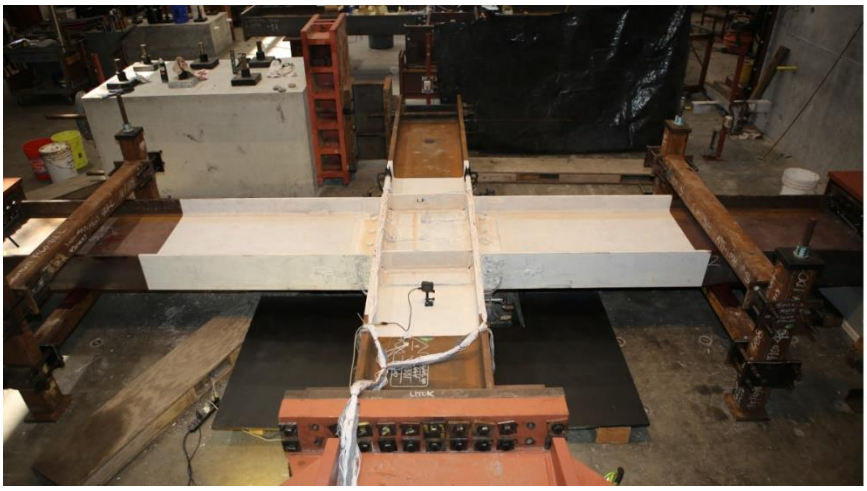

(a) Overview

(b) Connection Region

Figure 4.140 Specimen W3: Connection before Testing

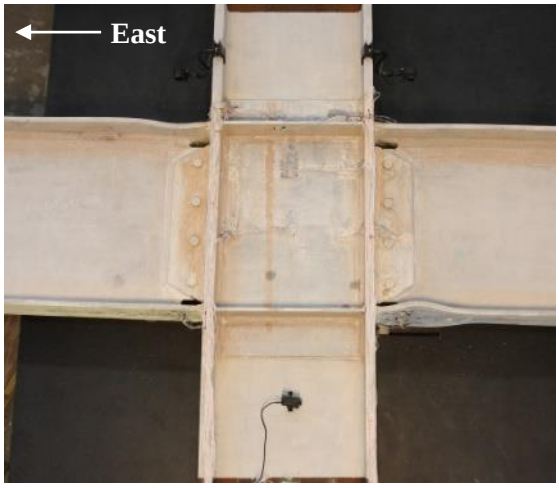

(a) +0.03 rad (2nd Cycle)

(b) -0.03 rad (2nd Cycle)

(c) +0.04 rad (2nd Cycle)

(d) -0.04 rad (2nd Cycle)

(e) +0.05 rad (1st Cycle)

(f) -0.05 rad (1st Cycle)

Figure 4.141 Specimen W3: Connection during Testing

(a) -0.02 rad (2nd Cycle)

(b) -0.03 rad (2nd Cycle)

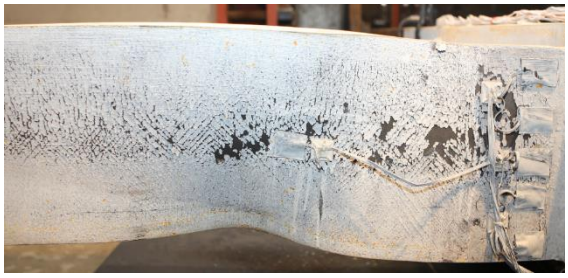

(c) -0.04 rad (2nd Cycle)

(d) -0.05 rad (1st Cycle)

Figure 4.142 Specimen W3: East Beam Bottom Flange Yielding

(a) -0.02 rad (2nd Cycle)

(b) -0.03 rad (2nd Cycle)

(c) -0.04 rad (2nd Cycle)

(d) -0.05 rad (1st Cycle)

Figure 4.143 Specimen W3: West Beam Bottom Flange Yielding

(a) +0.03 rad (2nd Cycle) (b) +0.04 rad (1st Cycle)

Figure 4.144 Specimen W3: East Beam Top Flange Local Buckling

(a) Overview (b) Weld Access Hole

Figure 4.145 Specimen W3: East Beam Top Flange Weld Access Hole Tearing at -0.05 rad (1st Cycle)

Figure 4.146 Specimen W3: Web Local Buckling at +0.05 rad (1st Cycle)

Figure 4.147 Specimen W3: Flange Local Buckling at -0.05 rad (1st Cycle)

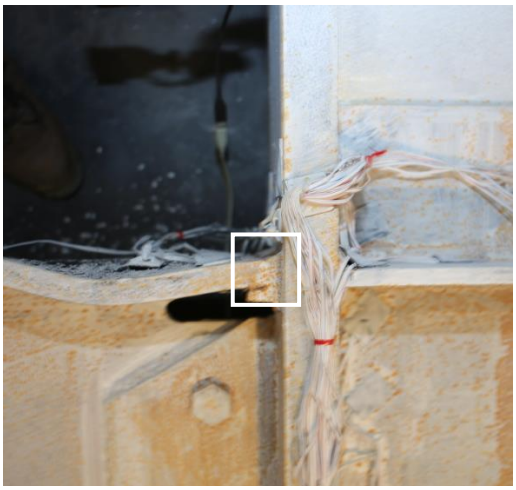

(a) Overview

(b) -0.04 rad (2nd Cycle)

(c) -0.05 rad (1st Cycle)

(d) -0.06 rad (1st Cycle)

Figure 4.148 Specimen W3: East Beam Top Flange CJP Weld Tear Progression

Figure 4.149 Specimen W3: East Beam Top Flange Weld Access Hole Tear

(a) Overview

(b) Weld Tear

Figure 4.150 Specimen W3: East Beam Top Flange Fracture at +0.06 rad (1st Cycle)

(a) -0.06 rad (1st Cycle)

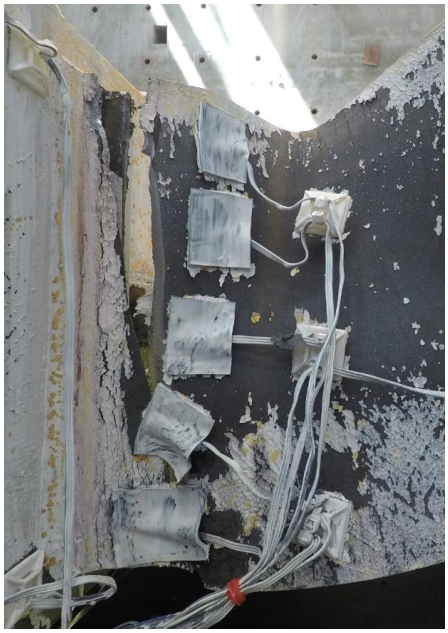

(b) -0.06 rad (2nd Cycle)

Figure 4.151 Specimen W3: East Beam Top Flange Fracture

Figure 4.152 Specimen W3: Connection at End of Test

Figure 4.153 Specimen W3: West Beam Top Flange (End of Test)

(a) Topside

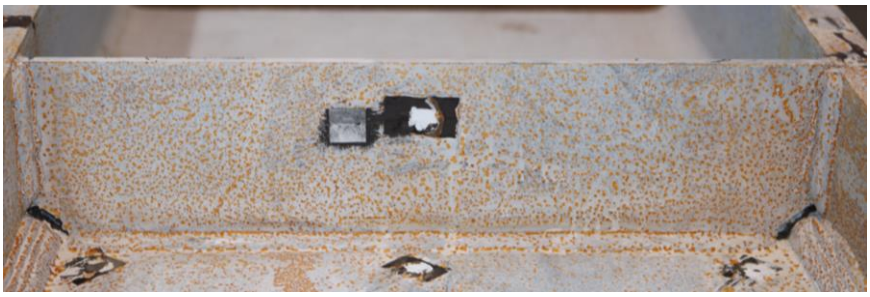

(b) Underside

Figure 4.154 Specimen W3: Top Flange Continuity Plate (End of Test)

(a) Topside

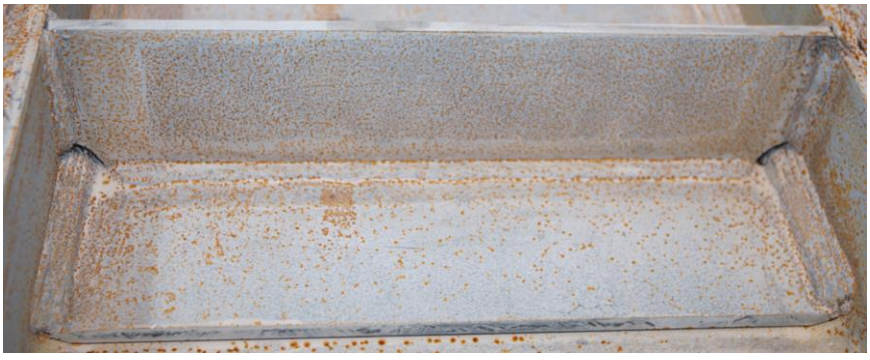

(b) Underside

Figure 4.155 Specimen W3: Bottom Flange Continuity Plate (End of Test)

(a) West Top Flange

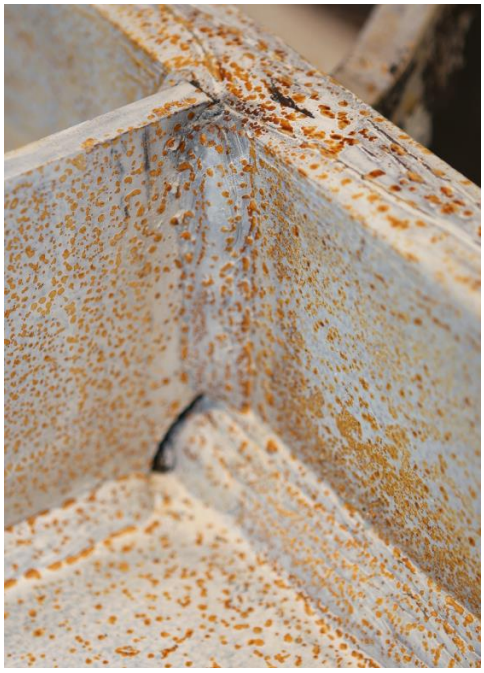

(b) East Top Flange

(c) West Bottom Flange

(d) East Bottom Flange

Figure 4.156 Specimen W3: Continuity Plate Fillet Welds (End of Test)

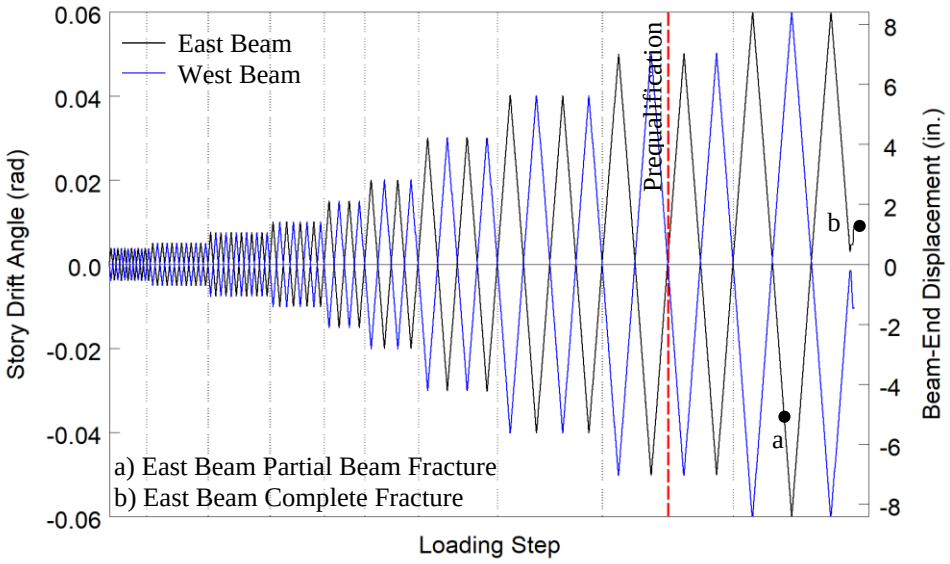

Figure 4.157 Specimen W3: Recorded Loading Sequence

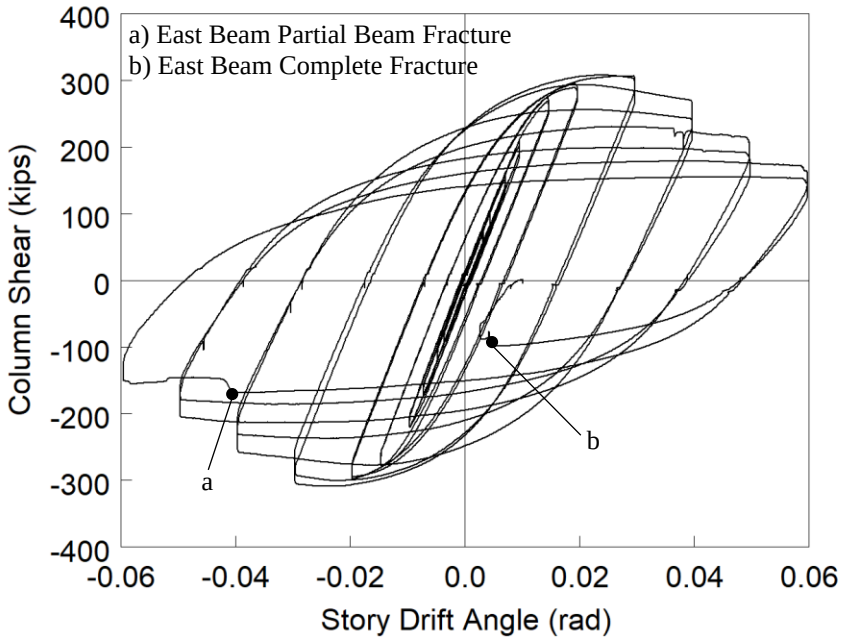

Figure 4.158 Specimen W3: Column Shear versus Story Drift Angle

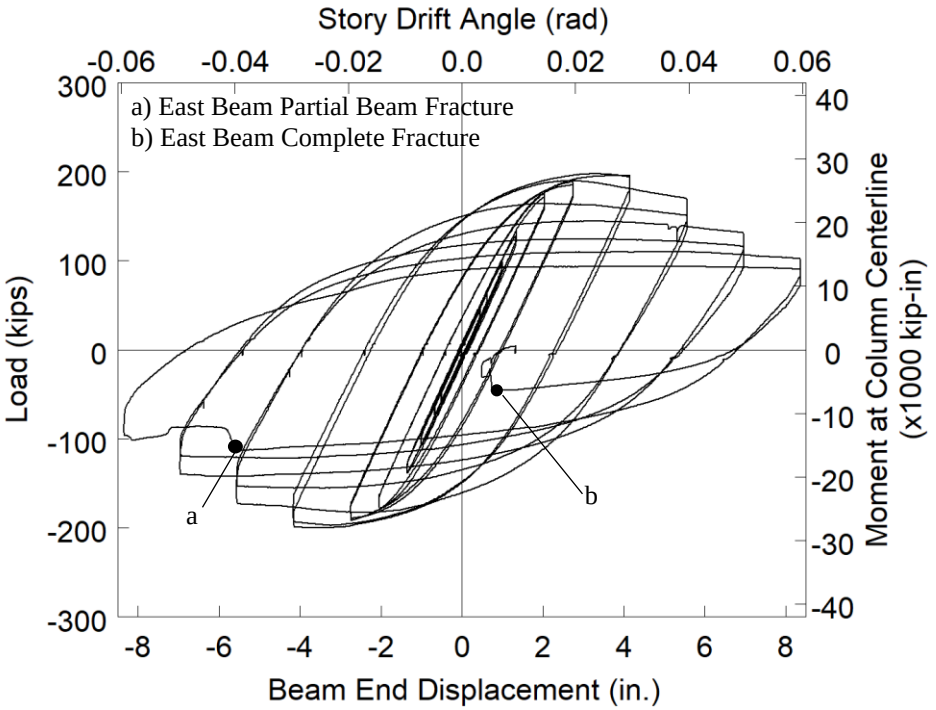

(a) East Beam

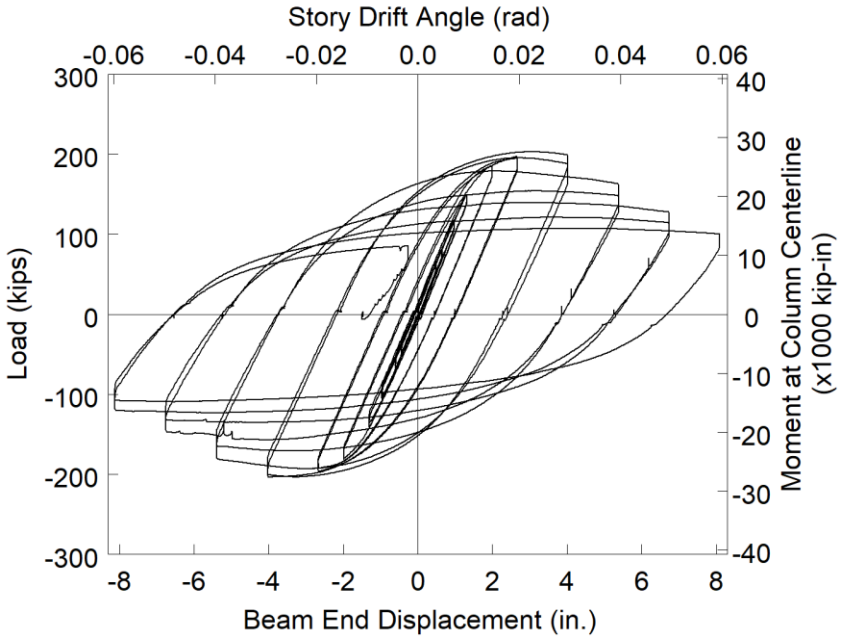

(b) West Beam

Figure 4.159 Specimen W3: Applied Load versus Beam End Displacement Response

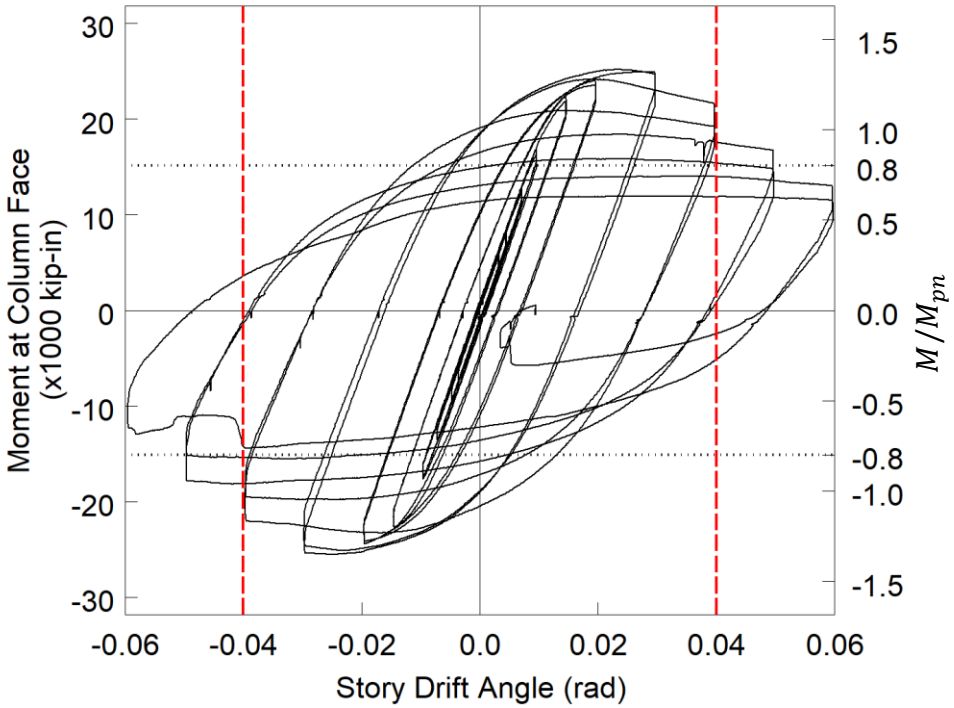

(a) East Beam

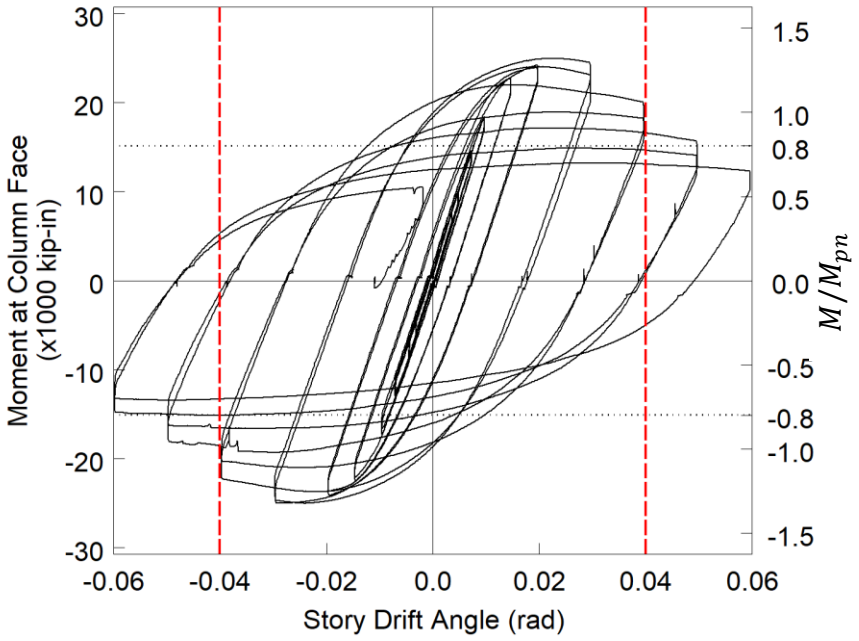

(b) West Beam

Figure 4.160 Specimen W3: Moment at Column Face versus Story Drift Response

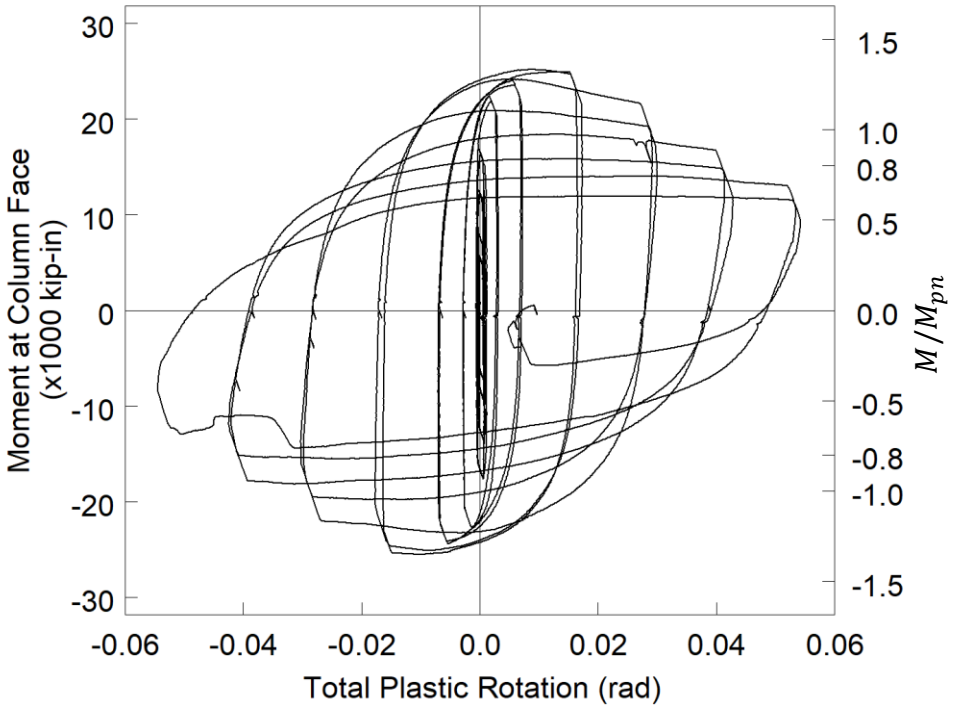

(a) East Beam

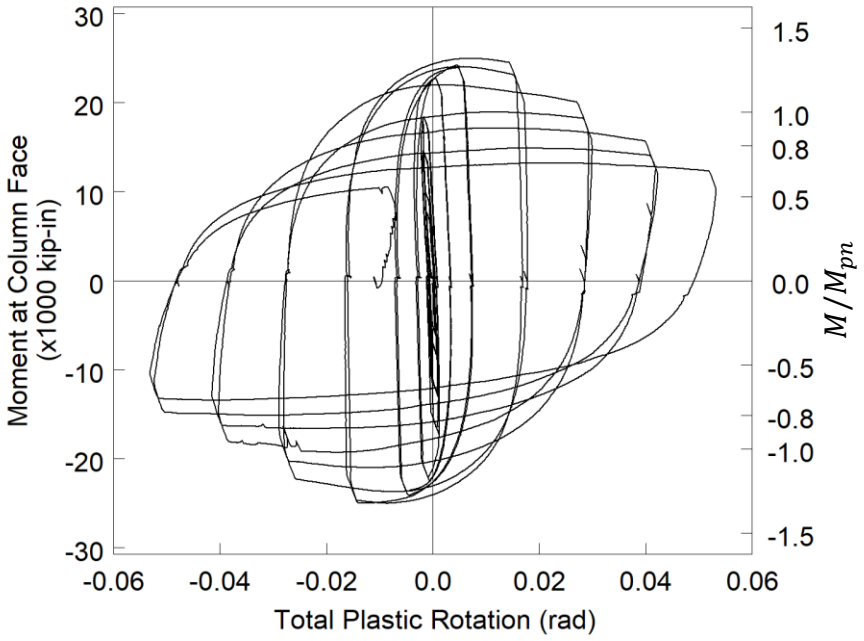

(b) West Beam

Figure 4.161 Specimen W3: Moment at Column Face versus Plastic Rotation Response

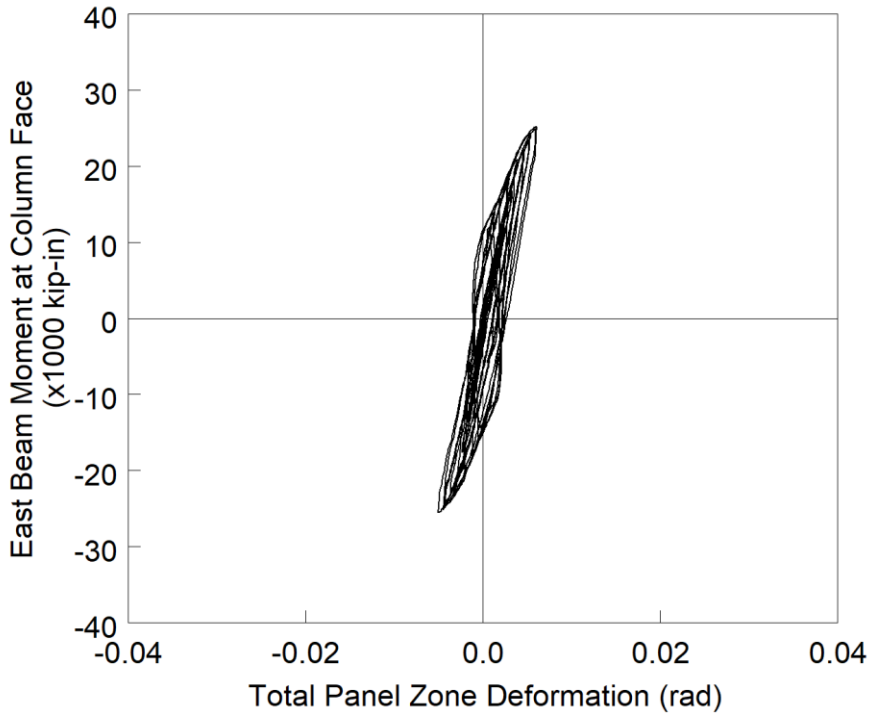

Figure 4.162 Specimen W3: Panel Zone Shear Deformation

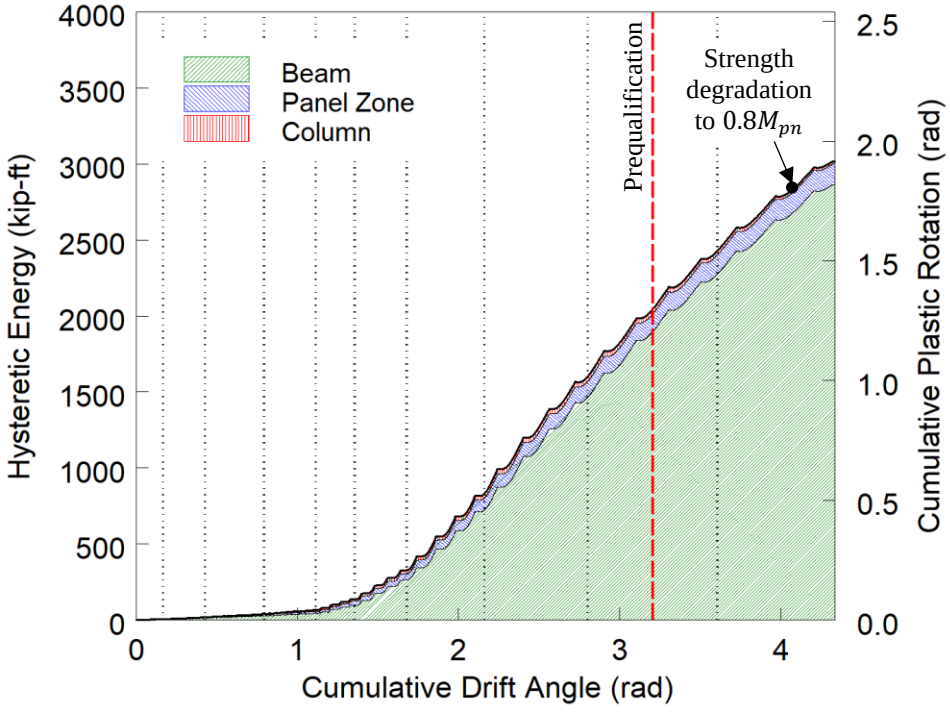

Figure 4.163 Specimen W3: Energy Dissipation

4.11. Specimen W4

4.11.1. General

Specimen W4 was designed to investigate use of the plastic methodology to design continuity plates. The resulting continuity plates satisfy the current minimum thickness requirements as per the AISC 341 Provisions. Continuity plate double-sided fillet welds were sized such that $w = 0.75t_{cp}$. A pair of doubler plates stiffen the web of the column for panel zone yielding. The doubler plate is placed within the panel zone and is welded to the continuity plates on the top and bottom edges. The doubler plate vertical welds use a fillet weld sized to develop the strength of the doubler plate. Horizontal fillet welds between the doubler plate and continuity plate were sized to develop 75% of the doubler plate shear capacity as per the current Provisions. Specimen W4 failed by a fracture of the east and west beam top beam flange CJP weld during the first cycle of 0.05 rad drift. Figure 4.164 shows the specimen before testing.

4.11.2. Observed Performance

The observed response for Specimen W4 is described below.

- Figure 4.165 shows the connection during testing. The specimen met the AISC acceptance criteria by completing one complete cycle at 0.04 rad drift while the flexural strength at either column face did not degrade below 80% of the beam nominal flexural strength.
- Figure 4.166 and Figure 4.167 show the east beam bottom flange and west beam bottom flange during testing. The progression of flange local buckling between the second cycle of 0.04 rad and the first cycle of 0.05 rad is shown in Figure 4.168.
- Figure 4.169 shows the initiation of web buckling during the first negative excursion of 0.04 rad drift.

- During the second negative excursion of 0.04 rad drift the east beam top flange partially fractured through 50% of the flange at the CJP weld (see Figure 4.170).
- During the first negative excursion of 0.05 rad drift the west beam top flange developed a partial fracture through 20% of the beam flange (see Figure 4.171).
- Severe lateral-torsional buckling developed in the east beam during the 0.05 rad drift cycles (see Figure 4.172).
- During the first negative excursion of 0.05 rad drift the east beam top flange completely fractured through the CJP weld (see Figure 4.173). This fracture propagated down the CJP weld bevel. Accompanying this fracture, the web of the east beam fractured (see Figure 4.174). This fracture propagated 5 in. from the radius of the weld access hole. Continuing the 0.05 rad drift cycles resulted in the complete fracture of the west beam top flange (see Figure 4.175). A close up of the east beam top flange fracture is shown in Figure 4.176.
- Figure 4.177 shows the connection at the end of testing. Continued negative excursion of the east beam resulted in the web continuing to fracture following a few inches outboard of the fillet welded shear tab.
- No yielding of the continuity plates was observed during testing (see Figure 4.178). Furthermore, no damage was observed in the continuity plate fillet welds. Minor yielding of the inside face of the column flange, above the top flange continuity plates, is shown in Figure 4.178(b).
- The top and bottom edge of the doubler plate of this specimen was welded to the continuity plate using a 5/8-in. fillet weld based on the Provisions. This weld was the sole attachment of the inside face of the continuity plate to the panel zone. The termination of the doubler

plate vertical welds was held back from the continuity plate by 1 in. as per the Provisions. No damage was observed in any of these welds (see Figure 4.179).

4.11.3. Recorded Response

- Figure 4.180 shows the recorded displacement response of the beam tip measured with transducer L1 for the east beam and L2 for the west beam. The response from the east and west beams are shown in black and blue, respectively. The east beam top flange fractured during the second negative excursion of 0.03 rad drift. Complete fracture occurred at a neutral position during the first negative excursion of 0.05 rad drift. Complete fracture of the west beam top flange occurred at 0.015 rad during the first negative excursion of 0.05 rad drift.
- Figure 4.182 shows the load-displacement response of the beams.
- Figure 4.183 shows the computed moment at the column face (M_f) versus the story drift angle. Two horizontal axes at 80% of the nominal plastic moment (M_{pn}) of the beam section are also added. In addition, two vertical axes at ±0.04 rad story drift show the drift required for SMF connections per AISC 341. It is observed that the beams developed 1.5 times its nominal plastic bending moment. If the moment is computed at the plastic hinge location and compared to the expected plastic moment, then the peak connection strength factor (C_{pr}) is 1.39 and 1.34 for the east and west beams respectively.
- Figure 4.184 shows the plastic response of the specimen. The plastic response is computed using the procedure outlined in Section 3.7. The computed elastic stiffness of the specimen was determined to be 54.9 kips/in.
- Figure 4.185 shows minor hysteretic behavior in the panel zone.

- Figure 4.186 shows the dissipated energy of Specimen W4. Dotted vertical lines on the graph demonstrate the completion of each group of cycles, and the dashed red vertical line shows the completion of the first cycle of 0.04 rad in the AISC loading. It is observed that the completion of the first drift cycle of 0.04 rad (the requirement for SMF connections per AISC 341) occurs after 852 kip-ft of energy has been dissipated. The connection did not degrade below $0.8M_{pn}$ until fracture of the east beam top flange occurred and 1,427 kip-ft of energy had been dissipated. Therefore only 60% of the energy dissipation capacity was utilized after the completion of the SMF requirement. It is observed that nearly all (96%) of the energy dissipation capacity occurred in the beam.

(a) Overview

(b) Connection Region

Figure 4.164 Specimen W4: Connection before Testing

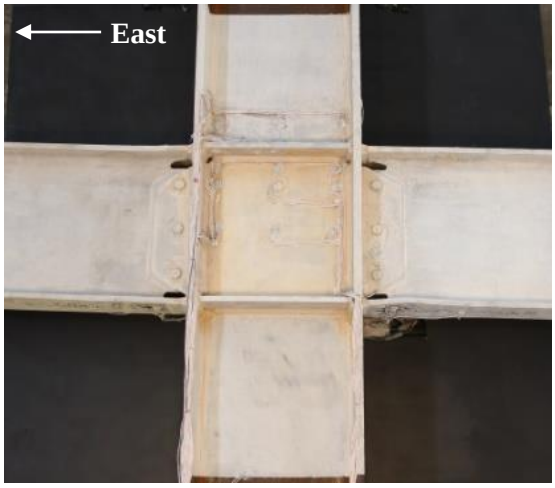

(a) +0.03 rad (2nd Cycle)

(b) -0.03 rad (2nd Cycle)

(c) +0.04 rad (2nd Cycle)

(d) -0.04 rad (2nd Cycle)

(e) +0.05 rad (1st Cycle)

(f) -0.05 rad (1st Cycle)

Figure 4.165 Specimen W4: Connection during Testing

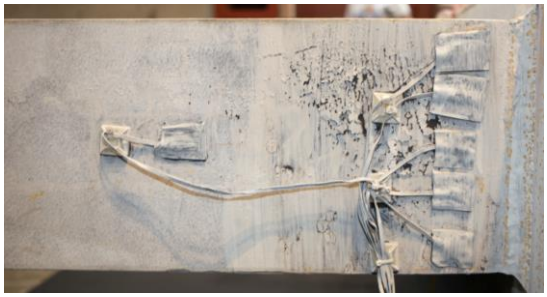

(a) +0.015 rad (1st Cycle)

(b) -0.02 rad (2nd Cycle)

(c) +0.03 rad (2nd Cycle)

(d) -0.04 rad (2nd Cycle)

Figure 4.166 Specimen W4: East Beam Bottom Flange Yielding

(a) +0.015 rad (1st Cycle)

(b) -0.02 rad (2nd Cycle)

(c) +0.03 rad (2nd Cycle)

(d) -0.04 rad (2nd Cycle)

Figure 4.167 Specimen W4: West Beam Bottom Flange Yielding

(a) +0.04 rad (2nd Cycle) (b) +0.05 rad (1st Cycle)

Figure 4.168 Specimen W4: West Beam Bottom Flange Local Buckling

Figure 4.169 Specimen W4: West Beam Web Buckling at +0.04 rad (1st Cycle)

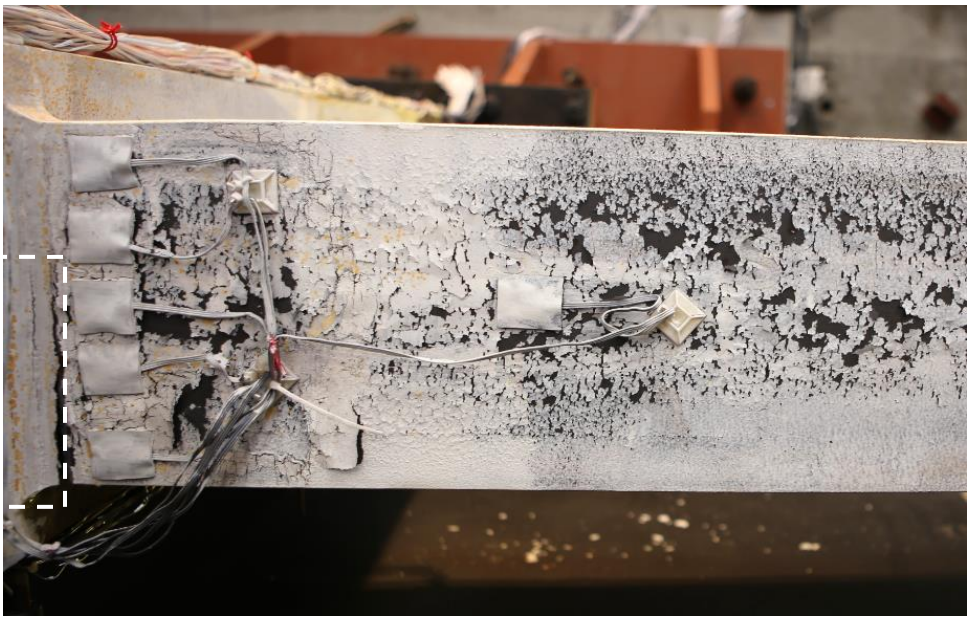

Figure 4.170 Specimen W4: East Beam Top Flange CJP Weld Fracture at -0.04 rad (2nd Cycle)

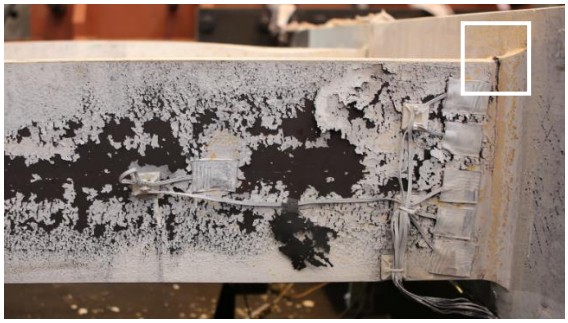

(a) Overview

(b) Weld Tear

Figure 4.171 Specimen W4: West Beam Top Flange CJP Weld Tear at +0.05 rad (1st Cycle)

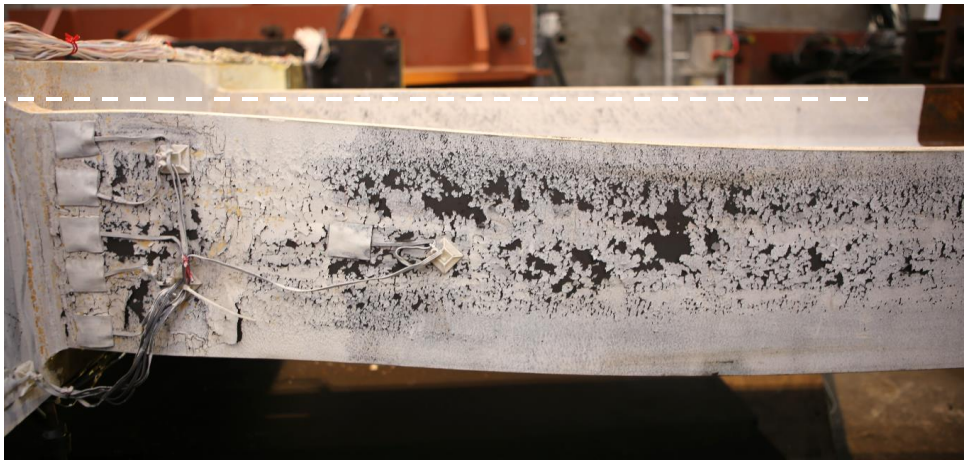

Figure 4.172 Specimen W4: East Beam Lateral-Torsional Buckling at +0.05 rad (1st Cycle)

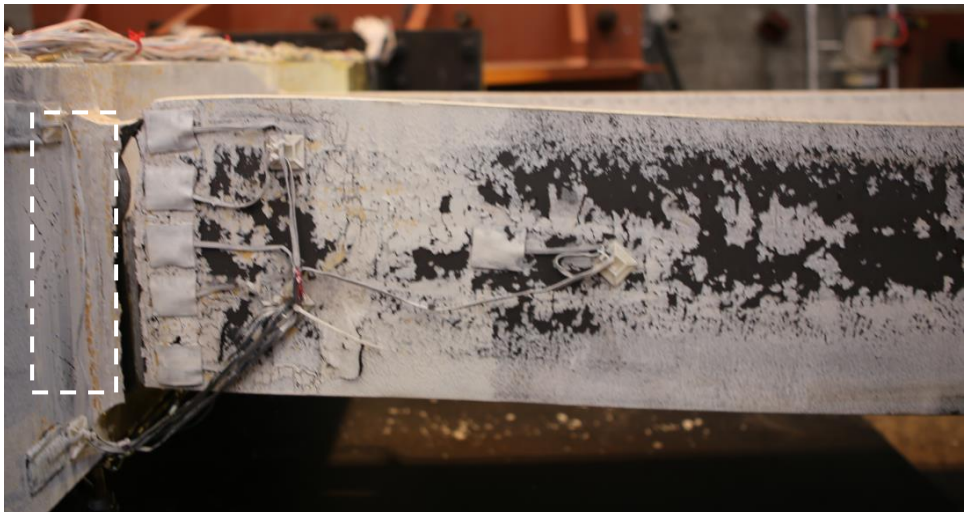

Figure 4.173 Specimen W4: East Beam Top Flange Fracture during First Excursion of -0.05 rad

Figure 4.174 Specimen W4: East Beam Top Flange Weld Access Hole Fracture during First of -0.05 rad

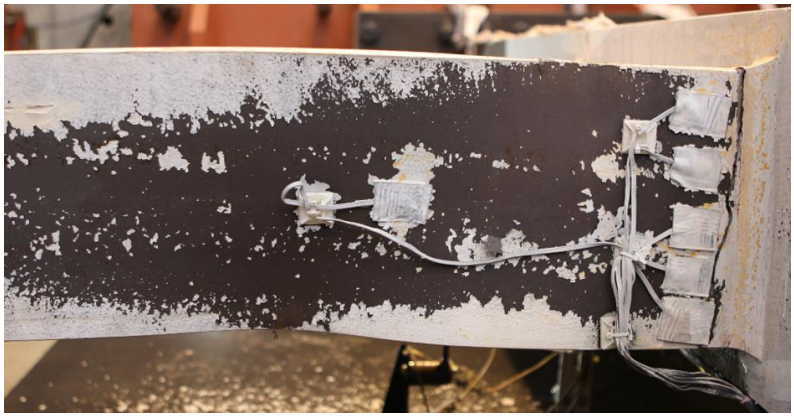

(a) Overview

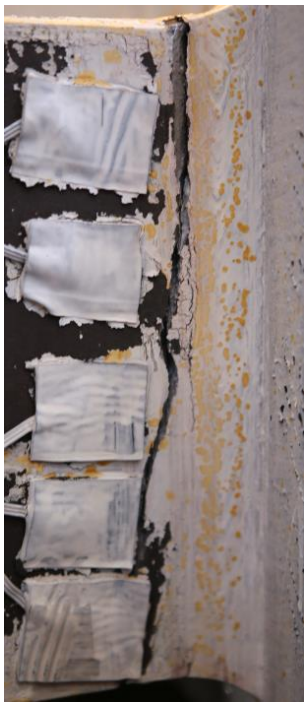

(b) Fracture

Figure 4.175 Specimen W4: West Beam Top Flange Fracture (End of Test)

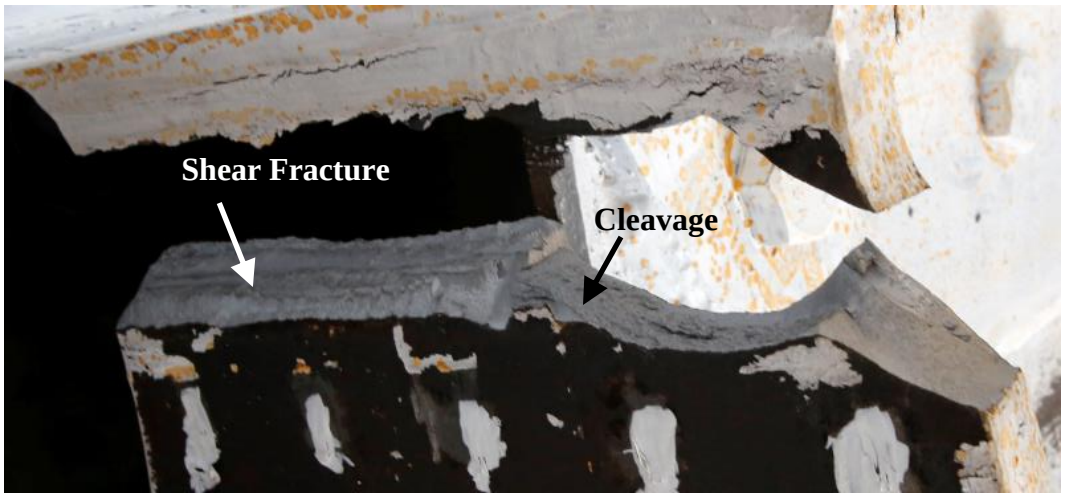

Figure 4.176 Specimen W4: East Beam Top Flange Fracture

Figure 4.177 Specimen W4: Connection at End of Testing

(a) Bottom Flange

(b) Top Flange

Figure 4.178 Specimen W4: Continuity Plates (End of Test)

Figure 4.179 Specimen W4: Panel Zone (End of Test)

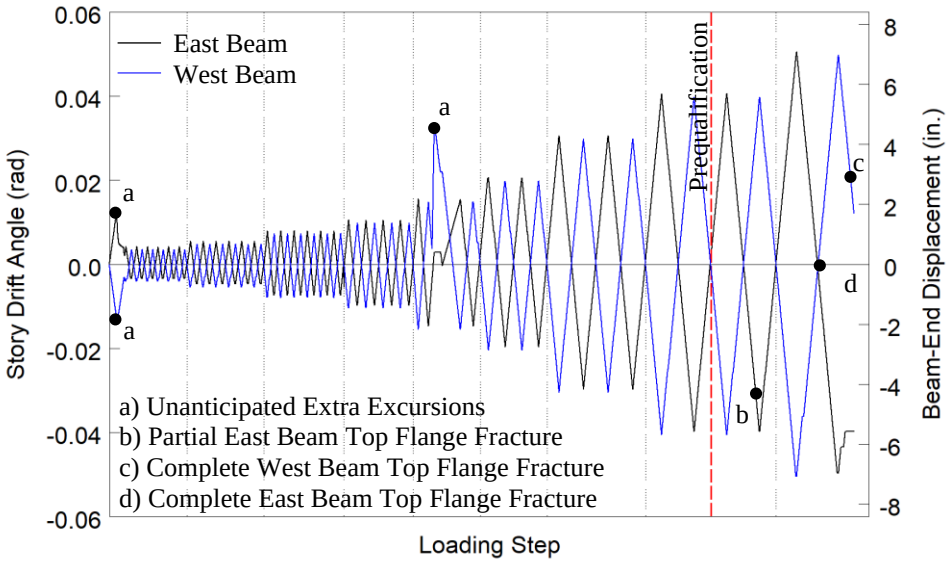

Figure 4.180 Specimen W4: Recorded Loading Sequence

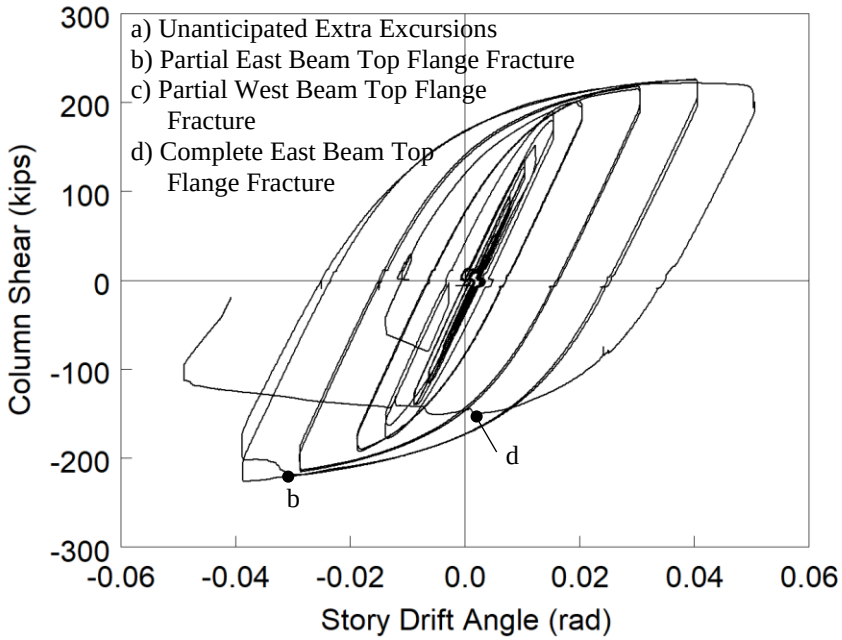

Figure 4.181 Specimen W4: Column Shear versus Story Drift Angle

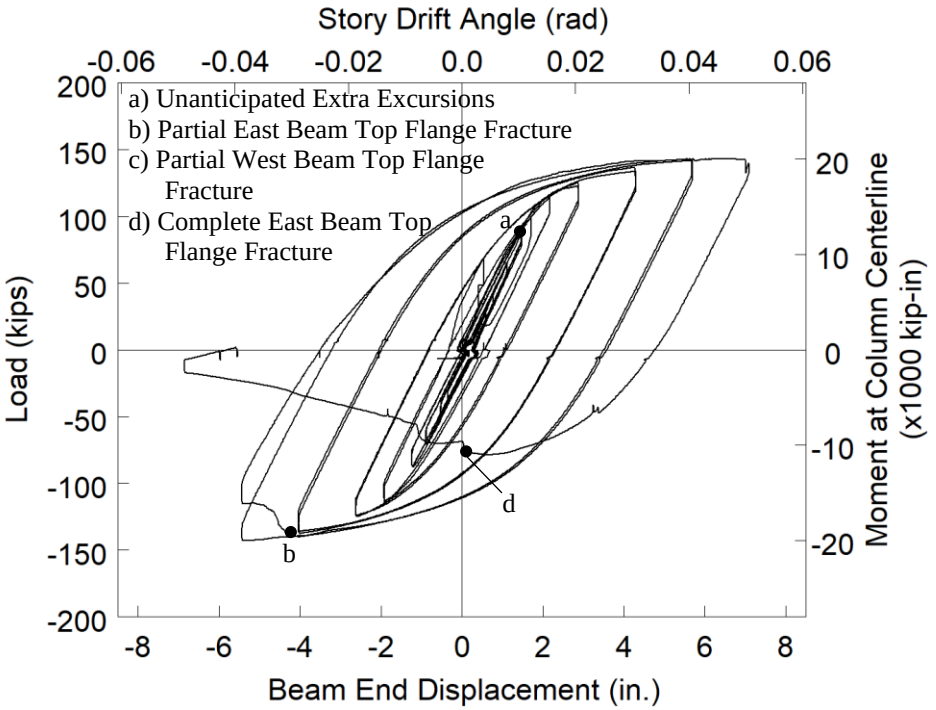

(a) East Beam

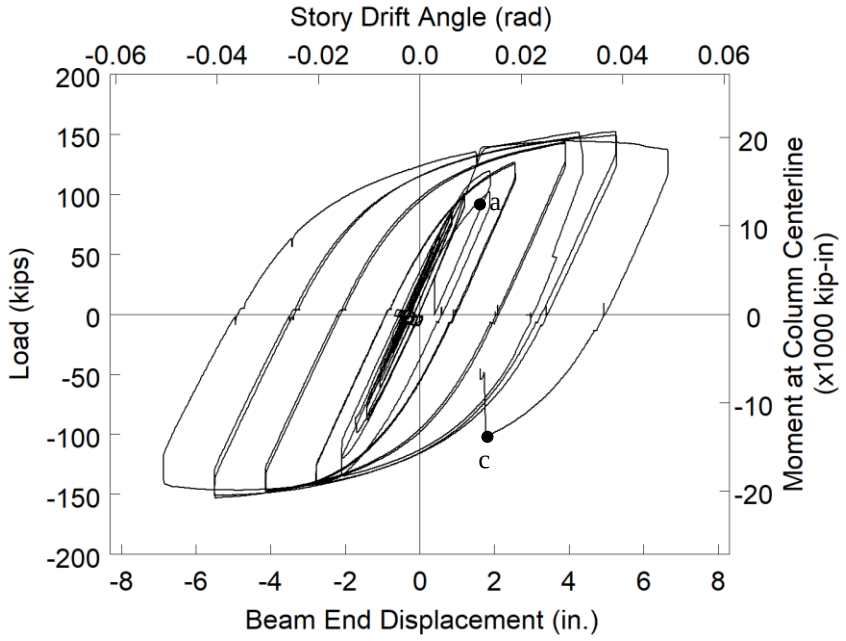

(b) West Beam

Figure 4.182 Specimen W4: Applied Load versus Beam End Displacement Response

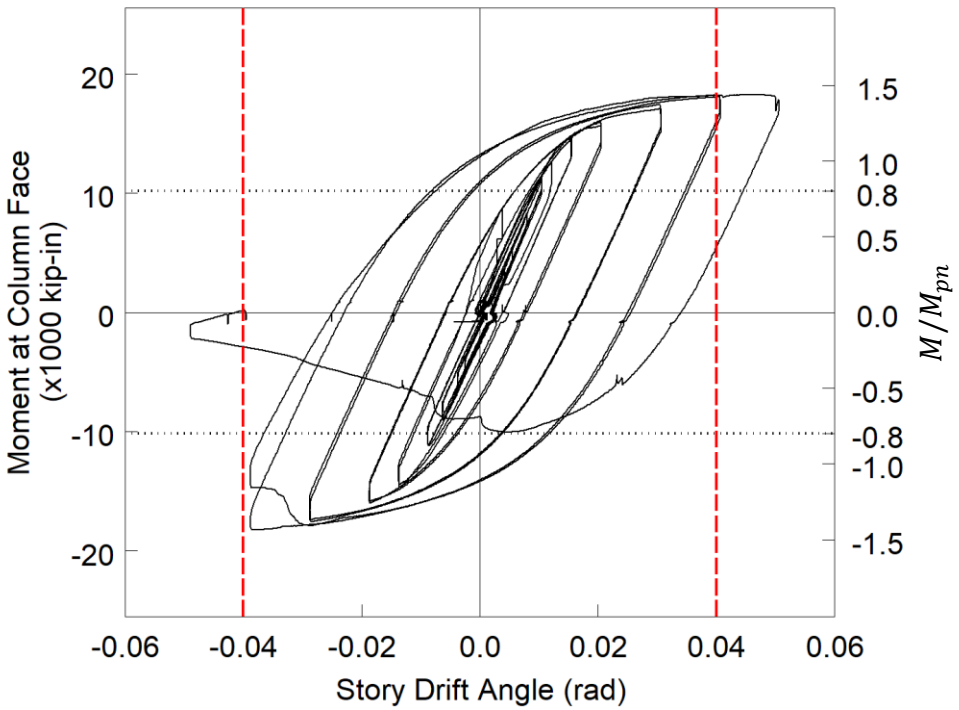

(a) East Beam

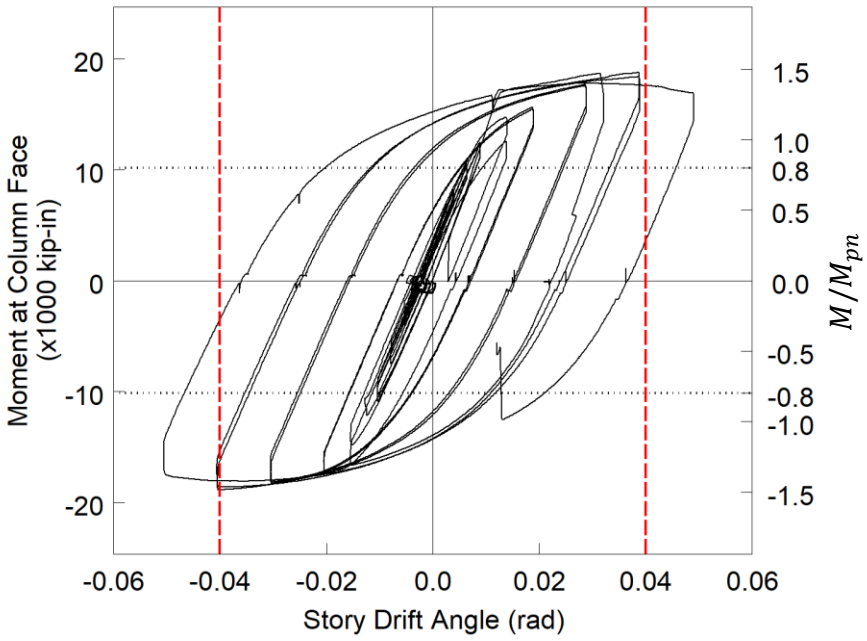

(b) West Beam

Figure 4.183 Specimen W4: Moment at Column Face versus Story Drift Response

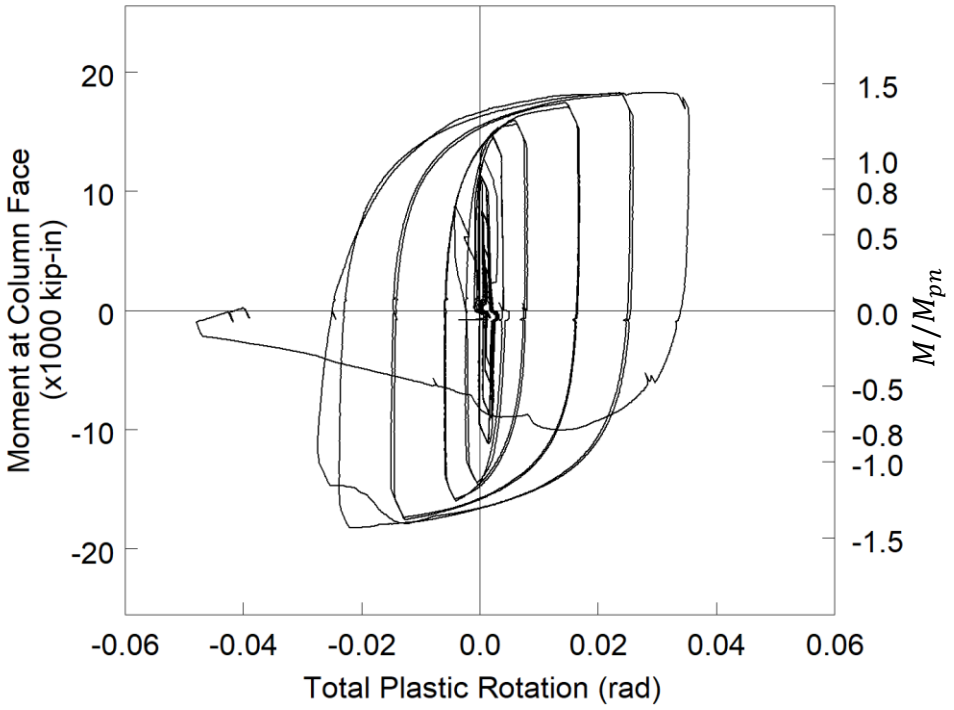

(a) East Beam

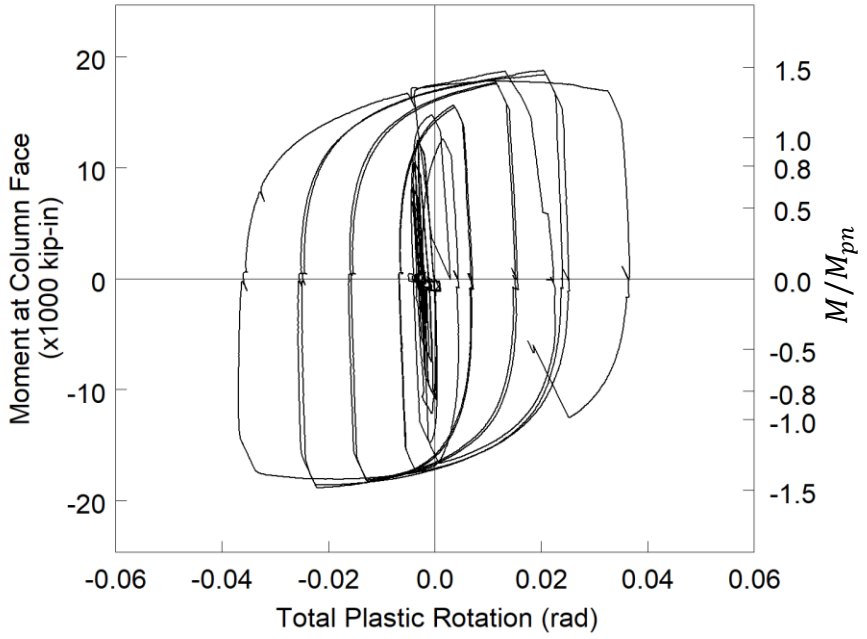

(b) West Beam

Figure 4.184 Specimen W4: Moment at Column Face versus Plastic Rotation Response

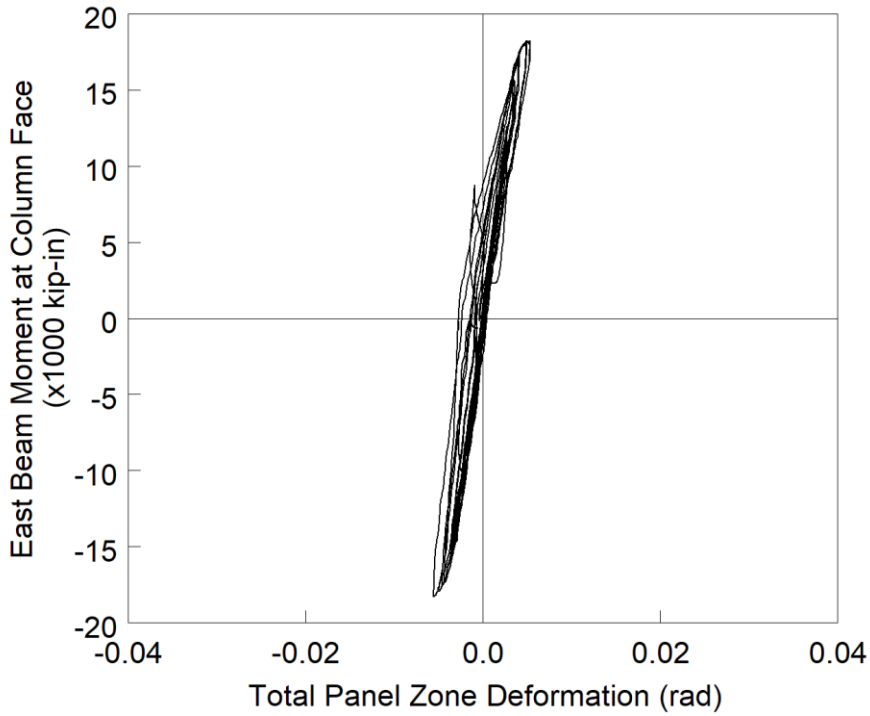

Figure 4.185 Specimen W4: Panel Zone Shear Deformation

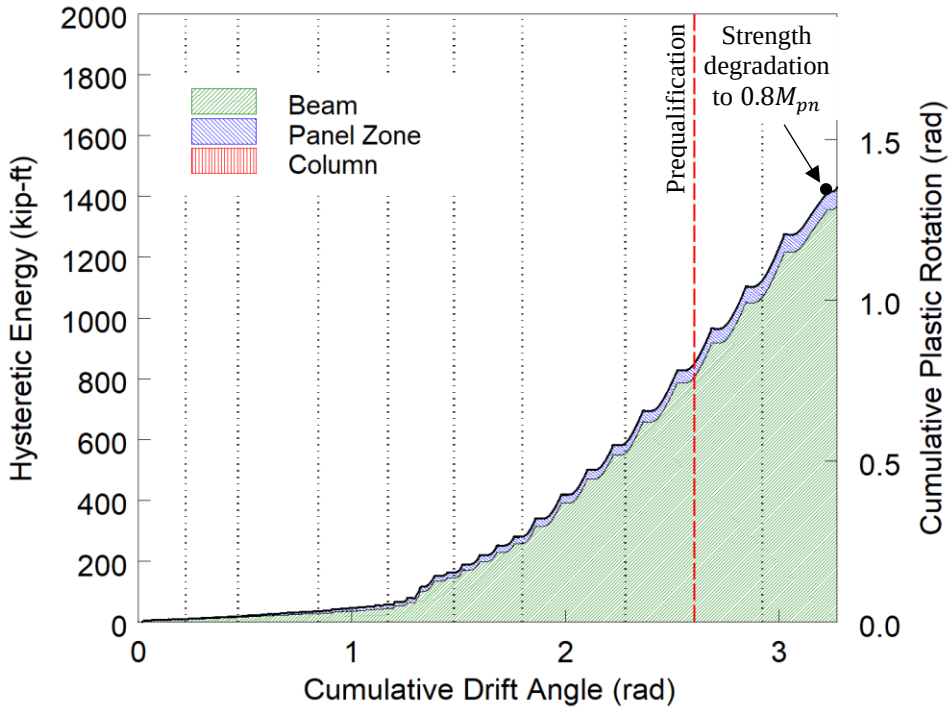

Figure 4.186 Specimen W4: Energy Dissipation

4.12. Specimen Macroetching

After testing, several sections of the specimens were cut out and sectioned using a cold saw. The surfaces of the sections were then polished and etched using a 5% Nital acid to reveal the formation of the welds. Figure 4.187 shows a macroetch of the beam bottom flange weld of Specimen C3; the beam bottom flange CJP weld did not fracture during testing. Evident in this figure is the beam flange CJP weld performed from the horizontal position and the reinforcing fillet placed on the underside of the beam in the overhead position after the backing bar is removed. Figure 4.188 shows the beam bottom and top flange welds of Specimen C5. The fractured top flange CJP weld is observed to propagate at a 35-degree angle through the weld metal, initiating at the reentrant corner formed between the weld and the column flange. Also shown in this figure are the continuity plate fillet welds, which show no indications of damage. A similar macroetch is performed on Specimen C6 (see Figure 4.189). In this case the beam top flange CJP weld fracture has two shear lips because the etching was taken closer to the edge of the beam flange. No damage to the fillet welds is observed. Figure 4.190 shows a similar section of the east beam flange welds from Specimen W1. The beam top flange CJP weld fracture is observed to follow the 30-degree bevel of the CJP weld.

Figure 4.191(a) shows a section through the doubler plate at an elevation which includes the beam web. This section shows the beam web CJP weld using the shear tab as a backing bar. The one-sided fillet weld fastening the shear tab to the column flange is also shown in the figure. The doubler plate fillet weld and bevel are shown in Figure 4.191(a) and (b).

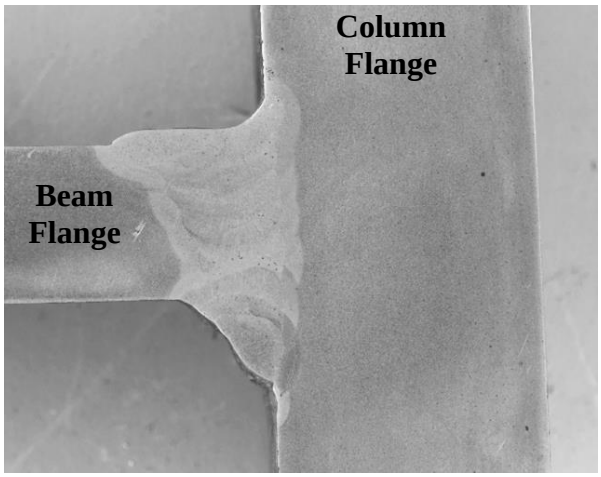

Figure 4.187 Macroetch of Specimen C3 Beam Bottom Flange CJP Weld

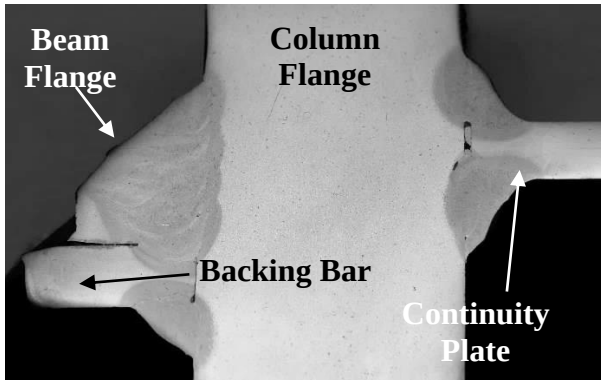

(a) Beam Top Flange

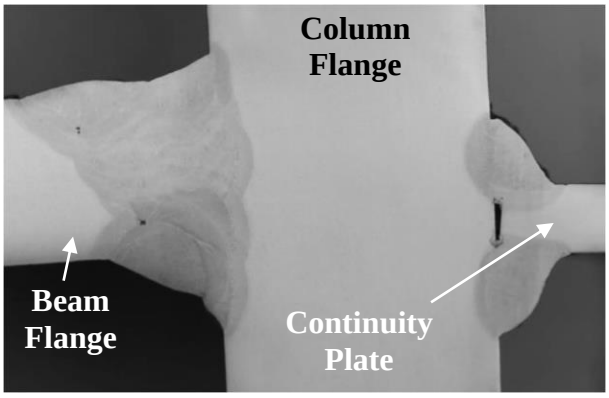

(b) Beam Bottom Flange

Figure 4.188 Macroetch of Specimen C5 Welds

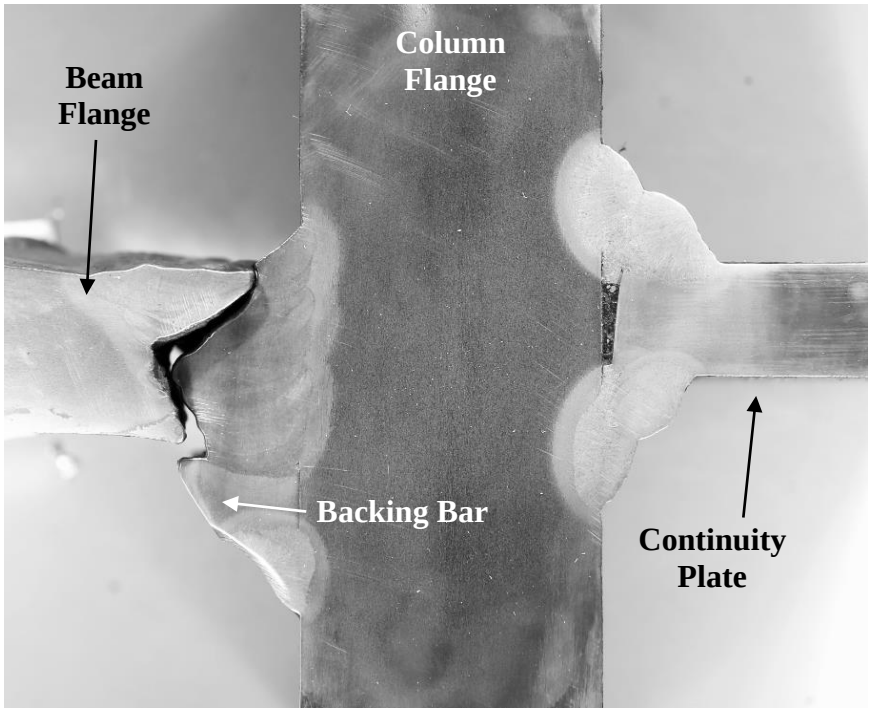

(a) Beam Top Flange

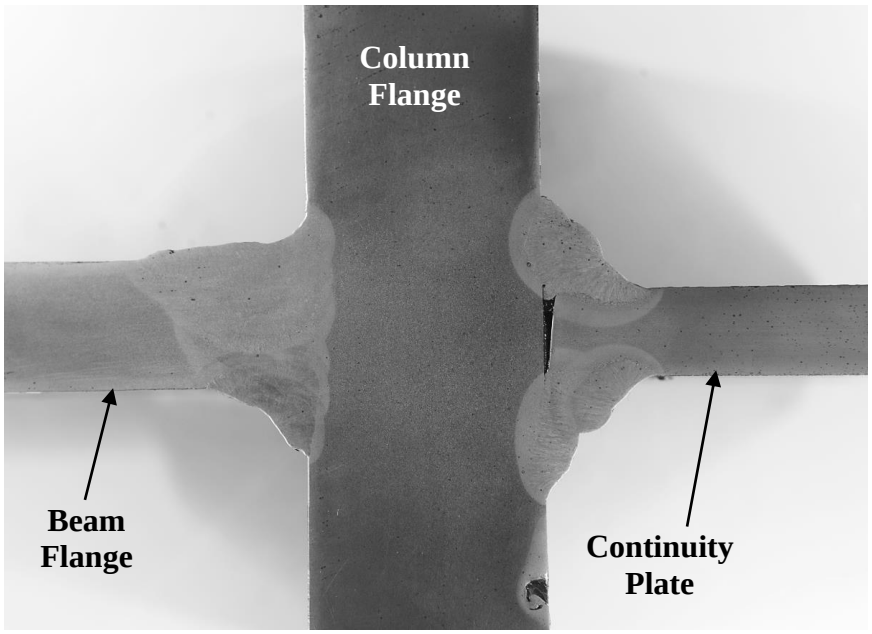

(b) Beam Bottom Flange

Figure 4.189 Macroetch of Specimen C6 Welds

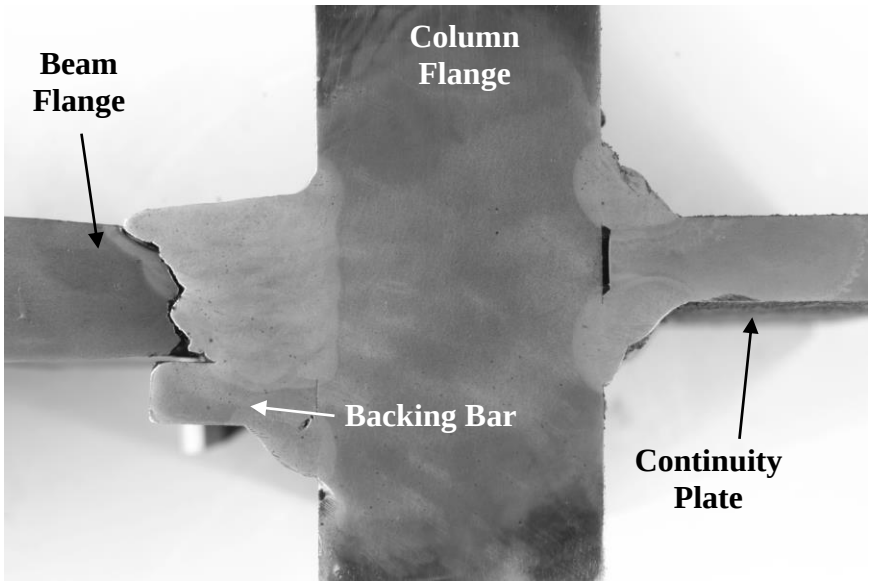

(a) Top Flange

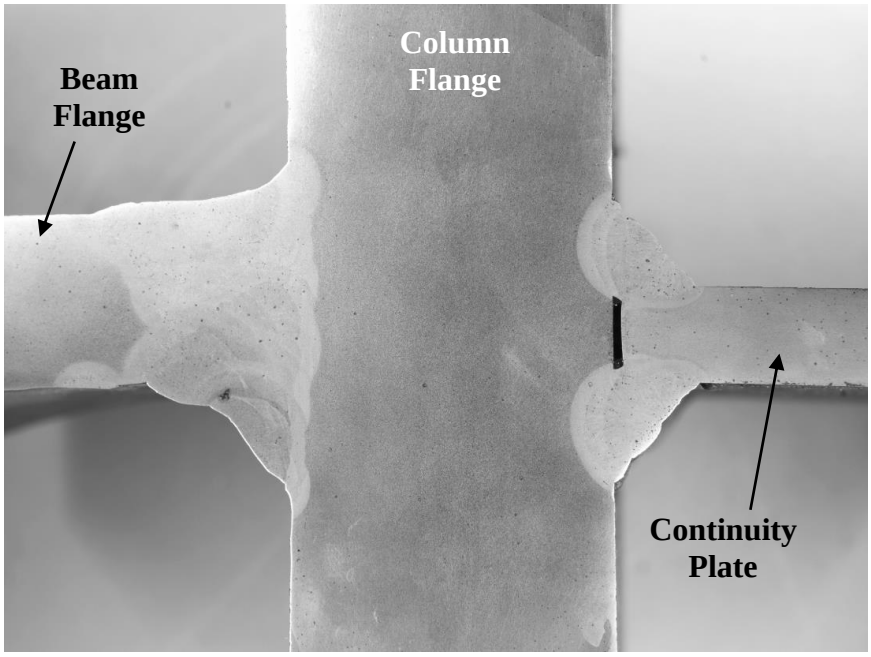

(b) Bottom Flange

Figure 4.190 Macroetch of Specimen W1 Welds (East Beam)

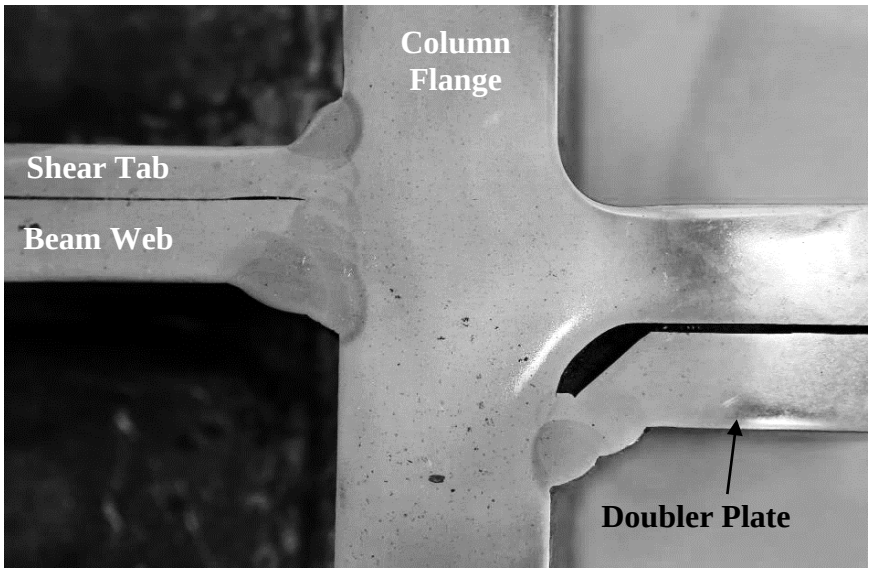

(a) Doubler Plate at Web

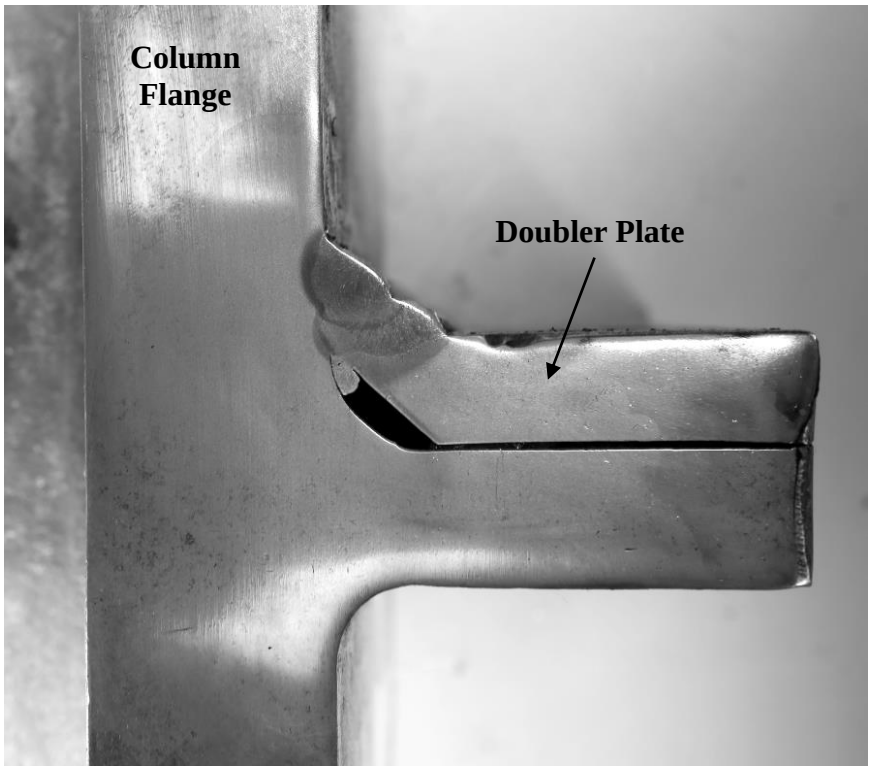

(b) Doubler Plate Above Beam Top Flange

Figure 4.191 Macroetch of Specimen C7 Welds

4.13. Beam Lateral Bracing Force

During testing of the Phase 1 specimens the lateral bracing force was monitored using a set of strain gauge rosettes placed on each lateral brace column. The lateral braces were placed approximately $d_b/2$ away from the end of the RBS. The response of each of the specimens is tabulated in Table 4.1 through Table 4.5. The table shows the expected flange force of the specimen as per AISC 341 and the computed flange force determined from the peak load during each cycle. Specimen C3, Specimen C5, and Specimen C6 develop about 2.0% of the flange force at the brace location at the end of testing. All three of these specimens failed during the 0.05 rad cycles. Specimen C4 develops about 5.0% of the flange force during the 1st cycle of 0.05 rad cycles. Specimen C6-G saw the most significant flange force equal to 6.0% of the expected flange force or 7.6% of the measured force. The bracing force of Specimen C7 was not measured during testing.

The measured flange force was determined by dividing the measured moment at the brace location by the centroid between flanges. This procedure is consistent with AISC 341 (2016) §D1.2b stipulating the required force of the lateral bracing for highly ductile members.

Table 4.1 Specimen C3: Beam Lateral Bracing Force

Drift (rad)	Cycle	Flange Force at Brace (kips)		Measured Brace Force (kips)	Normalized Brace Force	
		Expected	Measured		by Expected Flange Force (%)	by Measured Flange Force (%)
0.02	1	542	494	1.35	0.24	0.27
0.02	2		510	1.42	0.26	0.28
0.03	1		560	1.50	0.27	0.27
0.03	2		573	1.73	0.31	0.30
0.04	1		602	4.07	0.73	0.68
0.04	2		599	7.25	1.30	1.21
0.05	1		595	13.32	2.38	2.23

Table 4.2 Specimen C4: Beam Lateral Bracing Force

Drift (rad)	Cycle	Flange Force at Brace (kips)		Measured Brace Force (kips)	Normalized Brace Force	
		Expected	Measured		by Expected Flange Force (%)	by Measured Flange Force (%)
0.02	1	486	521	2.05	0.42	0.39
0.02	2		522	2.10	0.43	0.40
0.03	1		567	1.81	0.37	0.32
0.03	2		574	1.84	0.38	0.32
0.04	1		565	2.42	0.50	0.43
0.04	2		537	2.83	0.58	0.53
0.05	1		492	4.55	0.94	0.92
0.05	2		448	11.33	2.33	2.53
0.06	1		405	22.17	4.56	5.47

Table 4.3 Specimen C5: Beam Lateral Bracing Force

Drift (rad)	Cycle	Flange Force at Brace (kips)		Measured Brace Force (kips)	Normalized Brace Force	
		Expected	Measured		by Expected Flange Force (%)	by Measured Flange Force (%)
0.02	1	542	454	2.32	0.43	0.51
0.02	2		470	2.36	0.44	0.50
0.03	1		510	2.31	0.43	0.45
0.03	2		528	2.32	0.43	0.44
0.04	1		546	2.84	0.52	0.52
0.04	2		566	2.80	0.52	0.49
0.05	1		575	3.12	0.58	0.54
0.05	2		548	7.50	1.38	1.37

Table 4.4 Specimen C6: Beam Lateral Bracing Force

Drift (rad)	Cycle	Flange Force at Brace (kips)		Measured Brace Force (kips)	Normalized Brace Force	
		Expected	Measured		by Expected Flange Force (%)	by Measured Flange Force (%)
0.02	1	448	490	0.80	0.18	0.16
0.02	2		498	1.17	0.26	0.23
0.03	1		524	1.86	0.42	0.35
0.03	2		533	2.42	0.54	0.45
0.04	1		530	3.23	0.72	0.61
0.04	2		518	3.11	0.69	0.60
0.05	1		468	9.56	2.13	2.04

Table 4.5 Specimen C6-G: Beam Lateral Bracing Force

Drift (rad)	Cycle	Flange Force at Brace (kips)		Measured Brace Force (kips)	Normalized Brace Force	
		Expected	Measured		by Expected Flange Force (%)	by Measured Flange Force (%)
0.02	1	448	490	1.56	0.35	0.32
0.02	2		497	2.00	0.45	0.40
0.03	1		514	4.79	1.07	0.93
0.03	2		524	5.66	1.26	1.08
0.04	1		525	8.72	1.95	1.66
0.04	2		518	10.03	2.24	1.94
0.05	1		487	12.70	2.83	2.61
0.05	2		420	20.84	4.65	4.96
0.06	1		351	26.77	5.98	7.63

This chapter has been published as a Structural Systems Research Project (SSRP) Report: Reynolds, M., C-M., Uang, "Alternative Weld Details and Design for Continuity Plates and Doubler Plates for Applications in Special and Intermediate Moment Frames," *Report No. SSRP-19/03,* and submitted to AISC as the final project deliverable. This chapter is also being prepared for submission for publication and may appear in *AISC Engineering Journal*. The author of this dissertation is the primary author of this work; Prof. Chia-Ming Uang will coauthor this work.

5. ANALYSIS OF EXPERIMENTAL RESULTS

5.1. General

This chapter presents the comparison of the performance of specimens from Phase 1 (Specimens C3, C4, C6, C6-G, and C7), Phase 2 (Specimens W1, W2, W3, and W4), and the pilot study completed in 2016 (Specimens C1 and C2). All the specimens with a 'C' prefix were one-sided, simulating an exterior RBS moment connection with or without continuity plates. The careful design of these specimens for testing resulted in the ability to investigate the existing code criteria regarding the implementation of continuity plates in SMFs. Three of these specimens (Specimens C3, C4, and C7) directly challenge the Lehigh Criterion (Eq. 1.16) by omitting continuity plates, despite the ratio of beam flange width to column thickness being greater than 6.0. The one-sided specimens used either a W36×150 beam or a W30×116 beam. The tested columns consisted of two different shallow column shapes (W14×211 and W14×257) and several deeper column shapes (W24×176, W24×192, and W27×235). Specimens C1, C2, C5, C6, and C6-G used continuity plates. Only one specimen used a doubler plate (Specimen C7) consisting of a single-sided plate to reinforce the column web.

Specimens with a 'W' prefix were two-sided, simulating an interior WUF-W connection with continuity plates. Specimen W1 used two W36×150 beams, the largest beam size permitted by AISC 358-16, adjoined to a W27×258 column. Specimen W2 used two W33×141 beams fastened to a W27×217 column. Specimen W3 used two W30×116 beams connected to a W24×207 column. Finally, Specimen W4 used two W24×94 beams connected to a W24×182 column. All of the two-sided specimens used a pair of symmetric doubler plates with either a PJP or fillet weld attachment to the column flange. One specimen, Specimen W4, used a doubler plate

that was terminated inside the continuity plates, while the other three specimens used a typical extended doubler plate detail.

All of the specimens with a continuity plate used 2-sided fillet welds to attach the continuity plate to the column flange and column web. Except for Specimens C6 and C6-G, the size of these fillet welds satisfy the proposed design rule of $w = (3/4)t_{cp}$, where w is the specified weld size, and t_{cp} is the thickness of the continuity plate. The doubler plate in Specimen C7 is designed using the assumed shear flow (Eq. 2.25) derived from the equilibrium of the plate instead of, as required by AISC 341-16, developing the shear strength of the plate. Doubler plate welds for Phase 2 specimens develop the shear strength of the plate. Because the doubler plates of Specimen W4 do not extend beyond the continuity plates, this specimen uses a weld to attach the horizontal edge of the doubler plate, a requirement of AISC 341-16. This horizontal fillet weld is designed as per requirements to develop 75% of the shear strength of the doubler plate.

5.2. Observed Response and Governing Failure Modes

All of the specimens completed the AISC prequalification for SMF. Specifically, all the specimens completed at least one cycle of 0.04 rad drift without the strength of the connection degrading below $0.8M_{pn}$. The one-sided connections failed either by fracture of the beam flange within the reduced beam section or failure of the top flange CJP weld. Specimens, including those with and without continuity plates, which ultimately failed due to weld fracture demonstrated early signs of ductile weld tearing during the initial 0.03 rad cycle drifts. During each negative excursion where the top flange was in tension, the weld tear progressed until the complete fracture of the weld. The weld tears started in the center of the beam flange at the toe of a prominent weld pass in the reentrant corner. The typical fracture was a ductile shear fracture that propagated at a 35-degree angle through the weld metal until a fracture occurred perpendicular to the direction of

loading (e.g., see Figure 4.49). The specimens which ruptured through the beam flange at the reduced beam section developed fractures in the vicinity of the largest local buckling amplitudes. Specimen C7 had a multi-stage fracture, which originated with a cleavage fracture in the k-area of the beam adjacent to severe web local buckling of the beam. The final stage of the fracture resulted in a ductile fracture of the entire beam top flange. Specimen C1 from the pilot study was the only specimen not loaded to failure. Instead, loading of this specimen stopped once the strength of the connection had degraded below $0.8M_{pn}$. Finally, a single cycle of 0.07 rad was imposed on Specimen C2 after completing two cycles of 0.05 rad of the AISC loading protocol.

Phase 2 specimens all fractured through the beam top flange CJP weld (e.g., see Figure 4.182). This fracture developed at the CJP weld root at the notch at the junction between weld metal and steel backing. The initiation of this fracture was during the 0.03 rad drift cycles, and its gradual progression occurred through the weld metal along the CJP weld bevel. Final fracture surfaces resulted in a mixture of shear fracture and cleavage. Extreme local curvatures influenced the fractures by providing secondary initiation sites at other locations in the CJP weld. Several partial tears of the beam bottom flange CJP weld extending downward from the inside face of the flange was observed. In one specimen, Specimen W2, this resulted in a partial fracture of the beam bottom flange (see Figure 4.184). Table 5.1 compares the story drift capacities of all 12 specimens. (The drift capacity of two-sided specimens is the lowest obtained drift from either beam.) Figure 4.75 summarizes the completed drifts and the distribution of elastic and inelastic drift components. The expected and experimentally determined continuity plate and doubler plate forces are tabulated in Table 5.2 and Table 5.3.

The peak connection strength factor, C_{pr}, as determined by comparing the experimentally determined moment at the AISC 358-16 assumed plastic hinge location to the actual plastic

moment, M_{pa}, of the beam is shown in Figure 5.2. (The computed C_{pr} for the two-sided specimens is the average of the two beams.) The average C_{pr} for the eight RBS connections is 1.19, which is similar to the value of 1.15 assumed in AISC 341-16. The average C_{pr} for the four WUF-W connections (eight beams total) is 1.3, less than the value of 1.4 stipulated in AISC 358-16. Figure 5.3 shows the normalized dissipated energy of each specimen and the distribution of energy dissipation between the column, panel zone, and beams. The energy is normalized by the summation of the actual plastic moment, M_{pa}, of the beams at the connection (i.e., for the two-sided connections the energy is normalized by $2M_{pa}$). The distribution shows that Specimens C2 and C5 demonstrated significant panel zone yielding, while Specimen C3 showed moderate panel zone yielding. This conclusion is reinforced by comparing the measured panel zone shear force, V_{pz}, to the shear yielding strength of the panel zone (see Table 5.3). As predicted by the AISC 360-16 panel zone shear strength (Eq. 1.19), Specimens C4 and C7 did not dissipate energy through inelastic panel zone deformation.

Figure 5.4 shows the reserve energy ratio for each specimen. The reserve energy ratio is a metric that demonstrates a connection energy dissipation capacity beyond the single cycle of 0.04 rad drift as required by AISC 341-16. A value of 1 indicates no energy dissipation capacity after satisfying the minimum AISC qualification cycles. A value of 2, which was substantially achieved by Specimens C2, C4, C5, C6-G, W2, and W3, demonstrates that a connection has double the minimum required energy dissipation capacity. The tested clear span-to-depth ratios are shown in Figure 5.5. Only Specimen W1 violated the AISC 358-16 minimum ratio of 7 for either RBS or WUF-W connections; this may explain the lowest reserve energy ratio by this specimen.

5.3. Effect of Galvanization

Specimen C6-G was nominally identical to Specimen C6, except the specimen was hot-dip galvanized before shop welding. Removal of the galvanization in the area of the connection was required to perform the simulated field welding. Zinc paint was then applied to the welded area to simulate standard practice. The load-displacement response of the two specimens was identical until the beam flange CJP weld fractured during 0.05 rad drift of Specimen C6 (see Figure 5.6). The discrepancy in cyclic performance between the two specimens is attributed to variability in toughness and geometry of the beam flange CJP welds. Therefore, for the specimens tested it appears that the galvanization did not affect the strength or the ductility capacity.

5.4. Continuity Plate Response

The specimens with continuity plates did not demonstrate any damage to the fillet weldments between the continuity plates and the column flanges or column webs. Except for Specimens C6 and C6-G, the continuity plate-to-column flange weld used a proposed weld size of $(3/4)t_{cp}$. Specimens C2 and C5 used the closest weld size that would develop at least $(3/4)t_{cp}$ (see Table 2.3).

According to the recorded strain gauge response of the continuity plates, all specimens, including Specimens C1 and C2, realized yielding or nearly yielding levels of strain (Mashayekh 2017). The limited amount of cyclic strain precludes significant hysteresis and strain hardening of the continuity plate. The yielding of Specimen C1, which is designed to remain elastic according to the flexibility design method, is explained through high levels of residual stresses in the continuity plates due to the welding of the plates. With the exception of Specimen C5, the strains in the continuity plates were limited to $2.5\epsilon_y$ (see Figure 5.7). The addition of cyclic buckling of the continuity plate used in Specimen C5 contributed to the recorded strain approaching $12\epsilon_y$ in

tension; however, prior to buckling the strains were limited to $1.5\epsilon_y$ [see Figure 5.7(c)]. Therefore, most of the high strain response in C5 is attributed to the flexural buckling of the plate and not high membrane strains in the continuity plate. It is noted that the continuity plates of Specimen C2, which used a continuity plate despite not requiring stiffening to satisfy FLB or WLY, still demonstrated yielding. This is attributed to the relative stiffness of the continuity plate.

Specimens W1 and W3 also show an asymmetric strain response; however, in this case, it is attributed to the lateral-torsional buckling of the adjacent beam [see Figure 5.7(e) and (g)]. The lateral-torsional buckling of the beam imposes an in-plane flexural demand to the continuity plate that exaggerates the compressive strains in the plate. Specimen W2 was the only specimen designed with an intentionally undersized continuity plate with a *DCR* of 1.43 (see Table 2.3). Instead of satisfying the governing column limit state, this continuity plate was sized based on matching 75% of the adjacent beam flange thickness as per AISC 341-16. Despite being undersized, the principal strains in the plate were limited to ϵ_y. This is attributed to a combination of two factors: (1) the measured peak flange force was 0.88 times the expected, and (2) the measured F_y value of the continuity plate material was 58.0 ksi. There appears to be no detrimental effect of two-sided connections on continuity plates. Before any lateral-torsional response of the beams, the axial response in the continuity plate near the column flange approximates equal and opposite pairs (e.g., see Figure 4.203). The shear response along the column web is substantially uniform (e.g., see Figure 4.206).

Specimen C5 was the only specimen that demonstrated buckling of the continuity plate. This buckling initiated at 0.04 rad drift during the peak beam flange force; local continuity plate curvature was straightened out during the tension excursions of the adjacent beam flange. Specimen C5 was designed with a width-to-thickness ratio of a continuity plate of 16. Three

specimens were designed with a width-to-thickness ratio of 12—these specimens did not develop an instability during testing (see Table 5.2).

5.5. Doubler Plate Response

Only the design of the vertical welds adjoining the doubler plate to the column flange of Specimen C7 deviated from the provisions of AISC 341-16. This specimen and the four specimens with doubler plate weldments conforming to AISC 341 did not demonstrate any damage to the weldments. Specimen W4 utilized a doubler plate that was terminated within the continuity plates. The top and bottom edges of the doubler plate of this specimen was welded to the continuity plate using a fillet weld. This weld was the sole attachment of the inside face of the continuity plate to the panel zone. No damage was observed in any of the weldments of this specimen.

Table 5.3 shows that the measured panel zone shear exceeded the yield strength of the plate in Specimen W1. This specimen observes the largest recorded strain in the center of the doubler plate (see Figure 5.8). Specimens W2, W3, and W4 have strains approaching the yielding strain in the middle of the doubler plate—consistent with the predicted behavior from Table 5.3. The edge of the doubler plate demonstrated higher shear strains, above $2\gamma_y$, as shown in Chapter 4. These locations experience local loading effects and high levels of residual stress. Figure 5.8 shows that the extended portion of the doubler plate shows negligible shear stress. Specimen W4, without the extended doubler plate, demonstrates a minor shear response corresponding to the shear of the column.

Specimen W3 used a doubler plate with a ratio of $(d_z + w_z)/t_{dp}$ of 102, which violates the AISC 341-16, limiting width-to-thickness ratio to 90. Despite the violation, doubler plate instability was not observed.

5.6. Column Limit States

Although the limit states of column flanges and webs under concentrated loads are implicitly investigated by all specimens in this test program, Specimens C3, C4, and C7 without continuity plates provide a unique opportunity to isolate the limit states.

5.6.1. Web Local Yielding (WLY)

Specimens C4 and C7 challenged the Lehigh Criterion by omitting continuity plates. The expected flange force of Specimen C4 was 611 kips, while the expected strength of the WLY limit state was 620 kips, resulting in a *DCR* of 0.99. Instrumentation of this specimen illustrated the WLY limit state by distributing five uniaxial strain gauges over a distance of $5k$ behind the beam flange at the toe of the column flange-to-column web radius. As discussed in Section 1.5.2, the distance of $5k$ was derived from experimental results, which confirmed a 2.5:1 diffusion of the beam flange force in the column web. The experimentally determined flange force of Specimen C4 was 667 kips—1.09 times higher than the expected flange force. The peak force occurred during the second cycle of 0.03 rad drift. The resulting peak flange force exceeds the estimated strength of the WLY limit state of 620 kips based on the actual yield stress (see Table 5.2). The local response of Specimen C4 demonstrates that, during the 0.03 rad drift cycles, yielding had distributed over the $5k$ distance during the positive drift cycles (see Figure 5.13). Negative excursions do not demonstrate yielding extending beyond $5k$ during the testing. Continued positive excursions saw uniform incremental growth of the web strains. The difference between the positive and negative excursions is attributed to column warping producing an out-of-plane flexure of the column web during positive excursions when the beam top flange was in compression. Therefore, despite the experimentally determined flange force exceeding the WLY limit state of the column by 8%, the limit state was not violated until 0.03 rad. The local response

indicates peak cyclic strains of 0.01 in./in. ($5\epsilon_y$) directly behind the beam flange. The specimen failed by ductile tearing through the reduced beam section and not because the WLY was exceeded.

Specimen C7 was reinforced with a web doubler plate to satisfy the WLY limit state. The experimentally determined flange force of 594 kips is significantly lower than the actual WLY limit state of 917 kips. Despite this level of robustness, the local response of Specimen C7 demonstrated significant yielding in the column web and doubler plate over a distance of $5k$ (see Figure 5.10). This is attributed to the combined effect of warping of the column flange producing out-of-plane flexure of the column web and doubler plate. Additionally, the eccentric weldments of the doubler plate produce additional curvature, which exacerbates the extreme fiber measured strain response. Despite the additional flexural demands imposed on the column web and doubler plate, the specimen failed by ductile tearing through the reduced beam section.

Figure 5.11 shows that column web strains of Specimen W4 approached $1\epsilon_y$ adjacent to the continuity plate as the continuity plate yielded across its breadth (see Figure 5.12). This indicates that although the WLY limit state may be applicable to unreinforced columns that the significant plasticification that must occur to mobilize its full strength.

5.6.2. Flange Local Bending (FLB)

Localized yielding of the inside face of the column flange at the beam flange level was only observed in Specimen C4 (see Figure 5.13). Recorded strains in that region demonstrate strains of $4\epsilon_y$ at the edge of the column flange, diminishing to $2.5\epsilon_y$ several inches away [see Figure 5.14(a)]. Specimen C4 demonstrated strains on average of $3\epsilon_y$ with little gradient across the column flange [see Figure 5.14(b)]. Specimen C7 developed strains of $6\epsilon_y$, diminishing to $3.5\epsilon_y$ at the other gauge location [see Figure 5.14(c)]. It is noted that the recorded strains are influenced by the lateral-torsional response of the beam, which superimposes a weak-axis flexure

on the beam flanges. Weak-axis flexure of the beams changes the distribution of the flange forces between sides of the column while keeping the net flange force unchanged. For the specimens tested, at the gauge location, the positive excursion demonstrated the highest peak strain. Despite developing modest strains in an FLB type behavior, only Specimen C3 failed by fracture of the beam top flange CJP weld.

The moderate levels of strains recorded behind the beam flange suggest the initiation of a FLB yield line mechanism; however, the inclined yield line that would be expected to extend (Prochnow et al. 2000) from the radius of the column outward at an inclination away from the beam flange was not observed.

5.7. RBS Beam Lateral Bracing Force

During the Phase 1 testing program, the lateral bracing force of the lateral bracing at approximately $d_b/2$ away from the end of the RBS was monitored. The bracing force is normalized by the measured instantaneous beam flange force as determined from static equilibrium. Table 5.4 shows the computed normalized maximum bracing force recorded during testing. It is observed that the lateral bracing force of the specimens that terminated at 0.05 rad developed approximately 2% of the beam flange force. Specimen C6-G developed 5% of the measured flange force during the 0.05 rad drift cycles. Specimens C4 and C6-G developed 5.5% and 7.7%, respectively, of the measured flange force during the 0.06 rad drift cycles. The bracing force is compared to the required bracing force as per §D1.2b of AISC 341-16 for highly ductile members. This provision requires 6% of the expected beam flange force to be used when designing lateral bracing.

This chapter has been published as a Structural Systems Research Project (SSRP) Report: Reynolds, M., C-M., Uang, “Alternative Weld Details and Design for Continuity Plates and

Doubler Plates for Applications in Special and Intermediate Moment Frames," *Report No. SSRP-19/03,* and submitted to AISC as the final project deliverable.

Table 5.1 Specimen Performance Comparison

Spec. No.	Beam	Column	Continuity Plate (in.)	Doubler Plate	Cycle at Failure	Failure Mode
C1[a]	W30×116	W24×176	3/4	-	-	Not Tested to Failure (Stopped at 0.05 rad)
C2[a]	W36×150	W14×257	5/8	-	1st of 0.07 rad after 0.05 rad	RBS Fracture
C3	W36×150	W14×257	-	-	1st of 0.05 rad	Beam Top Flange CJP Weld
C4	W30×116	W27×235	-		1st of 0.06 rad	RBS Fracture
C5	W36×150	W14×211	3/8		2nd of 0.05 rad	Beam Top Flange CJP Weld
C6	W30×116	W24×176	1/2		1st of 0.05 rad	Beam Top Flange CJP Weld
C6-G[b]	W30×116	W24×176	1/2		1st of 0.06 rad	RBS Fracture
C7	W30×116	W24×192	-	1 × 5/8”	2nd of 0.05 rad	RBS Fracture
W1	W36×150	W27×258	1/2	2 × 5/8”	2nd of 0.04 rad	Beam Top Flange CJP Weld
W2	W33×141	W27×217	3/4	2 × 3/4”	2nd of 0.06 rad	Beam Top Flange CJP Weld
W3	W30×116	W24×207	1/2	2 × 1/2”	2nd of 0.06 rad	Beam Top Flange CJP Weld
W4	W24×94	W24×182	3/4	2 × 5/8”	1st of 0.05 rad	Beam Top Flange CJP Weld

a) Specimens tested and reported in Mashayekh and Uang (2018).

Table 5.2 Continuity Plate Design and Experimentally Determined Forces

Spec. No.	Expected per Design[a]					Experimental Results		
	Expected P_f (kips)	Cont. Plate b/t	w^b/t_{cp}	FLB (kips)	WLY (kips)	Measured P_f[c] (kips)	$\frac{\text{Measured } P_f}{\text{Expected } P_f}$	Local Buckling
C1	597	8.0	0.75	642	431	629	1.05	No
C2	745	9.6	0.80	1168	826	790	1.06	No
C3	738	-	-	1317	932	725	0.98	-
C4	611	-	-	859	620	667	1.09	-
C5	765	16.0	0.83	897	679	693	0.91	Yes
C6	582	12.0	1.00	640	430	627	1.08	No
C6-G	582	12.0	1.00	640	430	618	1.06	No
C7	558	-	-	799	917	594	1.07	-
W1	1127	12.0	0.75	1097	1716	997	0.88	No
W2	1002	7.8	0.75	816	1677	913	0.91	No
W3	826	11.0	0.75	894	1215	734	0.89	No
W4	745	7.3	0.75	527	1048	662	0.89	No

a) Values tabulated for F_{ya} and $\phi = 1$, FLB and WLY calculated as per AISC 360 §J10.1 and §J10.2.
b) Weld size, w, tabulated for continuity plate-to-column flange fillet weld.
c) Measured P_f derived by assuming 85% of the beam moment at the column face is resolved in the flanges.

Table 5.3 Doubler Plate Design and Experimentally Determined Forces

Spec.	Expected per Design							Experimental Results		
	t_{dp} (in.)	Expected V_{pz} (kips)	Panel Zone ϕR_n [a] (kips)	$0.6F_y d_c t_{pz}$ (kips)	$\frac{d_z + w_z}{t_{cw}}$	$\frac{d_z + w_z}{t_{dp}}$	Doubler Plate Vertical Weld	Measured V_{pz} [b] (kips)	$\frac{\text{Measured } V_{pz}}{\text{Expected } V_{pz}}$	Instability?
C1	-	596	745	664	68	-	-	620	1.04	No
C2	-	717	825	662	40	-	-	752	1.05	No
C3	-	710	761	611	40	-	-	691	0.97	No
C4	-	610	948	831	59	-	-	656	1.08	No
C5	-	678	626	518	48	-	-	661	0.97	No
C6	-	581	777	692	68	-	-	618	1.06	No
C6-G	-	581	777	692	68	-	-	609	1.05	No
C7	0.63	557	1494	1317	63	81	7/16 in. Fillet	585	1.05	No
W1	0.63	2040	2299	2173	61	95	PJP	1951	0.96	No
W2	0.75	2063	2402	2303	68	76	PJP	1747	0.85	No
W3	0.50	1729	1784	1672	58	102	11/16 in.	1439	0.83	No
W4	0.63	1472	1741	1661	64	72	7/8 in.	1367	0.93	No

a) Values tabulated a) Values tabulated for F_{ya} and $\phi = 1$; panel zone strength determined as per AISC 360 Eq. J10-11.
b) Panel zone shear, V_{pz}, determined from equilibrium.

Table 5.4 Specimen Beam Lateral Bracing Force Comparison

Spec. No.	Beam	Column	Connection	Failure of Specimen	Maximum Normalized Lateral Bracing Force (%)
C3	W36×150	W14×257	RBS	1st of 0.05 rad	2.2
C4	W30×116	W27×235	RBS	1st of 0.06 rad	5.5
C5	W36×150	W14×211	RBS	2nd of 0.05 rad	1.4
C6	W30×116	W24×176	RBS	1st of 0.05 rad	2.0
C6-G	W30×116	W24×176	RBS	1st of 0.06 rad	7.6

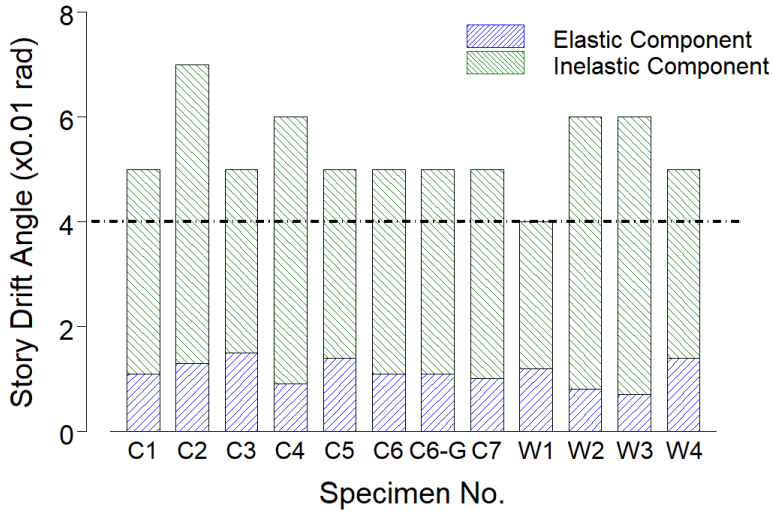

Figure 5.1 Summary of Specimen Story Drift Capacity

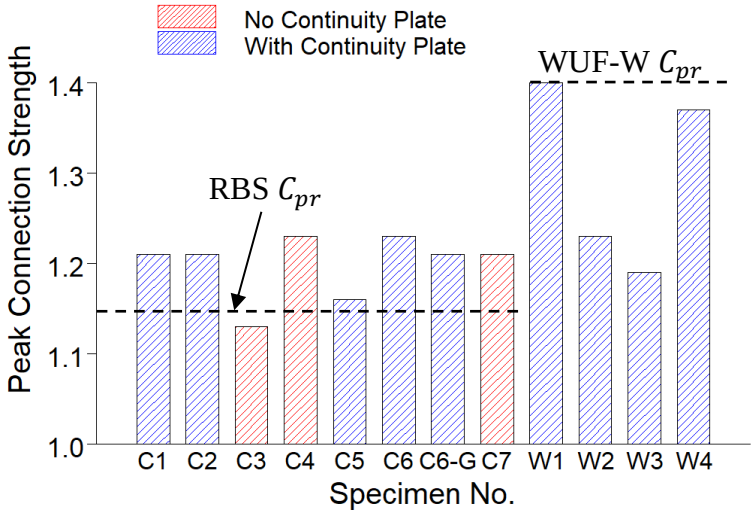

Figure 5.2 Summary of Measured Peak Connection Strength Factor, C_{pr}

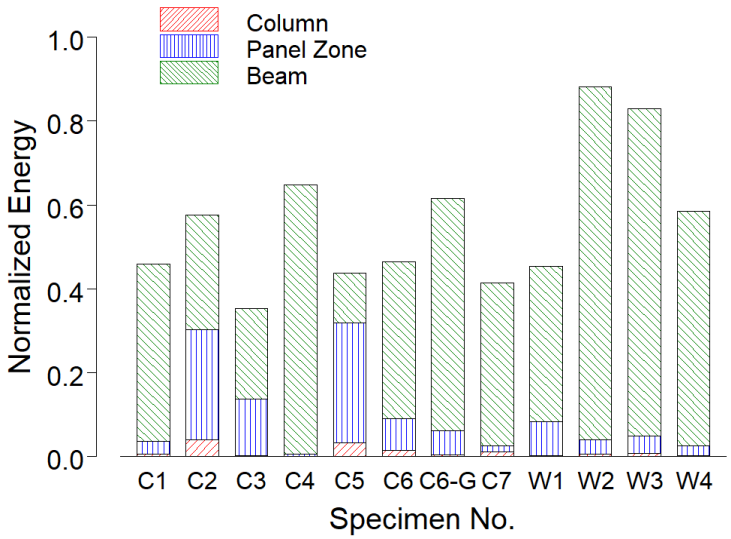

Figure 5.3 Summary of Normalized Energy Dissipation Capacity

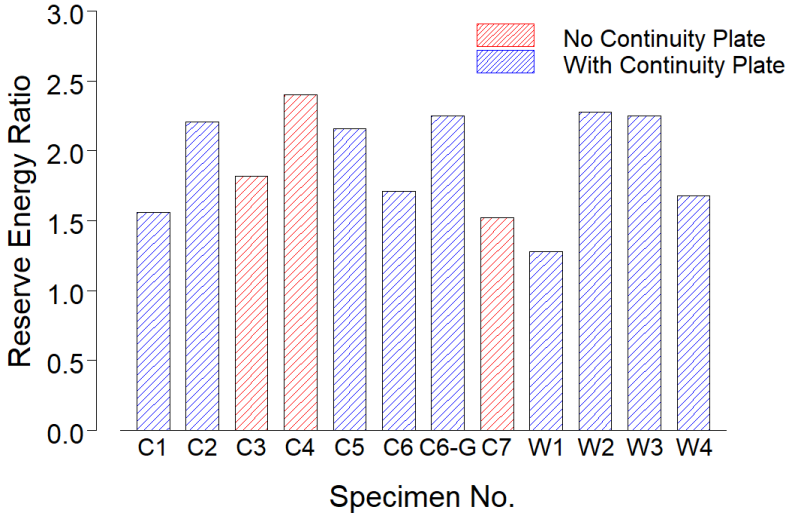

Figure 5.4 Summary of Reserve Energy Ratio

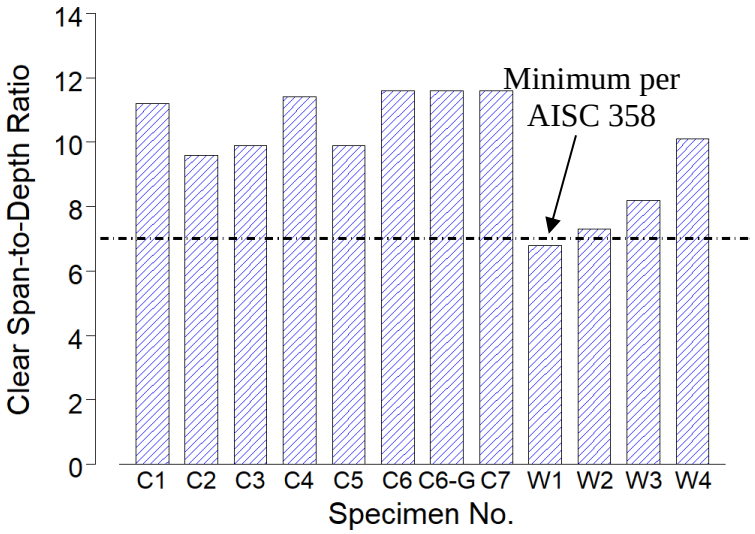

Figure 5.5 Summary of Beam Clear Span-to-Depth Ratio

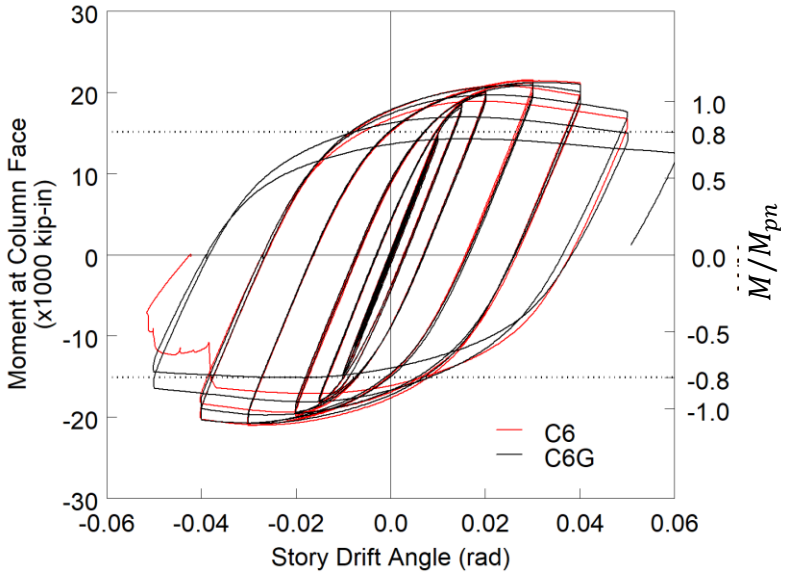

Figure 5.6 Comparison of Specimens C6 and C6-G Responses

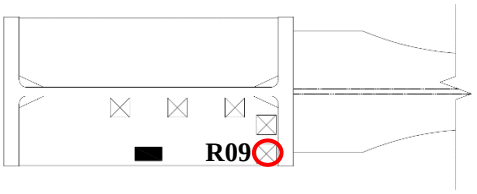

(a) One-Sided Gauge Position

(b) Two-Sided Gauge Position

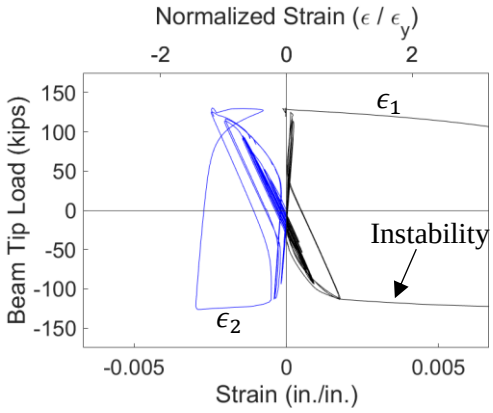

(c) Spec. C5 to (up to +0.04 rad, 1st Cycle)

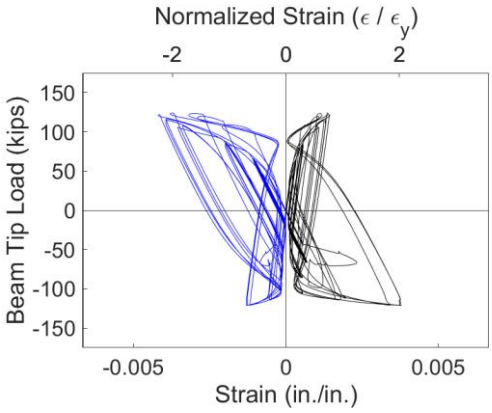

(d) Specimen C6

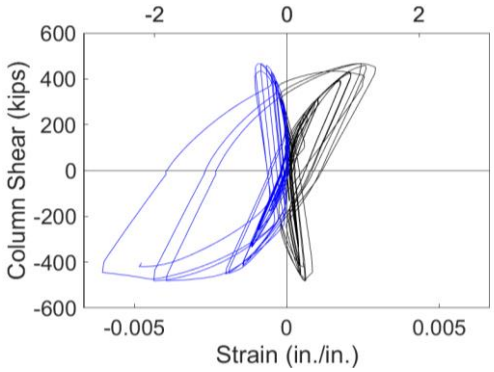

(e) Specimen W1

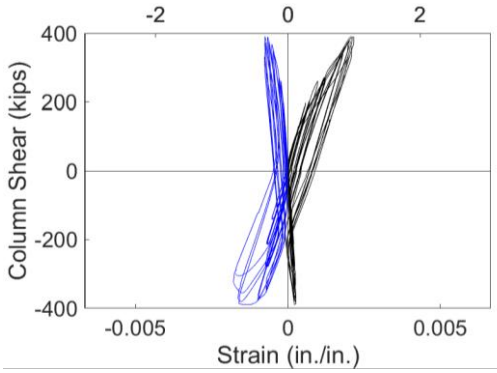

(f) Specimen W2

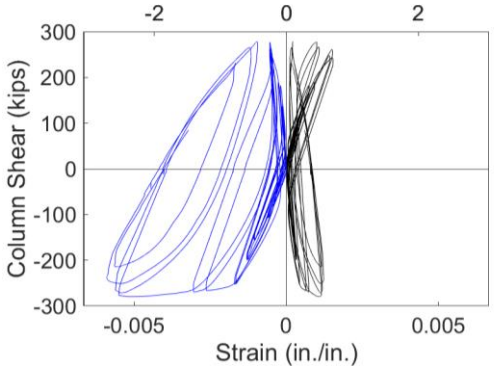

(g) Specimen W3

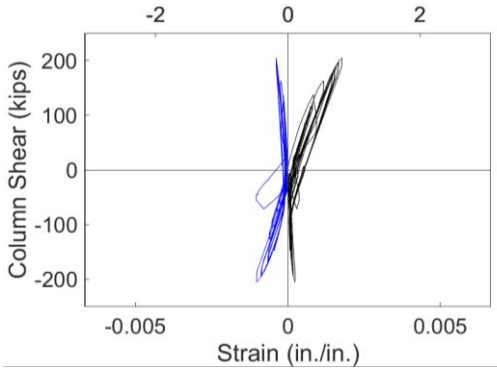

(h) Specimen W4

Figure 5.7 Continuity Plate Principal Strains

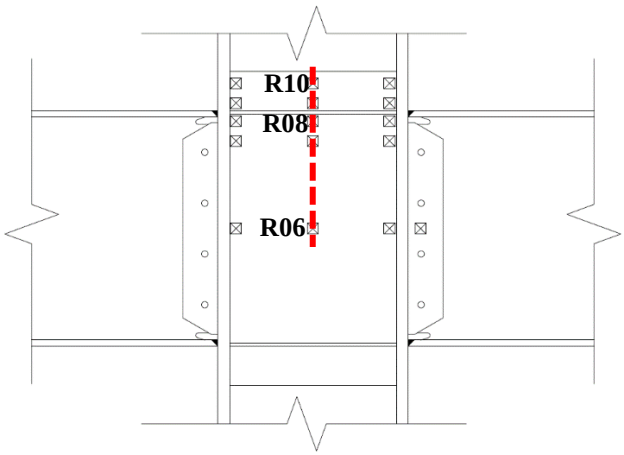

(a) Section Layout

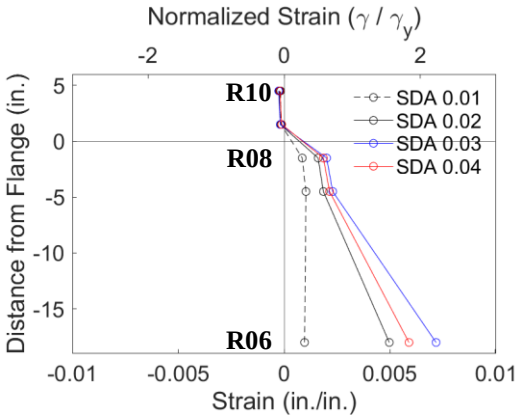

(b) Specimen W1

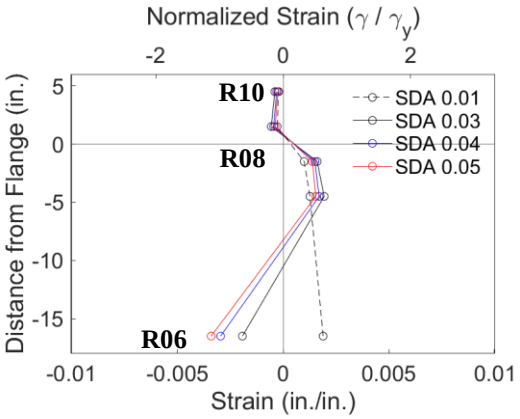

(c) Specimen W2

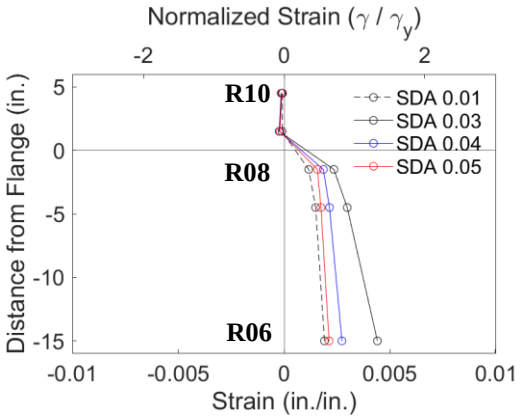

(d) Specimen W3

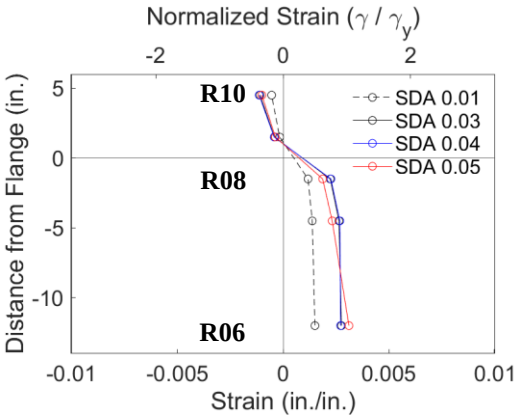

(e) Specimen W4

Figure 5.8 Doubler Plate Shear Strain Profiles (Positive Drift)

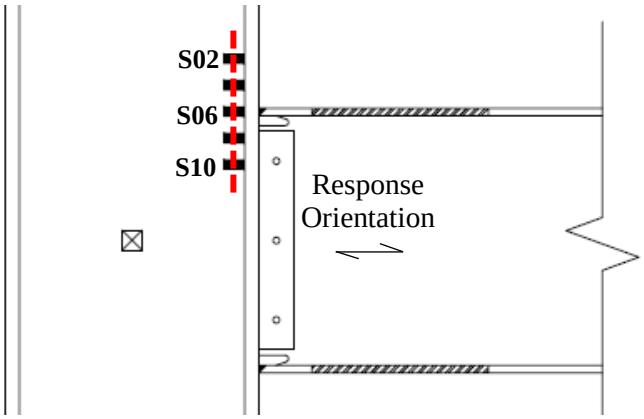

(a) Gauge Layout

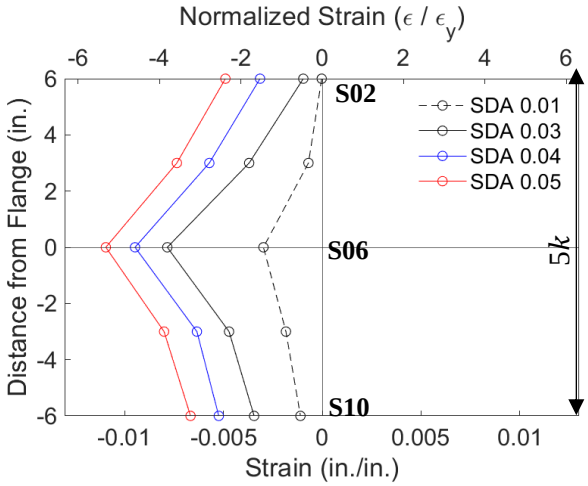

(b) Positive Drift

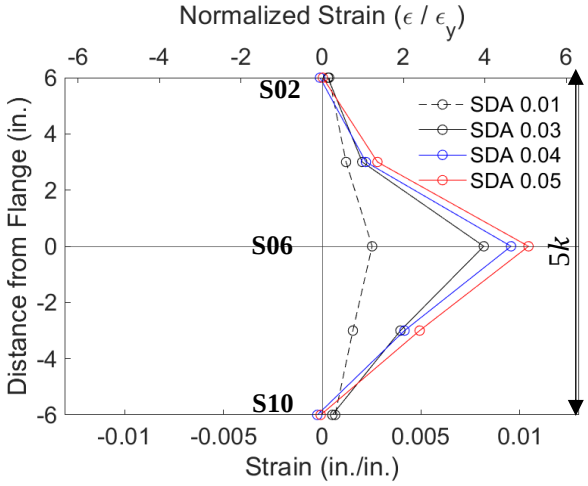

(c) Negative Drift

Figure 5.9 Specimen C4: Column Web Strain Profiles

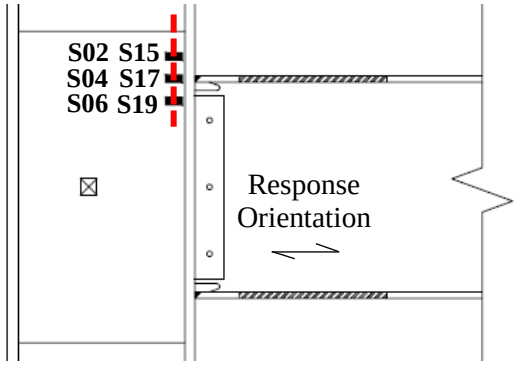

(a) Gauge Layout

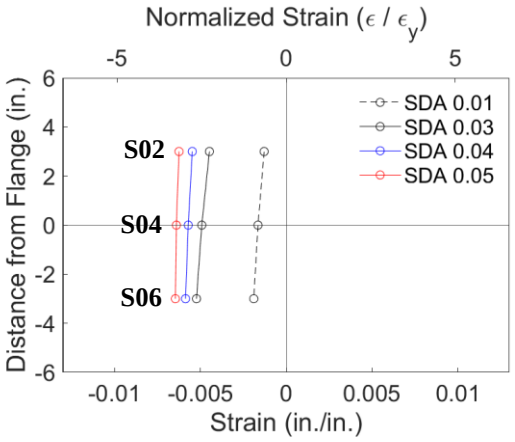

(b) Column Web (Positive Drift)

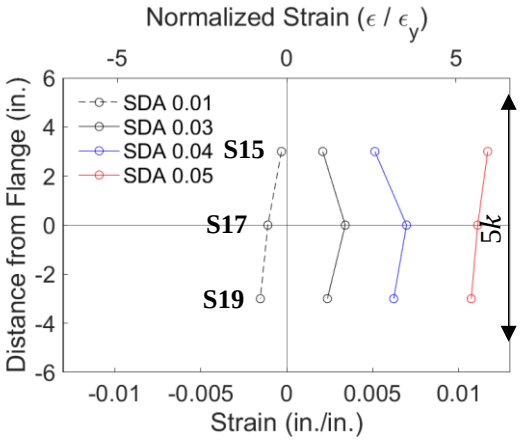

(c) Doubler Plate (Positive Drift)

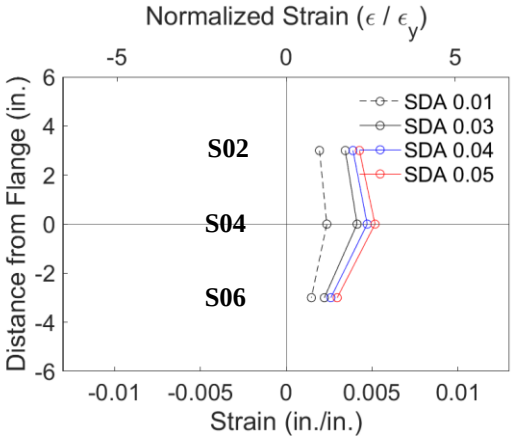

(d) Column Web (Negative Drift)

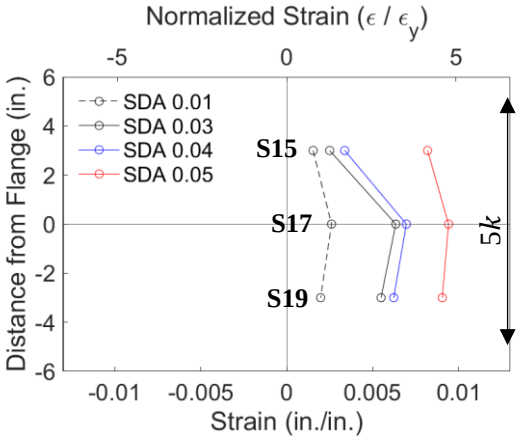

(e) Doubler Plate (Negative Drift)

Figure 5.10 Specimen C7: Comparison of Column Web and Doubler Plate Strains

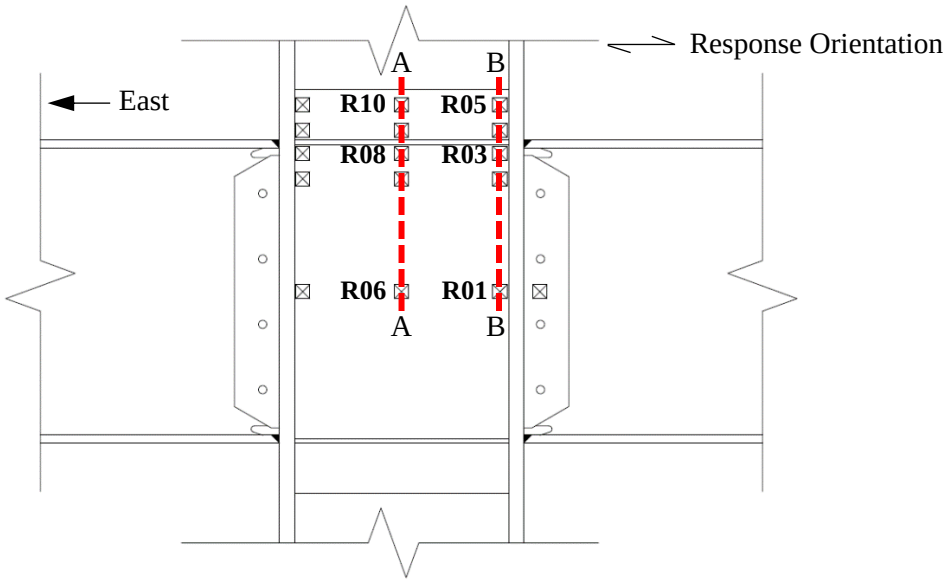

(a) Section Layout

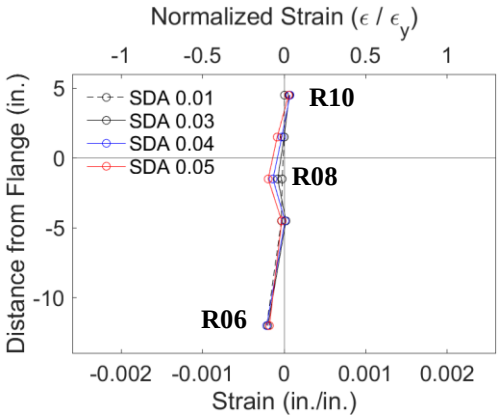

(b) Section A-A: Positive Drift

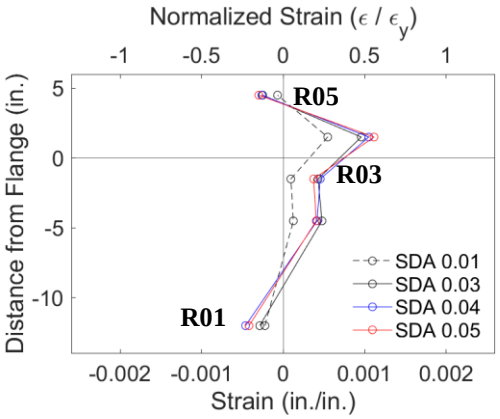

(c) Section B-B: Positive Drift

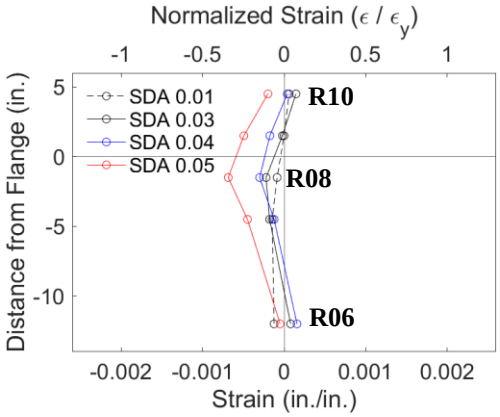

(d) Section A-A: Negative Drift

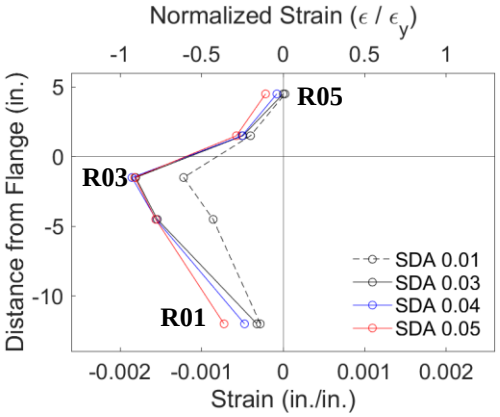

(e) Section B-B: Negative Drift

Figure 5.11 Specimen W4: Panel Zone Strain Profile

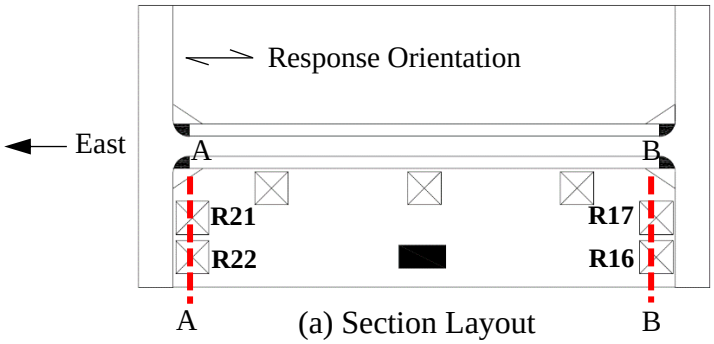

(a) Section Layout

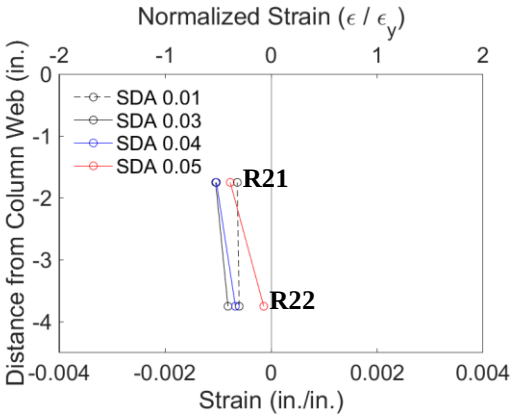

(b) Section A-A: Positive Drift

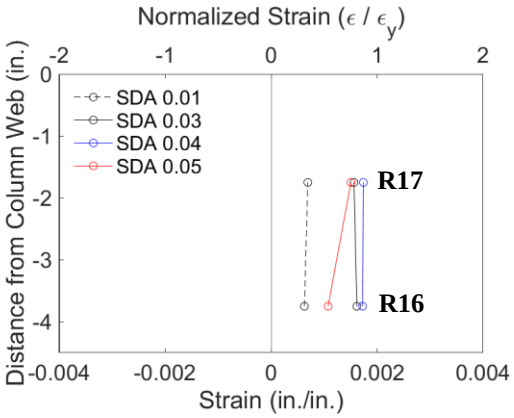

(c) Section B-B: Positive Drift

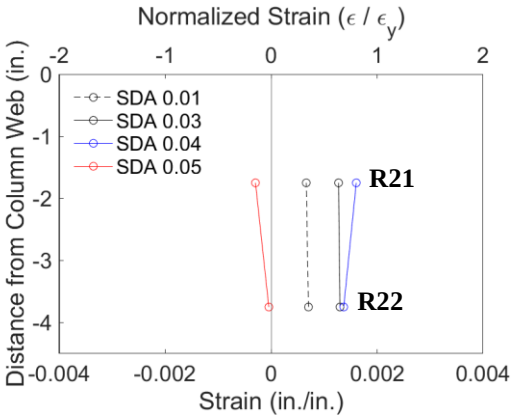

(d) Section A-A: Negative Drift

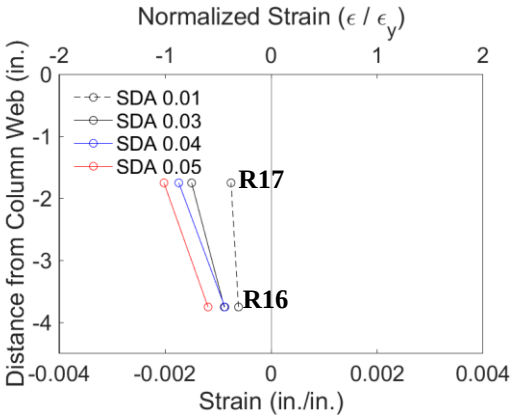

(e) Section B-B: Negative Drift

Figure 5.12 Specimen W4: Continuity Plate at Column Flange Edge Strain Profile

(a) Overview (b) Yielding

Figure 5.13 Specimen C4: Observed Column Flange Localized Yielding (End of Test)

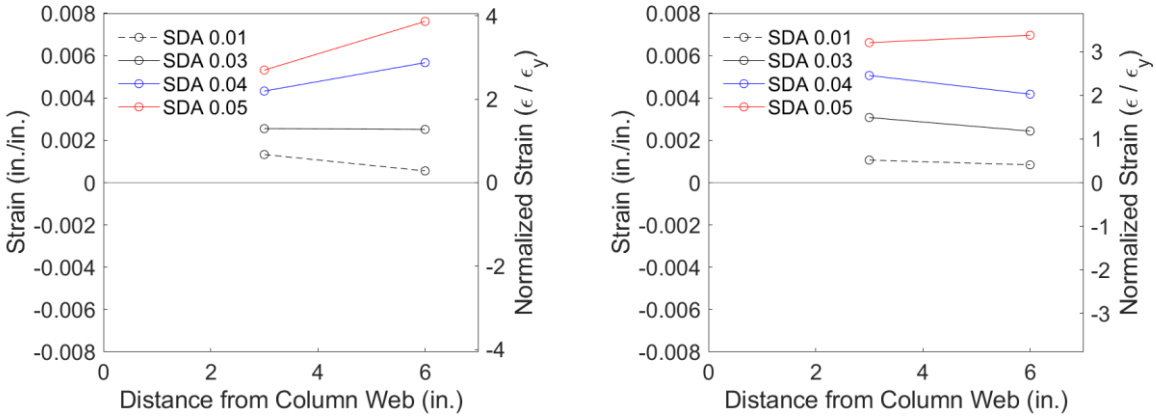

(a) Specimen C3 (b) Specimen C4

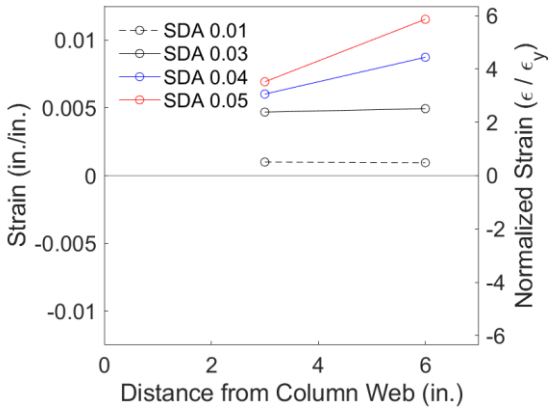

(c) Specimen C7

Figure 5.14 Recorded Column Flange Response (Positive Drift)

6. RESIDUAL STRESS MEASUREMENT OF CONTINUITY PLATE

6.1. General

Residual stress measurements have made for rolled and built-up I-shaped members (e.g., Tebedge et al. 1971). But such information on constructed moment connections i s very limited. Since this research is focused on alternative design and detailing of continuity plates in welded moment connections, it is of interest to know the magnitude and direction of residual stresses in continuity plates. This chapter presents a brief background of welding induced residual stress and measured residual stress levels of a subassemblage of a column (W27×258) with a $^{1}/_{2}$-in. welded continuity plate on each side of the column.

6.2. Background

Residual stresses are a set of self-equilibrating stresses in a component that remain in a part after the fabrication process. Residual stresses can arise due to uneven cooling of hot-rolled components and the latent stress fields from the intentional permanent deformation of cold-worked parts. Welding residual stresses develop from the uneven cooling of the weld metal and adjacent base metal. The newly joined parts typically restrain the contraction of the heated material; compatibility between the restraints and the newly welded part produce a set of self-equilibrating stresses. If the part was not restrained during cooling, the imposed global stress fields may be avoided at the cost of shrinkage or distortion of the parts. A simplified analysis to predict the amount of transverse shrinkage of welds is presented by Mandal and Sundar (1997). Despite avoiding global stress fields, localized residual tensile stress approaching the yield strength of the base material have been observed near the welds of welded joints (e.g., Pang and Pukas 1989). It is, therefore, understood that welding residual stresses belong to two distinct families: (1) stresses which develop locally near the interface between weld metal and base metal, and (2) stresses which

develop globally as a result of the restraint to the thermal contraction of the part following cooling (Macdonald 2011).

Significant residual stresses near the weld have led to fractures through the Heat-Affected Zone (HAZ) of the base metal (Miller 2015, and Ibrahim et al. 2016). This occurs when high, often near the yielding strength of the material, residual stress interacts with a microstructure susceptible to brittle fracture. The high residual stress near a weld increases the hydrostatic stress which leads to a diminished resistance to fracture (Hancock and Mackenzie 1976). The restraint that occurs when welding continuity plates has led to fractures of the k-area of rolled shapes which typically possess lower toughness due to the cold-working applied to the part to straighten the shape (Tide 2000). Residual stresses can be minimized by decreasing the heat deposition by selecting the minimum weld size required to weld the part and by weld detailing to avoid excess weld volumes. The restraint of the part can be limited by careful weld sequencing and preheating the parts to be welded (Ibrahim et al. 2018).

Measuring of residual stresses was first published in 1888 by measuring the change in length of bars extracted from a large part using a Whittemore strain gauge (Tebedge et al. 1971). The relaxation of the bars is related to the stress at that location in the part through the elastic modulus of material. This method is limited to extracting stresses in the longitudinal direction and averages the stress out over the volume of the bar extracted. In 1932, in order to determine the residual stress at a point instead of an aggregate, a similar concept of measuring the relaxation was instead performed surrounding a hole drilled through the material (Tebedge et al. 1971). The accuracy of this method was insufficient due to the resulting small gauge length across a drilled hole. Soete and Vancrombrugge (1950) extended the concept of measuring the relaxation strains during the drilling of a hole by drilling a hole through a set of strain gauges. A comparison between

the sectioning method and the hole-drilling method as presented by Soete and Vancrombrugge shows agreement between these two methods (Tebedge et al. 1971). However, the localized nature of the hole-drilling method can make interpretation of the result difficult. This was encountered by Sherry (2017), whose recorded spatial variation in residual stress of a hot-rolled member exceeded the magnitude of applied service loads.

Both the sectioning and hole-drilling methods of measuring residual stresses are destructive methods; several non-destructive methods exist which are not discussed because of their limited applicability or high cost in measuring residual stress in steel components. The hole-drilling method has been used to measure localized welding residual stresses (Pang and Pukas 1989) as well as global residual stresses due to the restraint (Hansen 2003).

6.3. Theory of Hole-Drilling Method

The preliminary theory is derived assuming a plate with a uniformly imposed uniaxial stress σ_x [see Figure 6.1(a)]. Consider the same plate with a through-hole of radius, R_o [see Figure 6.1(b)]. The stress state of Case A is $\boldsymbol{\sigma}'$, while the stress state of Case B is $\boldsymbol{\sigma}''$. The incremental stress caused by the drilling of the hole is expressed as $\boldsymbol{\Delta\sigma} = \boldsymbol{\sigma}'' - \boldsymbol{\sigma}'$. Expressing the incremental stress state in polar coordinates and substituting in equations of elasticity results in:

$$\varepsilon_r = \sigma_x[A + B\ cos(2\alpha)] \tag{6.1}$$

$$e_\theta = \sigma_x[-A + C\ cos(2\alpha)] \tag{6.2}$$

where ϵ_r and ϵ_θ are the radial and tangential strains as a function of α, the angle measured from an axis colinear with σ_x. The tangential strains are small and difficult to measure. To rectify this multiple sets of radial strains are taken to solve for the imposed stress, σ_x. The three constants, $A, B,$ and C are given as:

$$A = -\frac{1+\nu}{2E}\left(\frac{1}{r^2}\right) \tag{6.3}$$

$$B = -\frac{1+\nu}{2E}\left[\left(\frac{4}{1+\nu}\right)\frac{1}{r^2} - \frac{3}{r^4}\right] \tag{6.4}$$

$$C = -\frac{1+\nu}{2E}\left[-\left(\frac{4\nu}{1+\nu}\right)\frac{1}{r^2} + \frac{3}{r^4}\right] \tag{6.5}$$

where r is the normalized radial distance from the hole center, R/R_0. It is noted that constant C is not required if the tangential strains are not measured. The extension to a biaxial state of stress is readily accomplished by superposition:

$$\varepsilon_r = A(\sigma_x + \sigma_y) + B(\sigma_x - \sigma_y)\cos(2\alpha) \tag{6.6}$$

Solving for the three unknowns, σ_x, σ_y, and α requires at least three independent measurements of radial strains. Independence is readily achieved by offsetting the measurements by a known angle. For a typical 45° strain gauge rosette the offset is $\pi/4$. Numbering the three strain gauges as 1, 2, and 3, and their recorded strains as ϵ_1, ϵ_2, and ϵ_3 allows the determination of the principle stresses (σ_{max} and σ_{min}) as follows:

$$\sigma_{max} = \frac{\varepsilon_1 + \varepsilon_3}{4A} - \frac{1}{4B}\sqrt{(\varepsilon_3 - \varepsilon_1)^2 + (\varepsilon_3 + \varepsilon_1 - 2\varepsilon_2)^2} \tag{6.7}$$

$$\sigma_{min} = \frac{\varepsilon_1 + \varepsilon_3}{4A} + \frac{1}{4B}\sqrt{(\varepsilon_3 - \varepsilon_1)^2 + (\varepsilon_3 + \varepsilon_1 - 2\varepsilon_2)^2} \tag{6.8}$$

$$\tan(2\alpha) = \frac{\varepsilon_1 - 2\varepsilon_2 + \varepsilon_3}{\varepsilon_3 - \varepsilon_1} \tag{6.9}$$

where α is the angle measured from gauge 1 to the nearest principal axis. These equations assume an infinitesimal strain gauge. To extend Eq. 6.7 through Eq. 6.9 to a blind hole with a strain gauge of finite length, a set of modified coefficients ($\bar{A}$ and $\bar{B}$) are used. It assumed that the blind hole stress field possesses the same functional form as the through hole. The determination of constants $\bar{A}$ and $\bar{B}$ require numerical analysis as no analytical solution exists. In order to remove the material dependence, two alternative constants are used:

$$\bar{a} = \frac{2E\bar{A}}{1+\nu} \tag{6.10}$$

$$\bar{b} = -2E\bar{B} \tag{6.11}$$

The constants $\bar{a}$ and $\bar{b}$ are tabulated in ASTM E837 (ASTM 2008) as a function of the ratio of the drilled hole diameter D_o to the diameter of the measured radial strains D and the depth of the drilled hole normalized by the hole diameter (see Table 5.1). It is noted that this derivation assumes that the stress is uniform through the thickness of the material and that a state of plane stress is present. To increase the robustness of the method and minimize the influence of noise in the strain measurements the recommended procedure is to recorded data at many discrete hole depths as the hole is drilled. ASTM E837 provides a methodology to average out the reported strains using the appropriate $\bar{a}$ and $\bar{b}$ constants for each depth, i:

$$\sigma_x = E\frac{\sum\bar{b}_\iota\left(\epsilon_{3,i}-\epsilon_{1,i}\right)}{2\sum\bar{b}_\iota^{\,2}} - \frac{E}{1+\nu}\left(\frac{\sum\bar{a}_\iota\left(\epsilon_{3,i}+\epsilon_{1,i}\right)}{2\sum\bar{a}_\iota^{\,2}}\right) \tag{6.12}$$

$$\sigma_y = -E\frac{\sum\bar{b}_\iota\left(\epsilon_{3,i}-\epsilon_{1,i}\right)}{2\sum\bar{b}_\iota^{\,2}} - \frac{E}{1+\nu}\left(\frac{\sum\bar{a}_\iota\left(\epsilon_{3,i}+\epsilon_{1,i}\right)}{2\sum\bar{a}_\iota^{\,2}}\right) \tag{6.13}$$

$$\sigma_{xy} = -E\frac{\sum\bar{b}_\iota\left(\epsilon_{3,i}+\epsilon_{1,i}-2\epsilon_2\right)}{2\sum\bar{b}_\iota^{\,2}} \tag{6.14}$$

where σ_x is the component of stress colinear with gauge 1, and σ_y is the component of stress perpendicular to this and colinear with gauge 3 (see Figure 6.2).

6.4. Hole-Drilling Method Technique

The first step of performing the hole-drilling method is the typical installation of a strain gauge rosette (see Figure 6.3). Note that gauge 2 was omitted only for the verification of the method; typically all three gauges are recorded during drilling. For the research contained herein the strain gauge rosette designated as 062RE from Micro-Measurements with a gauge diameter,

D, of 0.202 in. is used. A drill holder is centered above the strain gauge using a microscope with the same bore diameter as the drill and securely held in place using three electromagnets (see Figure 6.4). The microscope is replaced with the pneumatic drill which was preconfigured to orbit the cutter to produce a hole diameter of $0.5D_0$—the maximum permitted hole diameter. This diameter was chosen to maximize the strain response of the strain gauge rosette. The cutter is lowered into contact with the strain gauge surface [see Figure 6.5(a)]. The cutter is then advanced until the bare metal is exposed under the gauge [see Figure 6.5(b)]. The drill is then advanced slowly and paused every 100 microns before recording the strains from all three strain gauges. Once the target depth is achieved of $0.4D$ (2.05 mm), the drill is removed from the holder [see Figure 6.6(a)]. Graduations on the microscope verify the diameter of the hole [see Figure 6.6(b)].

6.5. Hole-Drilling Method Verification

A verification of the hole-drilling method was performed by elastically loading a plate cut from the web of an W30×116 beam of A992 steel. A 36-in. long plate was used to mitigate boundary condition effects from the uniaxial load frame. Two uniaxial strain gauges and a strain gauge rosette was installed on each side of the plate at the mid length [see Figure 6.7(a)]. Uniaxial strain gauges placed on each quadrant of the plate allows correction of unintentional bending stresses in the plate. The plate was loaded uniaxially before (Case A) and after drilling a hole through one of the rosette gauges (Case B). To simplify the verification process, the final hole depth of $0.4D$ was drilled in a single session. Figure 6.8 shows the recorded strains before and after drilling the hole in the longitudinal and transverse directions.

The difference in gauge response between Case B and Case A at each load level is used to simulate the relaxation recorded while drilling a hole. Using experimentally determined values of Young's Modulus, E, of 29,500 ksi and Poisson's ratio, ν, of 0.25 and interpolating appropriate

values of $\bar{a}$ and $\bar{b}$ from Table 5.1, a predicted stress is generated for each load level (see Figure 6.9). Note that Poisson's ratio was evaluated by taking the ratio of the transverse to longitudinal strains of the strain gauge rosette prior to drilling the hole. Comparing the longitudinal stress response to the theoretical demonstrates excellent correlation [see Figure 6.9(a)]. The transverse strains demonstrate a peak of 0.25 ksi compared to the theoretical value of 0 ksi. A minor correction to the recorded stress values to remove the effect of unintentional plate bending was performed.

6.6. Measured Residual Stress in Continuity Plates

In order to evaluate the residual stresses in a continuity plate, the column top end of Specimen W1 was detailed such that one web side of the column's continuity plate conformed to the requirements of AISC 341 (2016b) with CJP groove welds to fasten the continuity plate to the column flange. The other web side of the column used fillet welds complying with the proposed fillet weld size of $(3/4)t$. Figure 6.10 shows the top end of the column of Specimen W1 after testing. It is anticipated that the top end of the column remained elastic during testing. Figure 6.11 shows the detailing used for the continuity plates at the top end of Specimen W1. Each continuity plate was sampled with 12 strain gauge rosettes placed within one-half of the continuity plate for residual stress measurements (see Figure 6.12).

Figure 6.13(a) shows a sample of the relieved strains recorded from one of the strain gauge rosettes during drilling; the strains correspond to the sign convention shown in Figure 6.12. As an intermediate step in computing the stress a series of combination strains are computed. Figure 6.13(b) shows the percent relieved combination strains, the resulting smoothness of the curve and conformance with theoretical curves in ASTM E837 indicates acceptable results. The measured residual stress patterns for the CJP and fillet welded continuity plates are shown in Figure 6.14 and

Figure 6.15. Both continuity plates demonstrate tension throughout the plate. The average tension in both plates is equal to 15 ksi. The tension in each continuity plate is a maximum at the outboard edge and decreases at the edge attached to the web. The CJP welded continuity plate demonstrates a small amount of compressive stress in the x direction. It is anticipated that the CJP welded, continuity plate was the first plate to be welded. When the fillet welded plate on the other side of the column was welded eccentrically compression load would be applied to the section, which may be the cause of the compressive stress. Furthermore, the more severe stress components of the fillet welded continuity plate are possibly due to the sequence of welding and not because of the type of weld used between the continuity plate and column flange. Figure 6.16 shows the measured residual stress across a transverse section at the centerline of the continuity plate (Section A) and at the web adjacent to the column flange (Section B). It is observed that the centerline of the continuity plate is in tension with the outboard edge experiencing the most severe tension. The edge adjacent to the column flange both develop a hat like response with the center of the continuity plate in excess of 20 ksi.

It is hypothesized that the magnitude of the residual stress in the continuity plate does not greatly influence the behavior of the connection after fabrication is complete due to the cyclic plastic behavior of the plate during loading. However, the minimizing of the residual stresses during fabrication will prevent premature fracture during weld cooling.

Table 6.1 Hole-Drilling Method: Table of Coefficients (ASTM 2008)

Normalized Depth, Z/D	$\bar{a}$					$\bar{b}$				
	Hole Diameter, D_o/D					Hole Diameter, D_o/D				
	0.3	0.35	0.4	0.45	0.5	0.3	0.35	0.4	0.45	0.5
0.00	0.000	0.000	0.000	0.000	0.000	0	0	0	0	0
0.05	0.027	0.037	0.049	0.063	0.080	0.051	0.069	0.090	0.113	0.140
0.10	0.059	0.081	0.108	0.138	0.176	0.118	0.159	0.206	0.255	0.317
0.15	0.085	0.115	0.151	0.192	0.238	0.180	0.239	0.305	0.375	0.453
0.20	0.101	0.137	0.177	0.223	0.273	0.227	0.299	0.377	0.459	0.545
0.25	0.110	0.147	0.190	0.238	0.288	0.259	0.339	0.425	0.513	0.603
0.30	0.113	0.151	0.195	0.243	0.293	0.279	0.364	0.454	0.546	0.638
0.35	0.113	0.151	0.195	0.242	0.292	0.292	0.379	0.472	0.566	0.657
0.40	0.111	0.149	0.192	0.239	0.289	0.297	0.387	0.482	0.576	0.668

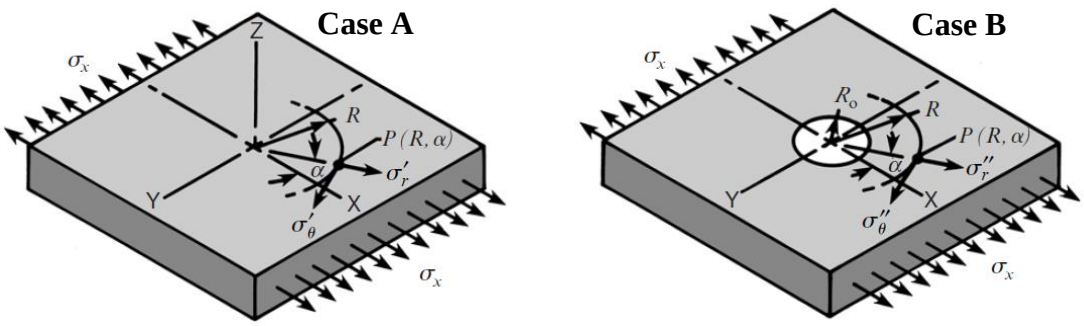

(a) Uniformly Loaded Plate (b) Uniformly Loaded Plate with Hole

Figure 6.1 Hole-Drilling Method: Stress Fields (Micro-Measurements 2010)

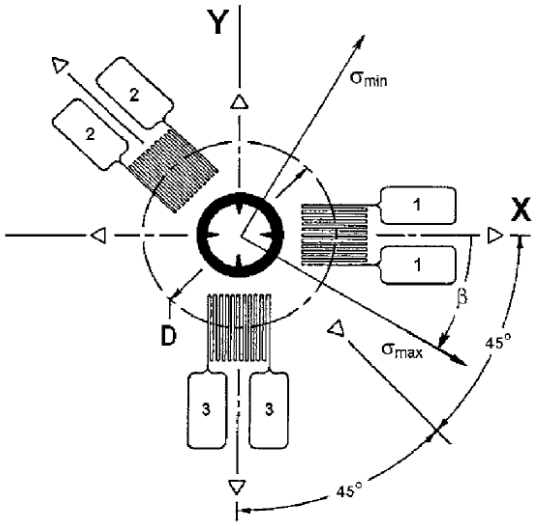

Figure 6.2 Hole-Drilling Method: Sign Convention (ASTM 2008)

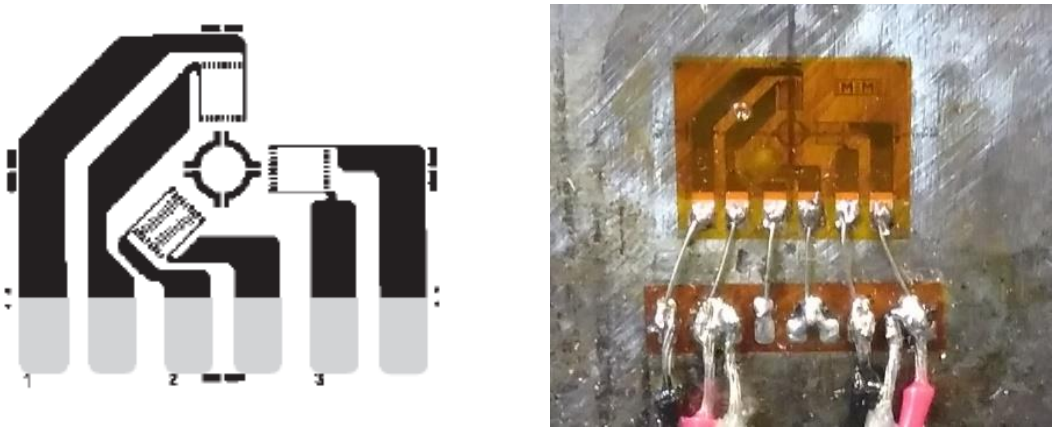

(a) Strain Gauge (062RE) (b) Installed Strain Gauge

Figure 6.3 Hole-Drilling Method: Strain Gauge Rosette

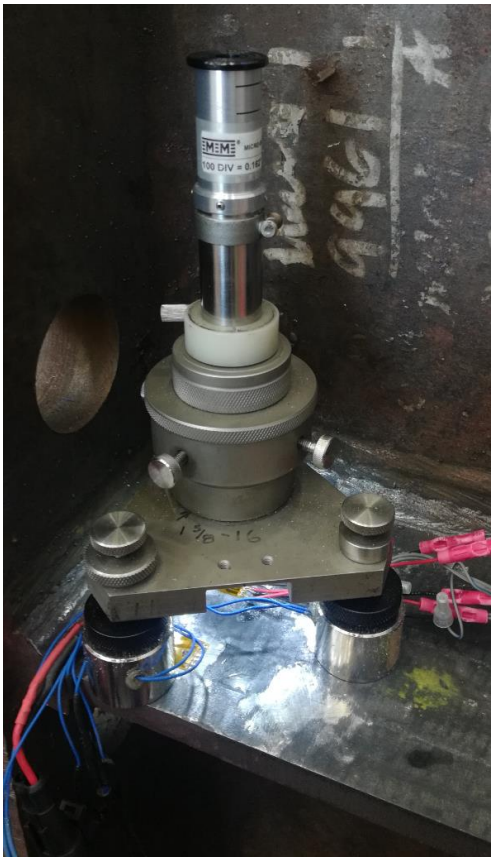

Figure 6.4 Hole-Drilling Method: Drill Positioning

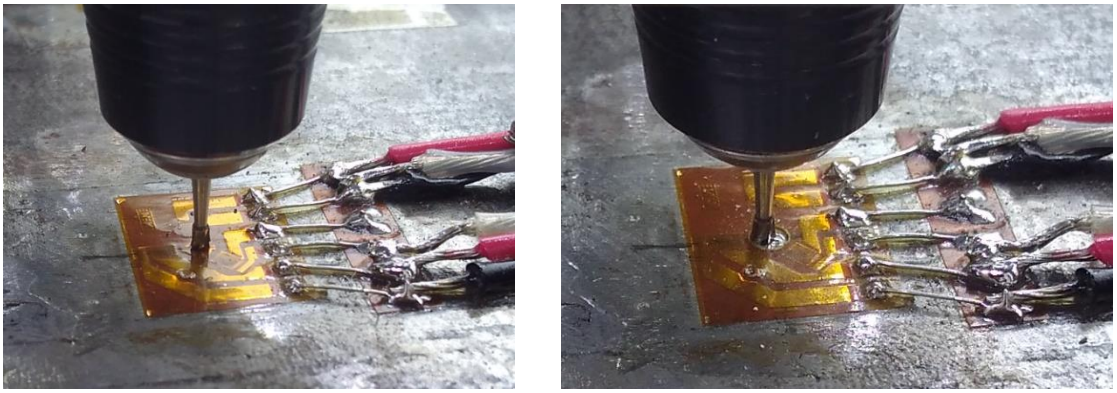

(a) Contact with Gauge (b) Exposed Bare Metal

Figure 6.5 Hole-Drilling Method: Initial Drilling

(a) Completed Gauge (b) Diameter Verification

Figure 6.6 Hole-Drilling Method: Completed Drilling

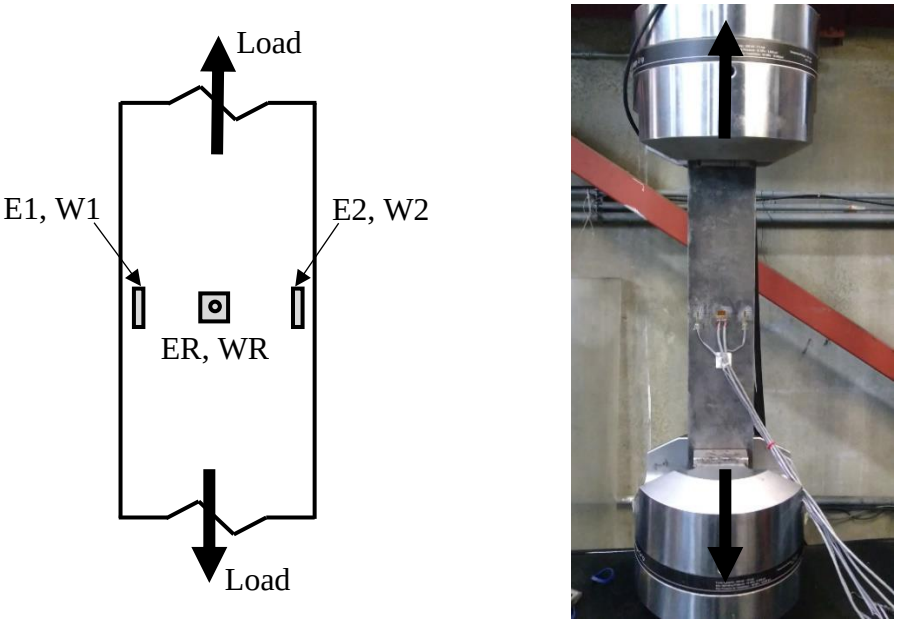

(a) Gauge Layout (b) Experimental Setup

Figure 6.7 Hole-Drilling Method: Verification Setup

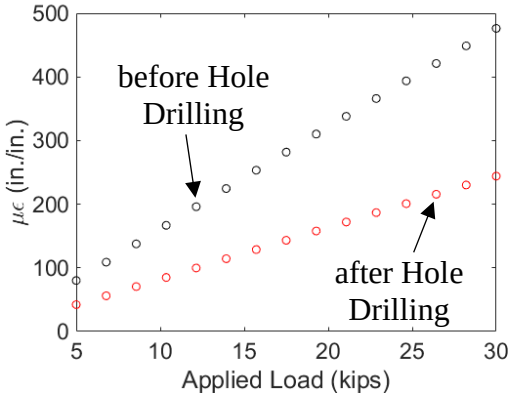

(a) Longitudinal Strains

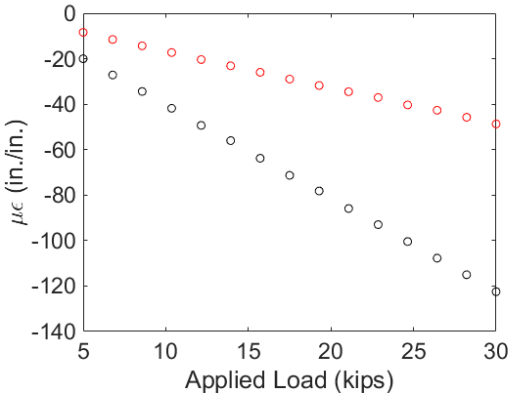

(b) Transverse Strains

Figure 6.8 Hole-Drilling Method: Verification Strains

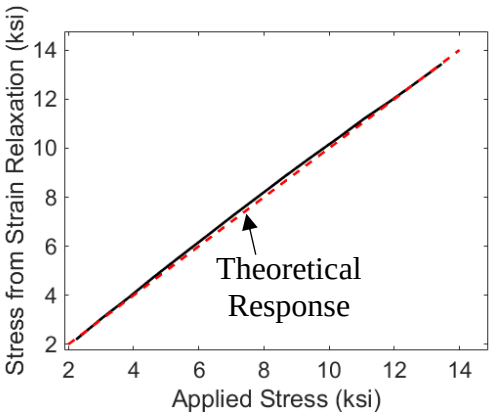

(a) Longitudinal Stress

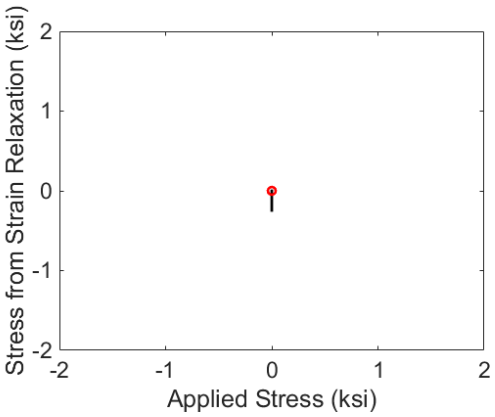

(b) Transverse Stress

Figure 6.9 Hole-Drilling Method: Verification Stresses

Figure 6.10 Specimen W1: Column Top-End Continuity Plates

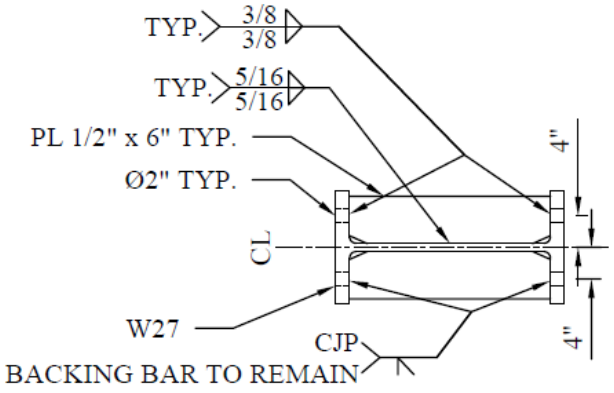

Figure 6.11 Specimen W1: Column Top-End Detail

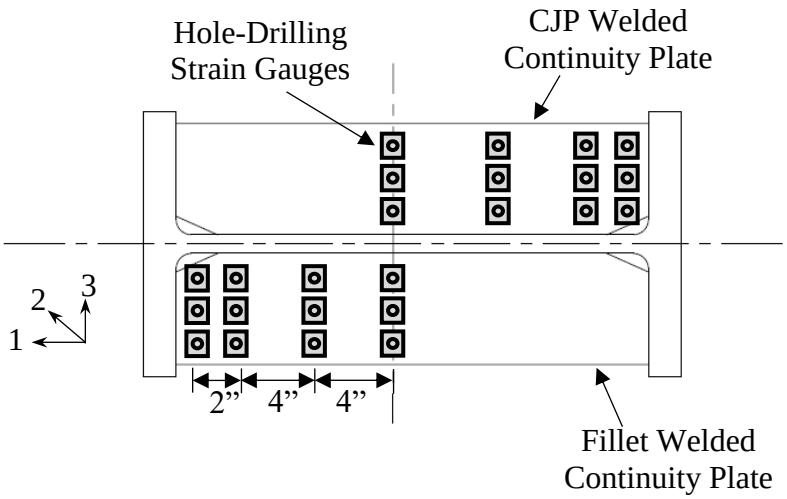

Figure 6.12 Specimen W1: Hole-Drilling Strain Gauge Layout

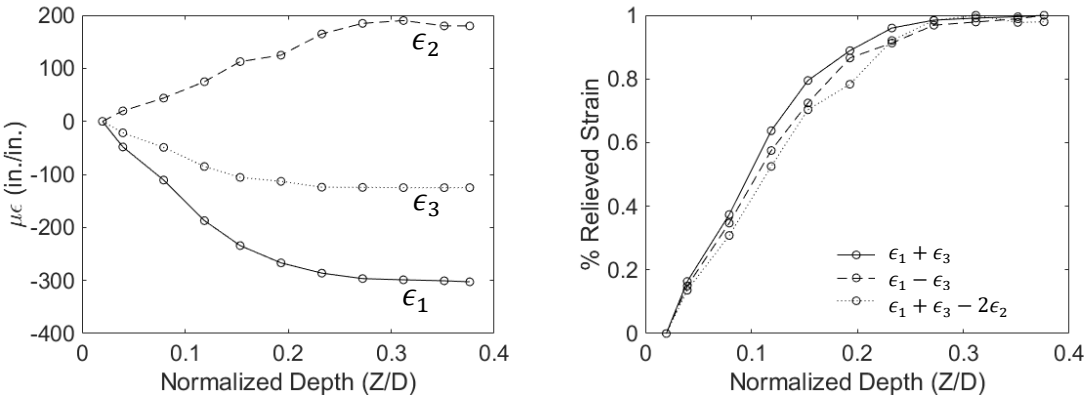

(a) Raw Strains (b) Combination Strains

Figure 6.13 Sample Relieved Strains

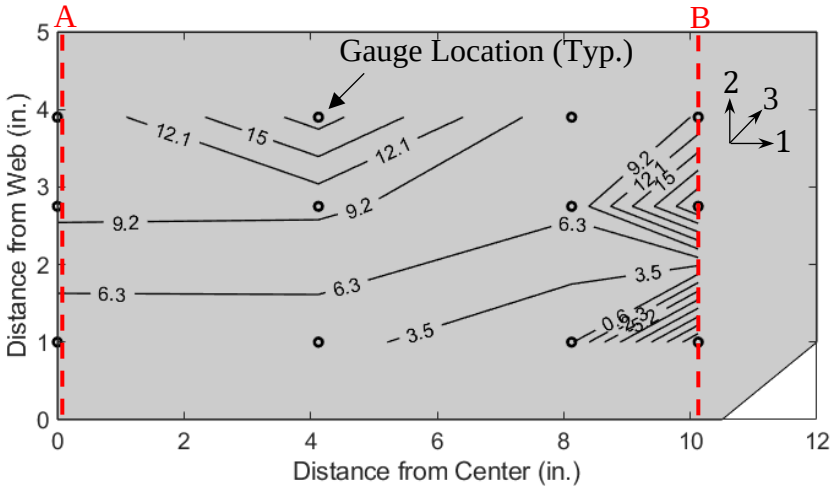

(a) Longitudinal Stress, σ_1 (ksi)

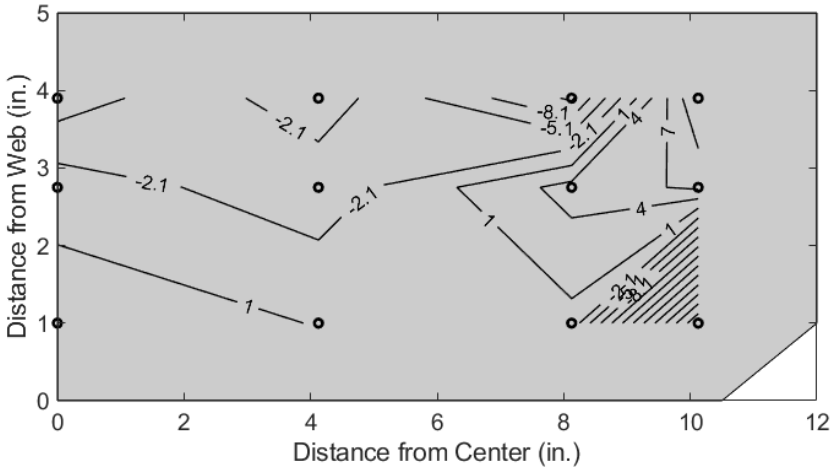

(b) Transverse Stress, σ_2 (ksi)

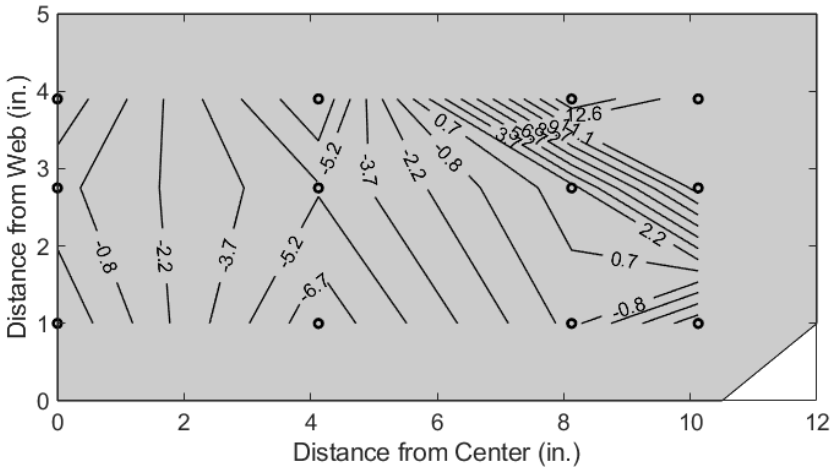

(c) Shear Stress, σ_3 (ksi)

Figure 6.14 CJP-Welded Continuity Plate Residual Stress Contours

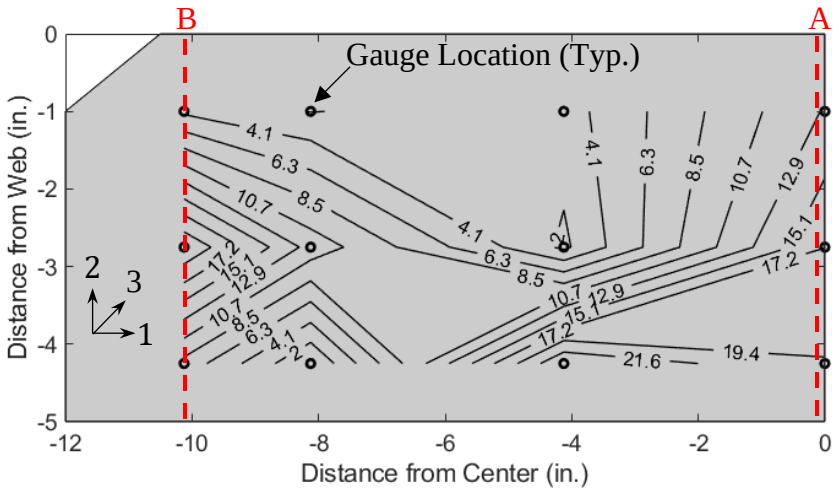

(a) Longitudinal Stress, σ_1 (ksi)

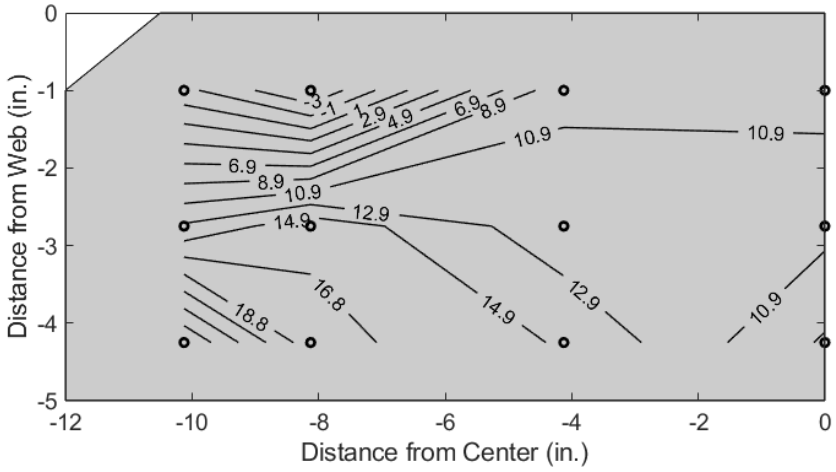

(b) Transverse Stress, σ_2 (ksi)

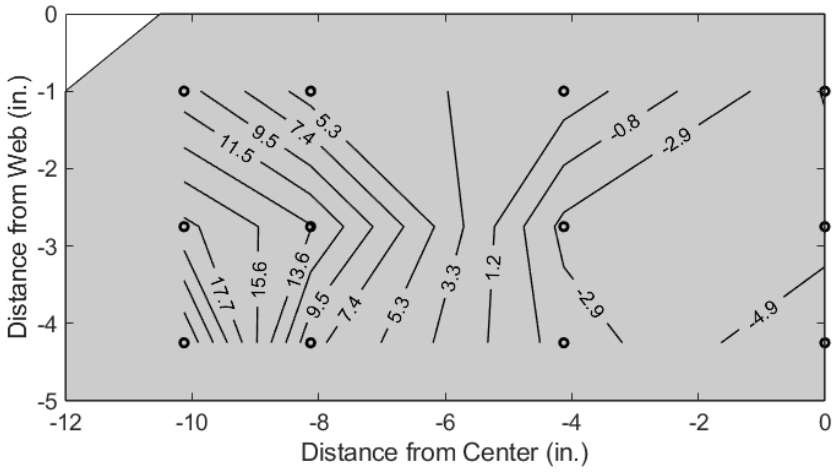

(c) Shear Stress, σ_3 (ksi)

Figure 6.15 Fillet-Welded Continuity Plate Residual Stress Contours

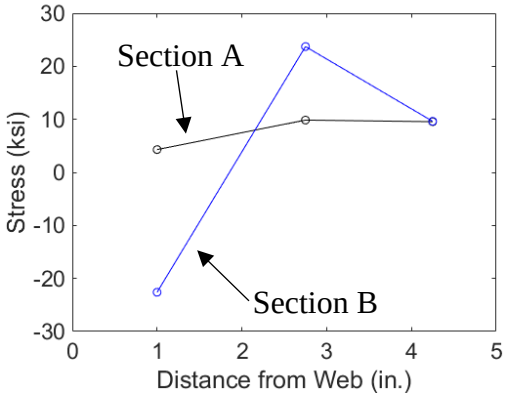

(a) CJP-Welded

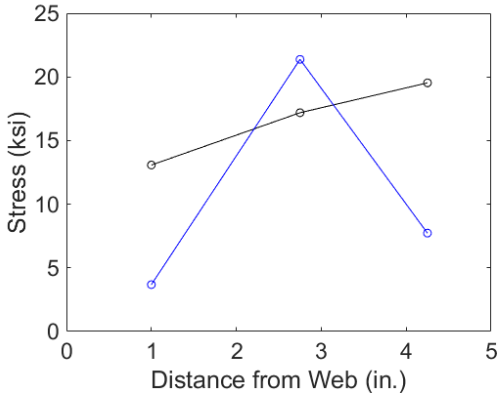

(b) Fillet Welded

Figure 6.16 Measured Continuity Plate Longitudinal Residual Stress

7. FINITE ELEMENT STUDIES AND VERIFICATION OF PROPOSED DESIGN

7.1. General

This chapter presents the modelling techniques used to create and analyze finite element models representing beam-column moment frame sub-assemblies. Finite element analysis was performed using the software package ABAQUS CAE (2014). Analysis workflow was improved through the incorporation of MATLAB and Python scripting. The finite element analysis is verified based on the global load-displacement response of the specimens, observed displacement patterns, and local estimates of accumulated plastic strain, $PEEQ$, recorded during the experimental testing.

Based on the finite element results and reinforced by experimental testing observations, a new design methodology is presented for continuity plates. Continuity and doubler plate weld design methodology remains unchanged from the derivations in Chapter 2. To verify the design methodology, a set of parametric analyses was performed on several representative connections.

7.2. Modeling Methodology

The models were made entirely with plate geometries and subsequently meshed with shell elements. Plate geometries of the beam and column were constructed first such that the web of the rolled shapes intersected the inside face of the flanges; the influence of the radius between the web and flange of the rolled shape was neglected. Subsequent section definition for the shells used the offset technique to define the thickness of the shell outward from its plate definition. Using this technique prevents double counting plate thickness where the flange and web would overlap if the shell plate centerline was used to define the shell elements. In models that utilize a Reduced Beam Section, the appropriate cut is removed from both flanges of the beam. Similarly cuts from the

beam web to represent the top and bottom weld access holes are made. Figure 7.1 shows the plate definition of a sample one-sided moment connection model.

Tie-constraints were used to fasten the beam subassembly to the column subassembly such that the beam end would be positioned at the outside surface of the shell definition (see Figure 7.2). The tie-constraints are set to honor the offset provided by the column flange thickness (ABAQUS 2014). The boundary conditions at either end of the column and far end of the beam utilize tie-constraints to link the ends of the column or beam to a master node (see Figure 7.3). Tie constraints honor the rotation of the displacement boundary conditions such that extra restraint is not accidently supplied to model. Additional boundary conditions are applied that prevent the lateral movement of the beam at a distance of $d_b/2$ away from the plastic hinge location to minimize lateral-torsional buckling of the beam and reflect the experimental setup. The model was meshed using a quad-dominated scheme to avoid issues of shear locking with triangular elements. Elements types were specified as S4 (four-node linear shell element with complete integration) with five integration layers through thickness. Complete integration was used to preclude a requirement for hourglass control; model sizes did not warrant reduced integration. Mesh refinement was performed in the connection region to provide better fidelity (see Figure 7.4).

In order to adequately capture the cyclic material non-linearity of the model, the material models must move beyond traditional non-linear material models using the true stress strain curve from a monotonic tension coupon (Crisan 2016). The simplest hardening rule would allow the yield surface of the material to expand or contract such that:

$$f(\sigma_{ij}) - K = 0 \tag{7.1}$$

where σ_{ij} are the Cauchy stress components and K is a state variable that governs the uniform change in size of the yield surface. This type of hardening is referred to as isotropic hardening.

Isotropic hardening is unable to capture the Bauschinger effect where a material will yield earlier upon a loading reversal then predicted by the current yield surface size if isotropic hardening had been assumed to act alone. To accommodate this effect, the yield surface is allowed to shift to produce kinematic hardening:

$$f(\sigma_{ij} - \alpha_{ij}) = 0 \tag{7.2}$$

where α_{ij} is the back-stress which describes the new evolved origin of the yield surface (Kelly 2019). To adequately capture the complexities of an expanding and shifting yield surface a mixed hardening model is required:

$$f(\sigma_{ij} - \alpha_{ij}) - K = 0 \tag{7.3}$$

The mixed model utilized in ABAQUS is from the work of Lemaitre and Chaboche (1990), which extends the classical Armstrong-Frederick model to use a non-linear evolution of the k'th back-stress as (ABAQUS 2014):

$$\dot{\boldsymbol{\alpha}}_{\boldsymbol{k}} = \frac{C_k \dot{\epsilon^p}}{\sigma^0}(\boldsymbol{\sigma} - \boldsymbol{\alpha}) - \gamma_k \boldsymbol{\alpha}_{\boldsymbol{k}} \dot{\epsilon^p} + \frac{1}{C_k}\boldsymbol{\alpha}_{\boldsymbol{k}} \dot{C}_k \tag{7.4}$$

where C_k is the initial kinematic modulus for the k'th backstress, and γ_k describes its decay rate with accumulated effective plastic strain. The current size of the yield surface, σ^o, is given by:

$$\sigma^o = \sigma_0 + Q_\infty\left(1 - e^{-b\epsilon^p}\right) \tag{7.5}$$

where Q_∞ describes the maximum change of the yield surface, and b is the rate of change of the yield surface. The initial size of the yield surface is σ_0. Calibration of the parameters (a minimum of four parameters if one back-stress is used) is readily accomplished by regression of a cyclic coupon test. The isotropic parameters, Q_∞ and b, are calibrated by curve fitting the evolved size of the peak stress over several cycles of a constant strain amplitude experiment. A key difficulty in this approximation is that these parameters vary based on the magnitude of strain chosen. It is

therefore recommended to implement several sets of variables or choose a set that best represents the magnitude of strains of interest. Kinematic hardening parameters are calibrated by calculating the evolution of the back-stress from a stabilized cycle, i.e., once the isotropic hardening capability of the material has been exhausted. To accomplish this multiple sets of back-stress parameters can be implemented.

Calibrating the material parameters is subject to errors of overfitting as a minimum of four parameters are fit to two independent variables of a global load-displacement response. The overfitting of variables can lead to solutions which may require manual intervention to find the best set of variables (Crisan 2016). To circumvent this issue, researchers have proposed fitting the models as a best fit across multiple cyclic tension coupons with unique strain histories (Smith et al. 2014). The cyclic hardening parameters used for this research are calibrated using the aforementioned procedure and are fine-tuned based on work at the University of California San Diego, where the parameters were calibrated based on the cyclic response of 23 full-scale deep column tests (Chansuk et al. 2018). These parameters utilize only one back-stress and are found to produce excellent correlations with the experimental results of the herein tested full-scale SMF moment connection specimens. Figure 7.5 shows the ability of the material parameters to reproduce to the stress-strain curve from the tension coupon obtained from the beam flange of Specimen C6. The black lines in this figure represent the true and engineering stress strain coupon results. The components of the reproduced stress-strain response are separated into the isotropic size of the yield surface, σ^o, and the kinematic evolution of the yield surface α. In order to produce a correlation with the tested AISC specimens, the beam and column flanges use the measured yield stress as the initial size of the yield surface, σ_0. However, to correlate with design specifications, the continuity and doubler plates in the finite element models assume that the nominal initial yield

surface of σ_0 is 50 ksi. Excellent correlation between the experimental load-displacement response is observed (see Figure 7.6).

Geometric non-linearity is modelled in ABAQUS by defining the NLGEOM option within each explicit analysis step. Often it is required to impose initial imperfections through the mode shapes of the stiffness matrix to trigger geometric instability and avoid issues of a perfect analysis model failing to buckle. However, it is found that imposing geometric imperfections is not necessary in these shell models to develop local buckling. The local buckling observed in the finite element analysis generally conform to the observed patterns (see Figure 7.7).

The parametric analysis was performed by interacting with the ABAQUS kernel through a software suite developed to perform moment frame finite element analysis. MATLAB was used to manage a set of Python scripts which in turn interact natively with ABAQUS. The MATLAB framework sequentially modifies the Python scripts responsible for constructing the geometry and mesh of the finite element models. MATLAB then manages the job queue by submitting each finite element model to the ABAQUS kernel. MATLAB is used to parse the finite element output database and perform numerical operations like integrate shells to develop section forces and create figures. For consistency the data from the parametric runs are extracted from the first negative excursion to 0.04 rad drift.

7.3. Representative Connection Behavior

To investigate detailed connection behavior, Specimen C6 was chosen to represent a standard one-sided RBS connection using continuity plates that conform to AISC 341-16. Figure 7.6 compares the global response of the finite element model to the experimentally recorded response. A qualitative comparison on the deformed shape of the specimen is shown in Figure 7.7; general conformance to the buckled shape is observed. Figure 7.8 identifies several sections that

are used throughout the finite element analysis discussion. The response of the continuity plates at the beam top flange level is shown in Figure 7.9. This figure shows the average von Mises stress at the centroid of each element along the continuity plate-to-column flange weldment. A gap in the center of the plot represents the continuity plate corner clips that are symmetric about the column web centerline. The elastic cycles (SDA = 0.01 rad) show a trapezoidal stress distribution; note that this trapezoidal distribution is inverted when compared with the original flexibility methodology introduced by Tran et al. (2013). In the elastic stage the higher relative stiffness of the continuity plate edge affixed the column web attracts more of the axial load.

When the continuity plate yields, the stress distribution across the edge (WCPf and ECPf) become essentially uniform. A small increase of the stress is observed at the outboard edge of the continuity plate due to the protrusion of the column flange beyond the continuity plate. It is observed that the lateral-torsional buckling of the beam significantly influences the stress in the continuity plate. In this case the more severe beam flange local buckling on the west side of the beam resulted in less force entering the west continuity plate. During negative excursions the continuity plates on either side of the column see nearly equal loading as the top flange of the beam is pulled straight.

The shear stress distribution of the continuity plates is observed in Figure 7.10. The elastic shear distribution mimics the von Mises stress distribution with the portion near the column web. East and west sides of the continuity plate show opposite signs of response—which respect equilibrium of the individual plates. The predicted average shear stress in the continuity plate is found by dividing Eq. 2.17 by the net area of the continuity plate:

$$\sigma_{12} = \frac{\gamma F_y}{\sqrt{1 + 3\gamma^2}} \tag{7.6}$$

The expected ratio of shear force-to-axial force in the continuity plate, γ, is found to be 0.175 (see Eq. 2.13), which results in an average shear stress of 8.6 ksi. The inelastic cycles of the continuity plate prior to the lateral-torsional buckling of the beam generally confirm this assertion.

Figure 7.11 shows the distribution of the equivalent plastic strain (Eq. 1.3), $PEEQ$, and the $PEEQ$ Index (Eq. 1.5) across the continuity plate. Higher $PEEQ$ values are obtained at the outboard edges of the continuity plate—an effect attributed to the higher flexibility. On average at a SDA of 0.04 rad an average value of $PEEQ$ Index of 40 is obtained. This corresponds to a cumulative strain ductility of 10 (i.e., 10 complete cycles of constant amplitude plastic strain equal to ϵ_y).

To compare the finite element results with obtained strain gauge data from Specimen C6, the strain gauge rosette is first manipulated to generate the plastic strain response:

$$R_i^p = R_i - \frac{P_{act}}{k_i} \tag{7.7}$$

where R_i are the three rosette strain channels, P_{act} is the measured actuator load and k_i is the channel stiffness obtained from a linear regression of the elastic portion of the gauge. The three strain gauge rosette channels represent their corresponding directions of strain (e.g., $R_1^p = \epsilon_{11}^p$). Manipulating Eq. 1.3 for plane strain produces the following metric for incremental plastic strain:

$$d\epsilon^p = \sqrt{\frac{2}{3}\left(d{\epsilon_{11}^p}^2 + d{\epsilon_{22}^p}^2 + 2d{\epsilon_{12}^p}^2\right)} \tag{7.8}$$

Integrating the incremental effective plastic strain produces the effective plastic strain:

$$\epsilon^p = PEEQ = \int_0^t d\epsilon^p \tag{7.9}$$

Figure 7.12 demonstrates the comparison of the accumulated effective plastic strain as computed from Eq. 7.9 from strain gauge rosette R09 placed on the continuity plate of Specimen C6. The finite element results are resolved in the at the mid depth of the shell to approximate plane strain.

Also shown in this figure are $PEEQ$ from FEA obtained from an element near the physical location of the R09 (see the strain sample point in Figure 7.8). It is observed that the accumulated effective plastic strain is dependent on the yield stress of the continuity plate. The actual yield strength of the plate is close to 55 ksi, which demonstrates a similar accumulated plastic strain. Residual stresses in the continuity plate (see Chapter 6) are believed to be responsible for the earlier yielding observed in the experimental results compared with the finite element results.

The integrated forces from the west and east continuity plate edges adjacent to the column flange, WCPf and ECPf respectively, and the beam top flange (BTF) for the negative excursions of the typical AISC loading protocol is shown in Figure 7.13. The red line (COL) indicates the force that transfers to the column, assumed as the remainder of BTF force once subtracting both continuity plate forces. The peak integrated flange force occurs during the first cycle of 0.04 rad drift and corresponds well with the assumed value as per AISC 341-16. It is observed that the design continuity plate force according to the method outlined in Chapter 2 of 93 kips (see Table 2.3) is exceeded as each continuity plate realizes a total force of at least $P_y = A_{cp}F_y$. This is attributed to the high stiffness of the continuity plate when contrasted to the distance of $5k$ that is required to be mobilized before reaching the WLY limit state. The critical column limit state of Specimen C6, Web Local Yielding, has a nominal capacity of 377 kips; the estimated force entering the column is significantly below this level due to the presence of the continuity plates. Figure 7.14 shows that the normalized proportions of flange force in the continuity plates and column remains consistent throughout loading until lateral-torsional buckling of the beam and its associated weak axis flexure shifts a higher proportion of force to the west continuity plate. However, the net force across both continuity plates at the beam top flange level is nearly

consistent. This effect is exacerbated when the beam top flange is in compression and the weak axis flexure is a maximum (see Figure 7.15).

Figure 7.16 shows the normalized force flow through the continuity plate during the negative excursions of the loading. The normalized shear force exiting the continuity plate along the column web (WCPw) makes up most of the force delivered to the continuity plate by the beam flange. The red line shows that only 6% of 26% of the beam flange force that entered the continuity plate exits at the far side of the continuity plate. The continuity plate average axial and shear forces integrated along the path WCPf during the negative excursions is shown in Figure 7.17. It is observed that the axial force in the continuity plate is moderately higher than anticipated. Part of this is attributed to material hardening. This figure also shows that the shear force plateaus as the plate hardens. Figure 7.18 shows the computed $\gamma = V_{cp}/P_{cp}$ determined from integrating the ratio of shear stress to axial stress along WCPf (see Eq. 2.12). It is observed that finite element results are in excellent agreement with the theory developed in Chapter 2 (see Eq. 2.13). During significant continuity plate yielding, the ratio diminishes as kinematic hardening influences the ratio of axial to shear force. Additionally, the development of γ assumed that the plate restraint stress (i.e., σ_{22}) was negligible (see Eq. 2.15).

7.4. Continuity and Doubler Plate Internal Force Predictions

The adequate design of continuity and doubler plates and their weldments relies on a sound understanding of the flow of forces through the connection. This section develops a new framework for the design of continuity plates, while the earlier proposed methodology for doubler plate welding (see Section 2.2.3) is reiterated. Integrated forces from the finite element models will be compared with these newly developed approaches.

In the testing program, the continuity plate was designed for the hardened beam flange force P_f less the governing column limit state of FLB or WLY (see Eq. 2.1). Then, using this force and a resolved shear force, the design of the continuity plate was based on a plastic interaction (see Eq. 2.2). Experimental testing of Specimens C3 and C7 demonstrated that the WLY limit state was accurate as an ultimate limit state for the web of an unreinforced column. It is, however, noted that the development of the full WLY limit state, which utilizes a 2.5:1 diffusion across the k dimension of a column section requires significant plastification of the column with peak strains approaching $6\epsilon_y$ (see Figure 5.9). This level of strain is inconsistent with a pair of sufficiently designed continuity plates and would result in significant inelastic behavior of the continuity plate which may lead to significant strain hardening.

Figure 5.11 shows strain response of about $1\epsilon_y$ of the column web area of Specimen W4 adjacent to the continuity plate. This specimen developed yielding of the continuity plate across its breadth (see Figure 5.10). It is therefore proposed that an amended WLY limit state be implemented which aims to develop uniform yielding across the web, doubler plates if applicable, and continuity plates. Consider the following amended WLY limit state:

$$R_n = \left(\alpha k + t_{bf}\right) F_y t_{pz} \tag{7.10}$$

where α denotes the diffusion angle (see Figure 7.19). By solving for the amount of force entering the column by using the integrated forces along the paths denoted in Figure 7.8 as:

$$P_{col} = \int_{\Omega_{\mathrm{BTF}}} \sigma_{11} d\Omega_{BTF} - \int_{\Omega_{\mathrm{WCPf}}} \sigma_{11} d\Omega_{WCPf} - \int_{\Omega_{\mathrm{ECPf}}} \sigma_{11} d\Omega_{ECPf} \tag{7.11}$$

where the first term on the right-hand side is the beam flange force, and the last two terms are the forces transmitted to the continuity plates. Equating Eq. 7.10 to Eq. 7.111 permits the determination of α:

$$\alpha = \frac{1}{k}\left(\frac{P_{col}}{F_y t_{pz}} - t_{bf}\right) \tag{7.12}$$

Figure 7.20 shows the determination of α as the thickness of the continuity plate is varied for Specimens C5 and C6 at the first negative excursion to 0.04 rad drift. It is observed that an α of 3 realizes an average von Mises continuity plate stress of F_y. This correlates with a 1.5:1 diffusion angle. Additionally, experimental testing failed to demonstrate a FLB-type phenomenon in either reinforced or unreinforced columns (see Figure 5.14). The development of the yield line mechanism that formed the foundation of the FLB limit state (see Figure 1.10) assumed that continuity plates were not present; formation of these yield lines are unlikely once the column is reinforced with a continuity plate.

It is therefore proposed that these two limit states, in their current form, be only used to evaluate the necessity of stiffening a column. However, when a continuity plate is present, an amended set of limit states that reflect a reinforced column is proposed:

(1) WLY:

$$R_n = \left(3k + t_{bf}\right) F_y t_{pz} \tag{7.13}$$

which is the new WLY limit state that modifies Eq. 1.27 by changing the diffusion from a slope of 2.5:1 to 1.5:1.

(2) FLB:

$$R_n = 0 \tag{7.14}$$

The nullity of the column flange bending resistance arises from the unlikeliness of a stiffened column to develop the requisite yield lines. The amendments to the limit states influence the procedure of designing continuity plates using Eq. 2.1 and Eq. 2.2 by removing the FLB limit state from consideration.

Subscribing to Eq. 7.13 allows the development of a force distribution based on the plastic strength of the continuity plates and column web (including additional doubler plate area if applicable). The force allocation to the continuity plate is therefore:

$$P_{cp} = P_f \left(\frac{A_{cp} F_{y,cp}}{2A_{cp} F_{y,cp} + A_{col} F_{y,col}} \right) \leq A_{cp} F_{y,cp} \tag{7.15}$$

where $A_{col} = \left(3k + t_{bf}\right) t_{pz}$, and A_{cp} is the net continuity plate area (i.e., $b_n t_{cp}$). The yield strength of the continuity plate and column are $F_{y,cp}$ and $F_{y,col}$, respectively. This expression degenerates to Eq. 2.1 if the 'correct' ($\alpha = 3$) continuity plate is used. If an inadequate continuity plate size is chosen, the continuity plate force is limited by the yielding of the continuity plate in tension, $A_{cp} F_y$, which implies $\alpha > 3$. If a continuity plate greater than that required, than Eq. 7.15 reflects an elastic distribution based on the axial stiffness of the continuity plate and column web.

The shear flow that develops around a doubler plate was derived in Chapter 2; a modified version which replaces the traditional 0.6 shear yielding factor with the exact expression is:

$$q_{dp,v} = \frac{V_{dp}}{d_c} \leq \frac{1}{\sqrt{3}} F_y t_{dp} \tag{7.16}$$

where V_{dp} is the proportion of the panel zone shear that is attributed to the doubler plate based on the elastic stiffness (see Eq. 2.22).

7.5. Parametric Study

To evaluate the influence of the continuity plate and column flange thicknesses three normalized metrics are used. The first is the normalized axial stress across the total width of continuity plates:

$$N_1 = \frac{1}{2A_{cp} F_{y,cp}} \int_{\Omega_{\mathrm{cp}}} \sigma_{11} d\Omega_{\mathrm{cp}} \tag{7.17}$$

where the domain $\Omega_{cp}$is the union of the area of both continuity plates (i.e., $\Omega_{WCPf} \cup \Omega_{ECPf}$). The second normalization normalizes the continuity plate force with the beam flange force:

$$N_2 = \frac{\frac{1}{2}\int_{\Omega_{\mathrm{cp}}} \sigma_{11} d\Omega_{\mathrm{cp}}}{\int_{\Omega_{\mathrm{BTF}}} \sigma_{11} d\Omega_{BTF}} \tag{7.18}$$

The final metric is the normalization of the estimated continuity plate force with the beam flange force from finite element analysis:

$$N_3 = \frac{P_f \left(\frac{A_{cp}}{2A_{cp} + A_{col}}\right)}{\int_{\Omega_{\mathrm{BTF}}} \sigma_{11} d\Omega_{BTF}} \leq \frac{A_{cp} F_y}{\int_{\Omega_{\mathrm{BTF}}} \sigma_{11} d\Omega_{BTF}} \tag{7.19}$$

7.5.1. Effect of Column Flange Thickness

Figure 7.21 shows the normalized continuity plate stress and the proportion of the beam flange force that is resolved in the continuity plate for Specimens C5 and C6. It is observed that increasing the column flange thickness is not an efficient mechanism for reducing force entering the continuity plate. This is attributed to the very low relative out-of-plane bending stiffness of the column flange compared to the axial stiffness of the continuity plate. Overall excellent correlation between Eq. 7.19 and the finite element results is shown. The underprediction of Eq. 7.19 when the column flange thickness is decreased is attributed to significant strain hardening of the continuity plate.

7.5.2. Effect of Continuity Plate Thickness

The integrated continuity plate force and resolved force entering the column for Specimen C6 is shown in Figure 7.22(a) as the normalized continuity plate thickness ($t_{cp}\ /t_{bf}$) is varied. The resolved column forces are determined by subtracting the integrated flange force by the integrated continuity plate forces. Finite element results of the column force result in the same governing

conclusions that without a continuity plate the column force exceeds both the FLB and WLY limit states. It is observed that a continuity plate in excess of $0.45t_{bf}$ is what is required to satisfy both limit states according to methods outlined in Chapter 2. Shown in red is the predicted continuity plate force according to the amended limit states (see Eq. 7.13)—which shows excellent correlation. The predicted force in the column is found by subtracting the integrated beam flange force by twice the predicted continuity plate force (see dashed blue line).

Figure 7.22(b) shows the normalized response of the continuity plate as the normalized continuity plate thickness ($t_{cp}\ /t_{bf}$) is varied. The blue line shows the normalized continuity stress (see Eq. 7.17) and the black line represents the normalized proportion of the beam flange force entering the continuity plate (see Eq. 7.18). Eq. 7.19 (represented by red line) shows excellent correlation with the finite element results. It is observed that the continuity plate tested in Specimen C6 based on the plastic limit state results in the continuity plate realizing $1.08P_y$ due to cyclic hardening of the continuity plate. It is observed that continuity plate yielding does not cease until a size of $0.8t_{bf}$ is selected. Using Eq. 7.13 to calculate the required continuity plate force generates a predicted force demand of 162 kips, which requires a 0.70-in. thick continuity plate ($t_{cp}/t_{bf} = 0.82$).

Figure 7.23(a) similarly shows the integrated forces for Specimen C5 as the continuity plate thickness is varied. It is observed that the resolved column force exceeds the WLY limit state as predicted in Table 2.3. The continuity plate force is predicted well with Eq. 7.13. The normalized continuity plate stress demonstrates that continuity plate hardening occurs until a normalized thickness continuity plate of $0.6t_{cp}/t_{bf}$ is selected [see Figure 7.23(b)]. Using Eq. 7.13 to calculate the continuity plate force generates a predicted force demand of 158 kips which requires a 0.60-in. thick continuity plate ($t_{cp}/t_{bf} = 0.65$). The same analysis was performed for Specimen W2

(see Figure 7.24). The predicted force in the continuity plate as per Eq. 7.13 underpredicts the force in the continuity plate because the continuity plate remains elastic. A better description of the force distribution for an elastic continuity plate is the Flexibility Method discussed in Section 1.4. Note that it was not intended for this continuity plate to remain elastic; however, the finite element results reveal significantly less beam flange force than anticipated using AISC 341-16. This was also observed during the experimental testing program (see Figure 5.2). In this case the required continuity plate size, using the code assumed level of force, while using Eq. 7.13 coincides with the AISC 341 $t_{min} = 0.75t_{bf}$. Specimen W2 has significant panel zone reinforcing which has been incorporated into Eq. 7.13 using $t_{pz} = t_{cw} + \sum t_{dp}$.

Specimen C5 demonstrated instability of the continuity plate; the width-to-thickness ratio of this continuity plate was 16 (see Figure 4.40). To evaluate if a geometric instability occurred during the finite element results the maximum bending stress along WCPf was extracted as the width-to-thickness ratio of the plate was varied (see Figure 7.25). As the width-to-thickness ratio (b/t) ratio decreases, a decrease in continuity plate bending is observed. At high slenderness ratios, plate instability results in significant bending stresses of the continuity plate. A width-to-thickness ratio of 13.5, selected to correspond to $0.56\sqrt{E/F_y}$, is shown as a dotted line; plate slenderness below this value generally do not develop instabilities for interior or exterior connections. The instability of the continuity plate during the 0.04 rad drift cycles is observed in Figure 7.26 to Figure 7.28.

7.5.3. Effect of Continuity Plate Thickness on Beam Flange $PEEQ$

The measure *PEEQ* indicates the accumulated plastic strain and has been used as a measure of fracture potential by other researchers (Ricles et al. 2003, Mashayekh and Uang 2018). This section evaluates the influential parameters affecting the development of *PEEQ* across the beam

flange. Figure 7.29 shows the distribution of *PEEQ* across the flange width (section BTF in Figure 7.8) of Specimen C6. It is observed that largest *PEEQ* that develops is observed at the center of the beam with the top fiber of the section developing significantly higher *PEEQ* values. This is attributed to role of secondary stresses in the beam flange exacerbating the strain at the beam flange extreme fiber. The careful detailing of the beam backing bar of a typical SMF beam bottom flange was found necessary because of the high *PEEQ* values in presence of the CJP notch is prone to fracture. The *PEEQ* values reported herein reflect a sharp reentrant corner at the beam flange-to-column flange intersection whereas typical welding would see this corner smoothed out with a weld bead. The *PEEQ* distribution once the continuity plate has been removed is shown in Figure 7.30. This analysis confirms that a continuity plate reduces the top fiber and average *PEEQ* values at the center of the flange by half. It is also observed that the inclusion of a continuity plate results in *PEEQ* demands across the flange instead of being concentrated at the center of the flange.

Figure 7.31 shows how *PEEQ* Index (Eq. 1.5) changes as the thickness of the continuity plate of Specimen C6 is increased. This figure is generated by recording the *PEEQ* value at peak negative excursion of 0.04 rad drift (i.e., the final excursion of the AISC prequalification protocol). It is observed that the average *PEEQ* is invariant as the continuity plate thickness is increased; however, the peak *PEEQ* Index experiences a two-fold reduction as the continuity plate thickness is increased. It is observed that both the minimum continuity plate thickness as specified in AISC 341 and the continuity plate thickness tested in Specimen C6 is still on the portion of the curve with significant negative slope. The continuity plate thickness predicted by Eq. 7.13 realizes the *PEEQ* branch with minimal negative slope. The diminishing return of continuity plate thickness has been described by Lee et al. (2005a) who predicted the transition point to exist at $0.6t_{bf}$. Figure 7.32 and Figure 7.33 show a similar result for the parametric analysis performed on Specimens C5

and W2. The results for Specimen W2 do not exhibit a bilinear response, an effect attributed to high plastic strain demands imposed by the WUF-W connection.

Figure 7.34 shows the distribution of *PEEQ* Index as the column flange thickness of Specimen C6 is varied. It is observed that the peak *PEEQ* occurs when the column flange thickness is equal to the actual. It is observed that below this thickness that significant twisting of the column occurs, and the ductility demands are transferred to the continuity plates. As the column flange thickness increases only, a moderate reduction in *PEEQ* demands is observed. This parrots the previous conclusion that increasing the column flange thickness is not as an effective method to stiffen the joint as thickening the continuity plates.

7.5.4. Effect of Doubler Plate Thickness

The last parametric study developed varies the thickness of a welded doubler plate to investigate the measured shear flow in the finite element analysis to the predicted value as per Eq. 7.13. The finite element shear flow is obtained by integrating the forward edge of the doubler plate and normalizing by the depth of the plate (see line DP in Figure 7.35). An additional concern observed by other researchers (Shirsat and Englehart 2012, Gupta 2013 and Shim 2017) identified that significant stresses develop in the corners of the doubler plate at the beam flange elevations. This effect is shown in Figure 7.35 by observing significant accumulated plastic strains in these regions. These high stresses develop from the combined effect of the shear flow along the doubler plate edges and the concentrated orthogonal force delivered by the beam flange. To address these high stresses, these researchers have recommended that doubler plate welds must develop the shear strength of the plate.

Figure 7.36 shows the peak von Mises stress and the average shear stress along line DP as the thickness of the doubler plate is incremented for Specimen C7. This specimen utilized a doubler

plate to reinforce for WLY—not because reinforcement was required for panel zone shear. Accordingly, relatively low shear stress is observed along edge DP. Despite this, peak von Mises stresses are observed to be $1.13F_y$ (see Figure 7.37). Also shown in this figure is the correlation between the normalized shear flow from the finite element analysis relative to the normalized shear flow as per Eq. 7.16. Since Specimen C7 did not require a doubler plate, the normalized shear flow does approach the upper bound of q_y.

In contrast the same analysis was performed on Specimen C5, which was tested without a doubler plate to investigate the influence of column kinking on the performance of continuity plate fillet welds. In this scenario a sufficiently thin doubler plate triggers the upper bound, as evidenced by a kink in the red line of Figure 7.38. Strain hardening of the doubler plate results in the required shear flow in the finite element analysis greater than unity. It is also observed that as the doubler plate is increased in size and the required shear flow diminishes the peak von Mises stress appears to asymptotically approach F_y.

To investigate the performance of a pair of symmetric doubler plates on an interior connection, the same parametric analysis was performed on Specimen W2 (see Figure 7.39). Relatively high von Mises stresses are observed as the doubler plate develops instability. An example of the doubler plate instability of Specimen W2 when the doubler plate width-to-thickness ratio is equal to 100 is observed in Figure 7.40.

Table 7.1 Hardening Parameters

Reference	C_1 (ksi)	γ_1	C_2 (ksi)	γ_2	Q_∞ (ksi)	b
Mashayekh and Uang (2018)	5,615	514	349	48.1	26	1.7
Elkady and Lignos (2014)	362	20	-	-	25	2.0
Myers et al. (2014)	409	15	-	-	15	5
Chansuk et al. (2018)	351	13.3	-	-	29	0.92

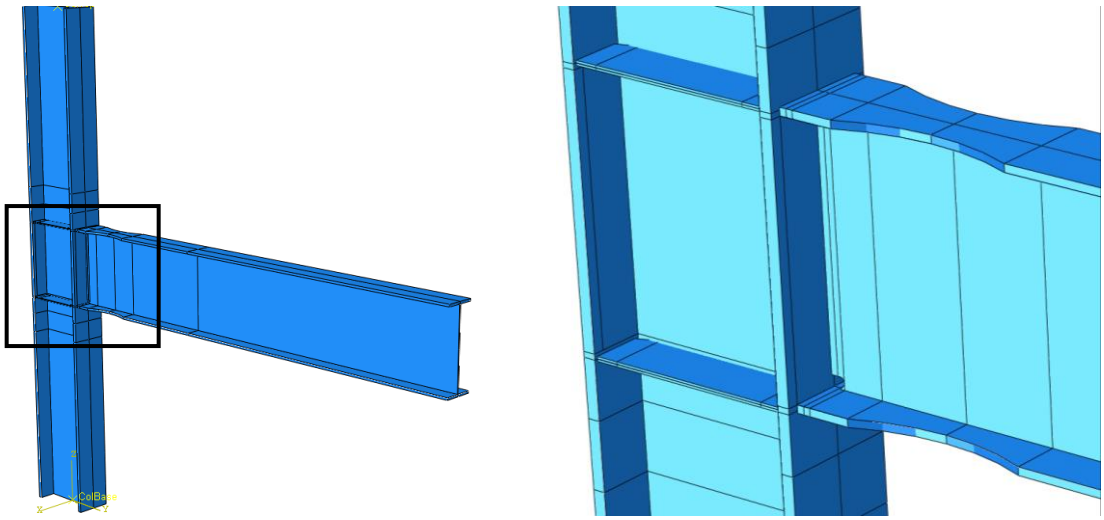

(a) Overview (b) Connection Region

Figure 7.1 Plate Description of Finite Element Model

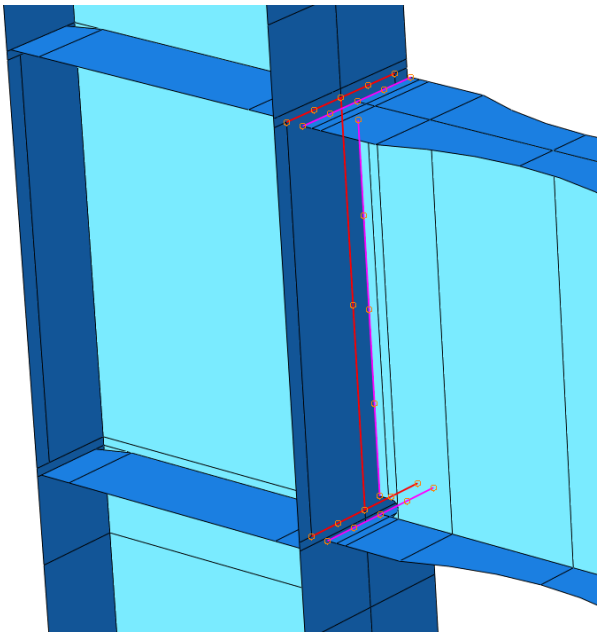

Figure 7.2 Beam-to-Column Joint Modelling with Tie Constraints

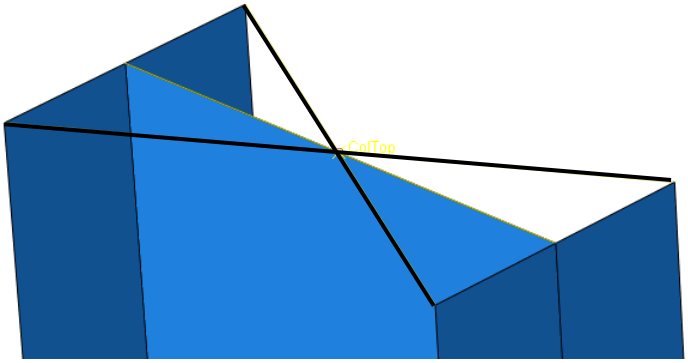

Figure 7.3 Typical Displacement Boundary Condition

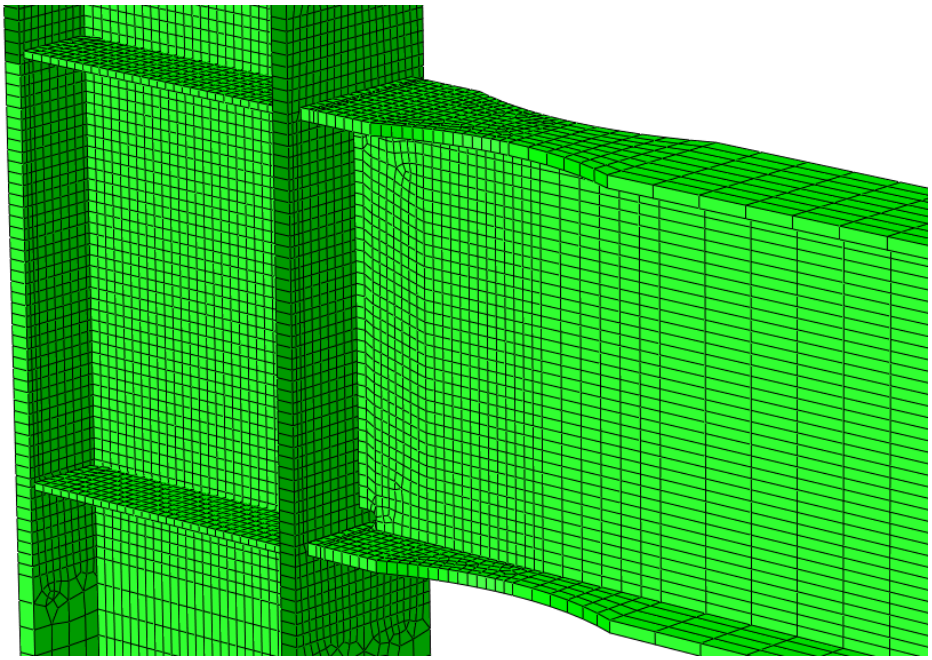

Figure 7.4 Typical Meshing

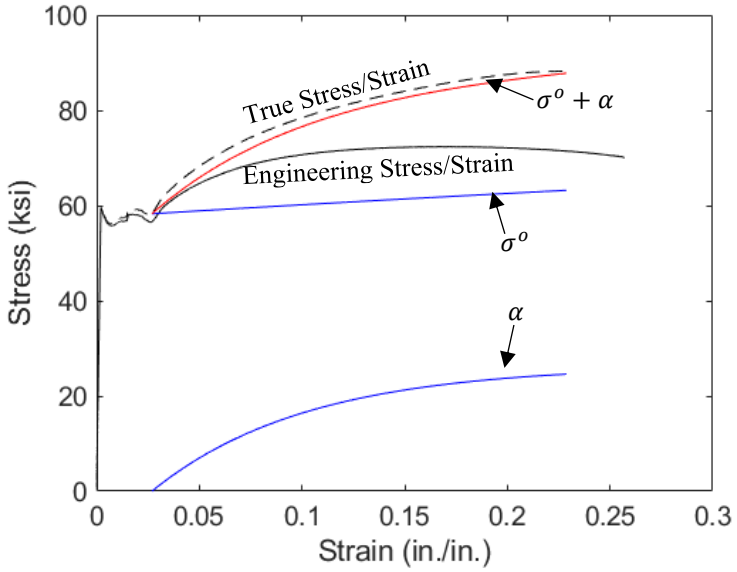

Figure 7.5 Specimen C6: Material Calibration Results

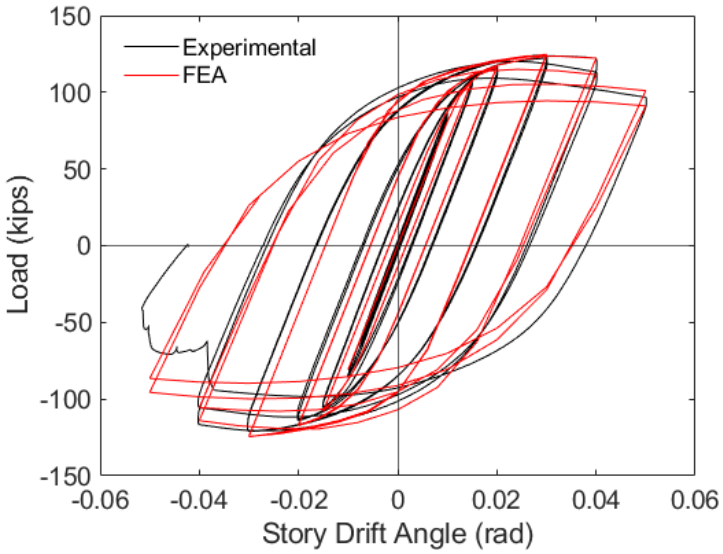

Figure 7.6 Specimen C6 FEA Results: Global Load Drift Response Comparison

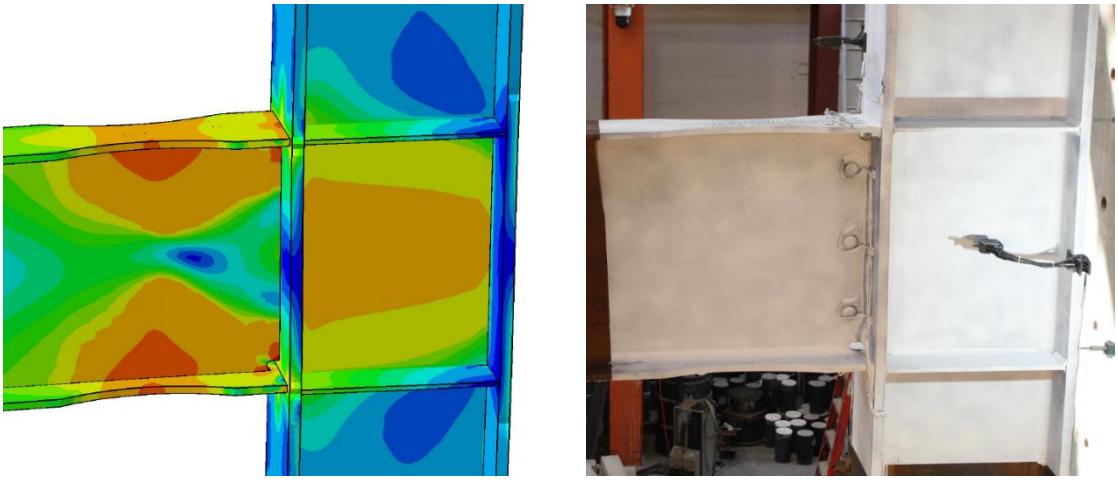

(a) -0.03 rad (2nd Cycle)

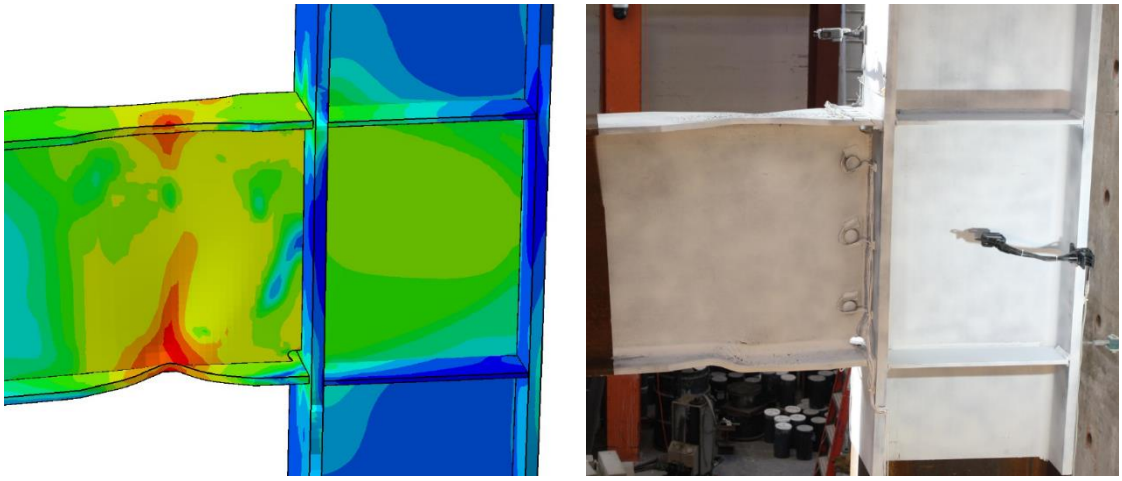

(b) -0.04 rad (2nd Cycle)

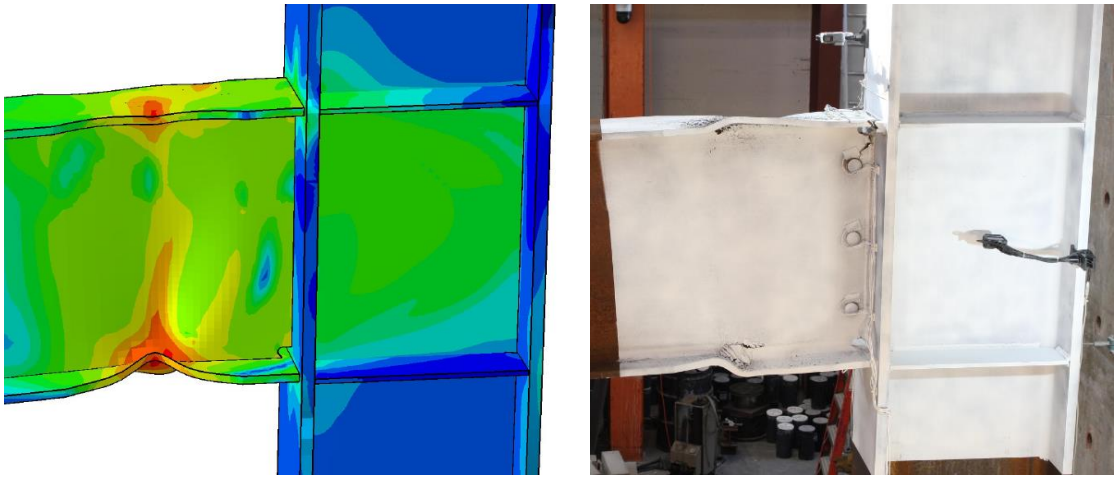

(c) -0.05 rad (1st Cycle)

Figure 7.7 Specimen C6 FEA Results: East Side of Connection

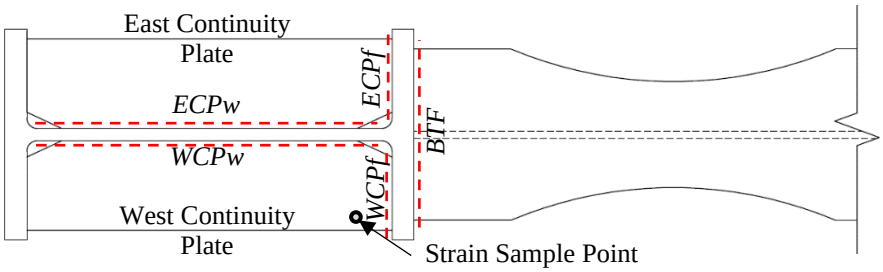

Figure 7.8 Specimen C6 FEA: Section Identification

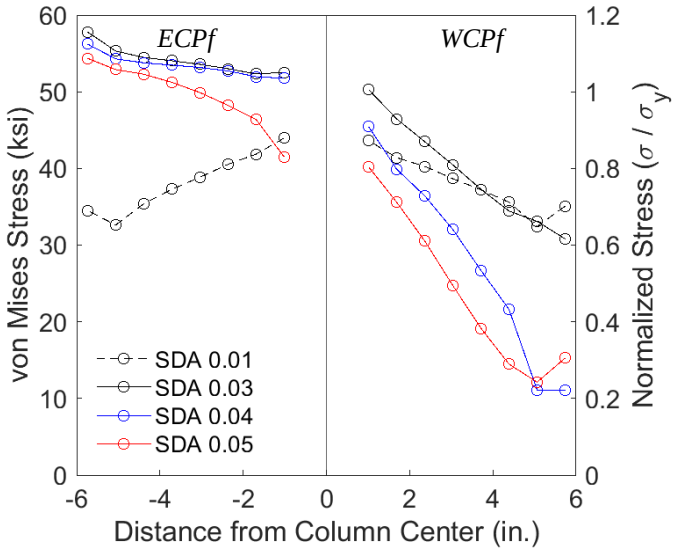

(a) Positive Excursions

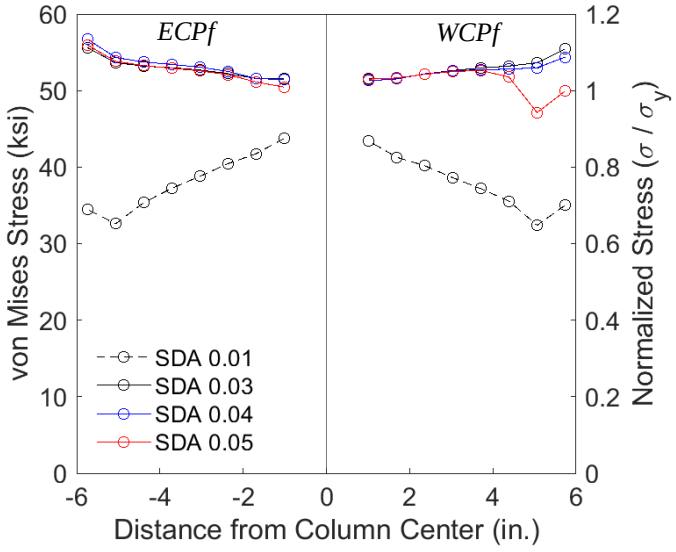

(b) Negative

Figure 7.9 Specimen C6 FEA: Beam Top Flange Continuity Plate von Mises Stresses

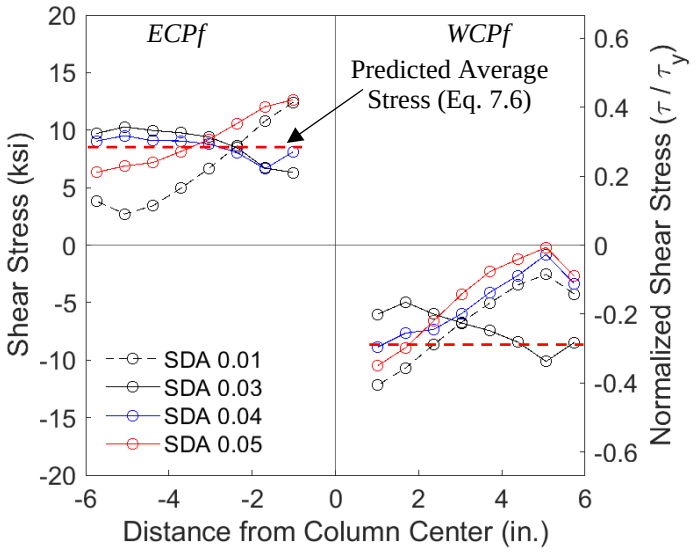

(a) Positive Excursions

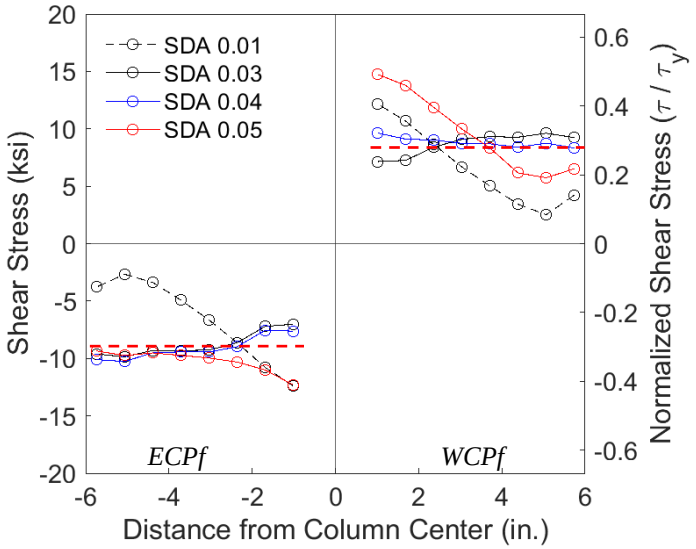

(b) Negative

Figure 7.10 Specimen C6 FEA: Beam Top Flange Continuity Plate Shear Stresses

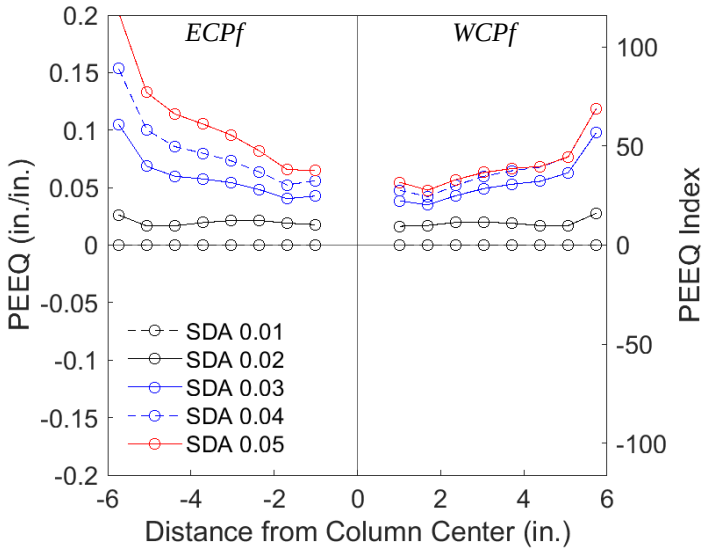

Figure 7.11 Specimen C6 FEA: *PEEQ* Distribution Across Plate

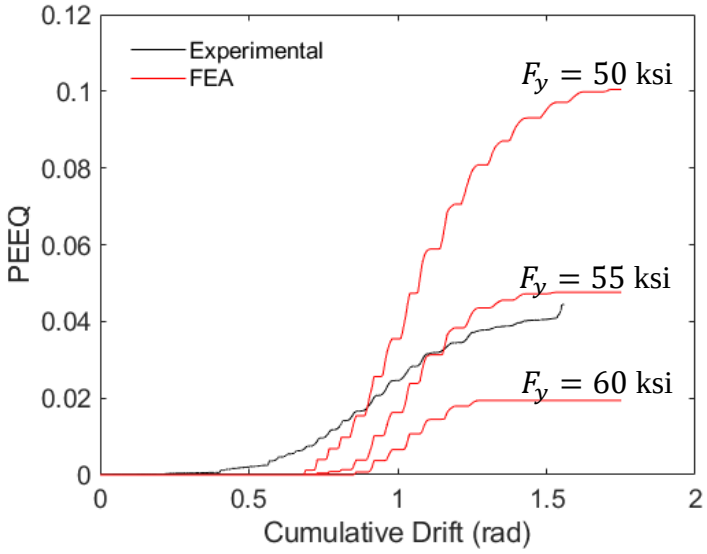

Figure 7.12 Specimen C6 FEA: Continuity Plate *PEEQ* Comparison

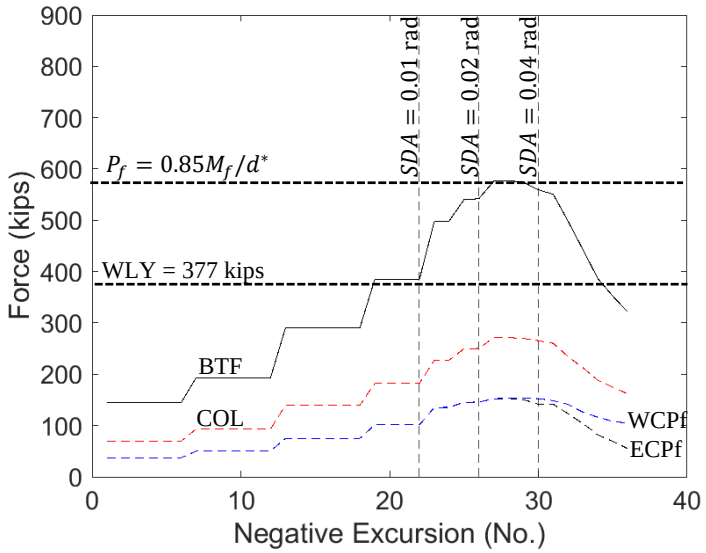

Figure 7.13 Specimen C6 FEA: Beam Top Flange Continuity Plate Forces during Negative Loading (Beam Flange in Tension)

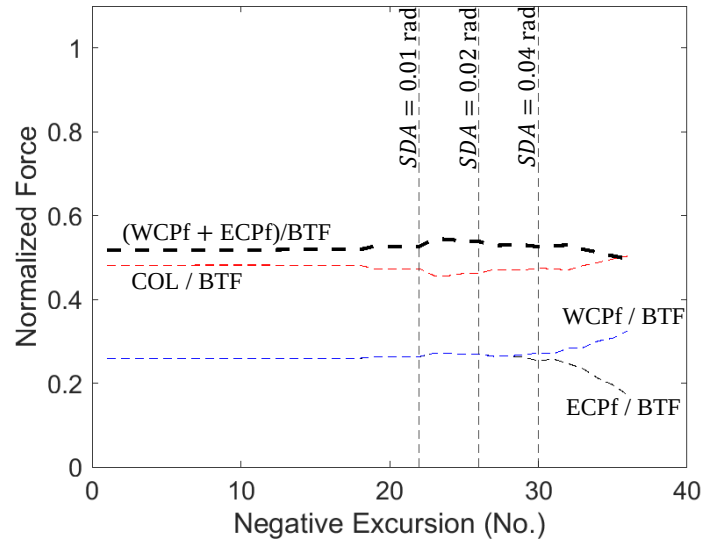

Figure 7.14 Specimen C6 FEA: Beam Top Flange Continuity Plate Force Distribution during Negative Excursions

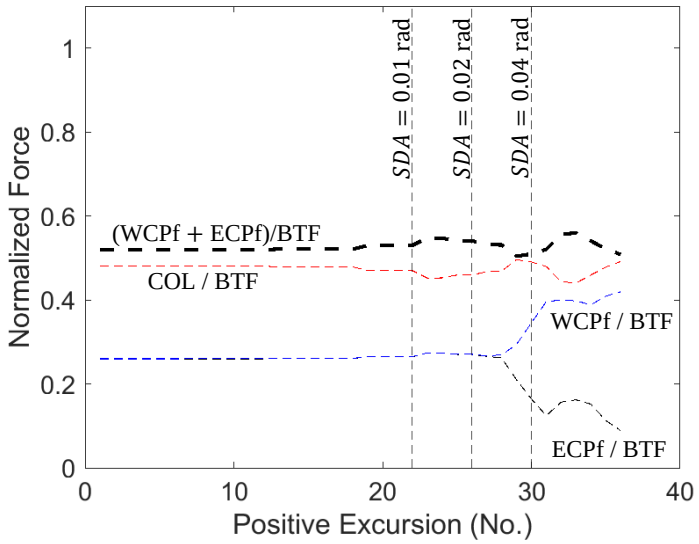

Figure 7.15 Specimen C6 FEA: Beam Top Flange Continuity Plate Force Distribution during Positive Excursions (Beam Flange in Compression)

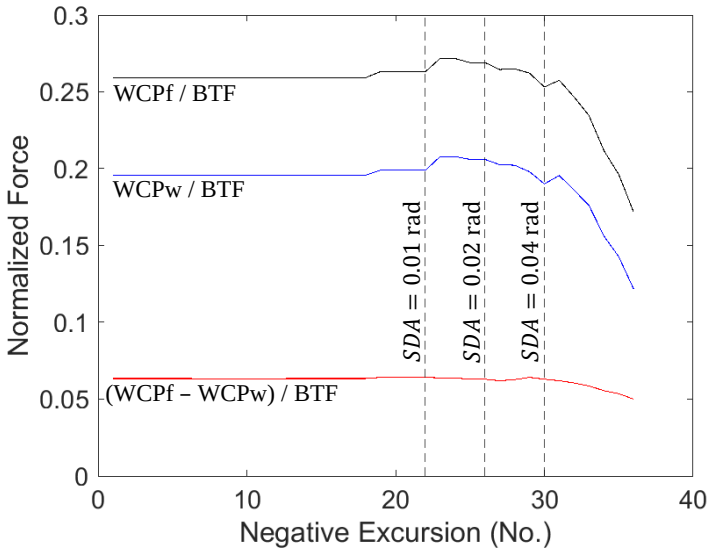

Figure 7.16 Specimen C6 FEA: Beam Top Flange Continuity Plate Forces during Loading

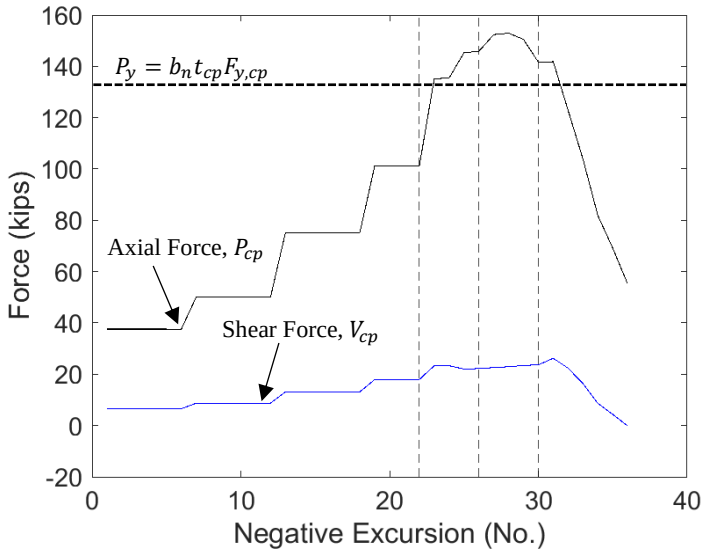

Figure 7.17 Specimen C6 FEA: Beam Top Flange Continuity Plate Integrated Axial and Shear Forces during Loading

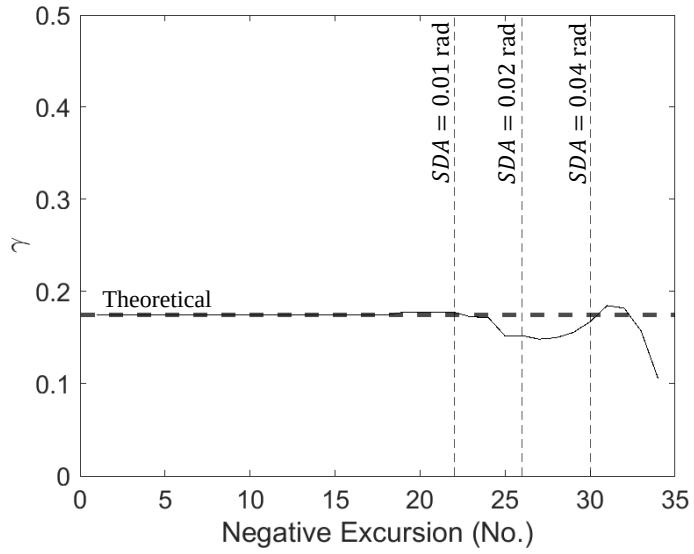

Figure 7.18 Specimen C6 FEA: Beam Top Flange Continuity Plate γ during Loading

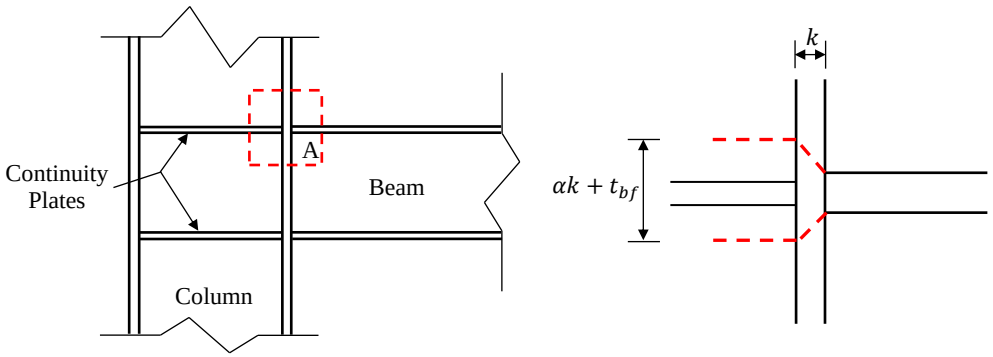

(a) Overview (b) Detail A

Figure 7.19 Definition of α

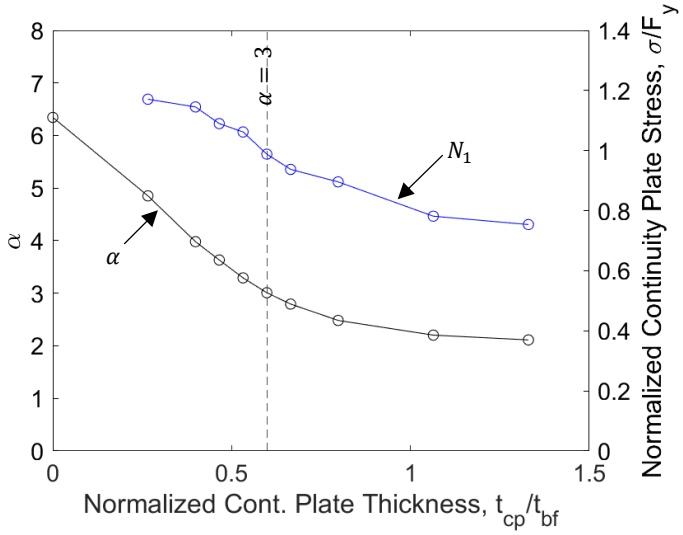

(a) Specimen C5

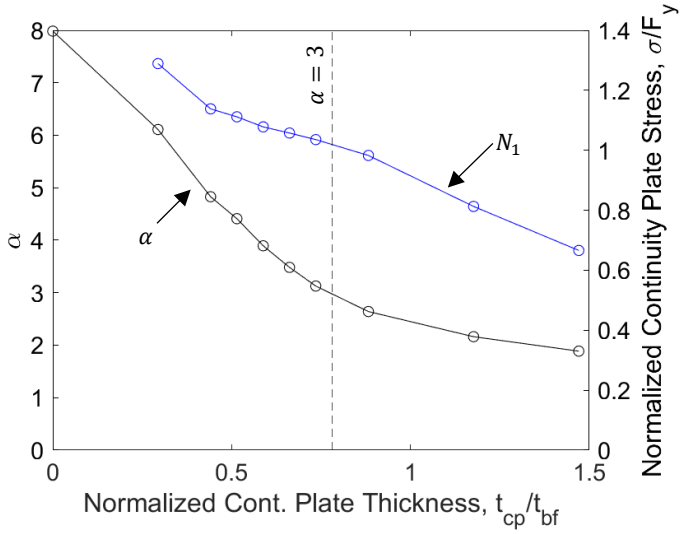

(b) Specimen C6

Figure 7.20 Determination of α of Proposed Column WLY Limit State

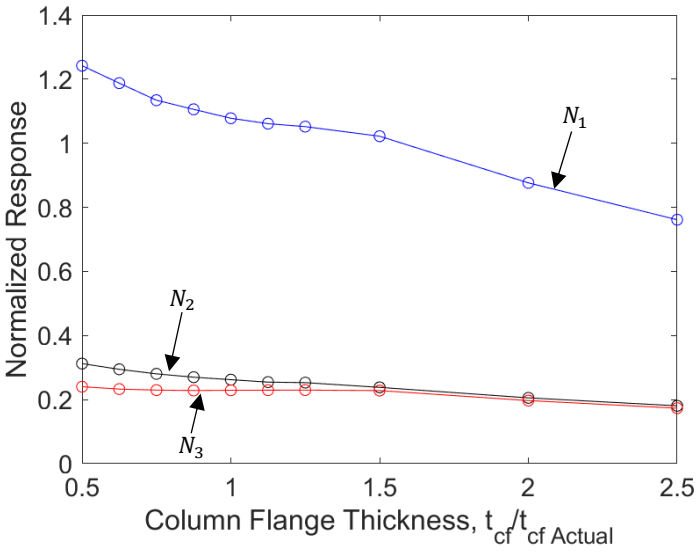

(a) Specimen C6

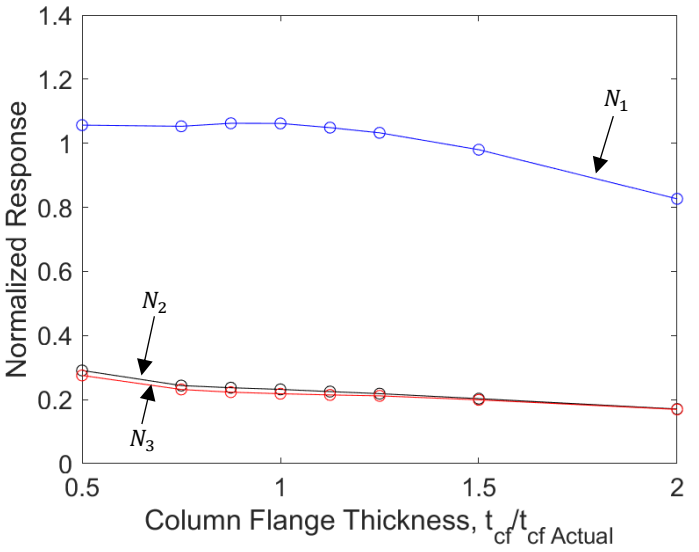

(b) Specimen C5

Figure 7.21 Parametric Response: Effect of t_{cf} on Normalized Continuity Plate Force

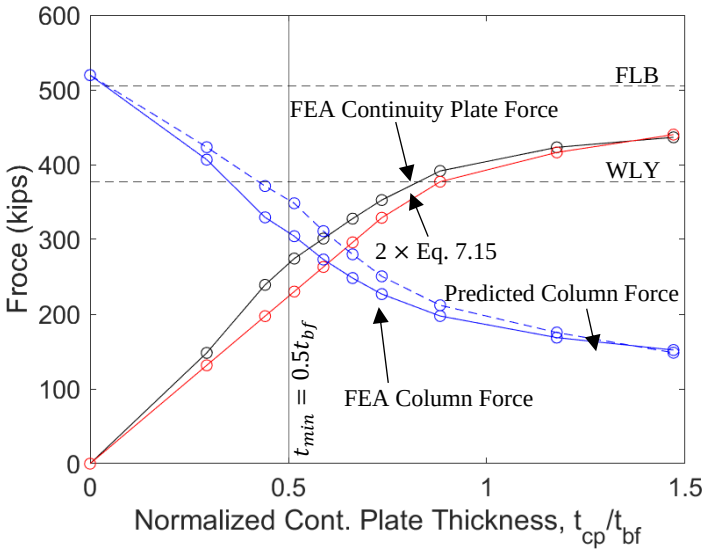

(a) System Forces

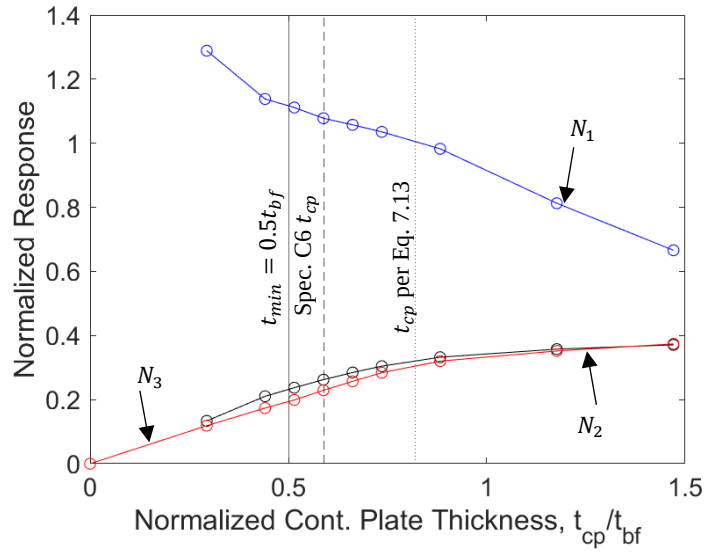

(b) Normalized Response

Figure 7.22 Parametric Response: Effect of t_{cp} on Specimen C6 Continuity Plate Force

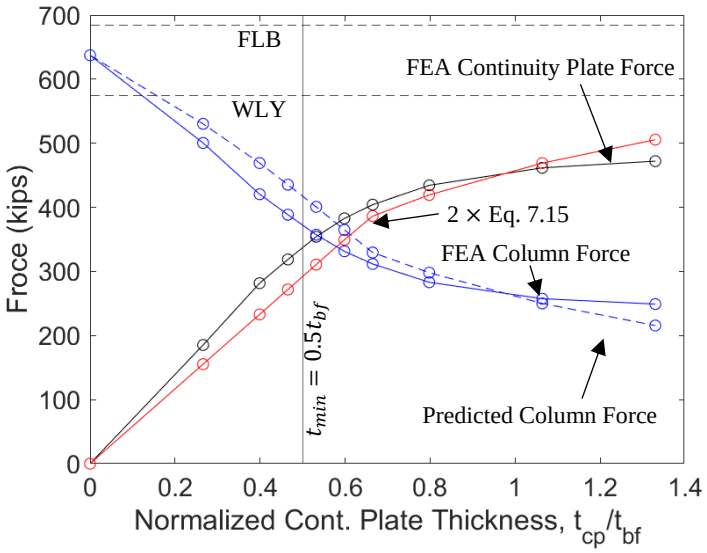

(a) System Forces

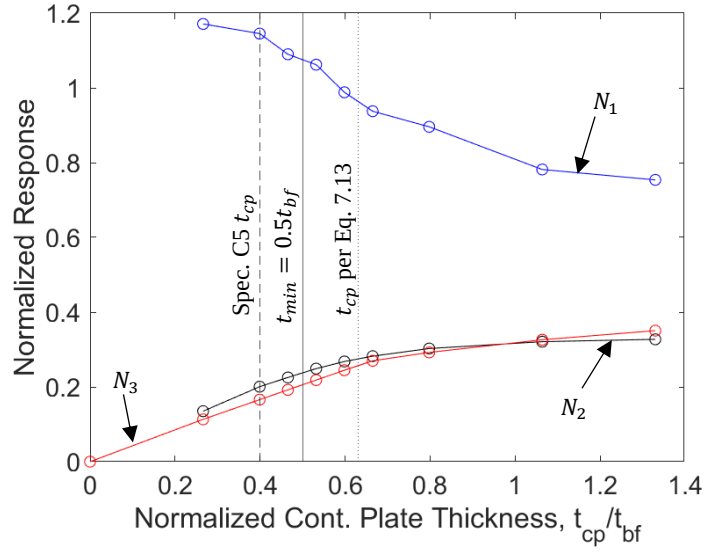

(b) Normalized Response

Figure 7.23 Parametric Response: Effect of t_{cp} on Specimen C5 Continuity Plate Force

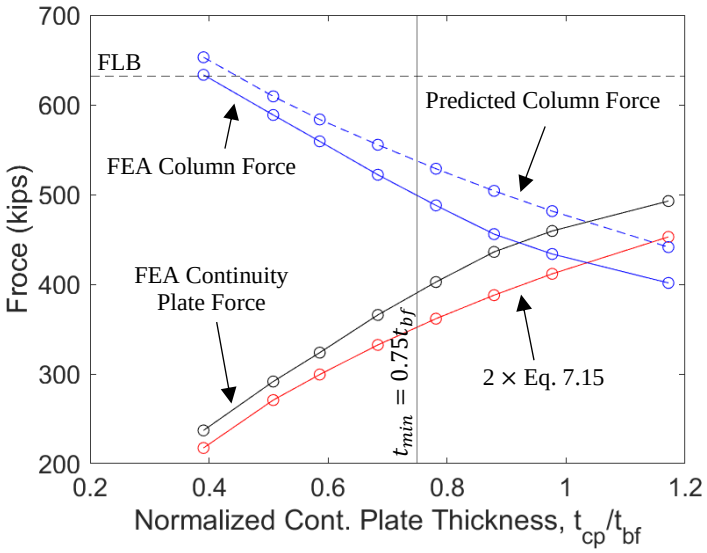

(a) System Forces

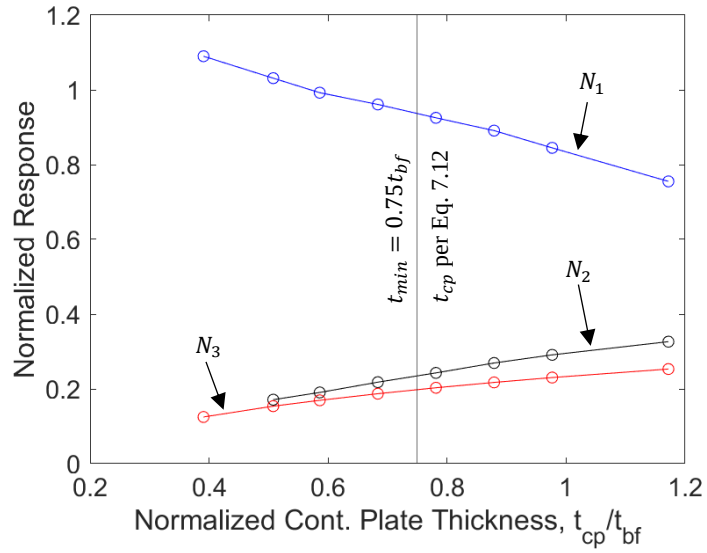

(b) Normalized Response

Figure 7.24 Parametric Response: Effect of t_{cp} on Specimen W2 Continuity Plate Force

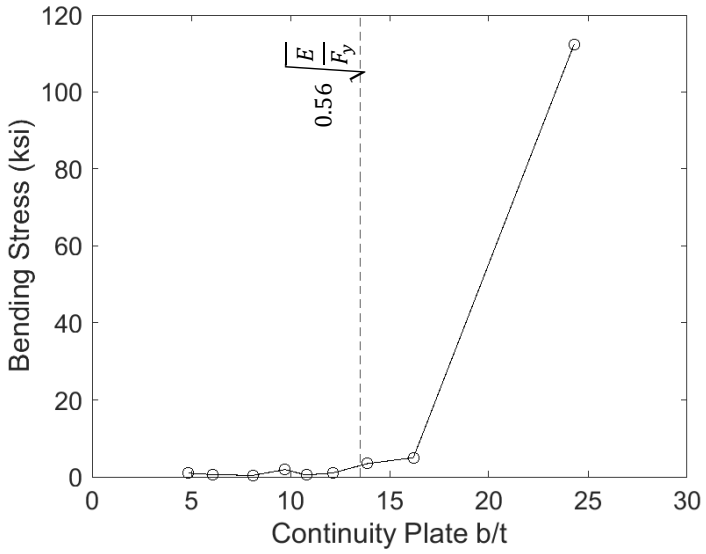

(a) Specimen C6

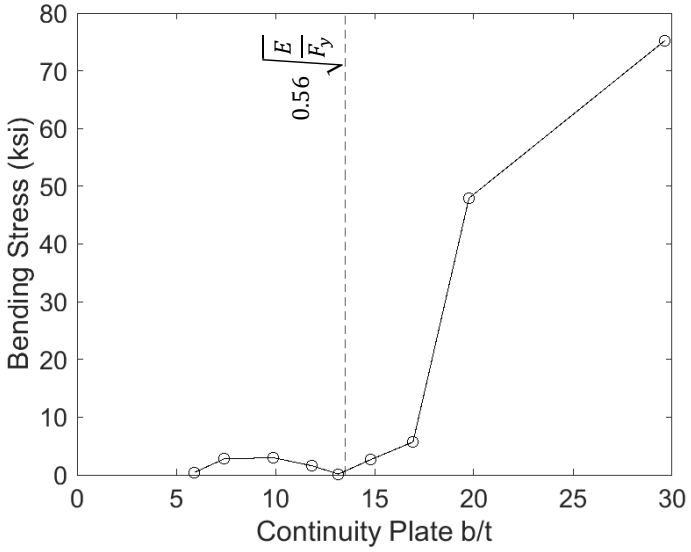

(b) Specimen C5

Figure 7.25 Parametric Response: Continuity Plate Bending Stress as *b/t* is Varied

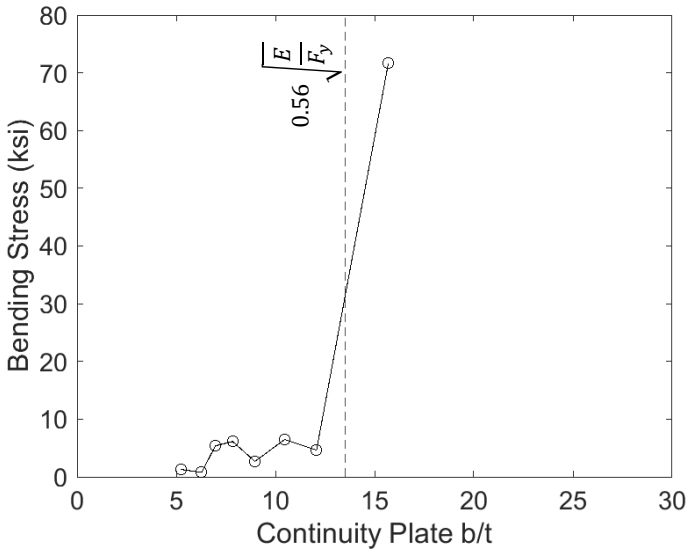

(c) Specimen W2

Figure 7.25 Parametric Response: Continuity Plate Bending Stress as *b/t* is Varied (continued)

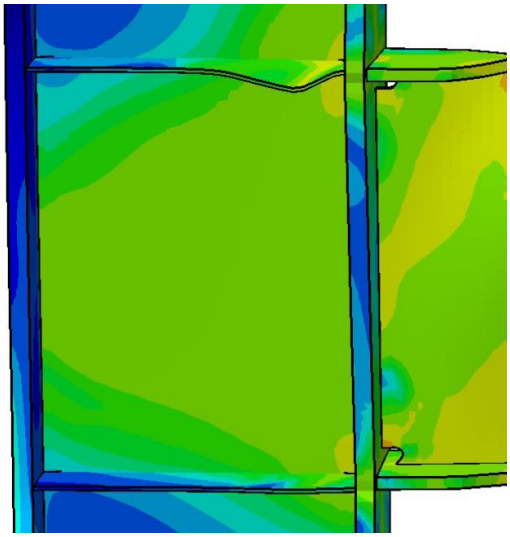

(a) $b/t = 20.8$

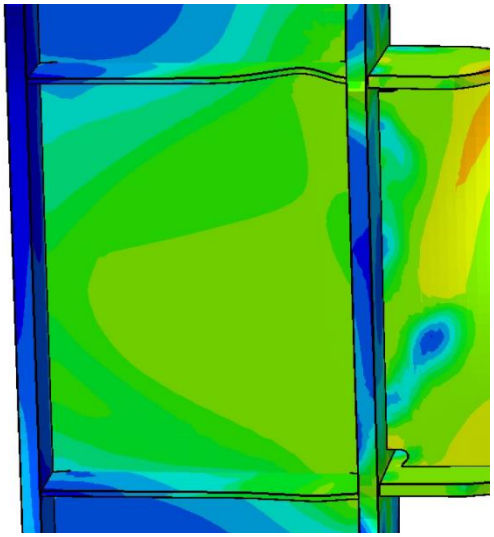

(b) $b/t = 13.9$

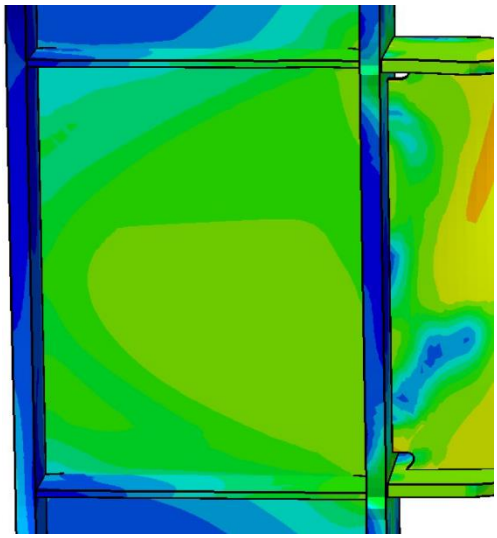

(c) $b/t = 11.9$

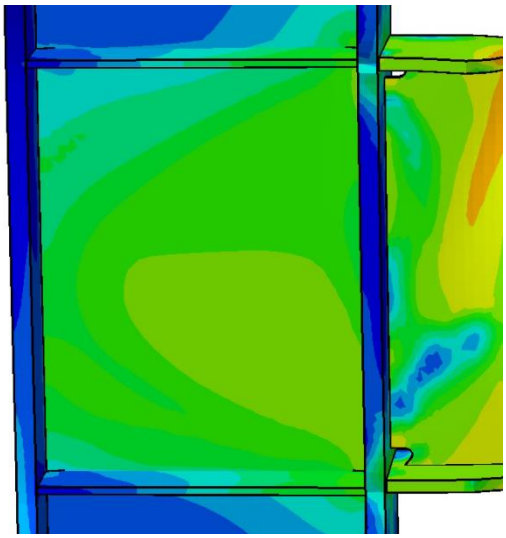

(d) $b/t = 10.4$

Figure 7.26 Parametric Response: Specimen C6 Continuity Plate Instability as *b/t* is Varied

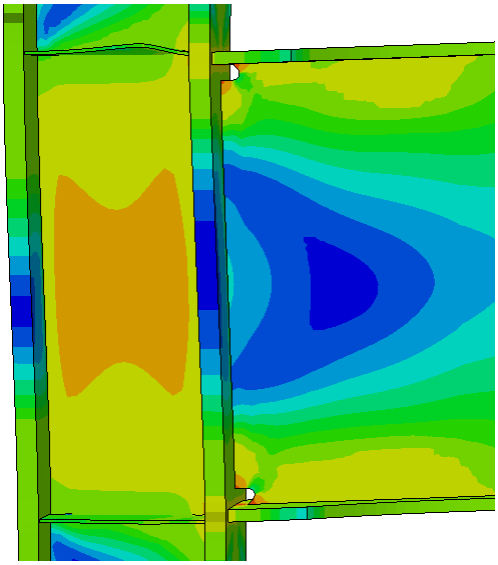

(a) $b/t = 24.6$

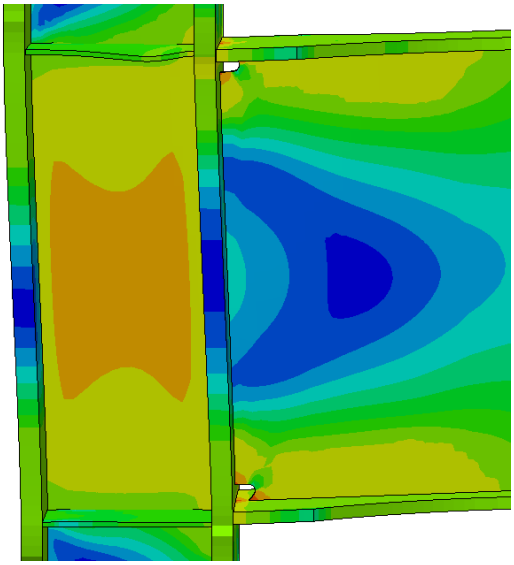

(b) $b/t = 16.4$

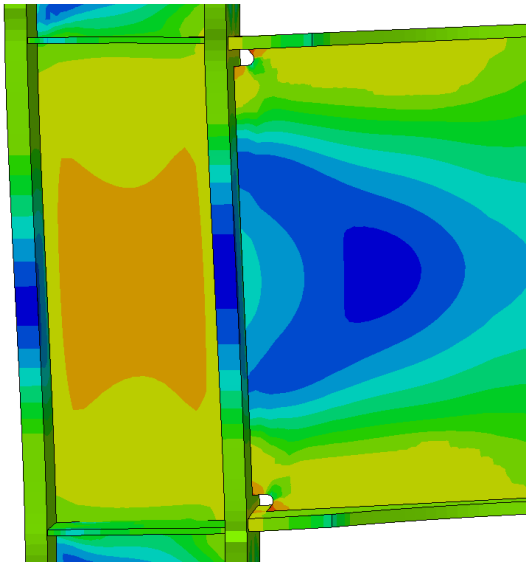

(c) $b/t = 14.1$

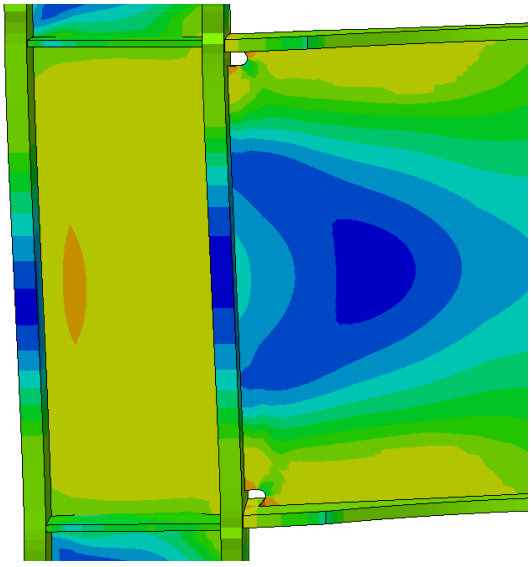

(d) b/t =12.3

Figure 7.27 Parametric Response: Specimen C5 Continuity Plate Instability as *b/t* is Varied

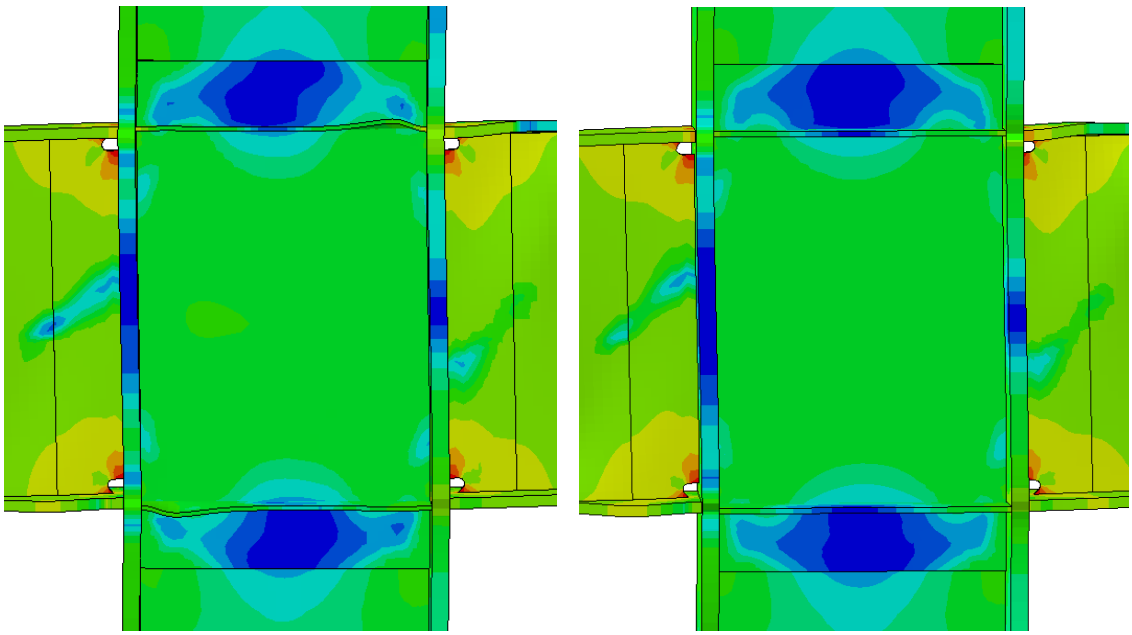

(c) $b/t = 15.7$ (d) $b/t = 11.9$

Figure 7.28 Parametric Response: Specimen W2 Continuity Plate Instability as *b/t* is Varied

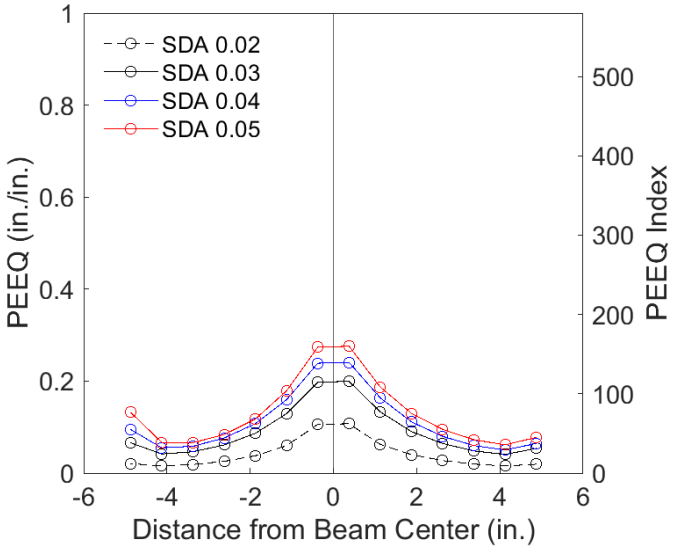

(a) Average *PEEQ*

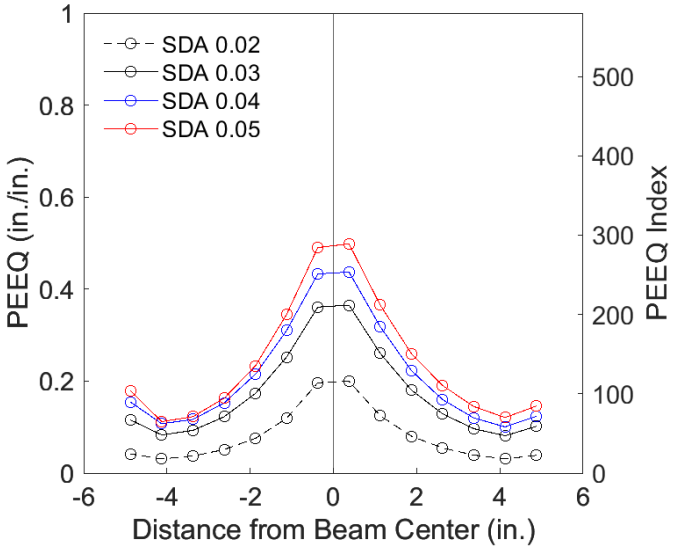

(b) Top Fiber *PEEQ*

Figure 7.29 Specimen C6: *PEEQ* across Beam Top Flange Width

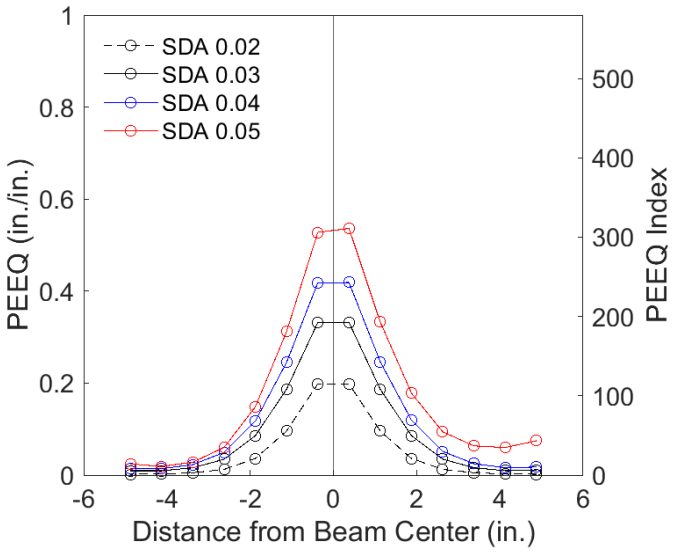

(a) Average *PEEQ*

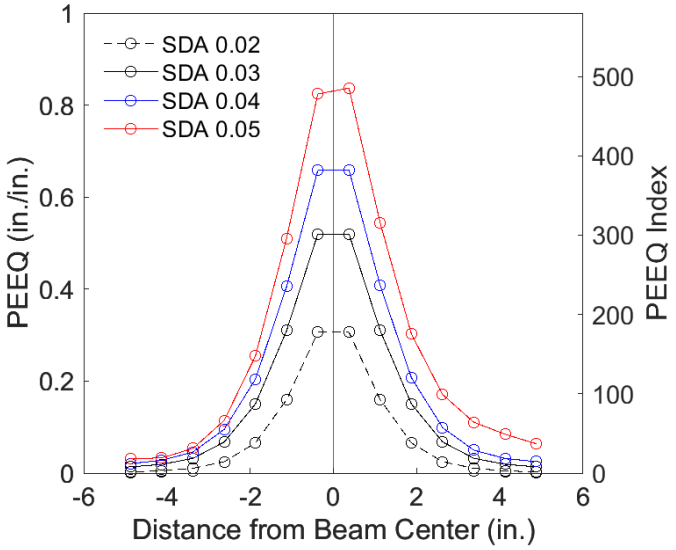

(b) Top Fiber *PEEQ*

Figure 7.30 Specimen C6 without Continuity Plate: *PEEQ* across Beam Top Flange Width

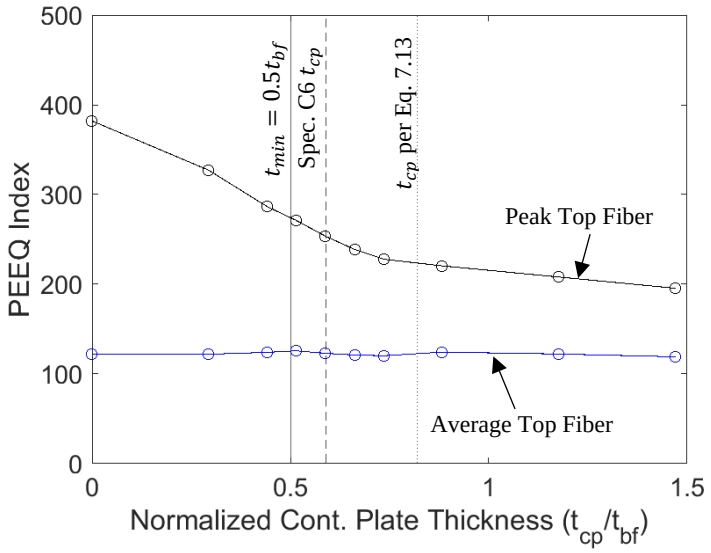

Figure 7.31 Parametric Response: Specimen C6 Beam Flange *PEEQ* as t_{cp} is Varied

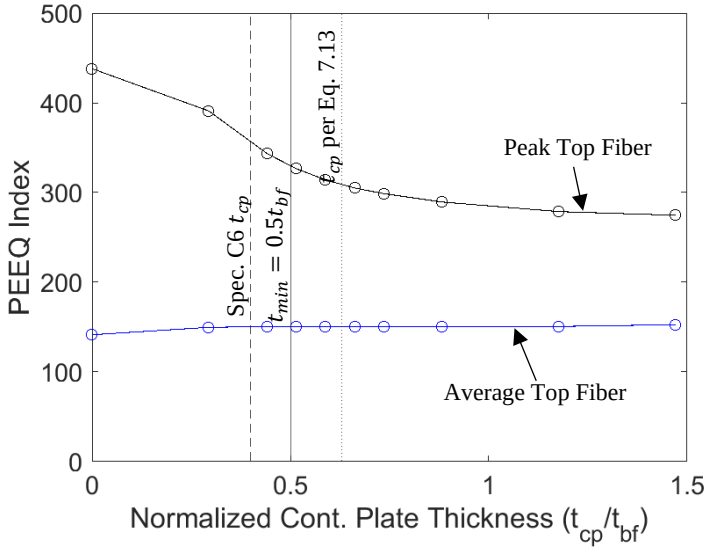

Figure 7.32 Parametric Response: Specimen C5 Beam Flange *PEEQ* as t_{cp} is Varied

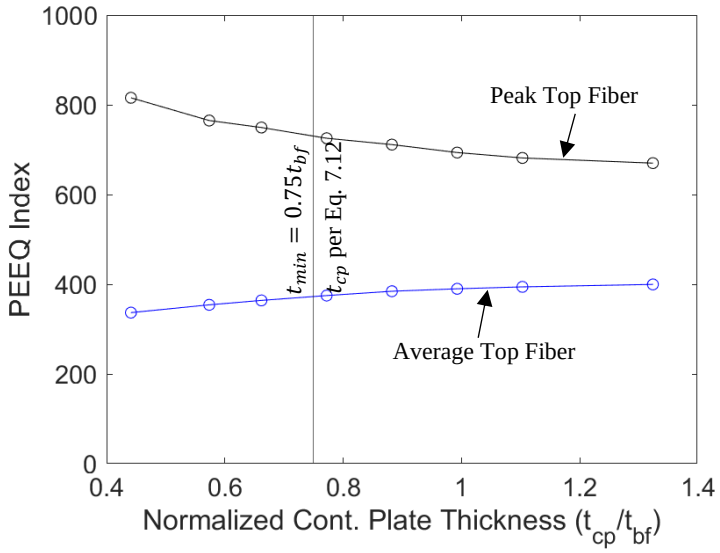

Figure 7.33 Parametric Response: Specimen W2 Beam Flange *PEEQ* as t_{cp} is Varied

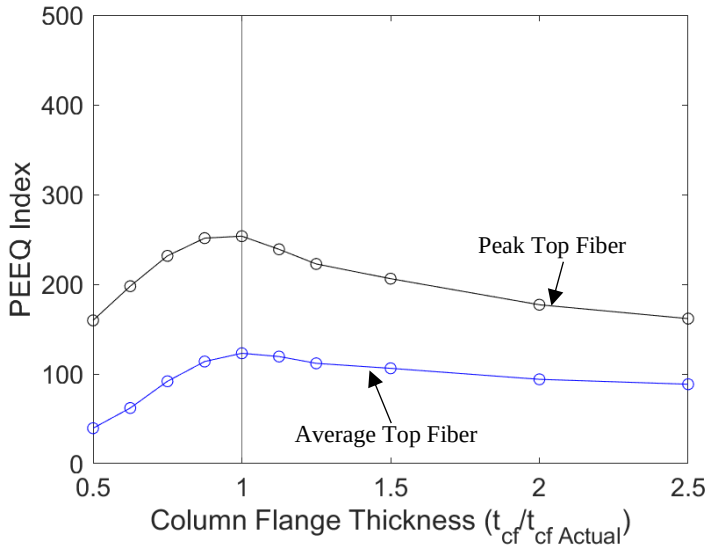

Figure 7.34 Parametric Response: Specimen C6 Beam Flange *PEEQ* as t_{cf} is Varied

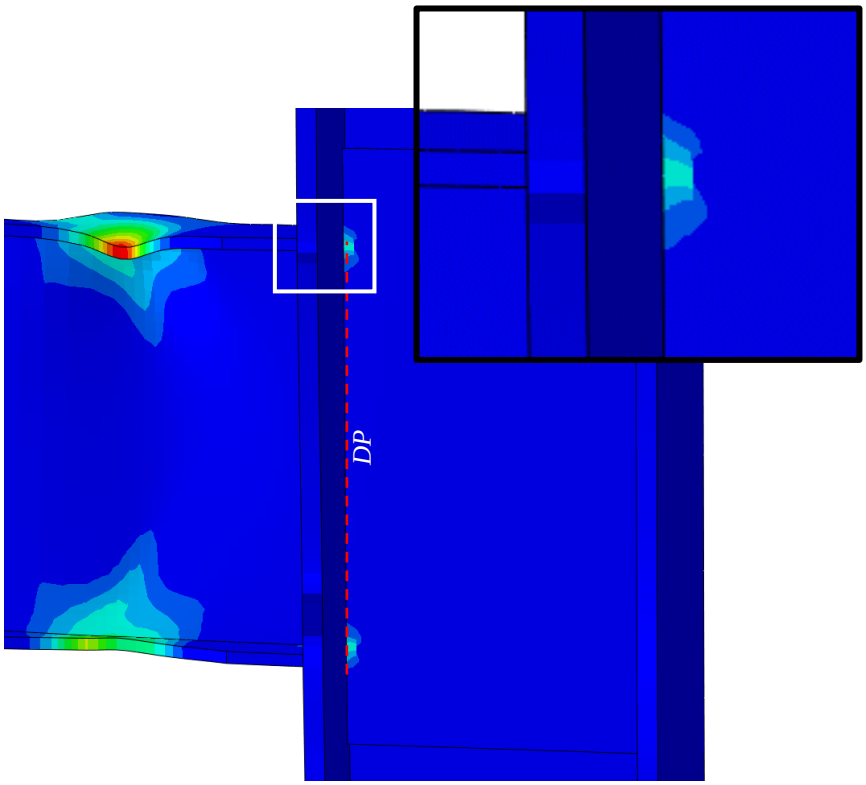

Figure 7.35 Parametric Response: Specimen C7 *PEEQ* of Doubler Plate

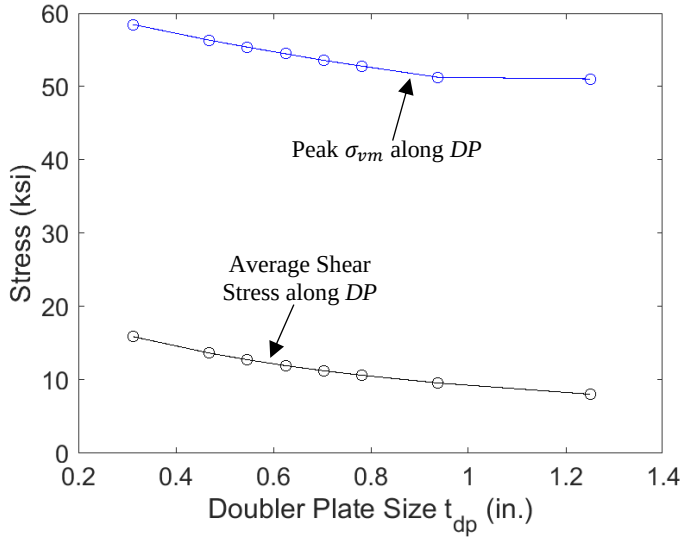

Figure 7.36 Parametric Response: Specimen C7 Doubler Plate Stress

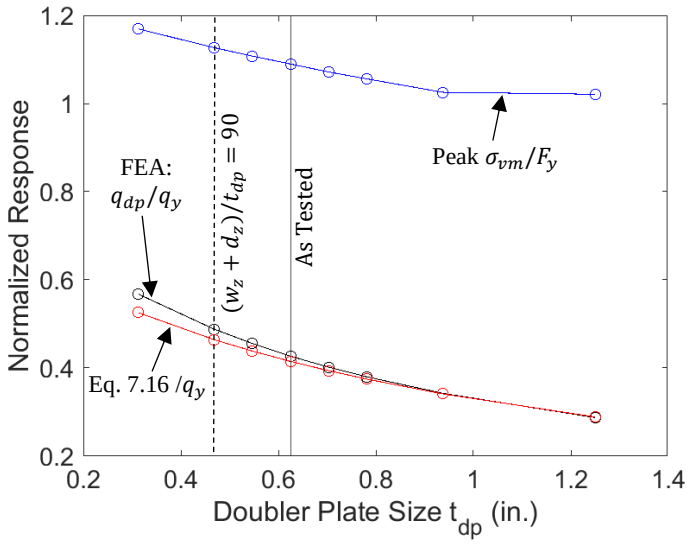

Figure 7.37 Parametric Response: Specimen C7 Normalized Response versus Doubler Plate Thickness

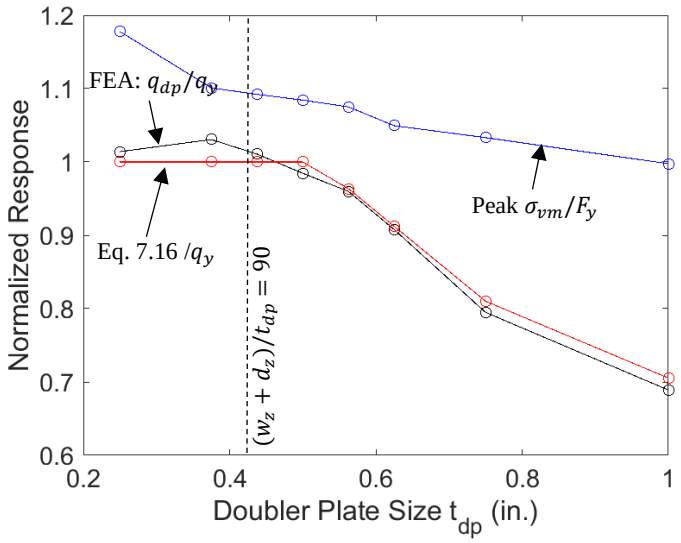

Figure 7.38 Parametric Response: Specimen C5 Normalized Response versus Doubler Plate Thickness

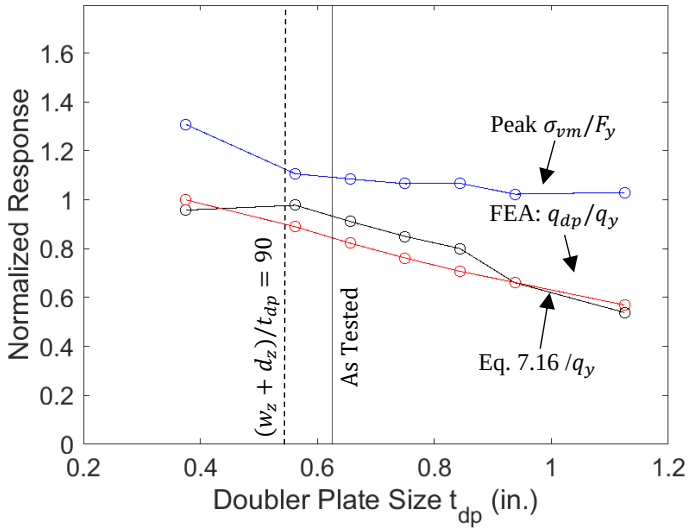

Figure 7.39 Parametric Response: Specimen W2 Normalized Response versus Doubler Plate Thickness

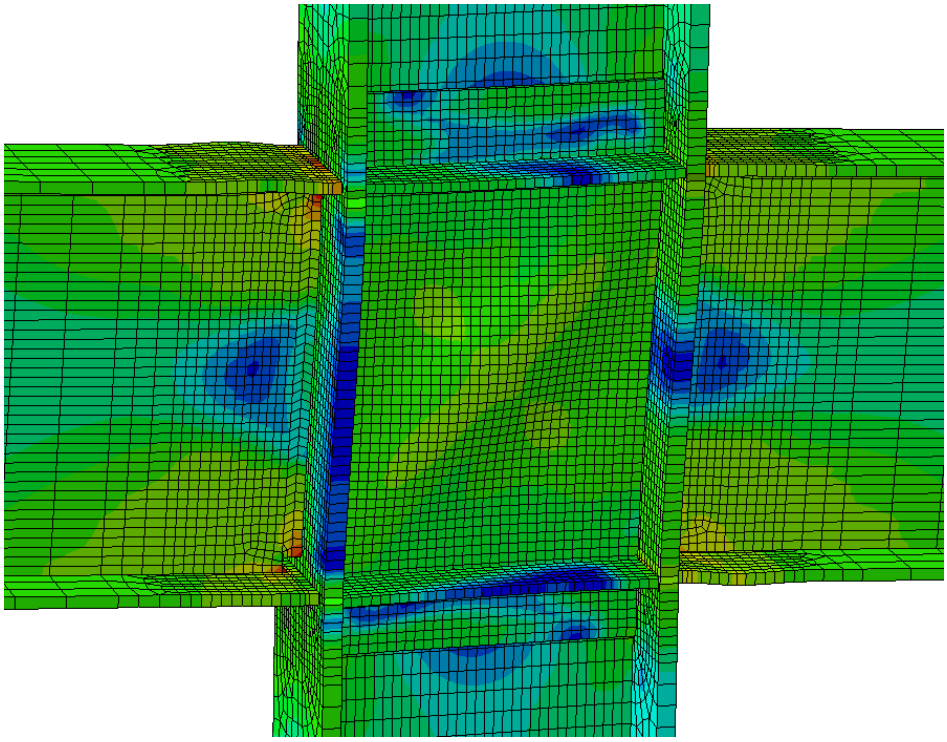

Figure 7.40 Parametric Response: Specimen W2 Doubler Plate Buckling during 0.04 rad Drift

8. FINITE ELEMENT DAMAGE MECHANICS

8.1. General

This chapter presents a discussion on modern fracture mechanics to predict fracture of SMF connections. This includes a discussion on the derivation of the state-of-the-art Cyclic Void Growth Model (CVGM) for predicting ductile fracture. Following this, the results of CVGM on several tested moment connections are showcased.

8.2. Ductile Fracture Background

As discussed in Section 1.3.4, the prediction of fractures in SMF connections requires novel fracture models beyond traditional Linear Elastic Fracture (LEFM) or Elastic-Plastic Fracture Mechanics (EPFM). This is because the large-scale yielding present in a post-Northridge moment connection coupled with non-proportional loading and a lack of an initial flaw violates the assumptions of LEFM and EPFM (Rolfe 1977). It is further anticipated that high levels of residual stress often lead to significant yielding well before applied service loads would generate a yielding level of stress. To meet this challenge the research community turned to local fracture mechanics which use high fidelity numerical models and avoid the singularity or energy-based philosophies used in traditional fracture mechanics. These modern local models attempt to predict fracture by simulating the specific mechanisms of fracture at a continuum scale (Kanvinde 2017). Although there are local models that aim to predict brittle cleavage fracture, the research presented herein will focus on local models to predict ductile fracture—the predominate fracture initiation mechanism observed in post-Northridge SMF connections.

Figure 8.1 shows the process of ductile fracture. The process starts when voids in the steel matrix around inclusions or carbides nucleate. Subsequent void growth occurs from the combined effect of plastic strain and hydrostatic stresses. As the voids continue to grow, the material between

voids undergoes necking and strain localization. Eventually, the voids coalesce, forming part of a crack or a larger void. In a standard monotonic tensile coupon test, the ubiquitous cup and cone fracture may be entirely a ductile fracture process. At the center of the coupon, high triaxial stresses result in a ductile fracture perpendicular to the applied stress. Once the center portion of the coupon has failed, the transition to the relatively restraint-free edges of the specimen result in a shear-type fracture. Shear type fractures develop from high concentrations of plastic strain which develop on slip bands associated with the highest resolved shear stress (Kanvinde and Deierlein 2004). The resulting fracture surface appears dimpled in the center of the coupon due to the equiaxial growth of voids while the shear lips take on a dull luster due to elongated smaller voids that coalesced to form the fracture surface.

The initiation of ductile fracture is found to depend on three factors: (1) the average strain at the location of interest, (2) the triaxiality of the stress state, and (3) the strain capacity of the material (Kuwamura 1997). In moment connections, the welded geometry often leads to strain risers and high levels of triaxiality due to the imposed restraint. Moreover, the through-thickness direction of heavy steel shapes tends to be pone to this type of fracture due to the high levels of restraint and relatively low toughness (Kuwamura and Akiyama 1994).

The propagation of a ductile crack is believed to occur as a growth of a tear between large islands of coalesced voids (see Figure 8.2). Figure 8.3 shows a cross-section through a crack front for different magnitudes of plastic strain. It is observed that, when in the elastic region, fatigue cracks generally remain sharp while the ductile crack opens up as new voids are incorporated. During typical high-cycle fatigue loading, the crack tip will dull during tension excursions due to plasticity at the crack tip (Anderson 2017). This is still true ductile tearing, except the dulling of the crack tip occurs due to the incorporation of new voids into the crack front. It is believed that

this contributes significantly to the stable propagation of a ductile crack. During compression excursions, the typical fatigue sharpening phenomenon is replaced with a sharpening of the spherical voids, resulting in further strain localization which may induce the nucleation of new voids along slip bands. As the curvature of the voids increases, a traditional stress singularity can develop, leading to a more traditional fracture phenomenon presenting pockets of cleavage fracture between the ruptured voids. Evidence of this has been shown by Scanning Electron Microscopy performed by Kanvinde and Deirelein (2004). The transition between traditional fatigue and low-cycle fatigue depends on the magnitude of the plastic strain during each excursion (see Figure 8.4). It is pertinent to note that the stable propagation of a ductile crack often leads to a brittle cleavage fracture as the material is exposed to an increasing amount of stress as the crack propagates.

Local models are either coupled in that accumulated damage is incorporated back into the finite element model to capture the softening effects of the damage or uncoupled in that the damage is estimated after the analysis. The classical coupled model is the Gurson-Tvergaard-Needleman (GTN) model which models steel as a porous medium. In this case, the porosity of the medium is permitted to change as a material is damaged (Anderson 2017). Uncoupled models use post-processing to evaluate local stress and strain fields to determine the extent of the damage. For example, Dufailly and Lemaitre (1995) developed a damage index related to the strain energy density, Y and the local stress triaxiality, T (Eq. 1.2):

$$D = \int \left(\frac{Y}{S}\right)^{T} d\bar{\epsilon}^{p} \text{ if } T > -\frac{1}{3} \tag{8.1}$$

where $d\bar{\epsilon}^{p}$ is an increment of effective plastic strain (see Eq. 1.3) and S is a material constant. When $D > 1$, the model predicts fracture.

These uncoupled models can be used in a pseudo-coupled methodology where the post-processing is performed during the analysis and, if an element is considered exhausted, then it is

removed from the analysis in subsequent analysis steps. Another popular local model is the Cyclic Void Growth Model (CVGM) developed by Kanvinde and Deierlein (2004). This model is rooted in the original work by Rice and Tracy (1969) on predicting the rate of growth of spherical void in a stress field (see Eq. 1.1). Abbas (2015) used Eq. 8.1 and the CVGM to successfully predict ductile fracture of steel subjected to high cyclic plastic strains in regions on intentional defects (i.e., shot-pins, shear studs or holes).

8.3. Development of the Cyclic Void Growth Model

This model is developed by integrating the void growth rate expression developed by Rice and Tracy (see Eq. 1.1):

$$\ln\left(\frac{R}{R_o}\right) = \int_0^{\epsilon^p} Ce^{1.5T} d\bar{\epsilon}^p \tag{8.2}$$

where C is a material-dependent coefficient. Assuming that fracture occurs at a critical void ratio:

$$\ln\left(\frac{R}{R_o}\right)_{critical} = \int_0^{\epsilon^p_{critical}} Ce^{1.5T} d\bar{\epsilon}^p \tag{8.3}$$

it permits the solution of the critical void growth capacity under monotonic tension:

$$\eta_{mono} = \frac{\ln\left(\frac{R}{R_o}\right)_{critical}}{C} = \int_0^{\epsilon^p_{critical}} e^{1.5T} d\bar{\epsilon}^p \tag{8.4}$$

For structural steels η_{mono}, is found to be in the range of 1 to 5 (Kanvinde 2017). Eq. 8.4 is referred to as the Void Growth Model (VGM). To generalize to the cyclic application, Eq. 1.1 is amended to:

$$\frac{dR}{dR_o} = sign(T) Ce^{1.5|T|} d\bar{\epsilon}^p \tag{8.5}$$

This expression can now predict the shrinking of voids when a hydrostatic compression (negative triaxiality) exists. Integrating this expression:

$$\ln\left(\frac{R}{R_o}\right)_{critical,\ cyclic} = \sum_{Tension} C_1 \int_{\epsilon_1}^{\epsilon_2} e^{1.5|T|} d\bar{\epsilon}^p - \sum_{Compression} C_2 \int_{\epsilon_1}^{\epsilon_2} e^{1.5|T|} d\bar{\epsilon}^p \tag{8.6}$$

where C_1 and C_2 are constants that reflect the rate of growth of voids during the tension and compression cycles. Assuming that the rate of growth is similar allows the solution of the critical void growth capacity during cyclic application and leads to CVGM:

$$\eta_{cyclic} = \frac{\ln\left(\frac{R}{R_o}\right)_{critical,\ cyclic}}{C} = \sum_{Tension} \int_{\epsilon_1}^{\epsilon_2} e^{1.5|T|} d\bar{\epsilon}^p - \sum_{Compression} \int_{\epsilon_1}^{\epsilon_2} e^{1.5|T|} d\bar{\epsilon}^p \tag{8.7}$$

The cyclic void growth capacity is assumed to be related to the monotonic void growth capacity through a damage function, $f(D)$:

$$\eta_{cyclic} = f(D)\eta_{mono} \tag{8.8}$$

The observed dependence of ductile fracture on accumulated plastic strain (Kanvinde and Deierlein 2004) leads to the adoption of a damage function:

$$F(D) = e^{-\lambda \bar{\epsilon}^p} \tag{8.9}$$

where λ is a material constant related to the decay of toughness due to accumulated plastic strain. This factor is found to be in the range of 0 to 1.0 for most structural steels (Kanvinde 2017). According to Myers et al. (2014), cyclic damage is due to three effects: (1) the compressive excursions tend to oblate microvoids and the increased local curvatures result in a higher degree of strain localization during subsequent tension excursions, (2) the large cyclic strains may nucleate secondary voids along dislocation bands, and (3) a strain-softening may occur in the inter-void ligament material which leads to further strain localization.

In order for the degradation of the CVGM to the VGM, the damage function must be equal to unity for the duration of the first monotonic tension excursion. To rectify this Kanvinde and Deierlein proposed that the damage evolution only be evaluated at the start of each tension excursion—resulting in a piecewise damage function. Myers et al. (2014) made the observation that using the total accumulated plastic strain as a damage function effectively double counts the influence of plastic strain during the tension excursion to void growth. Instead he proposed using the damage function:

$$F(D) = e^{-\lambda \bar{\epsilon}_c{}^p} \tag{8.10}$$

where $\bar{\epsilon}_c{}^p$ is the accumulated plastic strain during the compression excursions (i.e., when $T < 0$). This avoids double-counting the tension cycles and elegantly results in the CVGM degrading to the VGM during monotonic tension. Therefore, a fracture is predicted to occur when

$$\sum_{Tension} \int_{\epsilon_1}^{\epsilon_2} e^{1.5|T|} d\bar{\epsilon}^p - \sum_{Compression} \int_{\epsilon_1}^{\epsilon_2} e^{1.5|T|} d\bar{\epsilon}^p > e^{-\lambda \bar{\epsilon}_c{}^p} \eta_{mono} \tag{8.11}$$

The left-hand side of Eq. 8.11 represents the void growth demand, while the right-hand side represents the void growth capacity. This model requires three parameters: (1) a cyclic material degradation constant, λ, (2) a monotonic critical void growth ratio, η_{mono}, and (3) a characteristic length which defines the material volume to be considered. The characteristic length is a crucial parameter when considering fracture in a location with high-stress gradients (i.e., the reentrant corner of the beam-to-column junction). The recommended characteristic length is 2 to 10 times the average grain size (Kanvinde 2017).

When evaluating Eq. 8.11, a negative value demand may occur on the left-hand side, which is the case for a symmetric strain cycle. This would erroneously predict a negative void volume. To reconcile this, the left-hand side of the equation is bounded by a floor of zero. In a situation where the left-hand side is at the floor, the next tension excursion immediately produces void

growth demand (i.e., the negativity of the equation does not accumulate through the summation). This physically implies that void growth cannot be prevented by precompression.

Recent developments in void growth models have revealed that the relationship between void growth and triaxiality derived by Rice and Tracy (1969) was originally formulated as a hyperbolic sine function. The simplification that $2\sinh(1.5T)$ was equal to $e^{1.5T}$ to evaluate void growth at high triaxiality levels resulted in the contrived negative term in Eq. 8.11 to account for void shrinkage. This also resulted in an over-prediction of damage during low triaxiality (Smith et al. 2014). Reversing the simplification made by Rice and Tracy to amend the CVGM model developed by Kanvinde permits a simplification of the formulation:

$$\int_0^{\epsilon^p} (e^{1.5T} - e^{-1.5T}) d\bar{\epsilon}^p > e^{-\lambda \bar{\epsilon}_c{}^p} \eta_{mono} \tag{8.12}$$

or more succinctly:

$$\int_0^{\epsilon^p} 2\sinh(1.5T) d\bar{\epsilon}^p > e^{-\lambda \bar{\epsilon}_c{}^p} \eta_{mono} \tag{8.13}$$

For a high triaxial loading, Eq. 8.13 and Eq. 8.11 converge. When significant portions of loading occur with low levels or zero triaxiality, Eq. 8.13 predicts a lower ductility demand than Eq. 8.11. This is attributed to the mathematical formulation in Eq. 8.11, which predicts void growth when the triaxiality is zero.

It is found that Eq. 8.13 is only applicable at predicting fracture when the triaxiality is greater than 0.4. Below this limit, it is found that the fracture transitions to a shear dominated fracture and the mechanisms of void growth due to hydrostatic tension are insufficient to describe the mechanism of fracture (Jia and Kuwamura 2014). Experiments which decreased the triaxiality further found a fracture cut-off that exists when a triaxiality of -1/3 is reached. This corroborates the classic Bridgeman experiments which demonstrate that tensile coupons can be pulled to a fine

point when subjected to high levels of compressive triaxial stress (Fung 1965). Bao and Wierzbicki (2004) managed to describe this behavior by a set of carefully designed specimens (see Figure 8.5). This figure shows the sharp deviation that occurs at a triaxiality of 0.4 which is not captured by Eq. 8.13.

To correct the CVGM, Smith et al. (2014) proposed an amended model called the Stress Weighted Damage Model (SWDM). This new model incorporates a lode angle parameter. The lode angle reflects the angle formed by the projection of the current stress state on the π plane and the nearest principle stress axis. It is related to the third invariant of the deviatoric stress tensor, J_3, and quantifies the shear relationship of the stress tensor. The theory developed by Smith et al. degrades to Eq. 8.11 for axisymmetric conditions. For the beam flange-to-column CJP weld fracture the triaxiality is very high ($|T| \geq 1.0$) where the influence of the lode angle is found to be negligible (Smith et al. 2014). Therefore, the added complexity of the SWDM is not warranted for this analysis.

8.4. Material Properties

To use the CVGM to predict the initiation of ductile fracture, two material parameters are required. The first relates to the ductile fracture potential under monotonic tension and is calibrated by failing circumferentially notched (CNT) specimens. CNT specimens are convenient because of a known, relatively constant triaxiality across the notch. By varying the notch geometry, the amount of triaxiality is controlled and the resulting plastic strain at failure is used to perform a regression to find η_{mono}. Next, the cyclic degradation of the material is captured by the exponential decay parameter λ. This parameter is calibrated by comparing finite element results to the point of failure of cyclic CNT specimens.

The typical fracture that would prevent a SMF connection from performing its function is through the beam flange-to-column CJP groove weld. The weld metal usually has lower fracture toughness than the base metal and is exposed to discontinuities and strain rises which amplify the fracture demands (Myers et al. 2014). Therefore, the required ductile fracture parameters, η_{mono} and λ, are required for the weld metal. After the 1994 Northridge earthquake, there was a significant research effort on characterizing the toughness of welded beam-to-column connections. This was precipitated by fractures that appeared to originate in the weld near the fusion boundary between weld metal and base metal (FEMA 2000f). These fractures would then propagate in a few different paths. A common propagation path was through the Heat Affected Zone (HAZ) of the column base material just beyond the fusion boundary of the weld metal. This zone is characterized by a highly heterogeneous microstructure that was sufficiently heated during welding to illicit metallurgical changes in the metal structure but remain below the melting temperature of the metal. The HAZ that exists in the column base material consists of metallurgical changes to the metal which is loaded through the rolling thickness of the shape (or plate), which is believed to exacerbate the fracture potential.

The heterogeneous microstructure of a HAZ is further characterized by four regions: Coarse-Grained (CGHAZ), Fine-Grain (FGHAZ), intercritical (ICHAZ) and subcritical (SCHAZ) which are characterized by the temperature reached during welding (see Figure 8.6). The transition between weld metal and CGHAZ is easily observed under optical magnification as the transition between acicular (needle-like) ferrite grains and large ferrite grains (FEMA 2000f). Other brittle microstructures (bainite and martensite) exist in the CGHAZ. The combined effect of large ferrite grains provides fewer grain boundaries to interrupt the movement of dislocations and pockets of brittle microstructures that result in a low fracture toughness. Meanwhile, the FGHAZ has small

equiaxed ferrite grains which lead to ideal conditions and high fracture resistance. For a single pass weld, these zones exist in isolation of each other; however, for a multipass weld, the subsequent reheating of particular zones from a previous pass creates a complicated network of interacting microstructures. For example, the interaction of an ICHAZ of a subsequent weld bead and the CGHAZ of a previous weld bead is known to produce a pocket of brittle microstructures known as a Local Brittle Zone (LBZ) (Myers et al. 2014). However, in general, the subsequent reheating and grain size refinement of CGHAZ tends to minimize the volume fraction of CGHAZ in multipass welds. Therefore, it is typically found that smaller electrodes, which use less heat per weld pass, and more weld passes are more desirable than fewer weld passes which require higher heat inputs. This desire is at odds with the economy of fabrication.

Although most fractures observed following the 1994 Northridge and 1995 Kobe Earthquakes were characterized as brittle cleavage fractures, notch-tough electrodes and modern detailing have transitioned the predominate initial fracture mode to a ductile mode. The resistance to ductile fracture is still highly dependent on the pertinent microstructures and the heterogeneity of weld material and surrounding HAZ. This presents considerable difficulty in characterizing the ductile fracture parameters. Myers et al. (2014) attempted to characterize the ductile fracture parameters by extracting CNT specimens from welded joints fabricated with several AWS D1.8 Demand Critical compliant electrodes. The CNT specimens were polished and etched prior to fabricating the reduced section such that the notch could be located at a specific microstructure. This permits the variability in fracture toughness between the weld metal and HAZ to be estimated.

However, with standard notch geometries and geometric variation in the location of the HAZ across the weld sample, the determined ductile fracture parameters represent an aggregate of nearby microstructures. The average value of the monotonic ductile fracture resistance η_{mono} was

found to be 1.26. The research found significant variability of the monotonic parameter with a coefficient of variation of 0.22; variation is attributed to the heterogeneity of the tested microstructures. It was also found that the cyclic degradation parameter, λ, to be equal to 1.7 was nearly double that of typical A992 base metal (Kanvinde 2017). The significant degradation is attributed to the microstructure of the weld material being less tolerable of plastic flow prior to fracture.

8.5. Modeling Methodology

The models were developed by using the framework discussed in Chapter 7 to create the global finite element models. While the global finite element models were meshed entirely with S4 shell elements, a local submodel of the connection region was created using solid geometry and meshed with C3D8R elements (see Figure 8.7). Submodel geometry includes representative weld access hole geometry and beam and column radii at the flange-to-web junction. Material properties in the vicinity have been chosen to reflect the higher strength and lower hardening potential of the weld metal. Similar element sizes have been used with success for the CVGM (Zhou et al. 2012). The boundaries of the submodel are driven by the displacement field of the global model (see Figure 8.8). Mesh refinement was performed at the beam top flange such that the maximum element size was 0.05 in. (see Figure 8.9). The radius and weld access hole is refined such that the geometry was adequately captured [see Figure 8.9(b)].

8.6. Analysis Results

It is found that the critical location for Specimen C6 is at the center of the flange in the reentrant corner formed between the beam flange and column (see Figure 8.9). A plot of the von Mises stress at -0.04 rad drift is shown for the global and driven submodel (see Figure 8.13). A discontinuity at the interface between the beam top flange and weld metal is apparent in the stress

field due to the difference of yield stress of the material. The triaxiality of a section through the centerline of the submodel is shown in Figure 8.11. Figure 8.12 shows the resultant stress triaxiality at this location during the initial cycles from the finite element model; high levels of triaxiality justify the use of the CVGM as an applicable local model. Figure 8.13 shows the accumulated plastic strain of a section through the centerline of the submodel. The accumulated plastic strain at the critical location is observed in Figure 8.14. The expected flange force of Specimen C6 was 582 kips, which exceeds the expected WLY limit state of 430 kips (see Table 5.2). The maximum integrated beam flange force was found to be 576 kips, which is similar to the expected flange force. Therefore, according to the Specifications, we should expect that a continuity plate is required.

Figure 8.15 shows the computed void growth for Specimen C6 without a continuity plate. A thick line shows the right-hand side of Eq. 8.13, which denotes the capacity of the material. Relatviely poorer or higher quality welds are shown by a set of parallel lines based on a 95% confidence interval per the properties of welds recorded by Myers et al. (2014). The computed capacity of the material depends on the accumulated plastic strain, and as such depends on the sampled location. A thin line with a cyclic profile shows the left-hand side of Eq. 8.13. This line shows the void growth demand as a function of the integrated accumulated plastic strain and stress triaxiality. A decreasing excursion of this line indicates void shrinkage. It is observed that the CVGM would predict initiation of ductile fracture on the surface of the beam at the end of the 0.02 rad drift cycles [see Figure 8.15(a)]. For a relatively poor quality weld, this fracture would propagate 1/16 in. into the surface of the beam top flange [Figure 8.15(b)]. Since this analysis is not coupled, the fracture of the material is not progressively increasing the ductile fracture demand as a crack develops; therefore, Figure 8.15(b) is an unconservative estimation of the fracture.

Figure 8.16 shows the void growth at the surface of the beam top flange at the critical location as for three different continuity plate thicknesses. The minimum continuity plate thickness according to Eq. 1.18 is 7/16 in. ($t_{cp}/t_{bf} = 0.5$), while the continuity plate used during the physical testing program was 1/2 in. ($t_{cp}/t_{bf} = 0.6$). The newly developed WLY limit state (see Eq. 7.10) predicts a required continuity plate equal to 11/16 in. ($t_{cp}/t_{bf} = 0.7$). It is observed that ductile fracture initiation is expected to occur with a minimum thickness continuity plate ($t_{cp}/t_{bf} = 0.5$) at 0.03 rad drift for a low quality weld and 0.06 rad drift for an average quality weld. The continuity plate sized as per Eq. 7.10 ($t_{cp}/t_{bf} = 0.75$) essentially percludes the initiation of ductile fracture.

Specimen C3 was designed to challenge the use of the Lehigh Criterion. The expected flange force of this specimen was 738 kips, which is substantially lower than the expected FLB or WLY limit states of 1317 and 932 kips, respectively. Therefore, this specimen did not require a continuity plate based on a strength limit state. Figure 8.17 shows that ductile fracture initiation is expected to occur during 0.03 rad drift cycles for an average quality weld. In contrast to Specimen C6, which required a continuity plate based on the WLY limit state, Specimen C3 does not show fracture initiation 1/16 in. into the surface.

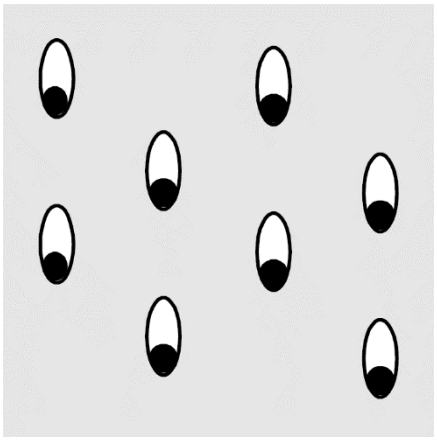

(a) Void Nucleation

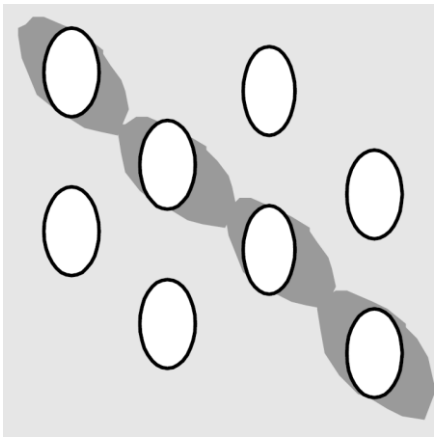

(b) Void Growth

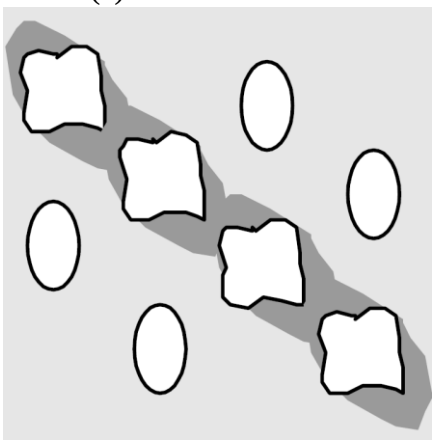

(c) Necking

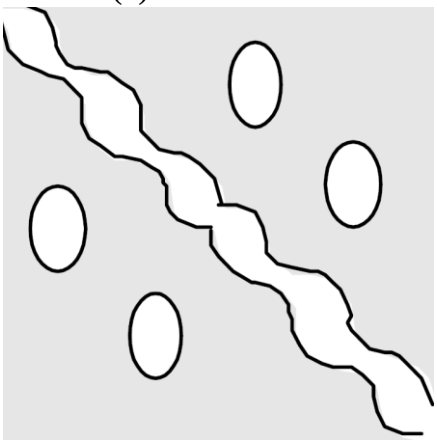

(c) Void Coalescence

Figure 8.1 Ductile Fracture Process (Kanvinde and Deierlein 2004)

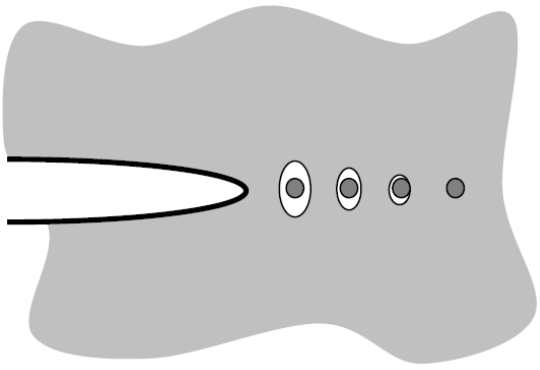

(a) Void Growth

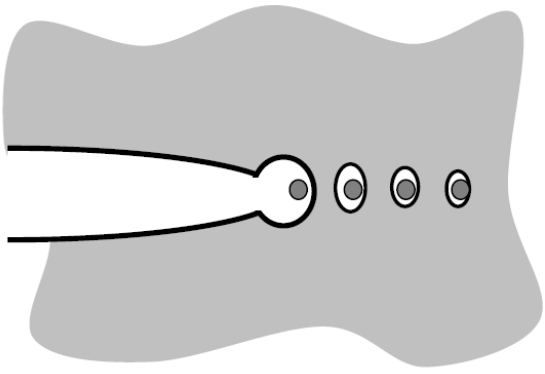

(b) Void and Crack Coalescence

Figure 8.2 Ductile Crack Propagation (Kanvinde and Deierlein 2004)

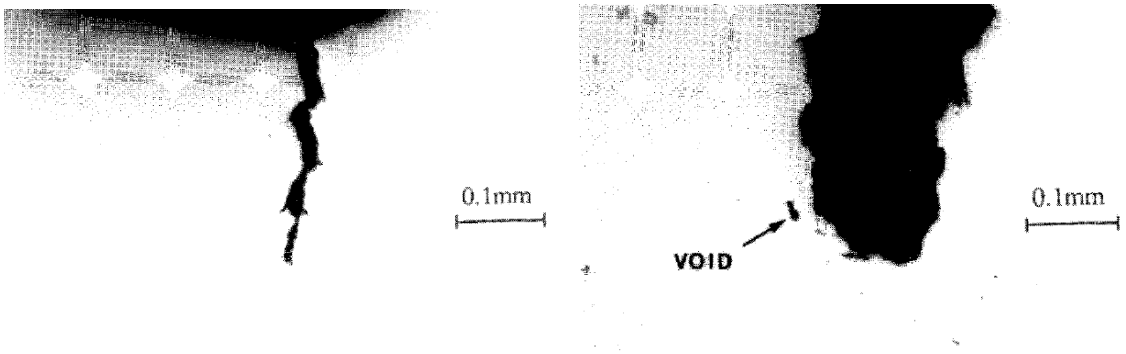

(a) $\epsilon^p = 0.4\%$ (b) $\epsilon^p = 3.6\%$

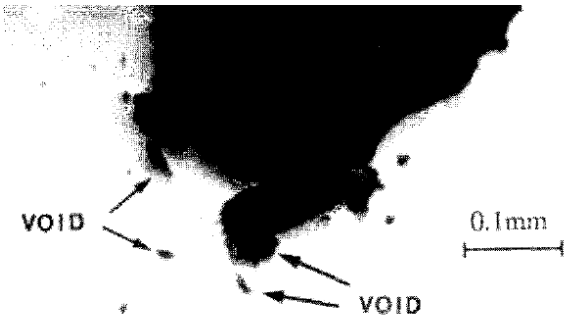

(c) $\epsilon^p = 7.2\%$

Figure 8.3 Crack Propagation during Constant-amplitude Cyclic Loading (Kuwamura 1997b)

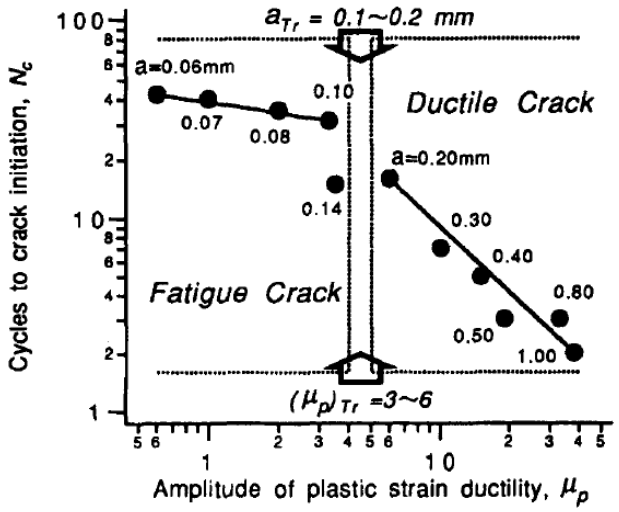

Figure 8.4 Transition from Fatigue to Ductile Fracture (Kuwamura 1997b)

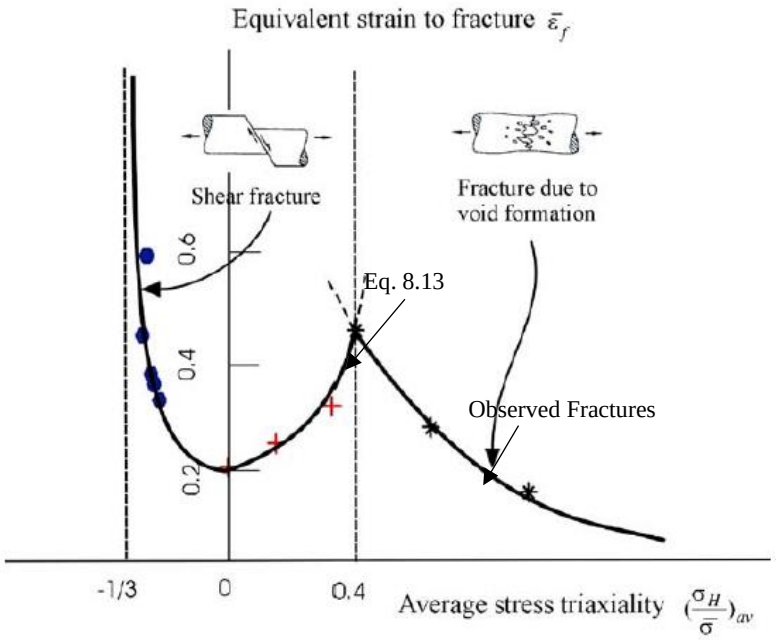

Figure 8.5 Equivalent Fracture Strain and Triaxiality (Bao and Wierzbicki 2004)

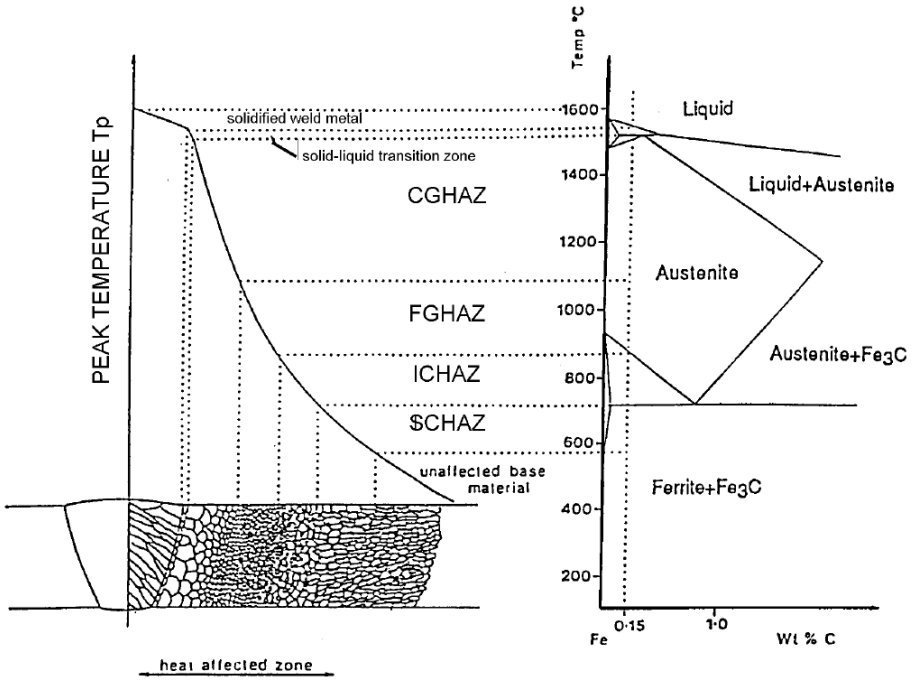

Figure 8.6 Microstructures of the Heat Affected Zone (FEMA 2000f)

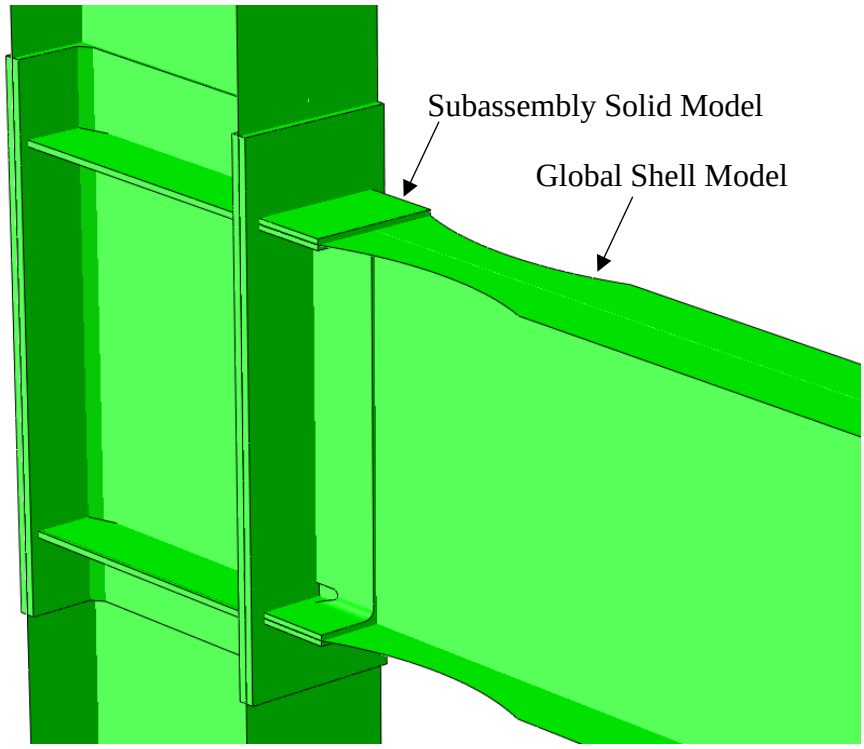

Figure 8.7 Subassembly Model Overview

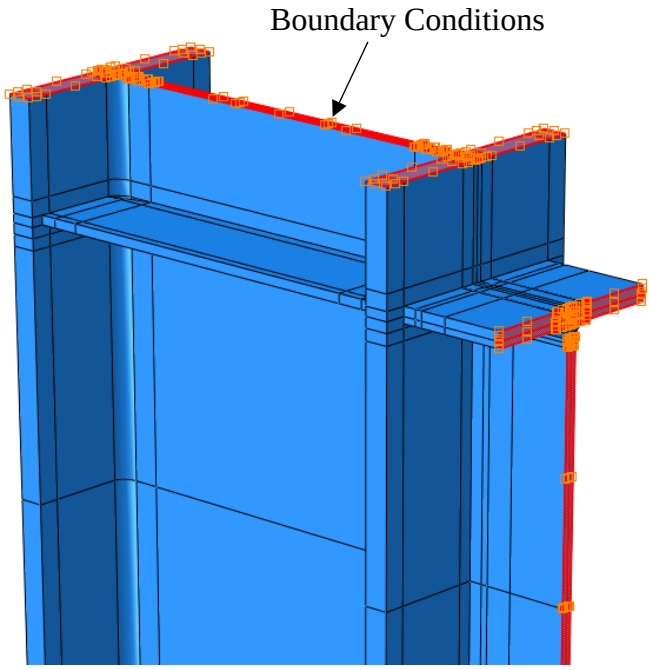

Figure 8.8 Subassembly Boundary Conditions

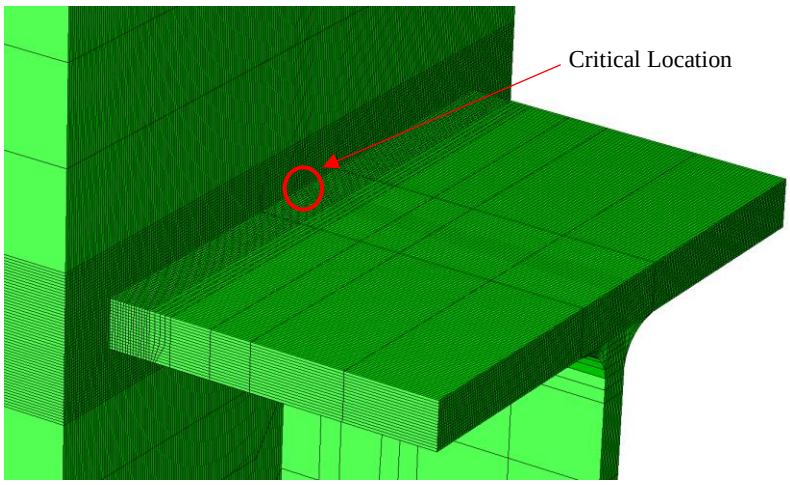

(a) Top side of Beam Top Flange

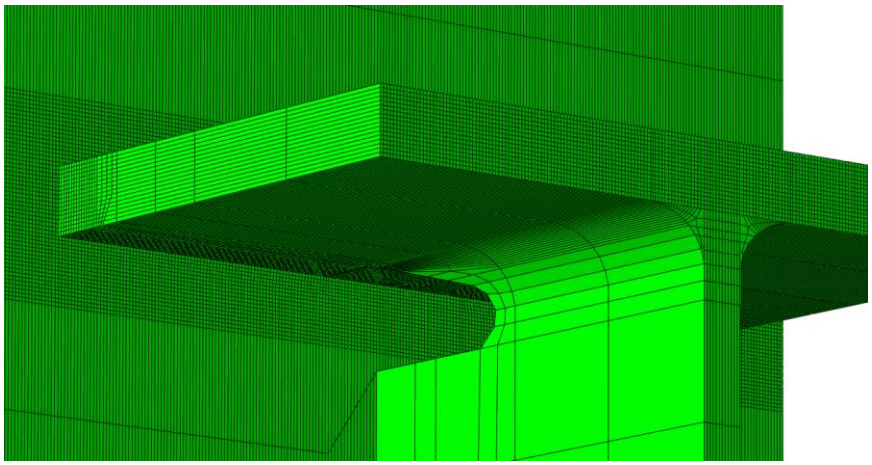

(b) Bottom Side of Beam Top Flange

Figure 8.9 Subassembly Modelling

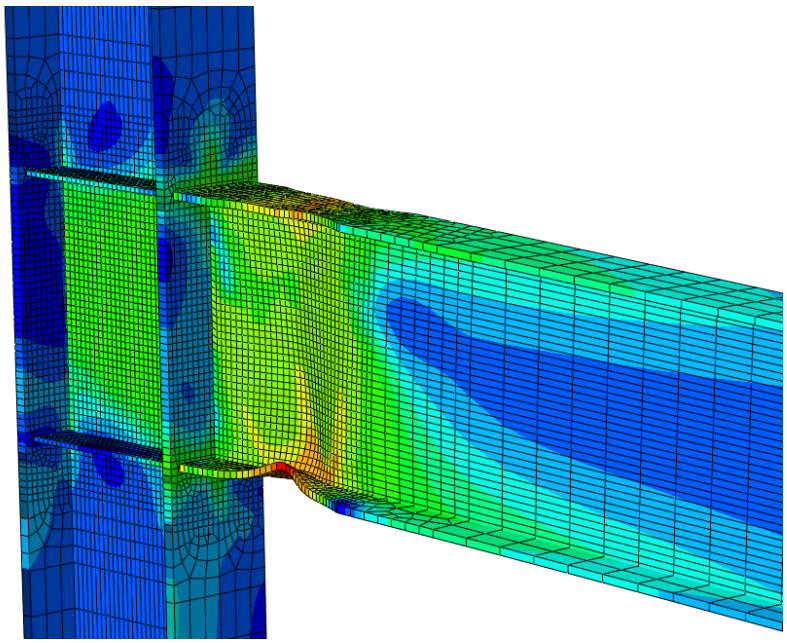

(a) Global Model

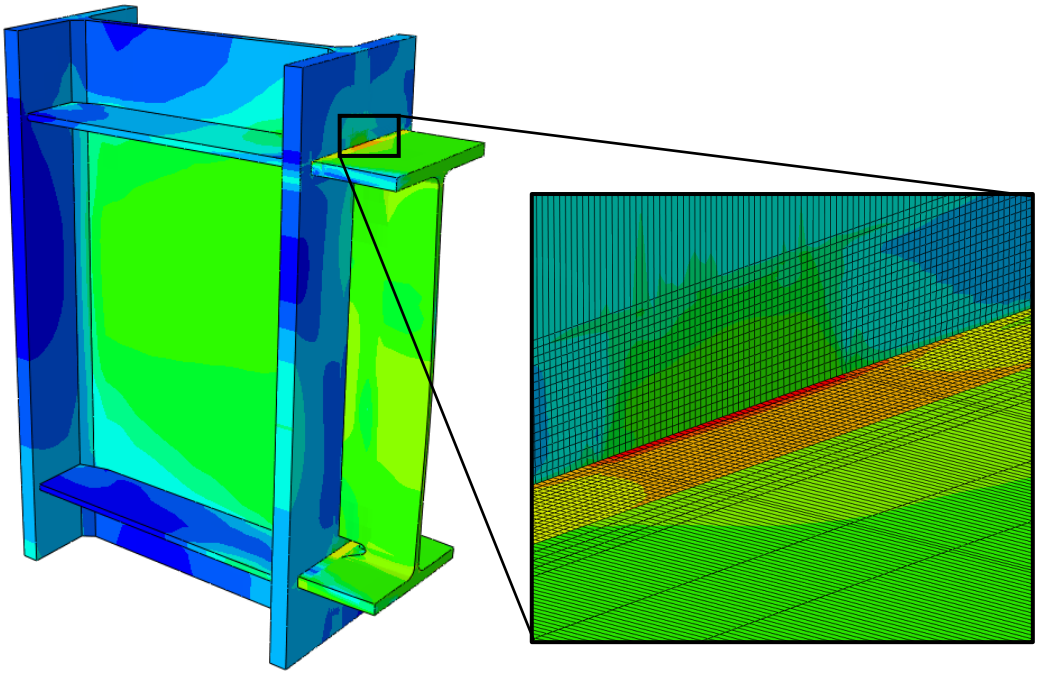

(b) Submodel

Figure 8.10 Specimen C6: Model Results at -0.04 rad Drift (1st Cycle)

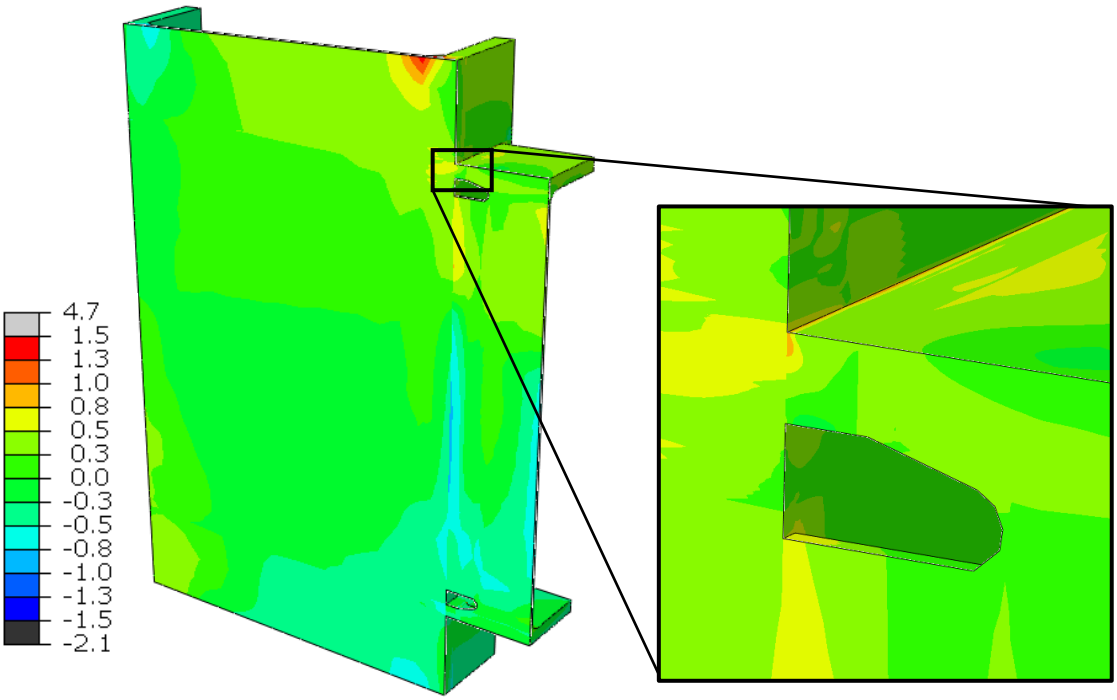

Figure 8.11 Specimen C6: Stress Triaxiality Contours at -0.04 rad Drift (1st Cycle)

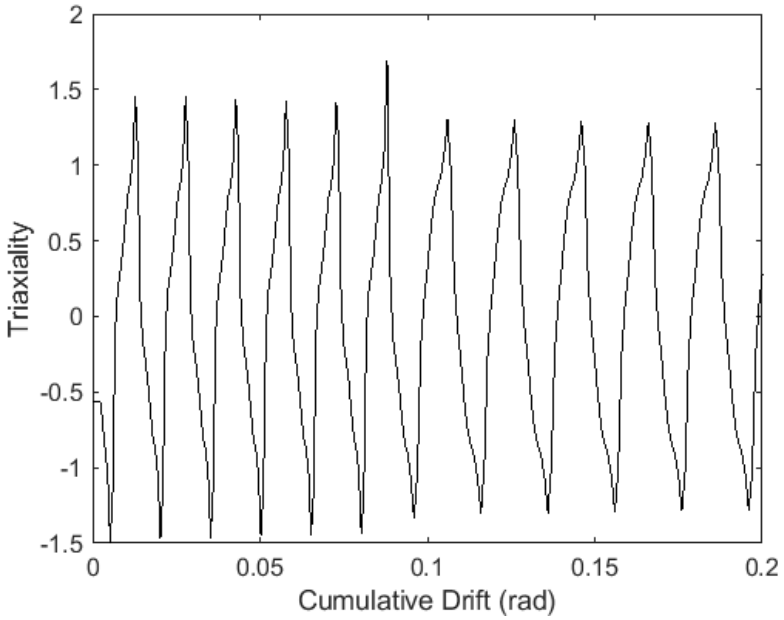

Figure 8.12 Stress Triaxiality at Critical Location

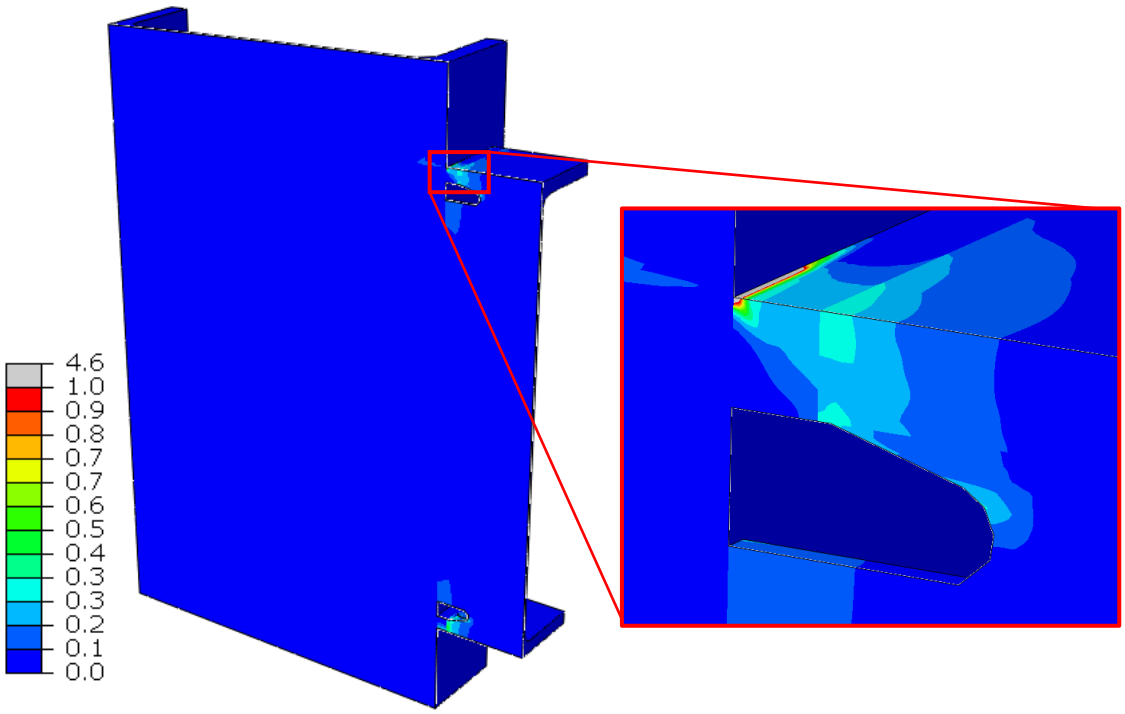

Figure 8.13 Specimen C6: Accumulated Plastic Strain (*PEEQ*) Contours at -0.04 rad Drift (1st Cycle)

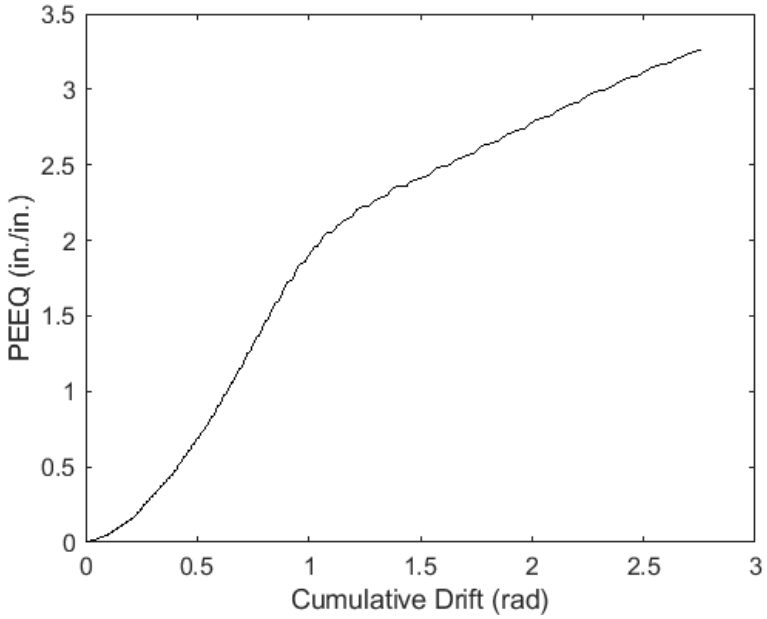

Figure 8.14 Accumulated Plastic Strain (*PEEQ*) at Critical Location

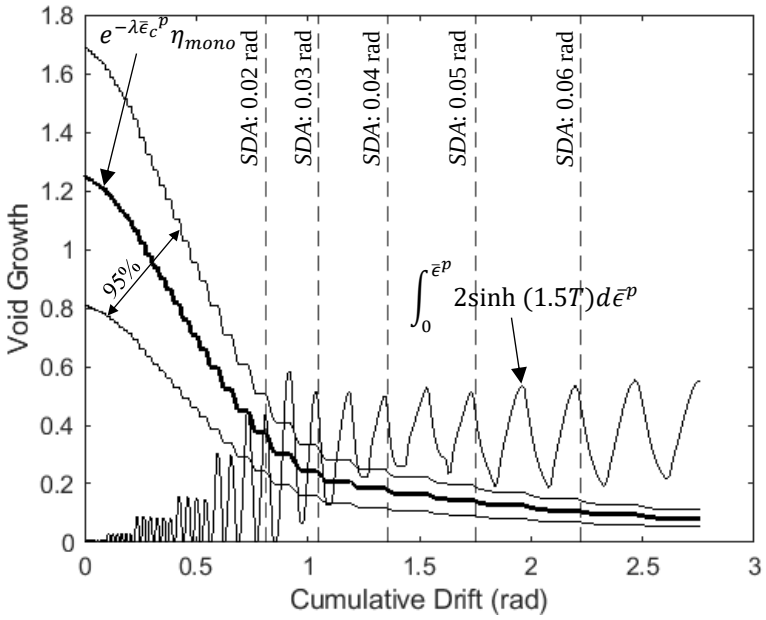

(a) at Beam Top Flange Surface

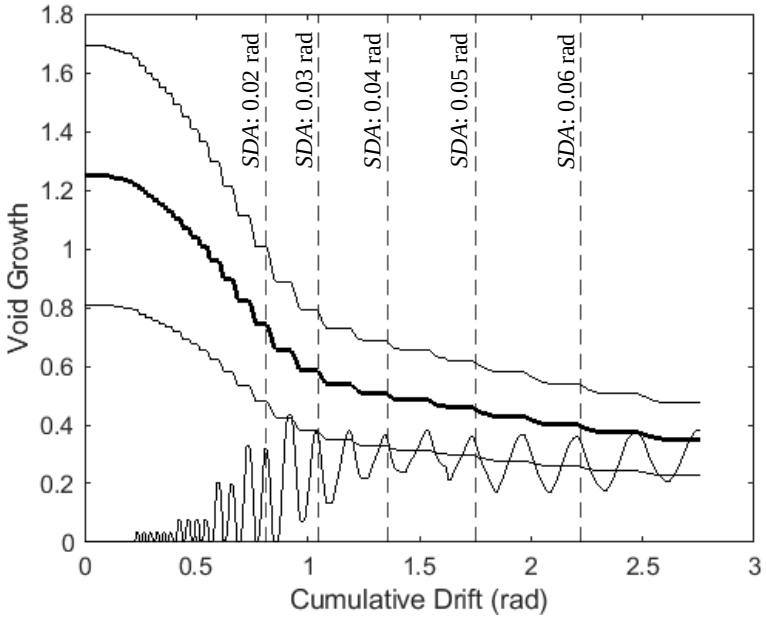

(b) 1/16 in. below Beam Top Flange Surface

Figure 8.15 Specimen C6: Void Growth with Continuity Plate is Removed

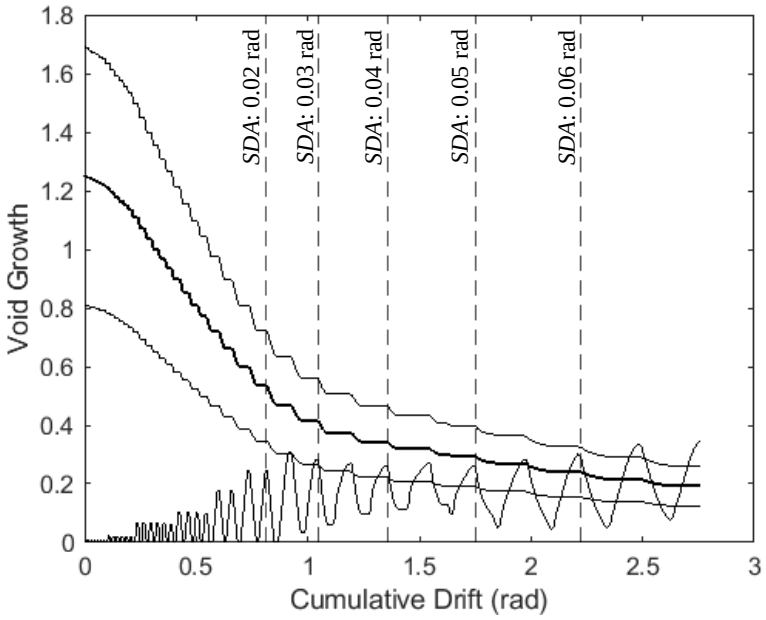

(a) Minimum Continuity Plate Thickness ($t_{cp}/t_{bf} = 0.5$)

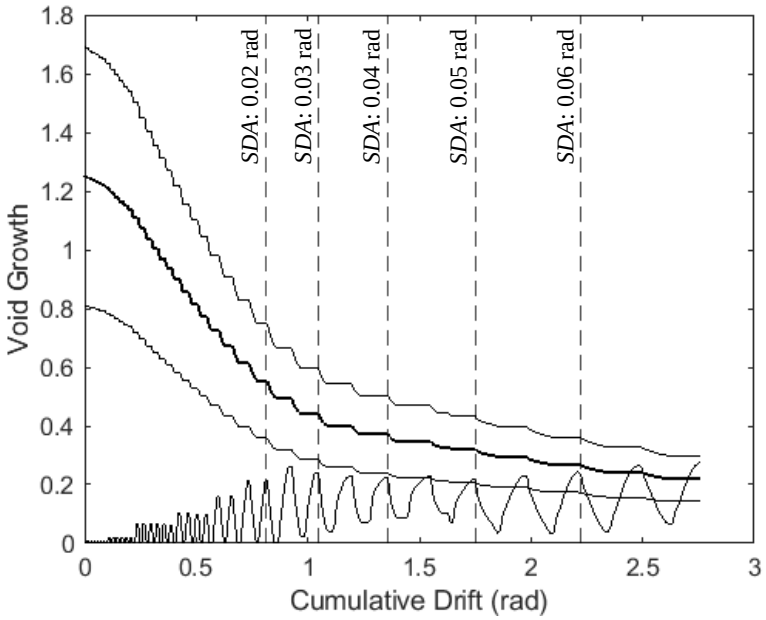

(b) Specimen C6 as Designed ($t_{cp}/t_{bf} = 0.6$)

Figure 8.16 Specimen C6 Void Growth at Beam Top Flange Surface as t_{cp} is Varied

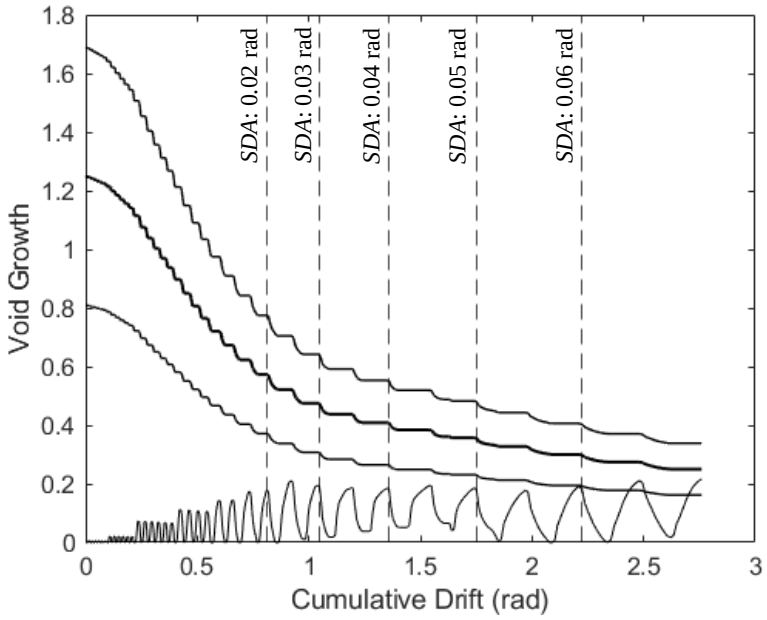

(c) Specimen C6 as Required by Eq. 7.10 ($t_{cp}/t_{bf} = 0.75$)

Figure 8.16 Specimen C6 Void Growth at Beam Top Flange Surface as t_{cp} is Varied (continued)

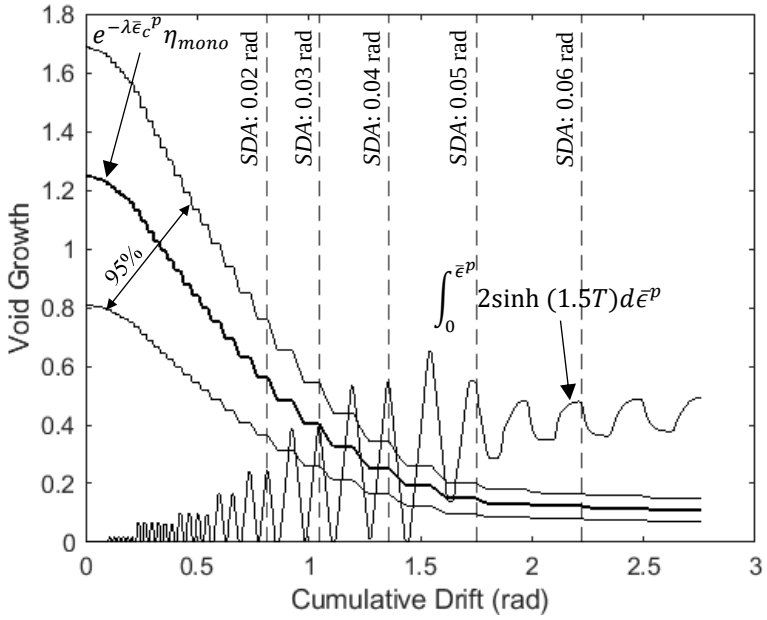

(a) At Beam Top Flange Surface

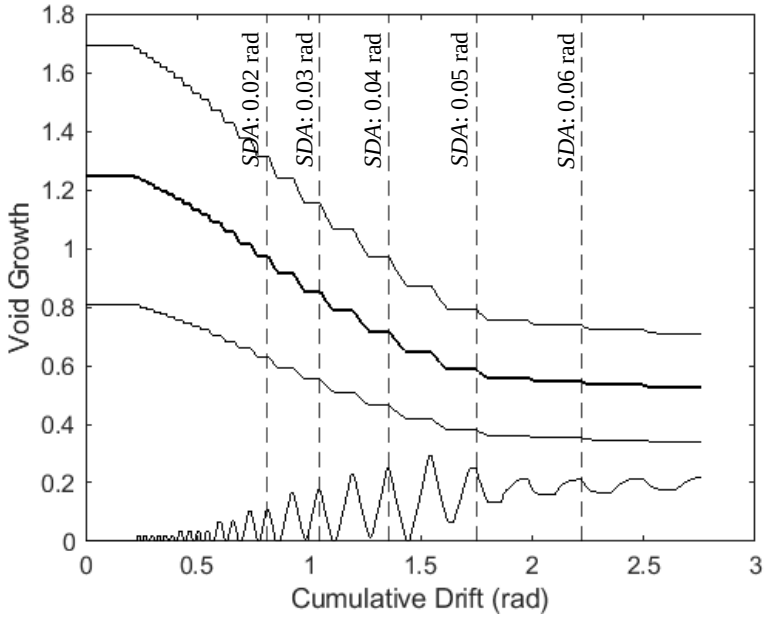

(b) 1/16 in. Below Beam Top Flange Surface

Figure 8.17 Specimen C3: Stress Triaxiality at Critical Location (No Continuity Plate)

9. SUMMARY AND CONCLUSIONS

9.1. Summary

Cyclic testing of ten full-scale steel moment frame connections was conducted to evaluate the efficacy of economized continuity plate and doubler plate weld details. Phase 1 of the testing included Specimens C3, C4, C5, C6, C6-G, and C7. The Phase 1 specimens were one-sided RBS connections tested in the upright position with a single 220-kip hydraulic actuator. Phase 2 of the testing included Specimens W1, W2, W3, and W4. The Phase 2 specimens were two-sided WUF-W connections tested in the horizontal position with two 500-kip hydraulic actuators. The testing was performed in displacement control to impose a prescribed drift according to the standard AISC cyclic loading sequence, as specified in the 2016 Seismic Provisions (AISC 341-16). In the case of the two-sided specimens, imposed drifts were applied equal and opposite on either side of the connection. These ten specimens are accompanied by Specimens C1 and C2, which were tested previously as part of a pilot project (Mashayekh and Uang 2018).

The Phase 1 specimens were carefully designed to investigate the applicable column limit states of Flange Local Bending (FLB) and Web Local Yielding (WLY). Web Local Crippling (WLC) was not investigated because it seldom governs the design of column stiffening of Special Moment Frames (SMFs). Three of these specimens were designed to directly challenge a criterion in AISC 341-16, which imposes a minimum thickness of an unstiffened column flange to be equal to the adjacent beam flange width divided by 6. This criterion is named as the Lehigh Criterion in this study after the institution of the founding study (Ricles et al. 2000). Specimen C7 challenged this criterion by reinforcing the governing column limit state, WLY, by the addition of a column web doubler plate. Since this doubler plate was not required based on the shear strength requirement of the panel zone, a new design methodology to design the vertical welds was applied

in lieu of the stringent requirements imposed by the provisions in AISC 341-16. FLB, WLY, and Lehigh Criterion were investigated because they directly influence the need and design of continuity plates.

The Phase 2 specimens were designed to subject the continuity plates to a higher level of force that is realized by the WUF-W connection and investigate the effect of a continuity plate stiffening of two-sided connections. Since a relatively high panel zone shear force was anticipated in the Phase 2 specimens, the doubler plate weldments were designed as per AISC 341-16 to develop the shear strength of the plate. Specimen W4 used a doubler plate that was terminated inside the continuity plates, while the other three specimens used an extended doubler plate detail.

All of the specimens that had continuity plates used two-sided fillet welds, not the code-specified complete-joint penetration (CJP) groove welds, to attach the continuity plate to the column flange and column web. Except for Specimens C6 and C6-G, the size of these fillet welds satisfy the proposed design rule of $w = (3/4)t_{cp}$, where w is the specified weld size, and t_{cp} is the thickness of the continuity plate. All of the W-shaped beams and columns were fabricated from ASTM A992 steel, while the continuity and doubler plates were fabricated from ASTM A572 Gr. 50 steel. Simulated field welding of the beam top and bottom flange CJP welds were performed in the shop with the frame standing in the upright position. Beam flange CJP welds used an E70T-6 (Lincoln Electric NR-305) electrode in the flat position. The beam web, the reinforcing fillet on the beam top flange backing, and the reinforcing fillet underneath the beam bottom flange were welded with an E71T-8 (Lincoln Electric NR-232) electrode in the vertical and overhead positions. The continuity plate and doubler plate welds were shop welded with an E70T-9C (Lincoln Electric OSXLH-70) electrode. The electrodes used for the continuity plate and doubler plate welding

satisfy the notch-toughness requirements of AWS D1.8 (2016) for demand critical welds. Specifically, they have a minimum notch-toughness of 20 ft-lb at 0°F and 40 ft-lb at 70°F.

All of the specimens passed the AISC Acceptance Criteria for SMF applications, i.e., all specimens achieved at least one cycle of 0.04 rad story drift angle while not experiencing a strength degradation resulting in a moment capacity less than 80% of the beam nominal plastic moment at the column face. After passing the Acceptance Criteria, the Phase 1 specimens eventually failed either through low-cycle fatigue of the beam in the reduced beam section (Specimens C4, C6-G, and C7) or through fracture of the beam top flange CJP weld (Specimens C3, C5, and C6). Specimens that failed through fracture of the beam top flange demonstrated initial tearing of the beam top flange CJP weld during the 0.03 rad drift cycles (e.g., see Figure 4.3). The tearing initiated at the toe of a prominent weld pass on the top surface of the CJP weld slightly outward of the re-entrant corner formed by the beam top flange and column flange. Continued ductile tearing of the weld occurred during each negative excursion when the beam top flange was loaded in tension. The fracture propagated through the weld metal at an angle of about 35° from vertical. Eventual fracture of the beam top flange CJP weld occurred primarily through cleavage and ductile fracture once the remaining material was overloaded.

The Phase 2 specimens all failed eventually through fracture of the beam top flange CJP weld. This fracture primarily initiated at the beam flange CJP weld root, where the root of the weld met the steel backing. Secondary initiation sites developed in the CJP weld from extreme local curvatures that developed due to the flange local buckling at the plastic hinge near the face of the column. Ductile tearing of the weld was observed during excursions which put the affected flange in tension. Tearing of the weld tended to propagate outward along the CJP weld bevel until a cleavage fracture occurred.

No damage was observed to any of the continuity plate welds or doubler plate welds. Except for the continuity plate of Specimen C5, yielding of the continuity plate was limited to $2.5\epsilon_y$ according to measurements of principal strains near the column flange edge. Specimen C5 was the only specimen that showed buckling of the continuity plate. The high strains observed in the continuity plate of Specimen C5 were due to local buckling of the plate.

Except for Specimens C2 and C5, the primary mechanism for energy dissipation was the plastic hinging of the beam. Instead, these two specimens developed significant energy dissipation in the panel zones. All of the specimens presented reserve energy ratios (Eq. 3.11) above 1.3, demonstrating that significant reserve energy dissipation potential exists beyond the AISC minimum criteria (including one cycle of 0.04 rad drift) for connection prequalification. The specimen which realized the least reserve energy capacity had a clear span-to-depth ratio of 6.8, slightly violating the limit imposed by the AISC 358-16 requirement of 7.0. The relatively poor performance of this specimen might be partially attributed to the relatively high beam moment gradient (i.e., high shear) of this specimen.

The experimental testing also included the first ever in situ recorded residual stresses of a continuity plate by using the hole-drilling method. The continuity plates measured as part of this test program included both a continuity plate with the newly proposed fillet weld design and conventional CJP groove welds. It was found on average that 15 ksi of longitudinal tension was realized in the longitudinal direction of the continuity plates. Moderately higher residual stresses in the fillet welded continuity plate is attributed to the sequence of welding to two plates adjacent to each other in a column and not due to the design of the weldments. Measurements also revealed significant transverse and shear residual stresses in the plates.

Following the experimental testing program, a detailed parametric finite element study was conducted. A detailed look at the response of the continuity plate during loading revealed moderate inelastic behavior with minor amounts of strain hardening. A good correlation between the predicted shear stress in the continuity plate (Eq. 7.6) while using a simplified von Mises yield surface was observed. It was also observed that beam lateral-torsional buckling results in a pronounced deviation from the assumption that the continuity plates are uniformly loaded. However, this was found to occur mostly during the later cycles of the loading (after 0.05 rad drift). Performing parametric studies on exterior RBS and interior WUF-W connections demonstrate the adequacy of a newly proposed width-to-thickness ratio of $0.56\sqrt{E/F_y}$ for local buckling control.

Parametric finite element analysis led to the development of modified column limit states for when a continuity plate (or more generally, a stiffener) is used. The existing column limit states of FLB (Eq. 1.26) and WLY (Eq. 1.27) are hypothesized to be correct prior to the installation of a stiffening element. This was observed during the experimental testing where unreinforced specimens developed yielding of the column web consistent with the assumed 2.5:1 diffusion assumed in AISC 360, and initiation of column hinging behind the beam flange. Finite element has reinforced the logical conclusion that these limit states cannot be true once the column is stiffened. Firstly, to achieve the 2.5:1 diffusion angle of force into the column web requires significant yielding at the center of loading (see Figure 5.9), which is prohibited once a continuity plate is present. Finite element analysis was used to solve for the diffusion angle (see Eq. 7.10) and revealed that a 1.5:1 diffusion angle was adequate (see Eq. 7.13). Secondly, the yield line mechanism (see Eq. 1.43) involves a deformation pattern that is unlikely once a continuity plate is present. It is therefore proposed that the FLB limit state be omitted, or simply set to a value of zero, when evaluating the force distribution into a stiffener (see Eq. 7.14). These two assertions

lead to the development of Eq. 7.15 to predict the continuity plate force at the plastic limit state. Finite element analysis demonstrates an excellent fit of Eq. 7.15 to the integrated continuity plate in the finite element models at the 0.04 rad story drift. It is also found that subscription to a diffusion angle of 1.5:1 leads to optimally thick continuity plates which reduce accumulated plastic strain in the beam flange. An additional parametric study reveals that using Eq. 7.16 provides an adequate estimate of the average shear flow along the vertical edges of a doubler plate. This analysis corroborates the results of Specimen C7, which show that the vertical weldments of a doubler plate may be sized based on the average shear flow of the doubler plate.

Incorporating an uncoupled ductile fracture metric into the finite element analysis reveals a critical location at the reentrant corner formed between the beam flange-to-column flange junction due to a combined effect of high triaxiality and significant plastic strain. The use of material properties from a representative E70T-6 (NR 305) weld electrode (Myers et al. 2014) results in variability of ductile fracture initiation for stiffened moment connections. It is revealed that there is a strong likelihood of ductile fracture propagation when the existing AISC 360 limit states are violated and a continuity plate is not used. The ductile fracture models reveal that a continuity plate designed per the proposed stiffened WLY limit state (Eq. 7.13) precludes ductile fracture for statistically poor-quality welds. Investigating a specimen which violates the Lehigh Criterion (Eq. 1.16) also shows ductile fracture initiation. Preliminary results show that this fracture may be arrested shortly depending on the quality of the weld material.

9.2. Conclusions

The following conclusions can be made

(1) All of the specimens tested in this program passed the AISC Acceptance Criteria for Special Moment Frames while violating the current requirements (FLB, WLY, and Lehigh Criterion) for SMF as stipulated in AISC 341-16.

(2) Three of eight RBS (including two specimens reported by Mashayekh and Uang 2017) connections failed through ductile tearing of the beam top flange CJP weld. The tear propagated for several tension excursions in a ductile manner through the weld metal until a brittle overload of the remaining flange material occurred. The propensity to fracture is attributed to variability in weld surface topology (i.e., how sharp the re-entrant corner is formed between the beam flange and column flange) and variability in weld notch toughness. This assertion is confirmed by the observation that the two nominally identical specimens (Specimens C6 and C6-G) failed through different mechanisms. Results from the CVGM indicate that ductile fracture of these specimens is precluded if a relatively high quality weld was present at the critical location.

(3) Including the pilot program (Specimens C1 and C2), a total of nine specimens were tested with fillet welds fastening the continuity plate to the column flange. Most of these specimens (seven) used a proposed fillet weld size, w, of $(3/4)t_{cp}$ based on the von Mises yield capacity of the continuity plate. The remaining two specimens were conservatively designed with $w = t_{cp}$. No damage was observed in any fillet welds. Therefore, the AISC 341-16 requirement to connect the continuity plate to the column flange with CJP groove welds is unnecessary.

(4) The continuity plate of Specimen C5 developed local buckling during the 0.04 rad drift cycles. The width-to-thickness ratio of this plate was 16. Three specimens (Specimens C6, C6-G, and W1) used a width-to-thickness ratio of 12 and did not develop any instability. A width-to-thickness ratio equal to $0.56\sqrt{E/F_y}$, which limits the width-to-thickness of continuity plates fabricated with Grade 50 material to 13.5, is recommended. Parametric finite element analysis reveals that this width-to-thickness limit is widely applicable to exterior and interior RBS and WUF-W connections.

(5) The Web Local Yielding (WLY) limit state in §J10.2 of AISC 360-16 appears to correspond well with the prediction for unstiffened column webs despite the application of cyclic loading. It is noted that column warping produces out-of-plane flexural strains in the column web, which are superimposed on the predicted web strains.

(6) The Flange Local Bending (FLB) limit state in §J10.1 of AISC 360-16 was found to be developed in a conservative way by selectively limiting parameters to conservative values. The level of conservatism that was enjoyed by the original derivation (Graham et al. 1960) is expected to drop off as heavier sections are selected. Although localized column flange yielding was observed on the inside face of the column flange at the beam flange level, a complete yield line mechanism was not observed.

(7) Finite element analysis reveals that the column limit states of WLY and FLB as currently stipulated in §J10 of AISC 360-16 do not sufficiently capture the plastic distribution of forces once a continuity plate is used. It is therefore suggested that once the decision has been made to stiffen the column by using these existing WLY and FLB limit states that a modified set of limit states be used which is compatible with resulting cruciform geometry.

A modified WLY limit state which decreases the diffusion of the beam flange force into the column web from a 2.5:1 slope to a 1.5:1 slope is compatible with the presence of a continuity plate. It is also found that the FLB limit state is unlikely to occur with the use of a continuity plate stiffener, and as such the FLB limit state should be taken as zero in the stiffened configuration. Continuity plates sized based on these criteria achieve a careful balance between permitting the continuity plate to yield when subjected to the expected hardened beam flange force without developing significant strain hardening. Continuity plates sized according to these amended limit states are found to be optimal in terms of reducing the accumulate plastic strain of the beam flange.

(8) A detailed review of the limiting column flange thickness of $b_{bf}/6$ given by §E3.6f.1(b) in AISC 341-16 provided in Chapter 1 reveals consecutive simplification of the limit from a low-cycle fatigue analysis performed on WUF-W connections. The violation of this criterion for three RBS specimens of Phase 1 (Specimens C3, C4, and C7) indicates that this criterion may be unnecessarily applied to RBS connections. As discussed in Chapter 1, this criterion triggers the mandatory use of continuity plates in a significant number of RBS connections, which may be relatively lightly loaded when compared to a typical WUF-W connection.

(9) Specimen C7 used a relatively lightly loaded doubler plate such that inelastic behavior of the plate was not anticipated. The vertical weldments attaching this plate to the inside faces of the column flanges were designed for the computed shear flow on the edge of the doubler plate based on the relative elastic stiffness. This fillet weld was undersized by a factor of 2, according to AISC 341-16, but did not demonstrate any damage during testing. The fillet weld throat was maintained through the doubler plate bevel by specifying that the bevel

angle shall be 45°. Parametric finite element studies reveal that the computed shear flow on the edge of the doubler plate, limited to yielding strength of the doubler plate, accurately predicts the average shear flow on the vertical edge of the doubler plate.

(10) One specimen, Specimen W3, used a doubler plate with a $(w_z + d_z)/t_{dp}$ ratio of 102, which violated the AISC 341-16 width-to-thickness limit of 90. No instability of this doubler occurred during testing.

(11) The lateral bracing force of a beam brace placed approximately $d/2$ away from the end of the RBS was limited to 5% of the flange force during the 0.05 rad drift cycles. During the 0.06 rad drift cycles, one specimen, Specimen C6-G, saw a lateral bracing force equal to 7.6% of the flange force. This column was a W24×176 shape, representing a deeper column section. Another specimen, Specimen C4, developed lateral bracing forces of 5.5% during the 0.06 rad drift cycles. In general, the deeper column sections require higher bracing forces, but the force requirements are bounded within the AISC 341-16 requirements during the cycles up to 0.05 rad drift.

(12) The average peak connection strength factor for the eight one-sided RBS connections of Phase 1 was determined to be 1.19. This is slightly higher than the recommended value of 1.15 as per AISC 341-16.

(13) The average peak connection strength factor for the four two-sided WUF-W connections of Phase 2 was determined to be 1.30. This results in a 10% reduction in estimated flange force when compared to the recommended value of 1.4 as per AISC 341-16.

(14) A duplicate RBS specimen that used the same design details and metallurgical properties was hot-dip galvanized before simulated field welding. This specimen performed better, completing one additional cycle of 0.05 rad drift and one additional cycle of 0.06 rad drift.

The better performance is not attributed to the effect of galvanization. Therefore, for the one specimen tested, it appears that the galvanization did not affect the strength or the ductility capacity of the connection.

(15) Detailed finite element models of the beam-to-column connection using the CVGM indicate that subscription to the newly proposed WLY and FLB limit states, which are compatible with a stiffener, result in prevention of the initiation of ductile fracture of the beam flange. This assertion uses the published variability of weld toughness to establish a 95% confidence interval.

REFERENCES

Abbas, E.K., (2015). "A low Cycle Fatigue Testing Framework for Evaluating the Effect of Artifacts on the Seismic Behavior of Moment Frames." *Ph.D Dissertation,* Virginia Polytechnic Institute, Blacksburg, VI.

ABAQUS. (2014). Abaqus Standard User's Manual, Version 6.14, Dassault Systemes Simulia Corp.

American Institute of Steel Construction (1992). "Seismic Provisions for Structural Steel Buildings." *ANSI/AISC 341,* Chicago, IL.

American Institute of Steel Construction (1997). "Seismic Provisions for Structural Steel Buildings." *ANSI/AISC 341,* Chicago, IL.

American Institute of Steel Construction (2005). "Seismic Provisions for Structural Steel Buildings." *ANSI/AISC 341-05,* Chicago, IL.

American Institute of Steel Construction (2010). "Seismic Provisions for Structural Steel Buildings." *ANSI/AISC 341-10,* Chicago, IL.

American Institute of Steel Construction (2016). "Specifications for Structural Steel Buildings." *ANSI/AISC 360-16,* Chicago, IL.

American Institute of Steel Construction (2016b). "Seismic Provisions for Structural Steel Buildings." *ANSI/AISC 341-16,* Chicago, IL.

American Institute of Steel Construction (2016c). "Prequalified Connections for Special and Intermediate Steel Moment Frames for Seismic Applications, including Supplement No. 2." *ANSI/AISC 358,* Chicago, IL.

American Institute of Steel Construction (1997). "AISC Advisory Statement on Mechanical Properties Near the Fillet of Wide Flange Shapes and Interim Recommendations January 10, 1997." *Modern Steel Construction,* Vol. 37, No. 2, pp. 18.

American Society of Civil Engineers 7 (2016). "Minimum Design Loads and Associated Criteria for Buildings and Other Structures." *ASCE/SEI 7-16,* Reston, VA.

American Society for Testing and Materials (2008). "Standard Test Method for Determining Residual Stresses by the Hole-Drilling Strain-Gage Method." *ASTM E837,* West Conshohocken, PA.

American Welding Society (2016). "Structural Welding Code–Seismic Supplement." *AWS D1.8,* Miami, FL.

Anderson, T.L. (2017). *Fracture Mechanics: Fundamentals and Applications*. Boca Raton, FL CRC Press.

Bao, Y., Wierzbicki, T. (2004). "On Fracture Locus in the Equivalent Strain and Stress Triaxiality Space," *International Journal of Mechanical Sciences,* Vol. 46, pp. 81-98.

Bjorhovde, R., Goland, L J., Benac, D. J. (1999). "Tests of Full-Scale Beam-to-Column Connections." *Internal Report*, Southwest Research Institute, San Antonio, Texas.

Carter, C. J. (1999). "Stiffening of Wide-Flange Columns at Moment Connections: Wind and Seismic Applications." *Design Guide 13*, AISC, Chicago, IL.

Chansuk, P., G Ozkula, Uang C.-M. (2018). "Seismic Behavior and Design of Deep, Slender Wide-Flange Structural Steel Beam-Columns: Phase 2 Testing," *Rep. No. SSRP-18/02*, University of California San Diego.

Chi, W.-M., Deirerlein G.G., Ingraffea, A. (1997). "Finite Element Fracture Mechanics Investigation of Welded Beam-Column Connections." *Report No. SAC/BD -97/05,* SAC Joint Venture, Sacramento, CA.

Chi, W.-M., Kanvinde, A.M., Deirelein, G.G. (2006). "Prediction of Ductile Fracture in Steel Connections using SMSC Criterion." *Journal of Structural Engineering*, ASCE Vol. 132, No. 2, pp. 171-181.

Chi, B., and Uang, C-M. (2002). "Cyclic Response and Design Recommendations of Reduced Beam Section Moment Connections with Deep Columns." *Journal of Structural Engineering*, ASCE, Vol. 128, No. 4, pp. 464-473.

Crisan, A. (2016) "Material Calibration for Static Cyclic Analysis," *Intersections/Intersectii*, Vol. 13, No. 2, pp. 43-58.

Deierlein, G. G., Chi W. M. (1999). "Integrative Analytical Investigation on the Fracture Behavior of Welded Moment Resisting Connections." *Report No. SAC/BD -99/15,* SAC Joint Venture, Sacramento, CA.

Dexter, R. J., Prochnow, S. D., Perez, M. I. (2001), "Constrained Through-Thickness Strength of Column Flanges of Various Grades and Chemistries." *Engineering Journal*, AISC, Vol. 38, No. 4, pp. 181-189.

Doswell, B. (2015) "Plastic Strength of Connection Elements." *Engineering Journal*¸ AISC, Vol 52, No. 1, pp. 47-66.

Dufailly, J., Lemaitre, J. (1995). "Modelling Very Low Cycle Fatigue," *International Journal of Damage Mechanics,* Vol. 4, No. 2, pp. 153-170.

Elkady, A., Lignos, G., D. (2014). "Analytical Investigation of the Cyclic Behavior and Plastic Hinge Formation in Deep Wide-Flange Steel Beam-Columns," *Earthquake Engineering*, Vol. 13, No. 4, pp. 1097-1118.

El-Tawil, S., Mikesell, T., Kunnath, S. K. (2000) "Effect of Local Details and Yield Ratio on Behavior of FR Steel Connections." *Journal of Structural Engineering*, ASCE, Vol. 126, No. 1, pp. 79-87.

El-Tawil, S., Vidarsson, E., Mikesell, T., Kunnath, S. (1999), "Inelastic Behavior and Design of Steel Panel Zones." *Journal of Structural Engineering*, ASCE, Vol 125, No. 2, pp. 183-193.

Engelhardt, M. D. (1999), "Design of Reduced Beam Section Moment Connections." *Proceedings, North American Steel Construction Conference*, Toronto, Ontario, May 19-21, 1999, AISC, Chicago, IL.

Engelhardt, M. D., Husain, A. S., (1993). "Cyclic-Loading Performance of Welded Flange-Bolted Web Connections." *Journal of Structural Engineering*, ASCE, Vol. 19, No. 12, pp. 3537-2550.

Engelhardt, M. D., Venti, M.J., Fry, G.T., Jones, S.L., Holliday, S.D. (2000), "Behavior and Design of Radius Cut Reduced Beam Section Connections." *Report No. SAC/BD-00/17*, SAC Joint Venture, Sacramento, CA.

Engelhardt, M. D., Sabol, T.A. (1997). "Seismic-resistant steel moment connections: developments since the 1994 Northridge earthquake." *Earthquake Engineering and Structural Dynamics*, Vol. 1, No.1, pp. 68-76.

Engelhardt, M. D., Winneberger, T., Zekany, A. J., Potyraj, T. J. (1998), "Experimental Investigation of Dogbone Moment Connections." *Engineering Journal*, AISC, Vol. 35, No. 4, pp. 128-139.

Federal Emergency Management Agency (2000a). "Recommended Seismic Design Criteria for New Steel Moment Frame Buildings." *FEMA 350*, Washington, DC.

Federal Emergency Management Agency (2000b). "Recommended Seismic Evaluation and Upgrade Criteria for Existing Welded Steel Moment Frame Buildings." *FEMA 351*, Washington, DC.

Federal Emergency Management Agency (2000c). "Recommended Postearthquake Evaluation and Repair Criteria for Welded Steel Moment-Frame Buildings." *FEMA 352*, Washington, DC.

Federal Emergency Management Agency (2000d). "Recommended Specifications and Quality Assurance for Steel Moment Frame Construction for Seismic Applications." *FEMA 353*, Washington, DC.

Federal Emergency Management Agency (2000e). "A Policy Guide to Steel Moment Frame Construction." *FEMA 354*, Washington, DC.

Federal Emergency Management Agency (2000f). "State of Art Reports on Steel Moment Frame Structures." *FEMA 355A through FEMA 355F*, Washington, DC.

Fung, Y.C. (1965). *Foundations of Solid Mechanics.* Englewood Cliffs, NJ. Prentice Hall.

Goel, S. C., Stojadinvic, B., Lee, K-H. (1997), "Truss Analogy for Steel Moment Connections." *Engineering Journal*, AISC, Vol. 34, No. 2, pp. 43-53.

Graham, J. D., Sherbourne, A.N., Khabaz, R. N., Jensen, C. D. (1960). "Welded Interior Beam-to-Column Connections." *Welding Research Council*, No. 63, pp. 1-28.

Gupta, U. (2013), "Cyclic Loading Analysis of Doubler Plate Attachment Details for Steel Moment Resisting Frames." *Masters Thesis*, University of Texas at Austin.

Hamburger, R. O. (2006). "Prequalified Connections for Special and Intermediate Steel Moment Frames for Seismic Applications." *Structures Congress*, ASCE.

Hamburger, R. O., and Malley, J.O. (2016), "Seismic Design of Steel Special Moment Frames: A Guide for Practicing Engineers." *Seismic Design Technical Brief No. 2*, National Institute of Standard and Technology, Gaithersburg, MD.

Hancock, J. W., Cowling, M. J. (1980). "Role of State of Stress in Crack-tip Failure Processes." *Metal Science*, Vol. 14, No. 8, pp. 234-304.

Hancock, J. W., Mackenzie, A. C. (1976), "On the Mechanisms of Ductile Failure in High-Strength Steels Subjected to Multi-Axial Stress-States." *Journal of the Mechanics and Physics of Solids*, Vol. 24, pp. 147-169.

Han, S. W., Moon, K.H., Jung, J. (2014), "Cyclic Performance of Welded Unreinforced Flange-Welded Web Moment Connections." *Earthquake Spectra*, Vol. 30, No. 4, pp. 1663-1681.

Han, S. W., Jung, J., Ha S. J. (2016), "Seismic Performance of WUF-W Moment Connections According to Access Hole Geometries." *Earthquake Spectra*, Vol. 32, No. 2, pp. 909-926.

Han, S. W., Kim, N., H, (2017), "Permissible Parameter Ranges of Access Hole Geometries for WUF-W Connections." *Earthquake Spectra*, Vol. 33, No. 2, pp. 687-707.

Hajjar, J. F, Dexter, R.J., Ojard, S.D., Ye, Y., Cotton S.C. (2003). "Continuity Plate Detailing for Steel Moment-Resisting Connections." *Engineering Journal*, AISC, Vol. 40, No. 4, pp. 189-211.

Hajjar, J. F., Leon, R. T., Gustafson, M. A., Shield, C. K. (1998). “Seismic Response of Composite Moment-Resisting Connections. II: Behavior.” *Journal of Structural Engineering*, ASCE, Vol. 124, No. 8, pp. 877-885.

Hansen, J.L. (2003). “Numerical Modelling of Welding Induced Stresses,” Doctoral Thesis, Technical University of Denmark, Lyngby, DK.

Ibrahim, O. A., Lignos, D. G., Rogers, C. A. (2016). "Proposed Modeling Approach of Welding Procedures for Heavy Steel Plates." *Engineering Structures*, Vol. 127, pp. 18-30.

Ibrahim, O. A., Lignos, D. G., Rogers, C. A. (2018). “Recommendations for Improved Welding Procedures for Thick Steel Plates Through Thermo-Mechanical Analysis,” International Journal of Steel Structures, Vol. 19, pp. 193-212.

Jia, L-J., Kuwamura, H. (2014). “Ductile Fracture Model For Structural Steel Under Cyclic Large Strain Loading,” *Journal of Constructional Streel Research*, Vol. 106, pp. 110-121.

Johnson, M. Q., Mohr, B., Barsom, J. (2000). “Evaluation of Mechanical Properties in Full-Scale Connections and Recommended Minimum Weld Toughness for Moment Resisting Frames.” *Report No. SAC/BD 00/14,* SAC Joint Venture, Sacramento, CA.

Kanvinde, A. M., Deierlein, G.G. (2004). “Micromechanical Simulation of Earthquake Induced Fracture in Steel Structures.” *Report No. TR. 145*, Blume Earthquake Engineering Center, Stanford University, Stanford, CA.

Kanvinde, A. M. (2017). “Predicting Fractures in Civil Engineering Steel Structures: State of the Art.” *Journal of Structural Engineering*, ASCE, Vol. 143, No. 3.

Kaufman, E. J, Xue, M., Lu, K-W., Fisher, J.W. (1996a). “Achieving Ductile Behavior of Moment Connections.” *Modern Steel Construction*, AISC, Vol. 36, No. 1, pp. 30-39.

Kelly, P. A. (2019 “Mechanics Lectures Notes: An Introduction to Solid Mechanics.” Available at: http://homepages.engineering.auckland.ac.nz/~pkel015/SolidMechanicsBooks/index.html

Kuwamura, H., Akiyama, H. (1994). “Brittle Fracture under Repeated High Stresses,” *Journal of Constructional Steel Research*, Vol. 29, pp. 5-19.

Kuwamura, H. (1997). “Ductile Crack and Trigger of Brittle Fracture in Steel,” *ASCE Journal of Structural Engineering*, Vol. 123, No. 6, pp. 729-735.

Kuwamura, H. (1997b). “Transition Between Fatigue and Ductile Fracture in Steel,” *ASCE Journal of Structural Engineering*, Vol. 123, No. 7, pp. 864-870.

Lee, C-H., Jeon, S-W., Kim, J-H., Uang, C-U. (2005), “Effects of Panel Zone Strength and Beam Web Connection Method on Seismic Performance of Reduced Beam Section Steel Moment Connections.” *Journal of Structural Engineering*, ASCE, Vol. 131, No. 2, pp. 1854-1865.

Lee, C-H., Cotton. S. C, Hajjar, J. F., Dexter, R. J. (2005a), "Cyclic Behavior of Steel Moment-Resisting Connections Reinforced by Alternative Column Stiffener Details I. Connection Performance and Continuity Plate Detailing." *Engineering Journal*, AISC, Vol. 42, No. 4, pp. 189-214.

Lee, C-H., Cotton. S. C, Hajjar, J. F., Dexter, R. J. (2005b), "Cyclic Behavior of Steel Moment-Resisting Connections Reinforced by Alternative Column Stiffener Details II. Panel Zone Behavior and Doubler Plate Detailing." *Engineering Journal*, ASCE, Vol. 42, No. 4, pp. 189-214.

Lemaitre, J., Chaboche, J.-L. (1990). "Mechanics of Solid Materials", *Cambridge International Press*

Macdonald, K. A. (2011). Fracture and Fatigue of Welded Joints and Structures, Woodhead Publishing, Cambridge, UK.

Malley, J. O., Frank, K. (2000), "Materials and Fracture Investigations in the FEMA/SAC Phase 2 Steel Project." *Proceedings, 12th World Conference on Earthquake Engineering*, Auckland, New Zealand.

Mandal, N. R, Sundar, C. V. M. (1997). "Analysis of Welding Shrinkage," Welding Research Supplement, Vol. 6, pp. 233-238.

Mashayekh, A. (2017). "Sloped Connections and Connections with Fillet Welded Continuity Plates for Seismic Design of Special Moment Frames." *Ph.D Dissertation*, Department of Structural Engineering, University of California San Diego, CA.

Mashayekh, A., Uang, C.-M. (2018). "Experimental Evaluation of a Procedure for SMF Continuity Plate and Weld Design." *Engineering Journal*, AISC, Vol 55, No. 2, pp. 109-122.

Mashayekh, A., Uang, C.-M. (2018). "Cyclic Response of Slopes Steel Moment Connections," *ASCE Journal of Structural Engineering*, Vol 145, No. 7.

Matos C. G., Dodds, R.H. (2000). "Modelling the Effects of Residual Stresses on Defects in Welds of Steel Frame Connections." *Engineering Structures*, Vol. 22, No. 9, pp. 1103-1120.

Mao, C., Ricles, J., Lu, L-W., Fisher, J. (2000). "Effect of Local Details on Ductility of Welded Moment Connections." *Journal of Structural Engineering*, ASCE, Vol. 127, No. 9, pp. 1036-1044.

Micro-Measurements (2010). "Measurement of Residual Stresses by the Hole-Drilling Strain Gage Method," *Tech Note TN-503*, Raleigh, NC.

Miller, D.K. (2015). "Welded Connections—A Primer for Engineers," *Steel Design Guide 21*, AISC, Chicago, IL.

Myers, A. T., Deierlein, G. G., Kanvinde, A. M. (2014). "Testing and Probabilistic Simulation of Ductile Fracture Initiation in Structural Steel Components and Weldments," *Report No. TR. 170.* Blume Earthquake Engineering Center, Stanford University, Stanford, CA.

Pang, H. L., Pukas, S. R. (1989). "Residual Stress Measurements in a Cruciform Welded Joint Using Hole Drilling and Strain Gauges," Strain, Vol. 7, No. 14. pp. 9-15.

Paret, T. F, (2000), "The W1 Issue. I: Extent of Weld Fracturing During Northridge Earthquake." *Journal of Structural Engineering,* ASCE, Vol .126, No. 1, pp. 10-18.

Popov, E. P., Amin, N.R., Louie, J.C., Stephen, R.M. (1986). "Cyclic Behavior of Large Beam-Column Assemblies." *Engineering Journal,* AISC, Vol. 23, No. 1, pp. 9-23.

Popov, E. P., Pinkney, B., (1971). "Cyclic Yield Reversals in Steel Building Connections." *Engineering Journal,* AISC, Vol. 8, No. 3, pp. 66-79.

Popov, E. P., Blondet, M., Stepanov, L., Stojadinovic, B. (1996). "Full-Scale Beam-Column Connection Tests." *Experimental Investigations of Beam-Column Subassemblages, Report No. SAC 96-01, Part 2,* Applied Technology Council, Redwood City, CA.

Prochnow, S. D., Dexter, R. J., Hajjar, J. F., Ye, Y., Cotton, S. C. (2000). "Local Flange Bending and Local Web Yielding Limit States in Steel Moment Resisting Connections." *Structural Engineering Report No. ST-00-4,* University of Minnesota, Minneapolis, MN.

Reynolds, M., Uang, C-M. (2019): Alternative Weld Details and Design for Continuity Plates and Doubler Plates for Applications in Special and Intermediate Moment Frames, Report No. SSRP 19/03, University of California San Diego, USA.

Rice, J. R., Tracey, D. M. (1969), "On the Ductile Enlargement of Voids in Triaxial Stress Fields." *Journal of the Mechanics and Physics of Solids,* Vol. 17, pp. 201-217.

Ricles, J. M, Mao, C., Lu, L-W., Fisher, J.W. (2000). "Development and Evaluation of Improved Details for Ductile Welded Unreinforced Flange Connections." *Report No. SAC/BD-00/24,* SAC Joint Venture, Sacramento, CA.

Ricles, J. M., Mao, C., Lu, L-W., Fisher, J. M. (2002), "Inelastic Cyclic Testing of Welded Unreinforced Moment Connections." *Journal of Structural Engineering,* ASCE, Vol. 128, No. 4, pp. 429-440.

Ricles, J. M., Mao, C., Lu, L-W., Fisher, J. M. (2003), "Ductile Details for Welded Unreinforced Moment Connections Subjected to Inelastic Cyclic Loading." *Engineering Structures,* Vol. 25, No. 5, pp. 667-680.

Rolfe, S. T. (1977). "Fracture and Fatigue Control in Steel Structures," *AISC Engineering Journal*, Vol 14, No. 1, pp. 2-15.

Sherbourne, A. N., Jensen C. D. (1957). “Direct Welded Beam Column Connections.” *Report No. 233.12*, Fritz Laboratory, Lehigh University, Bethlehem, PA.

Sherry, W. P. (2017). “Determination of Intrinsic Stresses Using the Hole-Drilling Method,” Masters Thesis, Tennessee Technological University, Cookeville, TN.

Shirsat, P. S., Engelhardt, M. D. (2012), “Preliminary Analysis of Doubler Plate Attachment Details for Steel Moment Frames.” *Proceedings, 15th World Conference on Earthquake Engineering*, Lisbon, Portugal.

Smith, C. M., Deierlein, G. G., Kanvinde, A. M. (2014). “A Stress-Weighted Damage Model for Ductile Fracture Initiation in Structural Steel Under Cyclic Loading and Generalized Stress States.” *Report No. TR. 187.* Blume Earthquake Engineering Center, Stanford University, Stanford, CA.

Soete, W., Vancrombrugge, R. (1950). “An Industrial Method for the Determination of Residual Stresses,” *Proceedings of the Society for Experimental Stress Analysis*, Vol 9, No. 1, pp. 17-28.

Tebedge, N., Alpsten, G. A., Tall, L. (1971). “Measurement of Residual Stresses a Study of Methods,” Report No. 337.8, Fritz Engineering Laboratory, Lehigh University, Bethlehem, PA.

Tide, R. H. R. (2000). “Evaluation of Steel Properties and Cracking in the “k”-Area of W Shapes.” *Engineering Structures*, Vol. 22, No. 2, pp. 128-134.

Tran, T. T, Hasset, P.M., Uang, C-M. (2013). “A Flexibility-Based Formulation for the Design of Continuity Plates in Steel Special Moment Frames.” *Engineering Journal*, AISC, Vol. 50, No. 3, pp. 181-200.

Tremblay, R., Timler, P., Bruneau, M., Filiatrault, A. (1998). “Performance of Steel Structures during the 1994 Northridge Earthquake.” *Canadian Journal of Civil Engineering*, Vol. 22, No. 2, pp. 338-360.

Uniform Building Code (1988). *International Conference of Building Officials*, Whittier, CA.

Uang, C.-M., Yu, Q.-S., Noel, S., Gross, J. (2000). “Cyclic Testing of Steel Moment Connections Rehabilitated with RBS of Welded Haunch.” *Journal of Structural Engineering*, Vol. 126, No. 1, pp. 57-68.

Uang, C.-M., Bondad, D. (1996). “Static cyclic Testing of pre-Northridge and Haunch Repaired Steel Moment Connections.” *Rep. No. SSRP-96/02*, SAC, Sacramento, CA.

Yee, R. K., Paterson, S. R., Egan, G. R. (1998), “Engineering Evaluations of Column Continuity Plate Detail Design and Welding Issues in Welded Steel Moment Frame Connections.”

Welding for Seismic Zones in New Zealand, Aptech Engineering Services, Inc., Sunnyvale, CA.

Zhou, H., Wang, Y., Shi, Y., Xiong, J., Yang, L. (2012). "Extremely Low Cycle Fatigue Prediction of Steel Beam-to-Column Connection by Using Micro-Mechanics Based Fracture Model," *International Journal of Fatigue*, Vol. 48, pp. 90-100.